Zh. Zhang

Pelton Turbines

Pelton Turbines

Zh. Zhang

Pelton Turbines

Springer

Zh. Zhang
Swiss Federal Institute of Technology in Zurich
Zurich
Switzerland

Foreword

Pelton turbines are classical hydraulic machines to convert stream flow energy into electricity for medium to high heads. Although invented already in the 1870s by the American Lester Allan Pelton, his runner design is still largely used today in the hydroelectric power industry. Compared to Francis turbines, Pelton wheels offer particularly favourable partial load efficiency degrees and are preferred for low flow rates. They are unrivalled for very high heads above some 700 m, so that their application is mainly in the high mountain regions all over the world. Pelton runners exist in all size classes, from very small Pico hydro applications, e.g. to use tap water from water delivery systems, to the largest units with capacities of more than 400 MW like in the Swiss Bieudron hydropower scheme with a current world-record head of 1883 m.

Despite the importance of these hydraulic impulse turbines in the hydropower domain, there is only marginal fundamental literature on their theory and design. This textbook of Dr. Zh. Zhang fills this gap, containing a broad analytical treatment of flow processes in real-world Pelton turbines, which renders it so unique and valuable for both the scientific and professional communities. Dr. Zhang not only has a sound scientific background in this topic, stemming from laser-based instrumentation to small and large-scale experimental investigations, but also successfully integrates his professional experience originating from decades of work in the hydraulic machinery or related industry into this textbook.

While the design of turbines is traditionally part of mechanical engineering, Dr. Zhang also demonstrates that it cannot stand alone without considering the solids contained in the power water in many Pelton turbine applications. Because often run-off from mountain streams is used, the fluid at Pelton wheels is a water–sediment mixture rather than a monophase liquid, despite significant efforts on the civil engineering side to exclude the solids from the water using desilting schemes and new types of flushing systems. At relative velocities of up to some hundreds of kilometres per hour between jet and runner, depending on the head, the impact energy of the flow is so enormous that even the most sophisticated coatings using tungsten carbide, for instance, cannot resist these loads on the long term. An

optimized turbine design is thus also needed to counter hydroabrasive wear phenomena, which grow in extent due to increased sediment production as a result of climate change.

I am convinced that this up-to-date textbook will have a great success among researchers and engineering professionals in the fields of hydroelectricity and hydromechanics, not least against the background of the growing worldwide need for sustainable energy production from hydropower.

Zurich, Switzerland   Robert M. Boes
January 2016

Preface

Pelton turbines have been used for over 100 years to convert hydraulic energy into mechanical work, as well as to generate electricity. The experiences achieved during this long period have enabled Pelton turbines nowadays to be designed and built with high hydraulic and mechanical performances. Nevertheless, there had been until the end of the last century a noticeable lack of fundamental explanations to the hydromechanics of this type of turbines.

To extend the general knowledge of Pelton turbines, the author started his experimental research on jet flows in Pelton turbines at the beginning of the twenty-first century within an R&D project of the company Andritz Hydro (former VA TECH Hydro) in Switzerland. Extended studies with the entire hydromechanics of Pelton turbines as a part of research and development activities were carried out at the Oberhasli Hydroelectric Power Company (KWO AG) from 2004 to 2007. The results achieved through these research works have already been published in both journals and conference proceedings and later summarized in German in the textbook "Freistrahlturbinen", Springer-Verlag, 2009. The current book originates from that German version and is extended with new knowledge, partly obtained at the Laboratory of Hydraulics, Hydrology and Glaciology (VAW) of ETH Zurich.

In this textbook, the foundations of hydromechanics of Pelton turbines are presented from an engineering viewpoint of hydraulic designs and optimizations. In terms of reference, the content thus concentrates on the detailed flow processes and their quantitative descriptions regarding all relevant hydro-mechanical aspects. This includes the computational methods for determining the interaction between the jet and the rotating buckets, quantifying diverse flow losses in the system and specifying flow phenomena like the frictional effect and load shedding, which leads to the acceleration of the Pelton wheel rotation towards its runaway speed. The book also reveals the possible potential for further enhancing the system efficiency by indicating the most significant sources causing the greatest efficiency drops. It, thus, provides a useful reference with design and operational criteria for practical applications.

For all these reasons, this textbook is suitable for development and design engineers of Pelton turbines, as well as for those working in the field of fluid machinery. The examples presented in this book generally apply to students in advanced "fluid mechanics". The author would especially welcome a lot of mechanical laws and rules presented in the textbook to be implemented in the context of Computational Fluid Dynamics (CFD). This should greatly contribute to the simplification of the CFD simulations without having always to start from the basic foundations, i.e. the Navier–Stokes equations.

Zurich, Switzerland   Zhengji Zhang
January 2016

Contents

Chapter 1
Introduction

In nature, hydraulic energy is a type of usable energy which can be directly converted into mechanical energy. It has since more than one hundred years mainly been utilized for the production of electricity. As a most important type of the renewable energy, hydraulic energy shows its very broad perspective in the future. More and more hydropower plants will be built or refurbished worldwide. In many countries, hydraulic energy will be the main source for producing electrical energy. In Norway, for example, almost the entire production of electricity is from the hydropower. According to the Swiss Federal Office of Energy (BFE 2004), the hydropower provides about 60 % of the total electricity production in Switzerland.

The hydraulic energy in our nature exists in two main forms: the flowing water in rivers and the stored water in reservoirs. Accordingly, different types of hydraulic turbines are used for generating electricity.

Among various types of hydraulic turbines, the Pelton turbine (Fig. 1.1), which is also called the constant-pressure turbine, represents an important and probably also the most widely applied turbine type. The first Pelton turbine was invented by Lester Allan Pelton in 1879 and tested successfully. The turbine is mainly used in mountainous areas where the available water, for example, is stored in a lake or reservoir which lies a few hundred to 1800 m above the turbine machines. The turbine power ranges from several kilowatts to 400 MW (Angehrn 2000). In Switzerland and Austria, Pelton turbines are predominantly installed in the Alpine regions, most of them since more than 80 years ago.

A Pelton turbine essentially consists of a Pelton wheel with blades of the bucket form and one or more injectors that generate the high-speed jets when leaving the nozzle. The energy transfer from the high-speed jet onto the Pelton wheel is performed through the interaction between the jet and the rotating buckets. Based on this kind of hydraulic and mechanical interactions, the Pelton turbine technology is divided into hydromechanics and structural mechanics. Both categories represent a broad spectrum of state-of-the-art technologies and comprise the entire technical and engineering aspects like the efficiency, reliability, and lifetime. Thus, on the one hand, maximum hydraulic efficiency should be achieved in the design of the

Fig. 1.1 Two-injector Pelton turbine installed at the Oberhasli Hydroelectric Power Company (KWO). Pressure head $H = 670\,\text{m}$, flow rate $\dot{Q} = 8.25\,\text{m}^3/\text{s}$, rotational speed $n = 428.6\,\text{rpm}$, power output $P = 48.6\,\text{MW}$

bucket profile, while on the other hand, the material safety and the expected lifetime must be assured.

1.1   Hydromechanics of the Pelton Turbine

1.1.1   General Developments

For Pelton turbines, hydromechanics serves as the core technology which describes the form and the extent of the exploitation of the hydraulic energy. This includes the generation of the high-speed jet and the power exchange between the jet and the Pelton wheel, aiming to achieve the maximum exploitation of the available hydraulic energy. Based on the present state-of the-art technologies, hydraulic efficiencies of about 90 % can be commonly achieved in both the new constructions and the refurbishment of existing Pelton turbines. This achievement is mainly attributed to the significant improvement of the jet quality as well as to the experimental and the

operational optimizations of the interaction between the jet and the Pelton buckets. In a great number of literature on fluid machines, such as Thomann (1931), Pfleiderer and Petermann (1986), Quantz and Meerwarth (1963), Bohl (2004, 2005), Menny (2005), Giesecke and Mosonyi (2005), and Sigloch (2006), general operation conditions and design rules for Pelton turbines can be found.

Despite the importance and the long history of Pelton turbines, nearly no advanced hydromechanical applications can be found in this engineering design specialty. At least physical flow processes in a Pelton turbine have not yet been as well understood as in other fluid machines such as pumps and Francis turbines. In hydraulic design of a Pelton turbine, the related practical experiences have thus always played a major role besides applying general design rules. Even the optimum bucket number of a Pelton wheel, for instance, is determined only by experience or model tests without relying on any hydromechanical background. The main reasons for the noticeable lack of knowledge regarding basic hydromechanics of Pelton turbines are, according to Zhang and Casey (2007), the complex flow conditions in both the high-speed jet and the unsteady interaction between the high-speed jet and the rotating Pelton buckets. These flow characteristics are fundamentally different from those in other types of fluid machines and also show the difficulty in the analytical descriptions of the entire flow processes, especially when the average shaft power needs to be determined from the unsteady flow and thus unsteady power exchange.

1.1.2 Development of Experimental Methods

The hydromechanical optimization of Pelton turbines is primarily aiming to achieve the maximum hydraulic efficiency. Owing to the difficulties in the calculation of unsteady flow processes, previous studies of Pelton turbines are almost exclusively confined to experimental methods and model tests. The experimental investigations have been primarily related to the measurements of the jet and the water flow both in fixed and rotating buckets, while the model tests are mainly conducted for flow visualization and measurement of the system efficiency.

In the experimental studies of high-speed jets, conventional methods of using Pitot tubes and techniques of flow visualizations have for a long time played an important role. The Pitot tubes were used for measurements of the flow distribution within the jets. In this regard, we refer to the research applications, among others, by Berntsen et al. (2001) and Brekke (2005). Photography and similar methods of flow visualizations have often been used to mainly view the surface structure and the stability of the jet. In the field test of a Pelton turbine, for instance, Staubli and Hauser (2004) applied the photography for direct determination of the jet expansion after leaving the injector nozzle. The measurements based on Pitot tubes and photography indeed could hardly provide any accurate information about the structure and dynamics of the jet. New advanced knowledge on the structure and dynamics of real jet flow has been achieved by Zhang et al. (2000a, b, 2003)

through flow field measurements by means of laser Doppler anemometry (LDA), which allows nonintrusive optical access in the high-speed jet. In particular, the secondary flow structure in high-speed jets, even very weak, can be exactly measured by the dual measurement method (DMM) developed by Zhang (2005). Existence of secondary flow in the jet, as confirmed by measurements, basically explains the observations of the jet instability and the disturbance on the jet surface. Essential characteristics of the jet flows and experimental investigations by means of the LDA measurement technique have been summarized by Zhang and Casey (2007).

Experimental measurements of flows in Pelton buckets are associated with great hindrance because of the difficult access to the flow there. Therefore, only flow visualization on the interaction between the jet and the rotating buckets as well as on the exit flow out of the buckets could be accomplished in most earlier investigations. The nonstationary spreading of water in the rotating buckets could not yet be reliably captured by experimental measurements. Very often, therefore, the water velocity relative to the rotating buckets has been assumed to be constant. However, this assumption, in fact, is realistic only for inviscid fluids and, additionally, when the effect of the centrifugal force is neglected. In many cases, nevertheless, the assumption is acceptable if only a qualitative flow and flow distribution in the rotating bucket is sought. Else, one must clearly specify when and for what purposes exact quantitative knowledge of the water flow in the rotating bucket would be required. To determine the hydraulic power exchange between the water and the rotating buckets, it is basically sufficient to only consider the flows at the bucket entry and exit, without scrutinizing the exact flow process in the bucket.

Since the beginning of this century, measurements have been widely extended to the pressure distributions on the bucket surface in the model turbine. Corresponding pressure measurements in the rotating Pelton buckets were published, for example, by Angehrn (2000), Kvicinsky et al. (2002), and Perrig et al. (2006). The pressure measurements in a Pelton bucket which is fixed on the ground of the laboratory were carried out by Zoppé et al. (2006). Strictly speaking, the measurement result from a fixed bucket should not and cannot be applied to a rotating bucket, because the available volume forces that determine the flow in the bucket are not the same. It should also be mentioned here that most pressure measurements were carried out with the aim to validate the numerical simulation of the flow in the rotating bucket. The pressure distribution itself on the bucket surface is not of practical significance, except for the simulation of the abrasive particle motion in the flow towards the bucket surface (see Chap. 22).

Most hydraulic measurements up to now have been carried out in the laboratory with model turbines. Since no reliable analyses of the flow in the Pelton turbines have been conducted, model tests remain the only way to verify and optimize the hydraulic design of a prototype Pelton turbine. As a matter of fact, there is always a discrepancy in the hydraulic efficiency between model and prototype Pelton turbines. One of the many reasons for this hydraulic discrepancy is the significant difference in the Reynolds number between the model and the prototype turbines. For this reason, the hydraulic efficiency, which is measured at a model turbine, has

always to be scaled up to the prototype turbine. Such a calculation was worked out by Grein et al. (1986) based on a great number of measurements. It was improved and simplified later by Zhang (2006).

Based on experimental studies of various Pelton wheels, Taygun (1946) could, e.g., optimize the number of buckets of a Pelton wheel as a function of the ratio of the Pelton wheel diameter to the jet diameter. In fact, this diameter ratio also represents the hydraulic specification of a Pelton turbine, i.e., the specific speed.

Continuous model tests of Pelton turbines in the past have been leading to an achievement of the hydraulic efficiency of over 90 %. Further optimization and enhancement of turbine efficiencies through model tests, however, seem to be difficult to achieve, because the potential for further improvement cannot be accurately revealed, identified, and quantified, neither by flow visualization nor by measurements of the system efficiency. Because of the related high costs in the model tests and mainly because of the advanced achievements in both the analytical calculations and the numerical simulations based on computational fluid dynamics (CFD), the model tests increasingly lose their original significance.

1.1.3   Development by Numerical CFD Methods

Another method for investigating the flows in Pelton turbines is numerical simulation based on computational fluid dynamics (CFD). Application of the CFD method to the hydromechanics of Pelton turbines began in the late 1990s of the last century and is becoming increasingly significant. Mention should be made of investigations carried out, for instance, by Kubota et al. (1998), Parkinson et al. (2002, 2005), Muggli et al. (2000), as well as Mack and Moser (2002). The main topic of investigations by the CFD method has focused on the interactions between the jet and the rotating buckets as well as the relative flows within the buckets. These are the flows that are so far not easily accessible by experimental measurements. CFD simulations are therefore likely considered as an available way for investigating complex flows in Pelton turbines, provided that they are reliable and able to reveal the possibility of improving the system efficiency. Until the fulfillment of these requirements, however, there is still a long way to go. Since there is hardly any available direct measurement of the flow in the rotating buckets, the numerical simulations can yet hardly be validated in most cases. The aforementioned pressure measurements on the inside of a Pelton bucket, as carried out by Kvicinsky et al. (2002), Perrig et al. (2006) and Zoppé et al. (2006), have all been conducted for validation purposes of the CFD simulations.

The necessity of validation of CFD simulations has its background in the fact that the CFD simulations are based on the use of particular and different turbulence models in solving the Navier-Stokes equations. So the computational results might first have to be validated. In implementations of the flow in Pelton turbines, the computational accuracy of the results of the CFD method is further endangered by the fact that in addition to the assumed turbulence model, the free surfaces of both

the water jet and water sheet in the bucket must be always assumed as a finite fluid domain of a two-phase flow. Furthermore, although the flows, e.g., in the rotating bucket, can be simulated by CFD methods, the physical basis of the related flow phenomena usually cannot be satisfactorily explained. With other words, it could not be made clear, for instance, how the centrifugal and Coriolis forces will, respectively, influence the flow. Because of these facts, it so happens that each time when the operation or design parameters change, a new expensive and complex CFD simulation must in general be performed.

1.1.4 Developments of the Analysis Methods

Based on the long history, continuous design, and operation optimizations in the past, primarily through model tests, Pelton turbines actually have already reached a very high technical level of their system efficiency. Further improvement of the system efficiency is almost only possible if the related improvement potential can be demonstrated by thorough analyses of all relevant flow mechanical processes taking place in the Pelton turbine. This actually means nothing else than to track first all the possible sources of the system's efficiency losses and then to accurately estimate their respective magnitudes. The second step is clearly based on the detailed hydromechanical analyses, even under certain assumptions. In other words, the outcomes and conclusions from such analyses do serve as guidance for further and purposeful hydromechanical optimizations.

   To describe the dynamical flow processes in a Pelton turbine, basically the Eulerian and the Lagrangian methods should be combined and applied. This is justified by the fact that the unsteady motion of the water sheet in the rotating bucket can be described in a first approximation by tracking the representative water particles. In fact, the Lagrangian method behaves in this case similarly as a method in analytical mechanics. This is so, because the movement of the water sheet in the rotating bucket takes place under nearly constant pressure. As for a solid particle only the centrifugal, Coriolis and inertial forces are active. The corresponding equations of motion could long be derived; however, they have not been treated further for deriving any useful conclusions. Kishioka and Osawa (1972) are among few research groups, who tried in their analytical studies to describe the flow in a rotating Pelton bucket and to determine the losses associated with various flow patterns. Apparently, the analyses were not further pursued because of the complex fluid mechanical relations and the related difficulties in the emergent inferences.

   Advanced analyses of the fluid mechanics in the rotating buckets were carried out by Zhang and Müller (2005, 2006, 2007) and Zhang (2007a, b, 2009a, b, c). The derived *jet layer method* in connection with the so-called *invariance equation* procedure highly contributes to the simplifications of calculating the unsteady flow in the rotating Pelton buckets. Especially, a sophisticated analysis shows that the viscous friction between the water sheet and the bucket surface represents the

most significant cause for the efficiency loss in a Pelton turbine. The corresponding relation to the viscous flow friction has been referred to as *flow friction theorem* (FFT). It provides for the first time the physical and the mechanical confirmation that in favor of the hydraulic efficiency the inner surface of Pelton buckets should be designed as smoothly as possible. It thus indicates that reducing the friction loss in the bucket flows is the most effective way for enhancing the system's efficiency.

1.1.5   Further Hydraulic Aspects

Other hydraulic aspects of Pelton turbines are confirmed as follows:

– Regulation of the flow rate through the injector concerning the water hammer in the system
– Determination of the hydraulic forces exerted on the servomotor of the injector
– Interaction between the high-speed jet and the rotating buckets at the bucket entry
– Hydraulic force arising from the momentum exchange
– Exit flow conditions for the flows out of the buckets
– Minimum offset angle between two adjacent injectors at a multi-jet Pelton turbine
– Bucket shape
– Water spray
– Design of the turbine casing
– Runaway speed of the Pelton wheel after the load rejection on the side of the generator

All these points are worth mentioning and highly relevant for the hydraulic design of a Pelton turbine. Some of them can be easily examined; some are still relying on empirical estimations. Worth mentioning is that among all these points, the exact determination of the runaway speed of the Pelton wheel for the load rejection was derived by Zhang and Müller (2007). The method also applies to accurately calculating the entire acceleration process of the Pelton wheel rotation after the load rejection and before reaching the maximum runaway speed.

1.2   Structural Mechanics of Pelton Turbines

Besides the hydromechanical specification of Pelton turbines, the structural mechanical design represents another important aspect of Pelton turbine technology. It pertains to the functionality and reliability of all elementary components, including the distributor, injector, wheel, turbine casing, and so on. In particular, the periodic mechanical loading of the Pelton buckets requires safe mechanical design and the selection of proper materials. All other mechanical components such as the

servomotor and the deflector must be designed in accordance with the maximum possible loads in terms of hydraulic forces.

One of the biggest problems in the operation of Pelton turbines is fatigue of the material and cracking of the Pelton buckets in the root region, where the greatest material stress is recorded as a result of the largest periodic bending moment. About the material strength of Pelton buckets, numerous studies have been conducted. These include, e.g., investigations carried out by Grein et al. (1984) and Grein and Angehrn (1986). From experience gained in the operation of Pelton turbines, the upper stress limit of materials under periodic loads has become reliably well known. It apparently depends on the material properties and is distinguished between the manufacturing processes. While earlier Pelton wheels were almost all made of cast steel or the Pelton buckets were screwed on a wheel disk, Pelton wheels nowadays are often directly machined from a forged stainless steel disk. A significant increase in the resistance capability of Pelton buckets against fatigue cracking and therefore in lifetime has, thus, been achieved.

In accordance with the state-of-the-art development of the finite element method (FEM), the material stress and thus the bucket strengths under each dynamic load can accurately be calculated. FEM calculations, therefore, become to be indispensable already in the design phase of a Pelton turbine, aiming to predict the bucket load capacity.

Of utmost significance of Pelton turbines in operation is sand abrasion of the Pelton buckets. The latter mostly occurs at the power station to which there is no reservoir available or this reservoir is too small for effective sand sedimentation. In the worst case, the season-depending flooding water directly flows to the Pelton turbines. The sand abrasion often leads to a significant decrease of the system efficiency as well as a shortening of the maintenance period of Pelton buckets (Maldet 2008). As a passive method against sand abrasion, one must shut down the Pelton turbine during the period of high particle concentration in the flow. As highly effective against wear and abrasion, the thermal spray coating of the inner surface of Pelton buckets with hard materials has been validated and increasingly applied in the praxis (Winkler and Dekumbis 2010). We mention that the coating of the bucket surface often leaves the rough surface texture which, if possible, should be smoothed for reducing the friction effect. The coating method against wear and abrasion has also been extended to the needle surface and the surface of injector nozzles, as these are also very likely to be worn out by sand abrasion.

1.3 Objectives of This Reference Book

This monograph summarizes all available relevant knowledge in Pelton turbine hydraulics and provides an overview of the related technology as of the year 2015. As a reference book, it thus provides useful operation and design criteria of Pelton turbines on a wide range of hydromechanics. On the hydromechanical side, all flow processes from the generation of the high-speed jet to the power output will

systematically be described. The detailed mathematical descriptions of all flow processes serve on the one side to quantitatively reveal the influences of different operation and design parameters on the operation performance of a Pelton turbine and on the other side to demonstrate the relations between different physical processes in a Pelton turbine. Since quite a lot of flow processes in a Pelton turbine and their effects on the power exchange can be represented explicitly and exactly, the knowledge can be utilized to further and more accurately specify all the empirical data in the hydraulic design of Pelton turbines. In particular, some computational results under certain conditions can be directly used to validate the numerical simulations. From the viewpoint of the author as well as from the author's previous successful applications, the knowledge and the associated flow mechanical laws can be directly implemented for instance in the CFD code. This will provide the prospective possibility of further improving the numerical simulation methods. It would then no longer be necessary, to start the numerical simulation each time from the Navier-Stokes equations. Since both the inaccurate turbulence model and the unrealistic assumption of the two-phase model on the free surface of the flow (water jet and water sheet) are not required, high-quality computational results should be obtained.

The present book originates from the German version of the book *Freistrahlturbinen* (Zhang 2009d), however with some extensions added to it.

References

Angehrn, R. (2000). Safety engineering for the 423 MW-Pelton-runners at Bieudron. *Proceeding of the 20th IAHR Symposium*, Charlotte, NC.

Berntsen, G., Brekke, H., Haugen, J., & Risberg, S. (2001). Analysis of the free surface non-stationary flow in a Pelton turbine. Hydro 2001, Riva del Garda, Italy.

BFE. (2004). *Ausbaupotential der Wasserkraft*. Bundesamt für Energie (BFE), Bern.

Bohl, W. (2004). *Strömungsmaschinen 1* (9. Auflage). Vogel Buchverlag.

Bohl, W. (2005). *Strömungsmaschinen 2* (7. Auflage). Vogel Buchverlag.

Brekke, H. (2005). State of the art of small hydro turbines versus large turbines. Hydro 2005, Villach, Austria.

Giesecke, J., & Mosonyi, E. (2005). *Wasserkraftanlagen* (4th ed.). Berlin: Springer.

Grein, H., & Angehrn, R. (1986). Service life of Pelton runners under corrosion fatigue. *International Symposium on Fluid Machinery Troubleshooting, ASME Winter Annual Meeting*, Anaheim, California, FED-Vol. 46/PWR-Vol. 2.

Grein, H., Angehrn, R., Lorenz, M., & Bezinge, A. (1984). Inspection periods of Pelton runners. *Proceedings of the 12th IAHR Symposium on Hydraulic Machinery*, Stirling.

Grein, H., Meier, J., & Klicov, D. (1986). Efficiency scale effects in Pelton turbines. *Proceedings of the XIII IAHR Symposium on Hydraulic Machinery and Cavitation*, Montreal, Canada.

Kishioka, E., & Osawa, K. (1972). Investigation into the problem of losses of the Pelton wheel. *2nd International JSME Symposium on Fluid Machinery and Fluidics*, Tokyo, Japan.

Kubota, T., Xia, J., Takeuchi, H., Saito, T., Masuda, J., & Nakanishi, Y. (1998). Numerical analysis of free water sheet flow on Pelton buckets. *Proceedings of the 19th IAHR Symposium*, Singapore.

Kvicinsky, S., Kueny, J., Avellan, F., & Parkinson, E. (2002). Experimental and numerical analysis of free surface flows in a rotating bucket. *Proceedings of the 21st IAHR Symposium on Hydraulic Machinery and Systems*, Lausanne, Switzerland.

Mack, R., & Moser, W. (2002). Numerical investigations of the flow in a Pelton turbine. *Proceedings of the 21st IAHR Symposium on Hydraulic Machinery and Systems*, Lausanne, Switzerland.

Maldet, R. (2008). Pelton runner with high erosion caused by glacier sediment: assessment and measures. *15th International Seminar on Hydropower Plants* (pp. 639–646), Vienna, Austria.

Menny, K. (2005). *Strömungsmaschinen* (5. Auflage). Teubner-Verlag.

Muggli, F., Zhang, Zh., Schärer, C., & Geppert, L. (2000). Numerical and experimental analysis of Pelton turbine flow, Part 2: The free surface jet flow. *Proceedings of the 20th IAHR Symposium*, Charlotte, NC.

Parkinson, E., Garcin, H., Vullioud, G., Zhang, Zh., Muggli, F., & Casartelli, E. (2002). Experimental and numerical investigations of the free jet flow at a model nozzle of a Pelton turbine. *Proceedings of the 21st IAHR Symposium on Hydraulic Machinery and Systems*, Lausanne, Switzerland.

Parkinson, E., Neury, C., Garcin, H., & Weiss, T. (2005). Unsteady analysis of a Pelton runner with flow and mechanical simulations. Hydro 2005, Villach, Austria.

Perrig, A., Avellan, F., Kueny, J., Farhat, M., & Parkinson, E. (2006). Flow in a Pelton turbine bucket: Numerical and experimental investigations. *Journal of Fluids Engineering, Transactions of the ASME, 128*, 350–358.

Pfleiderer, C., & Petermann, H. (1986). *Strömungsmaschinen* (5. Auflage). Springer.

Quantz, L., & Meerwarth, K. (1963). *Wasserkraftmaschinen* (11. Auflage). Springer.

Sigloch, H. (2006). *Strömungsmaschinen*. (3. Auflage). Hanser Verlag.

Staubli, T., & Hauser, H. (2004). Flow visualization – a diagnosis tool for Pelton turbines. *Fifth IGHEM Conference*, Lucerne, Switzerland.

Taygun, F. (1946). Untersuchungen über den Einfluss der Schaufelzahl auf die Wirkungsweise eines Freistrahlrades. Diss., Eidgenössische Technische Hochschule in Zürich.

Thomann, R. (1931). *Die Wasserturbinen und Turbinenpumpen, Teil 2*. Stuttgart: Wittwer-Verlag.

Winkler, K., & Dekumbis, R. (2010). Recent Developments in combating Hydro-abrasive erosion. *16th International Seminar on Hydropower Plants* (pp. 109-119), Vienna, Austria.

Zhang, Zh. (2005). Dual-Measurement-Method and its extension for accurately resolving the secondary flows in LDA applications. *Flow Measurement and Instrumentation, 16*, 57–62.

Zhang, Zh. (2006). Improvement of scale-up method for efficiency conversion of Pelton turbines. *14th International Seminar on Hydropower Plants* (pp. 63–68), Vienna, Austria.

Zhang, Zh. (2007a). Flow interactions in Pelton turbines and the hydraulic efficiency of the turbine system. *Proceedings of the IMechE Vol. 221, Part A: Journal of Power and Energy*, pp. 343–357.

Zhang, Zh. (2007b). Flow friction theorem of Pelton turbine hydraulics. *Proceedings of the IMechE Vol. 221, Part A: Journal of Power and Energy*, pp. 1173–1180.

Zhang, Zh. (2009a). Inlet flow condition and the jet impact work in a Pelton turbine. *Proceedings of the IMechE Vol. 223, Part A: Journal of Power and Energy*, pp. 589–596.

Zhang, Zh. (2009b). Analytical method for frictional flows in a Pelton turbine. *Proceedings of the IMechE Vol. 223, Part A: Journal of Power and Energy*, pp. 597–608.

Zhang, Zh. (2009c). Flow dynamics of the free surface flow in the rotating buckets of a Pelton turbine. *Proceedings of the IMechE Vol. 223, Part A: Journal of Power and Energy*, pp. 609–623.

Zhang, Zh. (2009d). *Freistrahlturbinen, Hydromechanik und Auslegung*. Berlin: Springer.

Zhang, Zh., Bissel, C., & Parkinson, E. (2003). LDA-Anwendung zu Freistrahlmessungen bei einem Pelton-Turbine-Modell mit der Fallhöhe von 90 Metern. 11. GALA-Tagung, Lasermethoden in der Strömungsmesstechnik, Braunschweig, Deutschland, Seite 13.1–13.6.

Zhang, Zh., & Casey, M. (2007). Experimental studies of the jet of a Pelton turbine. *Proceeding of the IMechE Vol. 221, Part A: Journal of Power and Energy*, pp. 1181–1192.

Zhang, Zh., Eisele, K., & Geppert, L. (2000a). Untersuchungen am Freistrahl aus einer Modell-düse von Pelton-Turbinen mittels LDA. 8. GALA-Tagung, Lasermethoden in der Strömungsmesstechnik, Freising/München, Deutschland, Seite 15.1–15.6.

Zhang, Zh., Muggli, F., Parkinson, E., & Schärer, C. (2000b). Experimental investigation of a low head jet flow at a model nozzle of a Pelton turbine. *11th International Seminar on Hydropower Plants* (pp. 181–188), Vienna, Austria.

Zhang, Zh., & Müller, J. (2005) On the flow interchanges between the jet and the bucket of Pelton turbines. Hydro 2005, Villach, Austria.

Zhang, Zh., & Müller, J. (2006). The effect of flow friction in the rotating bucket of Pelton turbine on the hydraulic efficiency. Hydro 2006, Porto Carras, Greece.

Zhang, Zh., & Müller, J. (2007). Efficiency and runaway characteristics of a Pelton turbine. Hydro 2007, Granada, Spain.

Zoppé, B., Pellone, C., Maitre, T., & Leroy, P. (2006). Flow analysis inside a Pelton turbine bucket. *Journal of Turbomachinery, Transactions of the ASME, 128*, 500–511.

Chapter 2
Working Principle of Pelton Turbines

2.1 Conversion of Hydraulic Energy into Mechanical Energy

In hydropower plants with Pelton turbines, the available hydraulic energy exists as potential energy, which is measured in the form of the geodetic height difference between the upper level of water in the reservoir and the turbines in the machine house of a lower altitude. This height difference is denoted as hydraulic head in the terminology of hydropower. The conversion of the potential energy into the usable mechanical energy is completed by first converting the potential energy into kinetic energy in the form of high-speed jets at the altitude of the turbine wheel. For the energy conversion, one or many injectors can be used. By neglecting the friction losses in the injector, the jet speed is calculated according to the Bernoulli equation by

$$C_0 = \sqrt{2gH}, \tag{2.1}$$

with H as the net pressure head at the inlet of the injector. This equation is generally called the Torricelli formula.

As second step, the conversion of the kinetic energy of the jet into the mechanical energy is accomplished by the interaction between the jet and the rotating buckets of the Pelton turbine. As a working principle for simplicity, a straight translating bucket of constant speed U is first considered (Fig. 2.1). This assumption of straight movement means that during the interaction between the jet and the bucket, only the *impulsive force* is effective.

The interaction between the water jet and the bucket is considered directly in the relative moving system. For the flow at the bucket entry (index 1) and with $C_1 = C_0$, the relative velocity between the jet and moving bucket is given by
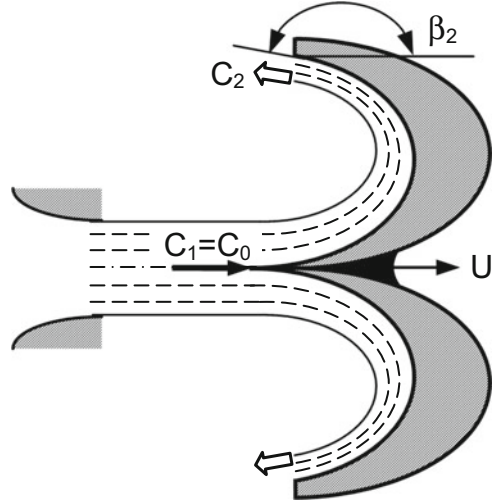
$$W_1 = C_1 - U. \tag{2.2}$$

With this relative velocity, the jet flow spreads in the bucket, forming a water sheet. The change in the direction of the flow along the bucket surface is coupled with a pressure increase below the water sheet as related to the impulsive force and determined by the law of momentum. On the surface of the water sheet where the atmospheric pressure is constant, the flow velocity is equal to W_1 provided that frictionless flow is assumed. The pressure as well as the velocity distribution across the thickness of the water sheet will be considered in more details in Sects. 6.1.2 and 7.3 by considering the relative flow in a rotating Pelton bucket.

Once the water flow reaches and then leaves the bucket exit (index 2) at an angle β_2, it is again subjected to atmospheric pressure. The relative velocity of the total water flow is then reset to its initial value according to Eq. (2.2), i.e., $W_2 = W_1 = W$. The absolute velocity is thus given by

$$C_2^2 = U^2 + W^2 + 2UW \cos \beta_2. \tag{2.3}$$

According to the balance law of momentum, the change of the flow direction is always related to an external impulsive force which acts perpendicular to the flow direction. This force is nothing else than the pressure below the water sheet. For its determination the *momentum flux* difference between the entry and the exit of the moving bucket must be evaluated. The component of the total force in the direction of the bucket motion is calculated by the following momentum balance equation:

$$F_{\text{bucket}} = \dot{m}_w (W_1 - W_2 \cos \beta_2) = \dot{m}_w W (1 - \cos \beta_2). \tag{2.4}$$

F_{bucket} denotes the force exerted by the water on the bucket. Moreover, $\dot{m}_{\text{w}} = \rho W A_{\text{jet}}$ is the total mass flow of water in the relative frame of the moving bucket. It is related to the mass flow rate $\dot{m}_{\text{c}} = \rho C_0 A_{\text{jet}}$ in the absolute frame by the relation

$$\dot{m}_{\text{w}} = \frac{W}{C_0} \cdot \dot{m}_{\text{c}}. \tag{2.5}$$

This equation states that because of $\kappa = C_0/W > 1$, a jet piece leaving the injector nozzle within one second will need κ seconds in order to completely reach and enter the moving bucket. The factor κ can therefore also be understood as a time factor. For this reason, the impulsive force exerted on the bucket, as given in Eq. (2.4), may be rewritten as

$$F_{\text{bucket}} = \dot{m}_{\text{c}} \frac{W^2}{C_0} (1 - \cos \beta_2). \tag{2.6}$$

The power, received by the bucket, is thus calculated as

$$P = F_{\text{bucket}} U = \dot{m}_{\text{c}} \frac{W^2}{C_0} (1 - \cos \beta_2) \cdot U. \tag{2.7}$$

Although the condition for maximum power output can be calculated from $dP/dU = 0$ leading to $U/C_0 = 1/3$, this condition, however, does not represent the condition for the maximum conversion of the kinetic energy stored in the jet into mechanical energy of the moving bucket. To reveal the energy conversion process, the specific energy (J/kg) of the jet must be taken into consideration. Therefore, a unit mass of water (1 kg) is assumed to flow out of the injector nozzle within the time $t_{\text{c}} = 1/\dot{m}_{\text{c}}$. This mass of fluid will then need a time of $t_{\text{c}}\kappa$ to completely reach and enter the moving bucket. The specific work, done by its interaction with the moving bucket, is given by

$$e = P \cdot t_{\text{c}} \kappa. \tag{2.8}$$

With Eq. (2.7) as well as $\kappa = C_0/W$ and $\dot{m}_{\text{c}} t_{\text{c}} = 1$ one thus obtains

$$e = UW(1 - \cos \beta_2). \tag{2.9}$$

The maximum specific work done by a unit mass of the fluid is then obtained by setting $de/dU = 0$. With $W = C_0 - U$ it follows

$$\frac{U}{C_0} = 0.5. \tag{2.10}$$

Such a speed ratio represents the condition under which Pelton turbine operations theoretically should always be configured. The specific work done by the unit mass of the jet flow is then obtained from Eq. (2.9) to

$$e = \frac{1}{4}C_0^2(1 - \cos\beta_2). \tag{2.11}$$

The exit velocity of water out of the bucket results from Eq. (2.3) as

$$C_2^2 = \frac{1}{2}C_0^2(1 + \cos\beta_2). \tag{2.12}$$

From Eq. (2.11) it is evident that the maximum specific work is obtained when the flow angle at the bucket exit is configured to $\beta_2 = 180°$. It then follows

$$e = \frac{1}{2}C_0^2. \tag{2.13}$$

It is obviously equal to the specific kinetic energy which is available in the jet. The exit velocity is obtained from Eq. (2.12) as

$$C_2 = 0. \tag{2.14}$$

This means that the total energy stored in the jet is entirely transferred to the moving bucket.

In practical design of Pelton turbines, the exit velocity C_2 cannot be zero because water, after leaving the bucket, has to fly away from the bucket to make the way free for the following buckets. As a consequence, the flow angle for the exit flow has usually been configured to be $\beta_2 \approx 170°$. The kinetic energy corresponding to the exit velocity $C_2 \neq 0$ and thus remains unexploited and must be regarded as a loss. In practice, it is often referred to as the exit or the *swirling loss*.

The model shown in Fig. 2.1 is a hydraulic model at which for inviscid fluids the exit loss represents the only loss in the model system. The hydraulic efficiency is then defined as the ratio of the specific work to the specific kinetic energy in the jet. From Eq. (2.9), with $W = C_0 - U$, this is calculated to be

$$\eta_h = \frac{e}{C_0^2/2} = 2 \cdot \left(1 - \frac{U}{C_0}\right)\frac{U}{C_0}(1 - \cos\beta_2), \tag{2.15}$$

or, with $k = U/C_0$,

$$\eta_h = 2k(1 - k)(1 - \cos\beta_2). \tag{2.16}$$

In Fig. 2.2, this hydraulic efficiency is illustrated as a function of the velocity ratio k and for the exit angle $\beta_2 = 180°$. The maximum hydraulic efficiency is obviously obtained at $k = 0.5$,

Fig. 2.2 Efficiency characteristic of the flow interaction system according to Fig. 2.1 with $\beta_2 = 180°$
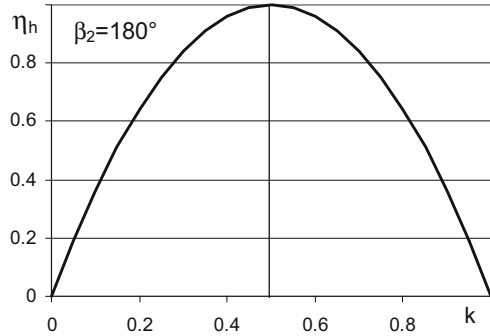
$$\eta_{h,max} = 0.5(1 - \cos\beta_2). \tag{2.17}$$

When the viscous friction loss in the flow of the water sheet cannot be neglected, the calculation of the hydraulic efficiency then has to be modified accordingly. This will be described in detail in Chaps. 10, 11, and 15.

2.2 Pelton Turbines and Specifications

A Pelton turbine essentially consists of one or more injectors for generating the high-speed jet and a wheel with buckets for receiving the jet energy (Fig. 2.3). An injector must primarily perform two tasks. Firstly, the injector nozzle converts the pressure energy of the water into the kinetic energy of the high-speed jet. Secondly, the injector regulates the flow rate via a built-in needle which is driven by a servomotor. The power exchange is finally achieved by the interaction between the jet and the Pelton buckets. Because of the rotation of the Pelton wheel, both the centrifugal and Coriolis forces are influencing the flow. The form of the flow and its distribution within the bucket therefore differ fundamentally from those in the straight-moving bucket. The basic principle of energy conversion, as described in Sect. 2.1, also applies to the Pelton turbines. For Pelton turbines, however, both the design and the flow parameters need to be specially specified as described in the following sections.

2.2.1 Geometric Specification of the Pelton Wheel

According to Fig. 2.4, a Pelton wheel is mainly configured by the following parameters:

Jet circle (also called pitch circle) diameter $D_m = 2R_m$
Wheel bucket inner diameter $D_b = 2R_b$
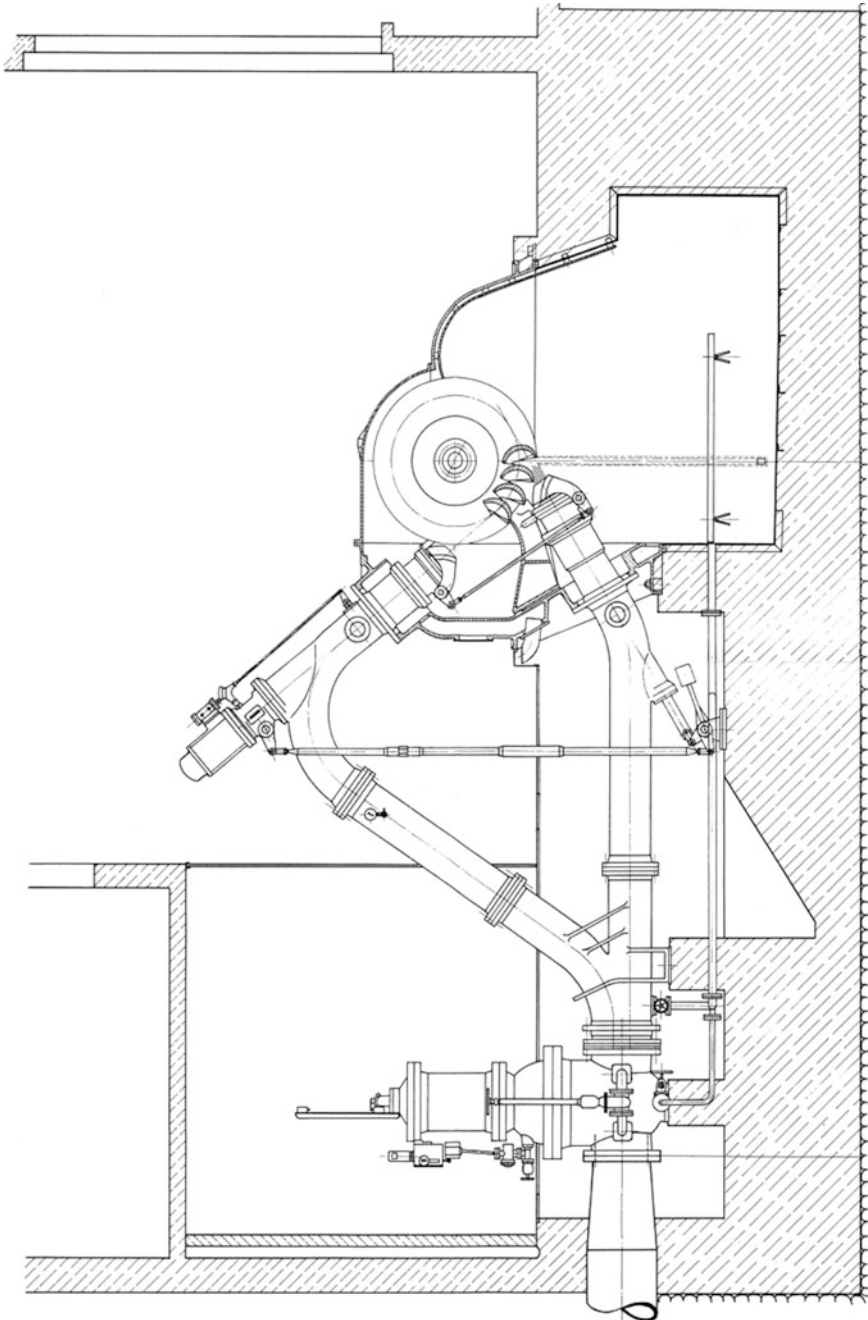
Fig. 2.3 Pelton turbine with two injectors at a hydropower plant in Kleintal
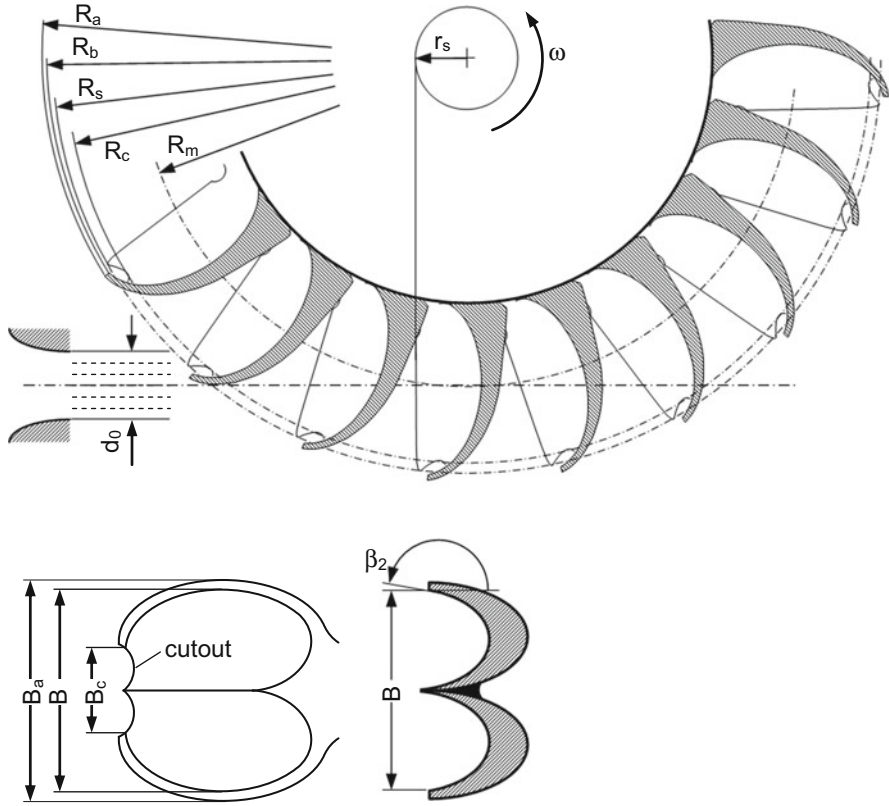
Fig. 2.4 Geometric parameter specification of a Pelton wheel

Wheel diameter $D_a = 2R_a$
Tip circle diameter of the main splitter $D_s = 2R_s$
Circle diameter of the bucket cutout edge $D_c = 2R_c$
Number of buckets N
Bucket inner width B
Bucket exit angle β_2
Base circle radius of the main splitter r_s

The basic design of a Pelton wheel relies on the flow specification in the turbine system. The dimensioning of the Pelton wheel additionally depends on the permissible rotational speed of the generator. Additional details can be found in Chap. 18. The bucket exit angle β_2 is determined under certain circumstances by the required exit flow conditions (Chap. 8), while the optimum bucket number will be derived from *coincidence* and *symmetry conditions* (Chap. 5).

2.2.2 Characteristic Hydromechanical Parameters

In the field of turbomachinery, diverse dimensionless numbers function as para-
metric quantities which are often used to specify the size of the machines and to
quantify the flow performances. For Pelton turbines, however, only few of them are
relevant for the geometric and hydraulic design as well as for the turbine operations.
The most important parametric quantities are summarized in this section.

2.2.2.1 Peripheral Speed Coefficient k_m

The *peripheral speed coefficient* is defined as the ratio of the peripheral speed U_m of
the Pelton wheel on the jet circle (R_m in Fig. 2.4) to the jet speed C_0

$$k_m = \frac{U_m}{C_0} = \frac{U_m}{\sqrt{2gH}}. \tag{2.18}$$

The peripheral speed coefficient is one of the most important parameters in the
design of Pelton turbines. It has the same meaning as the parameter k in Eq. (2.16)
and represents the hydraulic efficiency in a similar form as that in Fig. 2.2. In
practice, the peripheral speed coefficient has so far always been set in the range
0.45–0.48, at which the maximum possible hydraulic efficiency can be achieved.

In general considerations of turbomachinery, the pressure head coefficient,
defined as $\psi = Y/(U_m^2/2)$, is often used, where $Y = gH$ is the specific work of
water sources per unit mass. It can be shown that there exists the following relation
between the peripheral speed coefficient and the pressure head coefficient

$$k_m = \sqrt{\frac{1}{\psi}}. \tag{2.19}$$

For this reason, the head coefficient in Pelton turbine flows will not be used.

2.2.2.2 Bucket Volumetric Load φ_B

The jet thickness relative to the bucket width represents the dimensionless *bucket
volumetric load*.[1] Because the flow rate is proportional to the square of the jet
thickness, the bucket volumetric load can also be represented by the flow rate of a
single injector ($\dot{Q}_{jet}$). It is thus defined by

---

[1] In Chap. 23, the bucket mechanical load will be evaluated with respect to the jet impact force and
the material strength of the bucket.

$$\varphi_B = \frac{\dot{Q}_{jet}}{\pi/4 \cdot B^2 \sqrt{2gH}}, \tag{2.20}$$

with B as the bucket inner width.

The flow rate of a single injector is given by $\dot{Q}_{jet} = \pi/4 \cdot d_0^2 \sqrt{2gH}$, with d_0 as the jet diameter. Consequently, the *bucket volumetric load* is given by

$$\varphi_B = \left(\frac{d_0}{B}\right)^2. \tag{2.21}$$

It is simply expressed by the ratio of the jet thickness to the bucket width. Because of its geometric feature, the bucket volumetric load expressed by Eq. (2.21) is much more comprehensible than that of Eq. (2.20). For this reason, Eq. (2.21) will be preferably used in this book.

The bucket volumetric load is used on the one hand to represent the flow rate in a dimensionless form and on the other hand to determine the necessary width of the Pelton buckets. The bucket width is usually designed so that at nominal or maximum flow rate, the jet diameter d_0 does not exceed one-third of the bucket width B. This yields $\varphi_B = 0.09$ to 0.11 as design criterion for the bucket width.

2.2.2.3 Specific Speed n_q

The *specific speed* is a parametric quantity which has been widely used in all types of rotating fluid machinery. In the specification of Pelton wheels, the specific speed has a special explicit meaning. As directly taken over from the technical literature, for instance Pfleiderer and Petermann (1986), the specific speed is defined by

$$n_q = n \frac{\sqrt{\dot{Q}_{jet}}}{H^{3/4}}. \tag{2.22}$$

It is obviously not dimensionless, nor does it have the same dimension as the rotational speed n. To avoid confusion in applications, $\dot{Q}_{jet}$ and H in the above equation can be considered to be normalized by the unit flow rate $\dot{Q}_{jet} = 1\,\mathrm{m}^3/\mathrm{s}$ and the unit pressure head $H = 1\,\mathrm{m}$, respectively. Then n and n_q have the same unit, either 1/s or 1/min. In the present work, the specific speed n_q is mainly used with the unit 1/s.

As an alternative to the specific speed defined in Eq. (2.22), the following definition can also be found in the literature:

$$n_y = n\frac{\sqrt{\dot{Q}_{\text{jet}}}}{(gH)^{3/4}} = n\frac{\sqrt{\dot{Q}_{\text{jet}}}}{Y^{3/4}}. \tag{2.23}$$

In this definition, the unit of the rotational speed is 1/s.

Between the two definitions of the specific speed, the following relation exists:

$$n_q = g^{3/4}n_y = 5.54n_y(1/\text{s}). \tag{2.24}$$

One obtains further by using the unit 1/min for the speed,

$$n_q = 333n_y(1/\text{min}). \tag{2.25}$$

The specific speed is primarily used when for a given flow rate and a given pressure head, a Pelton turbine should be defined by specifying the injector number, the rotational speed, and the wheel dimension. The exact computational algorithm for the design of a Pelton turbine by using the specific speed is presented in detail in Chap. 18. For practical engineering applications, only the specific speed according to Eq. (2.22) is used in this book.

It should also be noted that the specific speed indeed represents the diameter ratio $\delta = D_{\text{m}}/d_0$ which is a dimensionless quantity and called the diameter number (Sigloch 2006). This can be confirmed using Eq. (2.22) by considering the flow rate $\dot{Q}_{\text{jet}} = \frac{1}{4}\pi d_0^2\sqrt{2gH}$ and the peripheral speed coefficient according to Eq. (2.18). One obtains

$$n_q = g^{3/4}\frac{k_{\text{m}}}{2^{1/4}\sqrt{\pi}}\frac{d_0}{D_{\text{m}}} = 2.63k_{\text{m}}\frac{d_0}{D_{\text{m}}}(1/\text{s}). \tag{2.26}$$

Here, the significance of the specific speed is clearly explained. Since the peripheral speed coefficient k_{m} of Pelton turbines is practically a constant, the specific speed represents exclusively the diameter ratio d_0/D_{m} and is therefore essentially a geometric parameter. With respect to the bucket volumetric load according to Eq. (2.21), the specific speed is also interpreted as

$$n_q = \frac{(2g)^{3/4}}{2\sqrt{\pi}}k_{\text{m}}\sqrt{\varphi_{\text{B}}}\frac{B}{D_{\text{m}}} = 2.63k_{\text{m}}\sqrt{\varphi_{\text{B}}}\frac{B}{D_{\text{m}}}. \tag{2.27}$$

According to this equation and under nominal operations, at which $\varphi_{\text{B}} \approx 0.11$, the specific speed also specifies the geometric design parameter (B/D_{m}) of the Pelton wheel.

As the specific speed is, according to its definition in Eq. (2.22), directly determinable from the flow rate and the pressure head, it is a particularly convenient parameter for the design of a Pelton turbine from the given $\dot{Q}_{\text{jet}}$ and H. For this reason, the diameter number $\delta = D_{\text{m}}/d_0$ will not be used in this book.

2.2.2.4 Characteristic Bucket Position Angle α_o

The bucket position angle α_o as shown in Fig. 2.5 represents an angle at which the cutout of the bucket just intersects the jet layer on the jet axis. This angle has a special meaning because it directly determines the so-called runaway speed of the Pelton turbine. Whereas the computation of the runaway speed will be treated in Chap. 17, the properties of this special bucket position angle and its connection with the specific speed should be explained here.

The Pelton bucket geometries are usually similar from turbine to turbine. Especially, the ratio of the bucket length to the bucket width is between 0.8 and 0.9. If, on this basis, the difference $D_c - D_m = 0.85B$ is applied, it follows from Fig. 2.5 that

$$\cos \alpha_o = \frac{R_m}{R_c} = \frac{1}{1 + 0.85B/D_m}. \tag{2.28}$$

To replace the term B/D_m, Eq. (2.27) is used. This results in

$$\cos \alpha_o = \frac{k_m \sqrt{\varphi_B}}{k_m \sqrt{\varphi_B} + 0.32 n_q}. \tag{2.29}$$

For nominal operations (index N) on average with $k_{m,N} = 0.47$ and $\varphi_{B,N} = 0.11$, it follows further that

$$\cos \alpha_o = \frac{1}{1 + 2n_q}. \tag{2.30}$$

The application of this *characteristic bucket position angle* α_o will be demonstrated in detail in Chap. 16 for calculating the real efficiency curve and in Chap. 17 for determining the runaway speed of the Pelton wheel.

Fig. 2.5 Geometric relation of the bucket position angle α_o
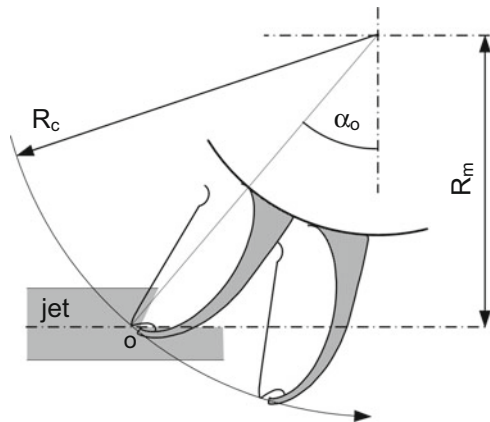
2.2.2.5 Peripheral Speed of the Bucket Cutout Edge

Another frequently used reference speed in flow calculations is the *peripheral speed* of the cutting edge of the bucket cutout. From Eqs. (2.28) and (2.30), one first obtains the diameter ratio

$$\frac{D_c}{D_m} = 1 + 2n_q. \tag{2.31}$$

The ratio of the corresponding peripheral speed to the jet speed is, in view of Eq. (2.18), given by

$$\frac{U_c}{C_0} = \frac{U_m}{C_0}\frac{U_c}{U_m} = k_m\frac{D_c}{D_m}. \tag{2.32}$$

With Eq. (2.31) it follows further that

$$\frac{U_c}{C_0} = k_m\bigl(1 + 2n_q\bigr). \tag{2.33}$$

2.2.3 Hydromechanical Specification of the Pelton Turbine

The main operating parameters of a Pelton turbine are the *peripheral speed coefficient* k_m and the *bucket volumetric load* φ_B, while the specific speed only determines the shape of the Pelton wheel and is thus related to the nominal operation. On the one hand, both parameters, k_m and φ_B, describe the hydraulic similarity between two Pelton wheels with similar geometric designs and therefore the same specific speed (see Chap. 20). On the other hand, they together determine the flow mechanical efficiency of a Pelton turbine. With regard to the maximum efficiency, the operation point of a Pelton turbine is commonly configured by the peripheral speed coefficient $k_m = 0.45{\sim}0.48$ and the bucket volumetric load $\varphi_B = 0.09{\sim}0.11$.

To describe the flow mechanical interaction between the jet and the rotating buckets of a Pelton turbine, basically the same calculation is used as described in Sect. 2.1 for the straight-moving bucket. The relative flow velocity at the bucket entry is assumed to be $W_1 = C_0 - U_m$. Analogous to Eq. (2.6), the interaction, i.e., the impulsive force exerted on a bucket, is obtained as

$$F_{\text{bucket}} = \dot{m}_c C_0 (1 - k_m)^2 (1 - \cos\beta_2). \tag{2.34}$$

Contrary to the case of the straight-moving bucket, each jet in a Pelton turbine with rotating buckets simultaneously interacts with about two buckets. More accurately, the number of buckets interacting with one jet is given by

$$2\lambda = \frac{\dot{m}_c}{\dot{m}_w} = \frac{C_0}{W_1}. \tag{2.35}$$

Here, λ denotes the *multi-bucket factor*. Its application will be explained in detail in Chap. 5. Accordingly, the total impulsive force resulting from one jet is given by

$$F_{jet} = 2\lambda F_{bucket} = \dot{m}_c \frac{C_0^2}{W_1}(1 - k_m)^2(1 - \cos\beta_2). \tag{2.36}$$

Because $W_1 = (C_0 - U_m) = C_0(1 - k_m)$, there follows

$$F_{jet} = \dot{m}_c C_0(1 - k_m)(1 - \cos\beta_2). \tag{2.37}$$

The power exchange achieved by one jet flow is thus

$$P = F_{jet}U_m = \dot{m}_c C_0^2 k_m(1 - k_m)(1 - \cos\beta_2). \tag{2.38}$$

The maximum power achieved is given at $k_{m,max}$ which is obtained by the condition $dP/dk_m = 0$ and obtains

$$k_{m,max} = 0.5. \tag{2.39}$$

From Eq. (2.38) the hydraulic efficiency thus results as

$$\eta_h = \frac{P}{\frac{1}{2}\dot{m}_c C_0^2} = 2k_m(1 - k_m)(1 - \cos\beta_2). \tag{2.40}$$

Formally this expression agrees with Eq. (2.16). The reason for this agreement is that perpendicular entry of the jet into the bucket was assumed and thus the relation $W_1 = C_0 - U_m$ was used. Therefore, Eq. (2.40) can be considered to be directly taken over from Eq. (2.16). Because of the assumption $W_1 = C_0 - U_m$, it, therefore, only applies to illustrate the working principle of a Pelton turbine and to roughly estimate the hydraulic efficiency. In particular, the speed ratio $\kappa = C_0/W_1$, which in Eq. (2.5) was referred to as a time factor, stands here for the number of buckets that simultaneously interact with a jet. In Chaps. 5 and 7, this factor will be replaced by the *multi-bucket factor* $\lambda = \kappa/2$ that is computed using other, different reasoning.

In fact, all equations derived so far for F_{jet}, P, and η_h only represent the operational principle of a Pelton turbine. Both the jet impact force and the power exchange in a Pelton turbine with rotating buckets behave somewhat differently than those in a nonrotating, i.e., linearly translating bucket. The interaction between
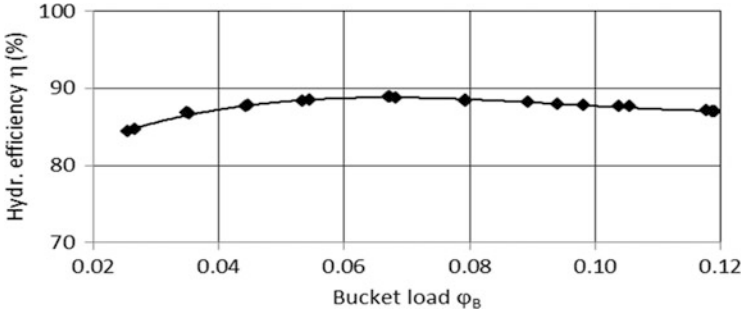
Fig. 2.6 Hydraulic efficiency of a Pelton turbine (KWO) plotted against the bucket volumetric load

the jet and the rotating buckets is no longer constant but varies with time. The consideration of a linearly translating bucket in Sect. 2.1 has led to the speed ratio $U/C_0 = 0.5$ at which the maximum hydromechanical performance is achieved. In practical operations of Pelton turbines, however, the nominal peripheral speed coefficient $k_{m,N}$ for maximum efficiency is found to be between 0.45 and 0.48. Here, particular attention should be focused on the fact that the water, after the energy exchange with the rotating buckets, still possesses sufficient kinetic energy to be able to leave the buckets in time. The associated loss is called the *exit* or *swirling loss*. The full term of the hydraulic efficiency will be presented in Chap. 15 once all individual hydromechanical losses, including the viscous friction effect, have been treated.

The hydraulic efficiency according to Eq. (2.40) has been shown to be a function of the peripheral speed coefficient and theoretically reaches its maximum at $k_{m,max} = 0.5$. On the other hand, the hydraulic efficiency of a Pelton turbine also depends on the bucket volumetric load φ_B. Figure 2.6 shows such a dependence of a Pelton turbine obtained by measurements. Usually, the nominal flow rate of a Pelton turbine is designed with a bucket load of about $\varphi_{B,N} = 0.1$. Most Pelton turbines, however, show maximum efficiencies at the flow rate below that value, as this is also confirmed in Fig. 2.6. The basic reason for this intention is that nearly all Pelton turbines also operate at partial loads. As can be recognized, the hydraulic efficiency of a Pelton turbine only insignificantly changes with bucket load when compared with other types of turbines. This is the reason why the Pelton turbines are often used to balance the load of the network. The perceptible decrease of the hydraulic efficiency at a partial load is ascribed to friction effects; see Sect. 10.4 as well as Sect. 11.4.

2.2.4 Installation Form of Pelton Turbines

The practical installation forms of Pelton turbines have been categorized by the orientation of the turbine axis. The turbines with horizontal axes are denoted horizontal turbines (Fig. 2.7a) and those with vertical axes are called vertical

(a) Horizontal
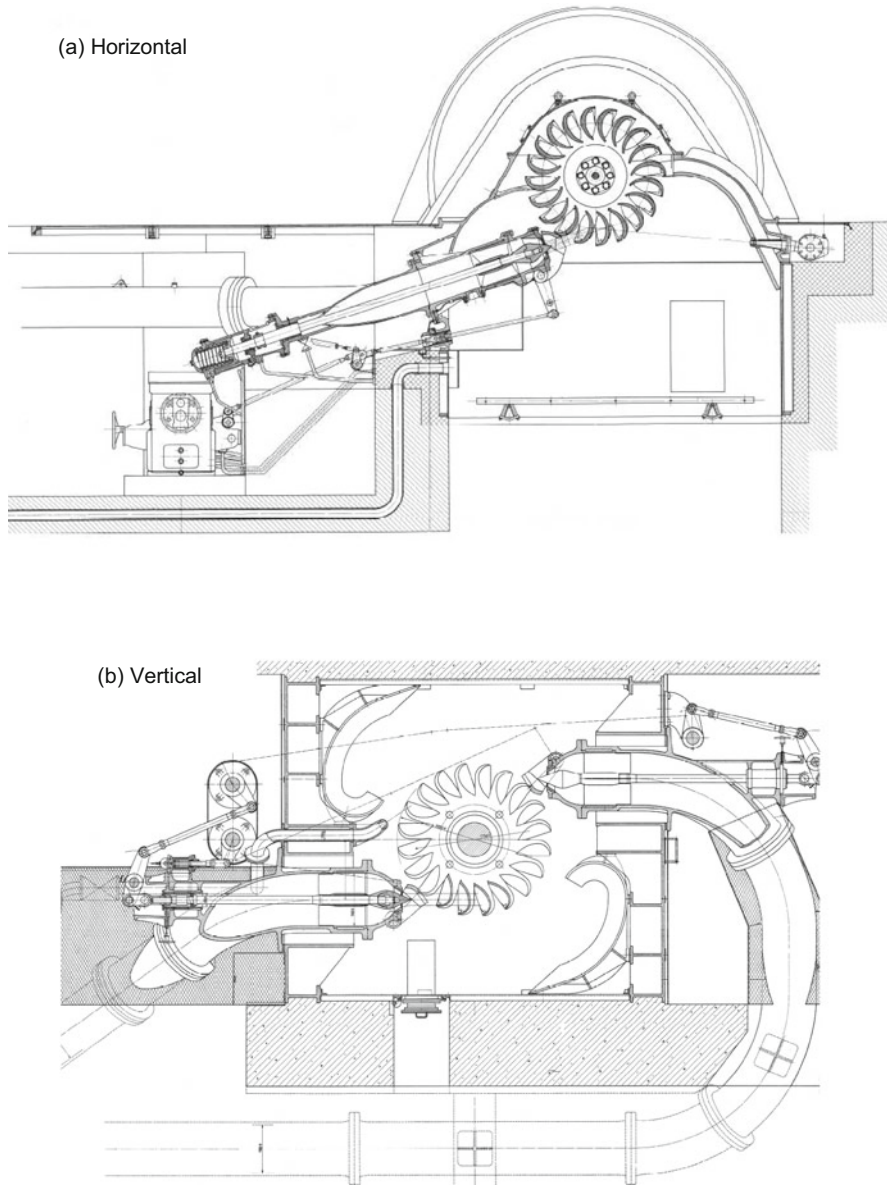
(b) Vertical

Fig. 2.7 Different installation forms of Pelton turbines at the Oberhasli Hydroelectric Power Company (KWO). (**a**) Horizontal, (**b**) vertical

turbines (Fig. 2.7b), respectively. The horizontal installation is only suitable for turbines with at most two injectors. Vertical turbines can be designed with up to six injectors. The significant advantage of the vertical installation is that the injectors can be and are distributed symmetrically around the wheel. For Pelton turbines with one injector or in all cases of turbines of horizontal installation, the destructive one-sided bearing load is inevitable. For turbines with two or more injectors, care should be taken that no collisions between two jets could occur in the same bucket. The offset angle between two adjacent injectors must be sufficiently large to ensure trouble-free interaction between the jet and the rotating buckets, as well as trouble-free exit flow of water out of the buckets. The relevant criterion will be elaborated in Chap. 19. In the design of vertical turbines, one has to ensure that water after leaving the upper bucket halves should not fall back on the wheel. The relevant criterion is explained in Chap. 8.

2.2.5 Parameter Notations

In addition to the geometric parameters of a Pelton wheel that have already been shown in Fig. 2.4, complete geometric and hydraulic parameters of both the injector and the Pelton wheel are summarized in Appendix A. Other derived parametric and dimensionless quantities are summarized in Appendix B.

References

Pfleiderer, C., & Petermann, H. (1986). *Strömungsmaschinen* (5. Auflage). Springer.
Sigloch, H. (2006). *Strömungsmaschinen*. (3. Auflage). Hanser Verlag.

Chapter 3
Injector Characteristics

One of the most important components in a Pelton turbine is the injector which is used on the one hand to entirely convert the pressure energy of water into the kinetic energy of the high quality jet and, on the other hand, to regulate the flow rate. Figure 3.1 shows the basic construction of an injector, which is mainly composed of a nozzle and a regulation needle connected to a servomotor. In most injector designs, the servomotor is found outside the pressure pipe. Based on the hydraulic optimization, the injector nozzle is frequently constructed with a contraction angle α_{nozzle} of about 42° to 45°. The regulation needle typically has a half vertex angle α_{N} of about 25°. The pressure drop due to flow friction and other disturbances in the injector is usually of the order of 1 % and will only be considered if the system efficiency is going to be estimated.

The conversion of the pressure energy into kinetic energy is governed by the Bernoulli equation from which the speed of the jet is a function of the net head at the inlet of the injector, explicitly:

$$C_0 = \sqrt{2gH}. \tag{3.1}$$

An ideal jet has a uniform velocity distribution in each cross section and a constant cross-sectional area without any jet expansion. The real jet in a Pelton turbine generally deviates from this perfect form. This can be confirmed simply by photographic observation of the jet. The in-depth investigations and the detailed characterization of the jet flows have been systematically carried out under the application of laser methods as summarized by Zhang and Casey (2007). The main features of a real jet will be described in Chap. 4.
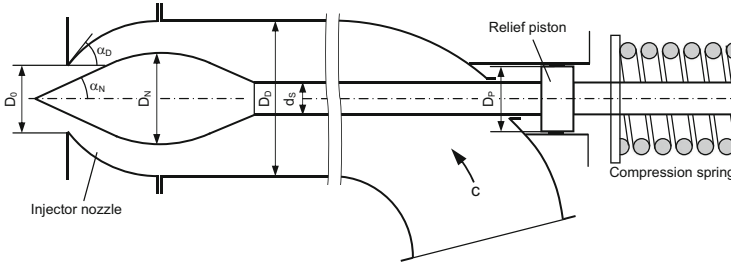
Fig. 3.1 Dimensioning and parameter specification of a Pelton turbine injector with the external servomotor

3.1   Flow Acceleration in the Injector Nozzle

The injector nozzle of a Pelton turbine is used to accelerate the flow and to convert the pressure energy into kinetic energy. From the constant flow rate $\dot{Q} = c_{\mathrm{m}}A$ = const through the injector nozzle, the acceleration of the mean flow velocity along the nozzle flow is calculated as a function of the nozzle geometry and the flow velocity itself:

$$\frac{\mathrm{d}c_{\mathrm{m}}}{\mathrm{d}x} = -\frac{c_{\mathrm{m}}}{A}\frac{\mathrm{d}A}{\mathrm{d}x}. \tag{3.2}$$

In fact, the flow acceleration within the nozzle according to Fig. 3.2 is not uniform. This will give rise to streamline curvature. For verifying this circumstance, the flow at the cross section A is assumed to be uniform and therefore a potential flow. At the nozzle exit in the region close to the nozzle casing surface B, where the ambient air pressure is present, the flow speed reaches its maximum value of $C_0 = \sqrt{2gH}$ if the boundary layer effect is neglected. Since the flow along the needle surface still undergoes further acceleration and thus the velocity is less than C_0, the velocity distribution at the nozzle exit is nonuniform. The acceleration of the flow from section A to section B is thus inhomogeneous. Along the needle surface, the flow acceleration is smaller than that on the casing side of the nozzle. By using the local coordinate system in Fig. 3.2, the streamline equation is given by

$$\frac{\mathrm{d}y}{\mathrm{d}x} = \frac{c_{\mathrm{y}}}{c_{\mathrm{x}}}. \tag{3.3}$$

Consider first the general case for which the velocity ratio $c_{\mathrm{y}}/c_{\mathrm{x}}$ in the flow varies from location to location, i.e., $c_{\mathrm{y}}/c_{\mathrm{x}} = f(x, y)$. Under this assumption Eq. (3.3) implies

Fig. 3.2 Flow acceleration
and the streamline curvature
in the injector nozzle
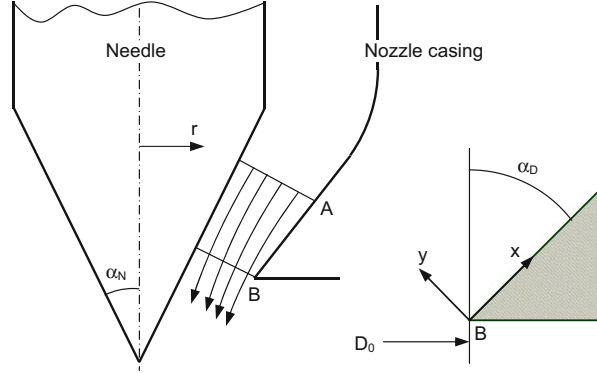
$$\frac{d^2y}{dx^2} = \frac{1}{c_x^2}\left(c_x\frac{\partial c_y}{\partial x} + c_x\frac{\partial c_y}{\partial y}\frac{dy}{dx} - c_y\frac{\partial c_x}{\partial x} - c_y\frac{\partial c_x}{\partial y}\frac{dy}{dx}\right). \tag{3.4}$$

Consider next a streamline, for which Eq. (3.3) applies again. If in addition potential flow is assumed, then one has $\partial c_y/\partial x = \partial c_x/\partial y$. Under this condition and with the continuity equation $\partial c_x/\partial x + \partial c_y/\partial y = 0$, Eq. (3.4) is simplified to

$$c_x\frac{d^2y}{dx^2} = \left(1 - \frac{c_y^2}{c_x^2}\right)\frac{\partial c_x}{\partial y} - 2\frac{c_y}{c_x}\frac{\partial c_x}{\partial x}. \tag{3.5}$$

A new coordinate system $\xi - \eta$ will be defined, in which the ξ-axis coincides with the tangent of the streamline. This is equivalent to a moving coordinate system along the streamline. Because $c_\eta = c_y = 0$ and $c_\xi = c_x = c$, Eq. (3.5) takes the new form

$$\frac{d^2\eta}{d\xi^2} = \frac{1}{c}\frac{dc}{d\eta}. \tag{3.6}$$

This equation is valid only for viewing along a streamline, because it is obtained from Eq. (3.4) by simultaneously using Eq. (3.3) for a streamline, along which $c_\eta = 0$ has been assumed.

Because of the nonuniform flow distribution in the nozzle, i.e., $dc/d\eta \neq 0$, it can be concluded that in the space between sections A and B, all streamlines are curved: $(d^2\eta/d\xi^2 \neq 0)$.

The above consideration may be extended to calculate the flow under the influence of the viscous friction on the nozzle casing wall. Detailed calculations have been performed (Zhang 2003), where the so-called head effect was investigated.

3.2 Discharge Coefficient φ_{D0} and the Injector Characteristics

The injector of a Pelton turbine is used to generate a high-speed jet in accordance with Eq. (3.1) on the one hand and to regulate the flow rate on the other hand. The regulation of the flow rate is performed by adjusting the needle stroke in the nozzle (Fig. 3.1). In order to calculate the flow rate ($\dot{Q}_{jet}$) through an injector nozzle as a function of the needle stroke, the *discharge coefficient* is commonly defined as follows:

$$\varphi_{D0} = \frac{4\dot{Q}_{jet}}{\pi \cdot D_0^2 \sqrt{2gH}}. \tag{3.7}$$

Here, D_0 is the constant aperture diameter of the nozzle. The net head at the injector entrance is designated by H.

The meaning of the discharge coefficient as defined in Eq. (3.7) should be illustrated here. The jet has its most narrow section (waist) where all streamlines run parallel and thus are found under constant pressure. The jet speed in the jet waist section, which is also referred to as the contraction section of the jet, can be calculated by using the Bernoulli equation. The related flow rate is obtained as

$$\dot{Q}_{jet} = \frac{1}{4}\pi d_0^2 \sqrt{2g(H - h_v)}. \tag{3.8}$$

Here, the pressure head drop in the injector is assumed to be h_v. The jet diameter at the jet waist is denoted by d_0.

The drop of the pressure head in the injector is usually very small if compared with the net head, i.e., $h_v/H \ll 1$. Under this condition Taylor expansion of the square root function in Eq. (3.8) leads to

$$\dot{Q}_{jet} = \frac{1}{4}\pi d_0^2 \left(1 - \frac{1}{2}\frac{h_v}{H}\right)\sqrt{2gH}. \tag{3.9}$$

Substituting this into Eq. (3.7) then yields

$$\varphi_{D0} = \frac{d_0^2}{D_0^2}\left(1 - \frac{1}{2}\frac{h_v}{H}\right). \tag{3.10}$$

When neglecting the head drop h_v in the injector, the *discharge coefficient* of an injector indeed represents the ratio of the jet diameter to the diameter of the nozzle aperture. It is therefore also called the *contraction factor of the nozzle* in some other applications. As a specific flow rate, the discharge coefficient is obviously a function of the needle stroke which determines the jet diameter. It is further

Fig. 3.3 Discharge coefficient of the injector plotted as a function of the needle stroke. Comparison between different needle vertex angles according to Zhang (2003)
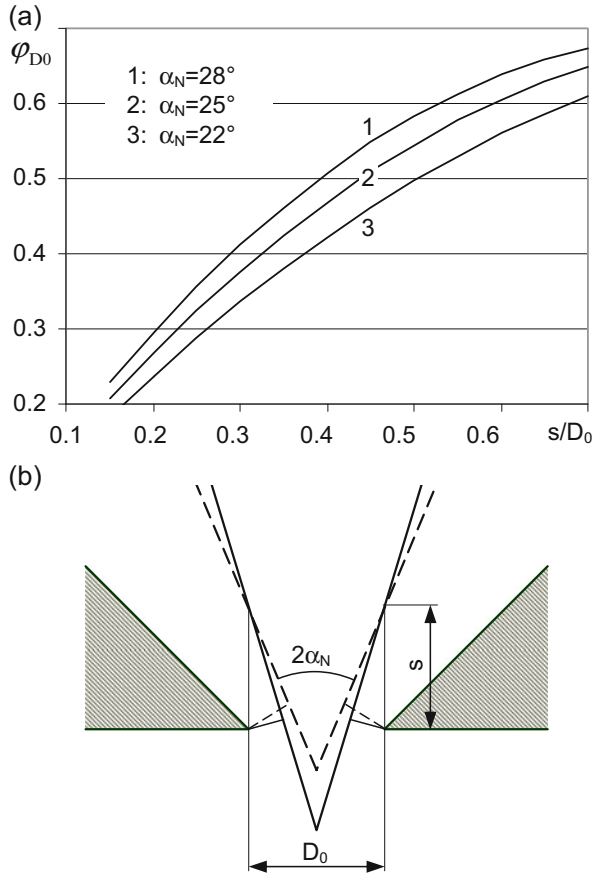
expected that the discharge coefficient depends on the nozzle geometry as shown in Fig. 3.3a. It is obtained from the calibration measurements of an injector with three needles of different geometries. For equal needle strokes, the use of an obtuse needle (large vertex angle) enables a larger flow rate to be generated (curve 1). This is due to the fact that for equal needle strokes, the effective opening area at the nozzle exit is correspondingly larger for the obtuse needle angle. According to Fig. 3.3b, the opening area is calculated as follows:

$$A_D = \pi \left(1 - \frac{s}{2D_0} \cdot \sin 2\alpha_N\right) D_0 s \cdot \sin \alpha_N. \tag{3.11}$$

This equation combines the needle stroke and the needle vertex angles. If the discharge coefficients shown in Fig. 3.3a are plotted against the nozzle opening area (A_D/A_{D0}), then a unified discharge curve is obtained as illustrated in Fig. 3.4. The influences of the needle vertex angle $2\alpha_N$ and the needle stroke s on the flow rate have been unified as the influence of the nozzle opening area. This
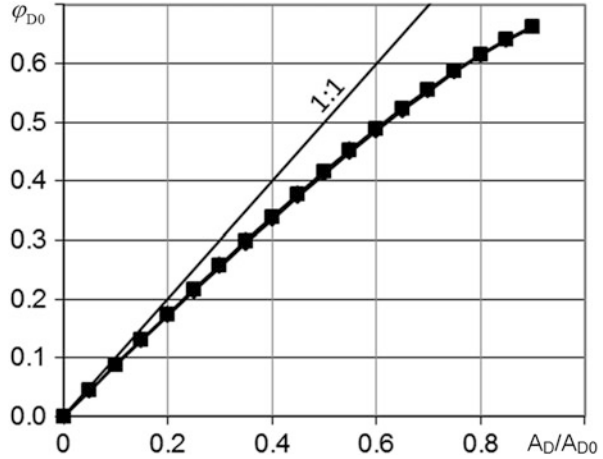
demonstrates that such an opening area is a characteristic parameter for the effective flow rate, i.e., the discharge coefficient $\varphi_{D0} = f(A_D)$. In other words, this means that only the opening area but not the needle geometry determines the flow through the injector. The prerequisite of this conclusion is that the nozzle contraction angle remains constant.

Generally, in nozzle flows, the jet section and, thus, the discharge coefficient are, according to Eq. (3.7), practically independent of the effective pressure head at the injector. In practical operations of Pelton turbines, however, a small dependence of the discharge coefficient on the pressure head has been recognized which is referred to as the *head effect*. As will be shown in Sect. 3.4, this is a *Reynolds number effect*.

For a concrete injector, the discharge coefficient defined above depends only on the needle stroke s. As already shown in Fig. 3.3a, this dependence can be determined by measurements. With sufficient accuracy its functional dependence can be represented as a quadratic polynomial of the needle stroke:

$$\varphi_{D0} = a\frac{s}{D_0} + b\left(\frac{s}{D_0}\right)^2. \tag{3.12}$$

Here, D_0 is the constant diameter of the nozzle aperture. The constants a and b usually have to be determined by calibration measurements. Equation (3.12) is called the *injector characteristic*.

Sometimes the injector characteristic of a prototype Pelton turbine is directly given by the related flow rate

$$\frac{\dot{Q}_{\text{jet}}}{\dot{Q}_{\text{jet,N}}} = \frac{s}{s_{\max}}\left(k_1 + k_2\frac{s}{s_{\max}}\right)\sqrt{\frac{H}{H_N}}, \tag{3.13}$$

in which both H_N and $\dot{Q}_{\text{jet,N}}$ are referred to the nominal operation point.

Equations (3.12) and (3.13) are related to one another by the constants a, b, k_1, and k_2 in the following form:

$$k_1 = \frac{1}{\varphi_{D0,N}} \frac{s_{max}}{D_0} a,$$ (3.14)

$$k_2 = \frac{1}{\varphi_{D0,N}} \left(\frac{s_{max}}{D_0}\right)^2 b.$$ (3.15)

Indeed, the nominal discharge coefficient $\varphi_{D0,N}$ is calculated by Eq. (3.7). Obviously both constants, k_1 and k_2, depend on the nominal discharge coefficient and hence on the nominal flow rate. They also depend on the setting of the maximum needle stroke (s_{max}) which is indeed only a virtual value and will in most applications never be reached.

Another form of expressing the injector characteristic is given by

$$\dot{Q}_1 = \frac{\dot{Q}_{jet}}{\sqrt{H}} = m_1 \frac{s}{s_{max}} + m_2 \left(\frac{s}{s_{max}}\right)^2.$$ (3.16)

Comparing it with Eq. (3.13) implies the following relations:

$$m_1 = k_1 \frac{\dot{Q}_{jet,N}}{\sqrt{H_N}},$$ (3.17)

$$m_2 = k_2 \frac{\dot{Q}_{jet,N}}{\sqrt{H_N}}.$$ (3.18)

The definition of the injector characteristic by Eq. (3.16) has the significant disadvantage that both coefficients, m_1 and m_2, will not remain constant for geometrically similar nozzles. This is simply so because both m_1 and m_2 are not dimensionless constants.

3.3 Discharge Coefficient φ_D Referred to the Effective Nozzle Opening Area

As can be inferred from the example shown in Fig. 3.4, the discharge coefficient is in effect a function of the opening area at the nozzle exit. In other words, the opening area combines the functional effects of the needle vertex angle and the needle stroke. For this reason, the discharge coefficient can also be defined by relating the flow rate to the opening area of the injector nozzle:

$$\varphi_D = \frac{\dot{Q}_{jet}}{A_D\sqrt{2gH}}. \tag{3.19}$$

Assuming a small head loss in the injector, i.e., $h_v/H \ll 1$, and analogously to Eq. (3.10), Eq. (3.19) can be rewritten as

$$\varphi_D = \frac{\pi d_0^2}{4A_D}\left(1 - \frac{1}{2}\frac{h_v}{H}\right). \tag{3.20}$$

It represents the ratio of the jet section area to the opening area of the injector nozzle.

Comparison with Eq. (3.10) yields a relation between the two definitions of the discharge coefficient, namely:

$$\frac{\varphi_{D0}}{\varphi_D} = \frac{4A_D}{\pi \cdot D_0^2} = \frac{A_D}{A_{D0}}. \tag{3.21}$$

It represents a geometric conversion factor. Practical significance of this conversion calculation should be explained here in more details. First, an injector with a regulation needle of vertex angle α_{N1} is assumed to be known with its characteristic $\varphi_{D0,1} = f(s/D_0, \alpha_{N1})$ from calibration measurements. Second, one calculates the characteristic $\varphi_{D0,2} = f(s/D_0, \alpha_{N2})$ of the same injector, however, with another regulation needle of vertex angle α_{N2}. The known characteristic $\varphi_{D0,1}$ of the first injector configuration is first converted, according to Eq. (3.21), to

$$\varphi_D = \varphi_{D0,1}\frac{A_{D0}}{A_{D,1}}. \tag{3.22}$$

Because the injector characteristic in this form is independent of the vertex angle of the used needle, it also applies to the injector configuration with the needle of the vertex angle α_{N2}. Thus one obtains

$$\varphi_{D0,2} = \varphi_D\frac{A_{D,2}}{A_{D0}} = \varphi_{D0,1}\frac{A_{D,2}}{A_{D,1}}. \tag{3.23}$$

This equation represents the *conversion law of the injector characteristics*. The conversion factor is simply a geometric quantity that can be easily determined with the aid of Eq. (3.11).

3.4 Reynolds Number Effect

The flow through an injector is determined by the discharge coefficient according to Eq. (3.7) or by using diagrams like that in Fig. 3.3a. Theoretically, the discharge coefficient and its graphic representation apply to both model turbines at low heads and prototypes at high heads. In practical operations of Pelton turbines, however, a difference of up to 5 % in the injector characteristics between the model turbine and the analogous prototype was observed (Keck et al. 2000). This means in fact that for the same injector opening ratio, the discharge coefficient decreases with an increase of the hydraulic heads. This phenomenon has been previously referred to as the *head effect*. Its cause has been unknown for a long time. According to Eq. (3.10), the difference in the discharge coefficient is certainly not simply due to the head loss in the injector, because this head loss is of the order of only about 1 %. The difference must be in the jet cross section. This means that the ratio of the jet section to the nozzle opening area must depend on the hydraulic head when this head is provisionally considered as the only variable. This in turn means that the stream-lines between the nozzle exit and the jet waist are not of similar look. The cause of these dissimilar streamlines, thus, lies in the inside of the nozzle. According to Zhang et al. (2000), the boundary layer on the side of the nozzle casing is responsible for such a dissimilarity in the streamlines. The detailed analysis of the related phenomenon was completed later by Zhang (2003). The analysis shows that not only the hydraulic head at a given nozzle alone acts as the cause for the head effect but also the dimensional difference between the model injector and the prototype exerts an influence on the dissimilarity in the streamlines. For this reason, the so-called head effect should be interpreted as a *Reynolds number effect*.

The analysis made by Zhang (2003) could experimentally be confirmed by measurements[1] by using laser Doppler anemometry (LDA).

3.5 Flow Dynamic Forces and the Force Balance in the Injector

The regulation needle in the injector serves to control the opening of the nozzle and thus the flow rate. Because the needle is surrounded by the water flow, each needle stroke regulation operates against the hydraulic force, which is formed by the pressure distribution on the needle surface. Depending on the needle stroke, this force may have a closing or opening trend. The unfavorable opening trend, which is found at large injector strokes, must be overbalanced commonly with the aid of a compression spring. This aims to create a closing trend, i.e., to ensure the automatic closing of the injector nozzle in case of emergency conditions. The adjustment of

---

[1] The measurements were carried out at the hydraulic laboratory of the company Andritz Hydro (former VA TECH Hydro) in Zurich in 2002.

the needle position in the nozzle is commonly performed with the help of a hydraulic servomotor that usually operates with oil pressure. To specify the design of the servomotor, thus, the force status of the needle at each needle position must be known.

The force generated by the flow and acting on the needle equals the integrated pressure force on the entire needle surface. The exact calculation of this flow-induced force is computationally quite expensive. On the one hand, the flow acceleration in the nozzle is coupled with the reduction of the static pressure along the flow in the direction of the nozzle exit. On the other hand, the static pressure in each cross section of the flow between the nozzle casing and the needle surface varies due to the streamline curvature. For simplicity, the mean pressure as determined by the Bernoulli equation can be applied at each cross section of the flow. The use of the Bernoulli equation, however, presumes that for each needle position, the cross section along the flow channel is known.

The total force exerted by the fluid on the needle consists of several contributions that have to be considered individually. For the calculations a distinction between the internal and external supports of the servomotor must also be made.

3.5.1 Injectors with External Servomotor

Most injectors of Pelton turbines are configured with servomotors outside the pressure pipe (Fig. 3.1). This design is advantageous because it provides easier access for repair and maintenance work on the servomotor. However, the pressure pipe must be curved ahead of each injector. As will be shown in Chap. 4, such a configuration of the pressure pipe with the bending curvature greatly influences the jet quality.

The flow-induced force acting on the needle surface is called *needle force*. At each nozzle opening or to each given needle stroke, diverse forces such as the needle force, the force on the relief piston, and the spring force and the force at the support of the servomotor must be in equilibrium. The objective of calculating the force balance in a Pelton injector is to determine the necessary support force which must be provided by the servomotor.

3.5.1.1 Needle Force

The needle force arises from the integration of the pressure distributed over the needle head. The integration of static pressures can easily be performed by numerical methods, for which the needle surface is divided into about 50 to 100 segments along the flow channel.

Fig. 3.5 Estimation of the flow sectional area and the static pressure in the injector nozzle
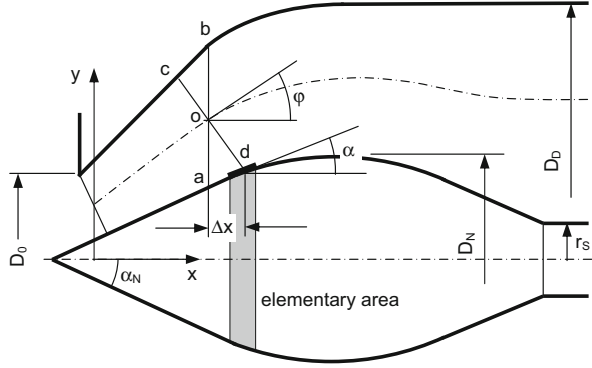
Needle Force from the Internal Pressure

The static pressure which acts on the needle surface depends on the local velocity distribution and thus on the cross section in the nozzle. To determine the cross section and its variation along the flow, the section perpendicular to the centerline (in fact, the mean lateral surface) of the flow channel according to Fig. 3.5 is considered. As centerline the line that divides the annular section into the inner and outer parts with the same content is meant. For simplicity, the centerline is considered to be that line which has the same distance to the needle surface and the nozzle casing at each position along the flow. According to Fig. 3.5, it is the distance $oc = od$. With the slope angle φ of the centerline, the flow cross-section area at point o is calculated to be

$$A = \frac{\pi\left(y_c^2 - y_d^2\right)}{\cos \varphi}. \tag{3.24}$$

The origin of the y-coordinate is located on the nozzle axis.

The mean static pressure in this flow section is calculated in accordance with the Bernoulli equation to

$$p = p_{tot} + p_0 - \frac{1}{2}\rho\left(\frac{\dot{Q}_{jet}}{A}\right)^2, \tag{3.25}$$

where p_{tot} is the total pressure above the atmospheric pressure p_0. It corresponds to the net pressure head at the inlet of the injector. It should be noted that the atmospheric pressure p_0 should be included, because in the application of the momentum law, the existing atmospheric pressure will not automatically cancel out. The flow rate $\dot{Q}_{jet}$ is a function of the nozzle opening, i.e., the needle stroke. For the calculation of the needle force, to each needle stroke, the corresponding flow rate must be known from the injector characteristics (Sects. 3.2 and 3.3).

The static pressure evaluated by Eq. (3.25), however, applies at point d rather than point a on the needle surface; see Fig. 3.5. The corresponding position shift is given by

$$\Delta x = od \cdot \sin \varphi. \tag{3.26}$$

The calculation of the static pressure can be gradually carried out along the needle surface. Figure 3.6 shows an example of the static pressure distribution in the injector nozzle for a particular needle position. The section with the maximum diameter of the needle is at the focus. Upstream of this section, the flow and the static pressure force the needle to have a closing trend. Downstream of this section, the static pressure results in an opening trend. For purposes of calculation, it is agreed here that the resulting force is positive if it is directed to the nozzle exit (causing the closing trend).

The total pressure force acting on the needle surface inside the nozzle is calculated as the sum of all the elementary forces:

$$F_{\text{Needle, In}} = -\sum_{i=1}^{m} p_i A_i \sin \alpha_i. \tag{3.27}$$

In this summation, it has been assumed that the needle surface along the needle axis is divided into m elementary annular surfaces A_i. The slope angle of the respective elementary area is α_i. Because, according to Fig. 3.5, a positive angle α_i is related to an elementary force with an opening trend and this force is negative according to the agreement, there appears in Eq. (3.27) a minus sign ahead of the summation.

The calculation, according to Eq. (3.27), applies to one needle position. For the full range of the nozzle opening, that is, for the needle stroke from zero to its maximum, the calculation must be repeated each time for a new needle position. The calculations may be easily performed, for instance, by using the tabular (spreadsheet) method. In Fig. 3.7, an example is shown (curve 1) as a function of the needle stroke. Throughout the entire opening range, the needle force is positive and thus acts as a closing force. It becomes, however, significantly smaller at large needle strokes.

Recoil Force Outside of the Injector

Another part of active forces acting on the needle is the force which arises from the overpressure around the outer part, i.e., the vertex of the needle as a result of the flow contraction. The fact that this force does really exist can be demonstrated by using the law of momentum. To this end, according to Fig. 3.8, a closed control volume between the section at the nozzle exit (index 1) and the section of the jet waist (index 0) is considered. The area of the annular section for the exit flow is calculated according to Eq. (3.11) to

Fig. 3.6 Pressure
distribution in the nozzle for
a particular given nozzle
opening
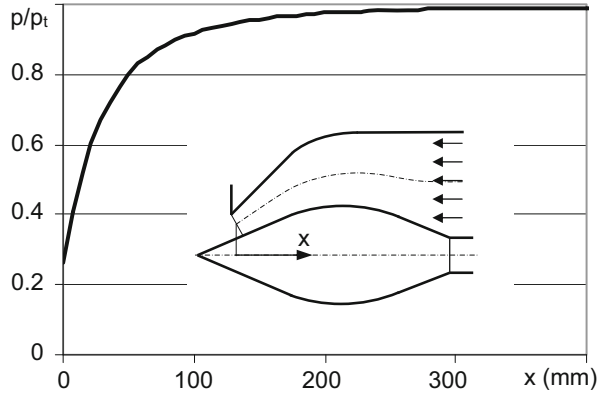
Fig. 3.7 Calculation
example for the forces in an
injector with external
servomotor regulation.
1 Internal needle force
(closing trend), *2* recoil
force (opening trend),
3 relief piston force
(opening trend), *4* spring
force (closing trend, without
prestressing), *5* support
force of the servomotor
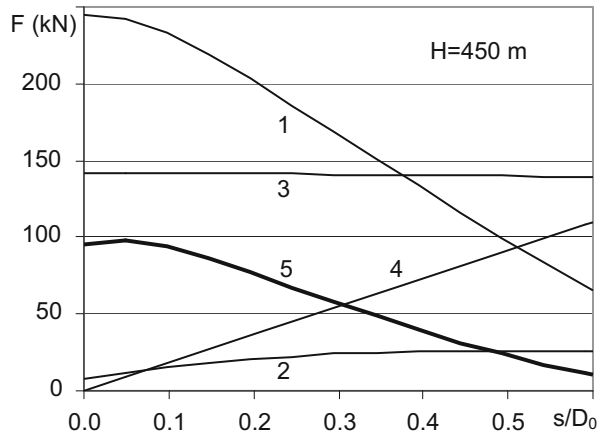
Fig. 3.8 Determination of
the recoil force by applying
the momentum balance
between cross sections "0"
and "1"
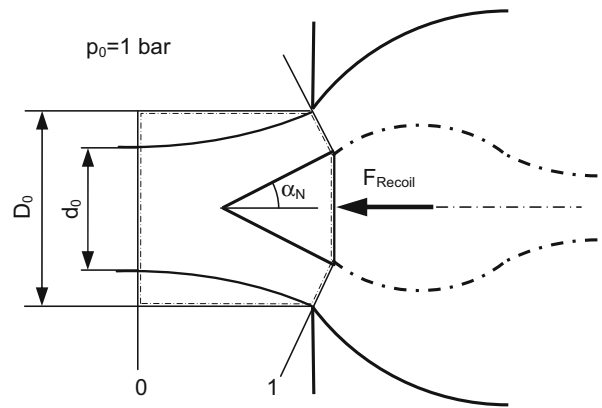
$$A_1 = \pi\left(1 - \frac{s}{2D_0} \cdot \sin 2\alpha_\text{N}\right)D_0 s \cdot \sin\alpha_\text{N}. \tag{3.28}$$

Between sections 0 and 1, the law of momentum is applied. As shown in Fig. 3.8, a positive force acting on the fluid is directed in the positive flow direction. Its reaction on the solid needle represents the force exerted backwards on the needle; this is why it is called the recoil force. From the law of momentum, it is calculated to be

$$F_\text{Recoil} = p_0 A_\text{D0} + \rho A_0 C_0^2 - p_1 A_1 \cos\alpha_\text{N} - \rho\dot{Q}_\text{D}C_1 \cos\alpha_\text{N}, \tag{3.29}$$

where the jet section A_0 is referred to the jet waist at which all streamlines are parallel.

With the mean velocity in section 1, given by $C_1 = \dot{Q}_\text{jet}/A_1$, the static pressure there is calculated from Eq. (3.25) as

$$p_1 = p_\text{tot} + p_0 - \frac{1}{2}\rho C_1^2. \tag{3.30}$$

At the waist section, the jet speed is given by the Bernoulli equation as

$$C_0^2 = \frac{2}{\rho}p_\text{tot}. \tag{3.31}$$

Inserting Eqs. (3.30) and (3.31) into Eq. (3.29) yields

$$F_\text{Recoil} = (2A_0 - A_1 \cos\alpha_\text{N})p_\text{tot} + (A_\text{D0} - A_1 \cos\alpha_\text{N})p_0 - \frac{1}{2}\rho\frac{\dot{Q}_\text{jet}^2}{A_1}\cos\alpha_\text{N}. \tag{3.32}$$

Because the cross section A_1 and the flow rate $\dot{Q}_\text{jet}$ and thus the jet section $A_0 = \dot{Q}_\text{jet}/C_0$ change with the needle stroke, the recoil force F_Recoil is a function of the needle position in the injector. It acts backwards on needles with opening trends. In the considered example, shown in Fig. 3.7, this force is represented by curve 2. At a large opening of the nozzle, it is even comparable to the needle force from the internal pressure (curve 1).

When the nozzle gets closed ($\dot{Q}_\text{jet} = 0, A_1 = 0, A_0 = 0$), the recoil force reduces to

$$F_{\text{Recoil},0} = p_0 A_\text{D0}. \tag{3.33}$$

From both equations, (3.32) and (3.33), it can be seen that the effect of the ambient atmospheric pressure does not automatically disappear. It contributes to the recoil force even in the closed state of the nozzle.

When $p_{tot} \gg p_0$ the effect of the ambient atmospheric pressure is negligible. In this case, there hold the proportionalities $\dot{Q}_{jet}^2 \sim p_{tot}$ for the total pressure and $p_i \sim \dot{Q}_{jet}^2$ for the static pressure along the needle surface, simply because of $C_0^2 \sim p_{tot}$ and $p_i = p_{tot} - k\dot{Q}_{jet}^2$ with k as a proportional constant. Thus, it follows from Eqs. (3.27) and (3.32) for a given injector configuration that

$$\frac{F_{Recoil}}{F_{Needle,\,In}} = f\left(\frac{s}{D_0}\right). \qquad (3.34)$$

The ratio of the recoil force to the internal needle force is only a function of the needle stroke and in particular independent of the pressure head.

Total Needle Force

The entire needle force is made up of the integrated needle force inside the nozzle (closing trend) and the recoil force at the nozzle exit (opening trend):

$$F_{Needle} = F_{Needle,\,In} - F_{Recoil}. \qquad (3.35)$$

The corresponding needle force in the closed state of the nozzle can be obtained straightforwardly. The pressure in the nozzle is simply equal to the total pressure p_{tot}, from which a force of the closing trend results. According to Fig. 3.9 and with $R_0 = D_0/2$, this force is calculated to

$$F_{Needle,\,0} = \pi\left(R_0^2 - r_S^2\right)(p_{tot} + p_0) - \pi R_0^2 p_0 = \pi\left(R_0^2 - r_S^2\right)p_{tot} - \pi r_S^2 p_0. \qquad (3.36)$$

Although the second term on the right-hand side of the equation, if compared with the first term, is negligible, the formula again indicates that even here the effect of the atmospheric pressure does not automatically disappear. This is why for the total pressure (the net head) in the nozzle, the atmospheric pressure should theoretically always be accounted for. Because the pressure head in a Pelton turbine is usually of several hundred up to over one thousand meters of water column, the effect of the atmospheric pressure on the needle force can be neglected.

The force that is calculated from Eq. (3.36) also applies as the asymptote of the summation calculations of Eq. (3.27), when the needle gradually moves to the closed position of the nozzle. They can therefore be used to verify the accuracy of the summation calculations.

Similar to Eq. (3.34) with $p_{tot} \gg p_0$ as well as owing to the proportionalities $p_{tot} \sim H$ and $p_i \sim H$, the following dependence can be confirmed:

Fig. 3.9 Closed nozzle
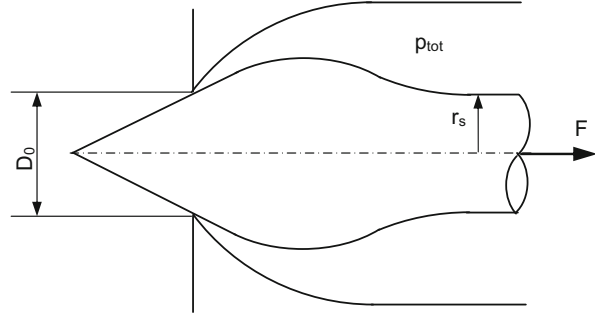
$$F_{\text{Needle}} = f\left(\frac{s}{D_0}\right) \cdot H. \tag{3.37}$$

To a given needle stroke (s), the needle force is directly proportional to the available pressure head.

To estimate the needle force which is basically calculated by the use of Eq. (3.35), i.e., (3.37), the following empirical approach has been quoted in Bohl (2005):

$$F_{\text{Needle}} = K_D\left(D_0^2 - d_S^2\right)gH. \tag{3.38}$$

In this formula, K_D is a geometric constant and d_s the diameter of the needle shaft as indicated in Fig. 3.9 ($d_S = 2r_S$). Obviously, this empirical equation has its background in Eq. (3.37). Calculations with Eq. (3.35), which includes both parts of the total needle force, were used to determine the constant K_D as a function of the needle stroke as shown in Fig. 3.10.

3.5.1.2   Force at the Relief Piston

According to Fig. 3.1, the pressure in the flow acts directly on one side of the relief piston with diameter D_P. The effective pressure is the static pressure. The force acting on the relief piston, thus, acts as an opening force on the needle shaft and is obtained as

$$F_{\text{Piston}} = \frac{\pi}{4}\left(D_P^2 - d_S^2\right)\left(p_{\text{tot}} - \frac{1}{2}\rho c^2\right), \tag{3.39}$$

where $1/2\rho c^2$ is the dynamic pressure in the flow. It directly depends on the flow rate and therefore on the magnitude of the needle stroke. Because this dynamic pressure is negligibly small compared to the total pressure, the force F_{Piston} in the above equation is almost independent of the needle position. This is clearly evidenced by curve 3 in Fig. 3.7.

Fig. 3.10 K_D values of the needle force in the injector with an external servomotor
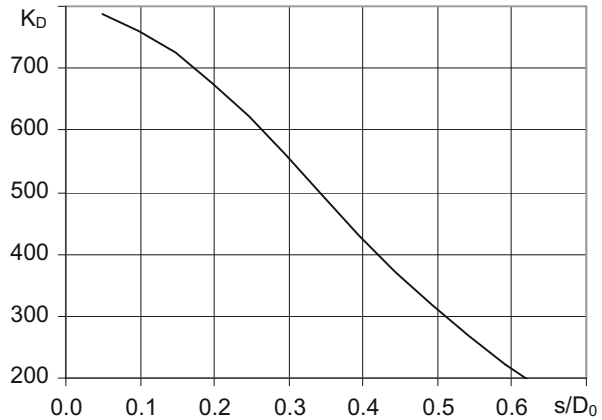
3.5.1.3 Spring Force

From the foregoing considerations and in connection with Fig. 3.7, it can be seen that the sum of the needle force (1, closing trend), recoil force (2, opening trend), and balancing force at the relief piston (3, opening trend) does not always represent the closing trend, especially at the large nozzle openings, at which the needle force with a closing trend is even significantly smaller than the balancing force at the relief piston with an opening trend. In order to safely close the nozzle under all operation conditions of the injector, an appropriate compression spring is installed in almost all servomotors of Pelton turbines. Depending on the required spring force, the compression spring has often been prestressed at a closed nozzle by a length s_0. According to Hooke's law, the spring force in function of the needle stroke s is then given by

$$F_{\text{Spring}} = R(s_0 + s), \qquad (3.40)$$

where the spring constant is designated by R (N/mm).

The spring force, calculated in this way for the considered injector example, is shown in Fig. 3.7 as a function of the needle stroke s/D_0 (curve 4).

3.5.1.4 Regulation Force of the Servomotor

The force composed of the sum of the needle force, the relief piston force, and the spring force must exercise a closing tendency throughout the opening of the nozzle so that the latter can close in any situation by itself. For a given needle stroke, the total closing force has to be balanced by the support force which is provided by the servomotor and calculated as

$$F_{\text{Motor}} = F_{\text{Needle, In}} - F_{\text{Recoil}} - F_{\text{Piston}} + F_{\text{Spring}}. \tag{3.41}$$

In Fig. 3.7, this force is shown as curve 5. It represents a balancing force against the closing force in the whole range of the needle stroke. For large openings of the nozzle, the total closing force becomes significantly smaller. If this force is negative, then a stronger compression spring must be used.

3.5.2 Injectors with an Internal Servomotor

In the configuration of Pelton turbine injectors, the servomotor is sometimes installed in the pressure pipe. The advantage of such a configuration is that the pressure pipe ahead of the injector does not have to be bent. The approaching flow to the injector thus remains undisturbed. However, the associated disadvantage is the poor accessibility for maintenance and inspections.

An injector with an internal servomotor is sketched in Fig. 3.11. To determine the required support force from the servomotor, the needle force as well as the spring force must be known. The condition that the nozzle in each situation is able to close automatically also applies here. The needle force mainly consists of an integrated force which exercises an opening trend and a pressure force on the rear side of the needle, causing a closing trend. The determination of the opening force from the integration of the static pressure over the needle head can be carried out by the same computational procedure as described in Sect. 3.5.1 for the injector with the external servomotor. For a second example, the calculated needle force has been shown in Fig. 3.12 by curve 1 (opening trend). The recoil force is calculated again by Eq. (3.32) and is shown in Fig. 3.12 by curve 2. The constant static pressure force (p) on the rear side of the needle results in a force with a closing trend; it is given by

$$F_{\text{Rear P}} = \left(p_{\text{tot}} + p_0 - \frac{1}{2}\rho c^2\right)\frac{\pi}{4}\left(D_{\text{N}}^2 - D_{\text{S}}^2\right). \tag{3.42}$$

The flow velocity c is calculated from the flow rate and the constant flow section at the corresponding position. In Fig. 3.12, this force is denoted by curve 3. It is almost independent of the needle stroke and thus of the flow rate.

The spring force is calculated with Eq. (3.40) on account of a prestress length s_0 at the closed nozzle. In Fig. 3.12, it is shown by curve 4 for $s_0 = 0$.

The total force with a closing trend represents the support force which has to be provided by the servomotor for balancing the needle at each given position. It is calculated as

$$F_{\text{Motor}} = -F_{\text{Needle, In}} - F_{\text{Recoil}} + F_{\text{Rear, P}} + F_{\text{Spring}}. \tag{3.43}$$

In Fig. 3.12 this force is shown by curve 5.
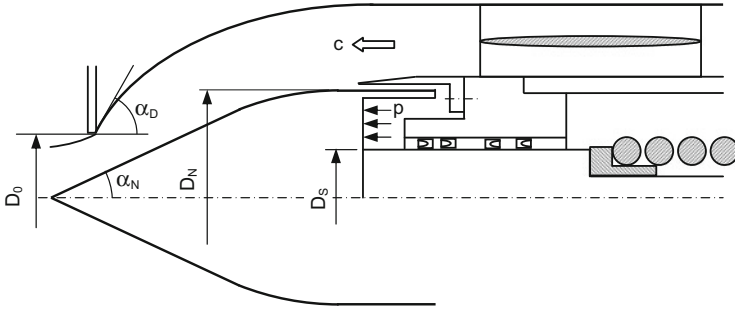
Fig. 3.11 Injector with internal servomotor regulation
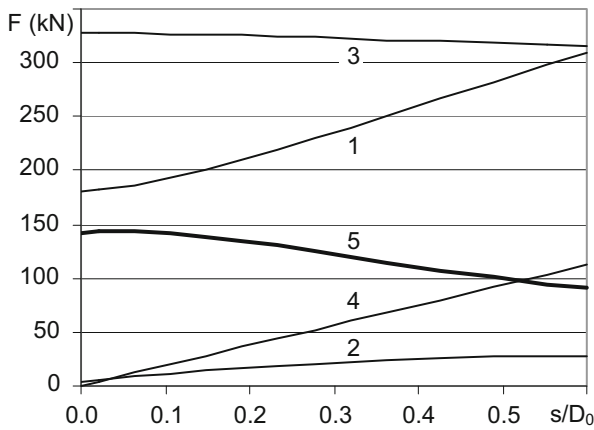
Fig. 3.12 Calculation example for the forces in an injector with internal servomotor regulation. *1* Internal needle force (opening trend), *2* recoil force (opening trend), *3* rear side force (closing trend), *4* spring force (closing trend, without prestressing), *5* support force of the servomotor

In general, the support force provided by the servomotor must be ensured at any time of operation. Otherwise, it could happen that the injector needle under the flow-induced forces would abruptly close the injector, which thus leads to a rapid pressure increase (water hammer) in the pipe system. This also means that each closing of the injector must follow predefined steps as outlined in the next section.

3.6   Closing Law of the Injector Nozzle

The injector of a Pelton turbine is used to convert the pressure energy of water into the kinetic energy of the high-speed jet on the one hand and to regulate the flow rate on the other hand. Because Pelton turbines are highly flexible in balancing the load of the network, they are frequently started and shut off even within hours. When shutting off the turbine, the injector has to be closed within a given time by

Fig. 3.13 Linear regulation of the injector and nonlinear response of the flow rate
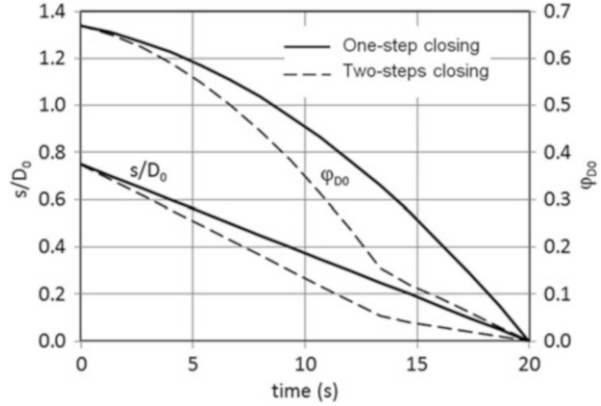
prescribed steps. Such a predefined closing law is generally based on the analysis of the system response in terms of a water hammer. Rapid closing of the injector will always cause a rapid increase of the system pressure and may lead to damage of system components.

Linear closing of the injector through linear changing of the needle stroke is practically not recommended. As shown in Fig. 3.13, which is calculated with the aid of Eq. (3.12), linear closing of the injector (solid line) leads to a nonlinear change of the flow rate. A rapid change in the flow rate, while reaching the needle stroke $s = 0$, will certainly cause a rapid increase in the system pressure and should, thus, most possibly be avoided. One effective method is to define the closing process by two steps. The outcome in the flow rate for the calculation example is shown in Fig. 3.13 by the dashed line.

In practice, a nonlinear closing law is often utilized for achieving a better pressure response in the system. Figure 3.14 shows such a pressure response in a common hydraulic system, both from measurements and calculations. Within the closing time ($t < 47\,\text{s}$), the increase of the pressure at the injector could be successfully damped. For reasons of comparison, the possible pressure response at the injector to a linear closing law of the injector should be considered. This is shown in Fig. 3.15 based on the transient flow calculations with the same algorithm which has already been satisfactorily validated in Fig. 3.14. Obviously, the pressure response during the closing time strongly depends on the closing law of the injector.

The above results suggest the question of how the closing law of the injector should look like in order to minimize the pressure increase in the system. In general, the closing law can be approximated by a parabolic equation. For the nominal flow rate, i.e., the nominal opening ($s_{0,N}$) of the injector nozzle and for a closing time $t_{0,N}$, the closing law can be defined by

$$s = s_{0,N} - s_{0,N} \left(2 - \frac{t}{t_{0,N}} \right) \frac{t}{t_{0,N}}. \tag{3.44}$$

This equation satisfies the condition that for $t = t_{0,N}$ one has $s = 0$ and $\mathrm{d}s/\mathrm{d}t = 0$.
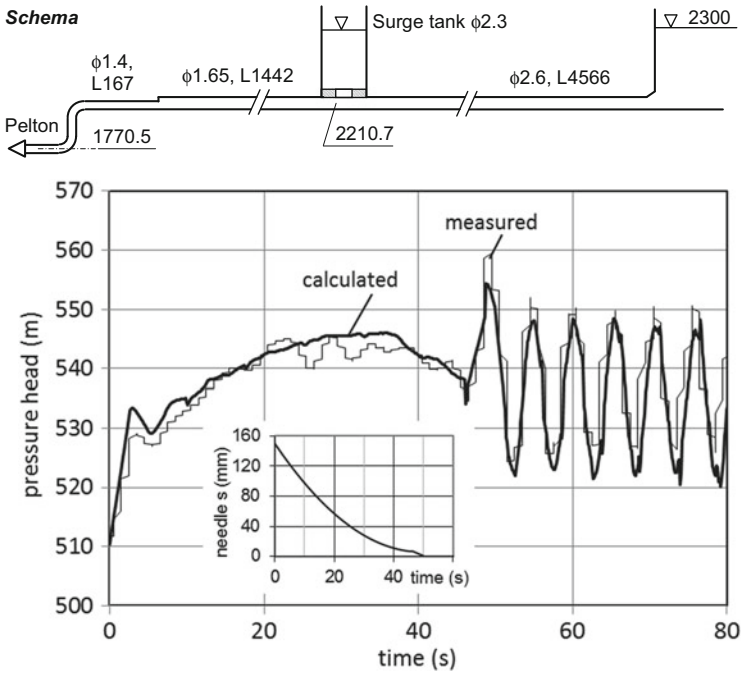
Fig. 3.14 Response of the pressure head at the injector to a nonlinear closing law. Comparison between calculations and measurements in the hydraulic system Gr.1 of the company KWO (transient flow calculation carried out by the author)
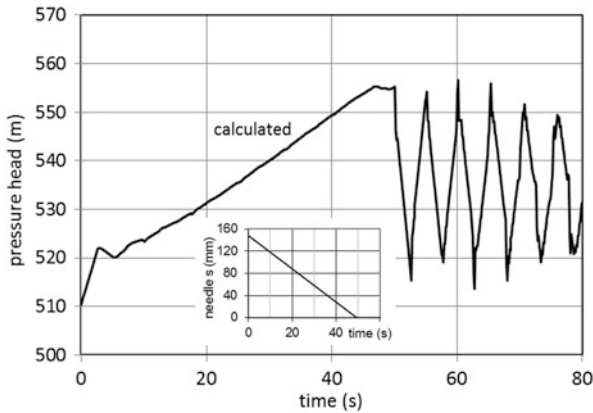
Fig. 3.15 Response of the pressure head at the injector to a linear closing law for the same hydraulic system as in Fig. 3.14

The definition of the closing law at the nominal flow is basically determined by the choice of the closing time $t_{0,N}$. For this reason the changing rate of the needle stroke at $t = 0$, i.e., $(ds/dt)_{t=0}$, should be kept below a permissible value:
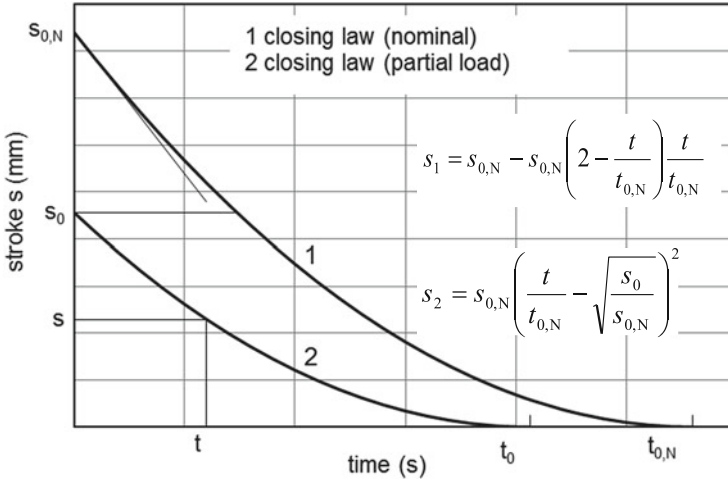
Fig. 3.16 Parabolic closing law of the injector nozzle

$$2\frac{s_{0,N}}{t_{0,N}} < \left(\frac{ds}{dt}\right)_{max}. \tag{3.45}$$

For partial nozzle opening (s_0) at partial load operation, the same closing law should be followed, however, with a correspondingly shorter closing time as sketched in Fig. 3.16. The closing law 2 is exactly a shifting to the left of the nominal closing law 1. Corresponding to the nozzle opening s_0, the new closing time is calculated as

$$\frac{t_0}{t_{0,N}} = \sqrt{\frac{s_0}{s_{0,N}}}. \tag{3.46}$$

Based on the coordinate translation for obtaining the shifting of the curve towards the left, the new closing law is obtained as

$$s = s_{0,N}\left(\frac{t - t_0}{t_{0,N}}\right)^2 \tag{3.47}$$

or because of Eq. (3.46) as

$$s = s_{0,N}\left(\frac{t}{t_{0,N}} - \sqrt{\frac{s_0}{s_{0,N}}}\right)^2. \tag{3.48}$$

The time needed to reach a given needle stroke is given by

$$\frac{t}{t_{0,\mathrm{N}}} = \frac{t_0}{t_{0,\mathrm{N}}} - \sqrt{\frac{s}{s_{0,\mathrm{N}}}}. \tag{3.49}$$

When the injector nozzle is intended to regulate the flow by changing the needle position from $s_{0,\mathrm{N}}$ (for the nominal flow rate) to s_P (for the partial flow rate), then the closing time is calculated from Eq. (3.44) as

$$\frac{t_\mathrm{P}}{t_{0,\mathrm{N}}} = 1 - \sqrt{\frac{s_\mathrm{P}}{s_{0,\mathrm{N}}}}. \tag{3.50}$$

For complete closing of the injector nozzle ($s_\mathrm{P} = 0$), the closing time is equal to $t_{0,\mathrm{N}}$.

References

Bohl, W. (2005). *Strömungsmaschinen 2* (7. Auflage). Vogel Buchverlag.

Keck, H., Vullioud, G., & Joye, P. (2000). Commissioning and operation experience with the world's largest Pelton turbines Bieudron. *Hydro Vision*, Charlotte, USA.

Zhang, Zh. (2003). Theoretical and experimental investigations on the sources of the head effect in Pelton turbines. Sulzer Innotec report, Nr.: TB03_0160, Winterthur, Switzerland.

Zhang, Zh., & Casey, M. (2007). Experimental studies of the jet of a Pelton turbine. *Proceeding of the IMechE Vol. 221, Part A: Journal of Power and Energy*, pp. 1181–1192.

Zhang, Zh., Muggli, F., Parkinson, E., & Schärer, C. (2000). Experimental investigation of a low head jet flow at a model nozzle of a Pelton turbine. *11th International Seminar on Hydropower Plants* (pp. 181–188), Vienna, Austria.

Chapter 4
Jet Characteristics and Measurements

A jet formed by the injector nozzle is highly dynamic and thus subject to an intensive turbulent exchange with the ambient air. Most available knowledge of the dynamics of water jets has been obtained almost exclusively by experimental measurements and is generally restricted to photographic observation of the jet form and the axial velocity distribution within the jet. In principle, by neglecting the fluid friction loss at the injector, the overall jet speed is directly obtained from the Bernoulli equation and equals $\sqrt{2gH}$ where H is the pressure head at the injector inlet. The measurement of the velocity distribution in the jet was almost exclusively conducted by the use of Pitot tubes (Berntsen et al. 2001; Brekke 2005). The accuracy of this measurement technique is very limited. So one was, for example, unable to measure the velocity distribution where the streamlines are curved. The photographic method was mainly used to investigate the jet expansion and insta-bility. Both the velocity measurements by means of Pitot tubes and photographic flow visualizations are unable to fully capture the hydrodynamic features of high-speed jets.

A decisive advance in experimental measurements of the jets in Pelton turbines could be achieved by applying laser measurement methods, i.e., the laser Doppler anemometry (LDA); see Zhang et al. (2000a, b, 2003) and Zhang and Parkinson (2001). A summary of important knowledge from measurements can be found in Zhang and Casey (2007). These investigations have helped to systematically understand the jet mechanics and the stability behaviors.

The following sections discuss, after a brief explanation of the LDA technique, the general characterization of jet flows based on experimental measurements at a model injector. For the purpose of considering the common features of the jet flow, there is no need to distinguish between model turbines and their prototypes.

4.1 Laser Doppler Anemometry

The LDA method is a widely used method for flow investigations. It is highly accurate and nonintrusive and shows the high time-resolution capability. Detailed descriptions of the working principles and the applications of the LDA method can be found, for example, in Durst et al. (1987), Albrecht et al. (2003), Ruck (1987), and Zhang (2010). The development of the LDA method in the past three decades includes both hardware and software development on the one hand and the development that are directed to application methods (Zhang 2004a, b, 2005) on the other hand. To measure the jet under water, Richter and Leder (2006) as well as Hüttmann et al. (2007) directly used a submergible LDA system. For measurements of jets in Pelton turbines, the applicability of the LDA method has been demonstrated by attaching a small wedge of Plexiglas on the jet according to Fig. 4.1. Such a window method aims to smooth the rough and turbulent jet surface, so that the laser beams are enabled to be transmitted into the jet. The disturbance in the flow, as caused by the wedge, is limited to the turbulent boundary layer of a thickness less than 0.1 mm on the surface of the wedge. The LDA method has been demonstrated to be highly accurate for high-speed jet measurements, even in areas of the jet with curved streamlines. Especially, the LDA method has been confirmed as the only effective method to precisely measure the secondary flows in the jet. For this purpose the dual measurement method (DMM) was developed (Zhang and Parkinson 2001, 2002) and has also been generally extended (Zhang 2005).

For more about the LDA application methods under many other measurement conditions, see Zhang (2010).

Based on LDA measurements at a model injector, the most important features of the jet flow are discussed and summarized below.

4.2 Axially Symmetric Jet Flow

Although the jet flow property strongly depends on the flow form at the injector inlet, the simplest case is considered first, as the inlet flow is fully developed in a straight circular pipe. The flow before entering the injector is therefore axially symmetric. Correspondingly, one expects an axially symmetric jet flow. Figure 4.2 shows such expected velocity distributions that are measured at various cross sections along the jet. They represent axial velocity components and have been normalized by the theoretical value of $\sqrt{2gH}$. Based on these first measurements, the following general properties of the jet flow can be observed:

1. In the center of the jet, a clearly separated jet core with a velocity deficit can be recognized. It is simply due to the boundary layer development on the needle surface and is partly equalized along the jet flow. The energy loss associated with the velocity deficit can be determined from measurements on the second
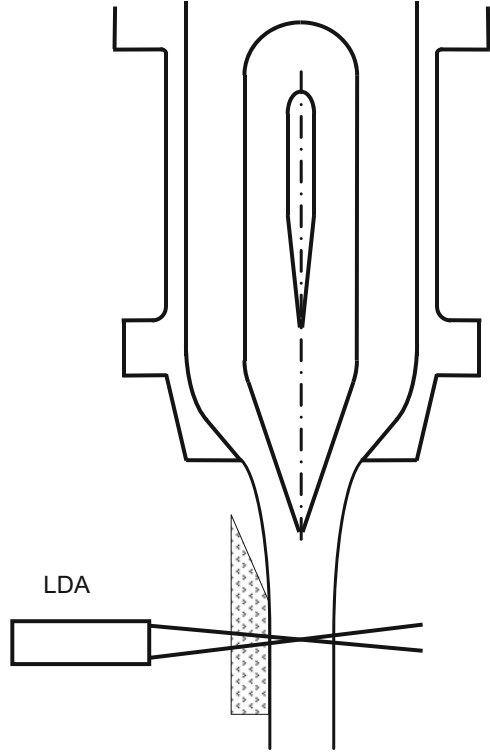
measurement section ($2D_0$), where all streamlines are straight and parallel. The
calculation shows that the related overall head loss is about 0.3 %. Since the
nozzle opening in this case corresponds to the nominal operation point, the head
loss of about 0.3 % can be considered to be general in all injectors under the
nominal flow rate.

The nonuniform velocity distribution in a jet section also means that for calcu-
lations of the overall mass, momentum, and energy flow rates each time the
different mean velocities have to be applied according to the following
definitions:

$$\overline{C}_M = \frac{8}{d_0^2} \int_0^{d_0/2} c \cdot r \cdot dr, \tag{4.1}$$

$$\overline{C}_I = \frac{8}{d_0^2 \overline{C}_M} \int_0^{d_0/2} c^2 \cdot r \cdot dr, \tag{4.2}$$

$$\overline{C}_E^2 = \frac{8}{d_0^2 \overline{C}_M} \int_0^{d_0/2} c^3 \cdot r \cdot dr. \tag{4.3}$$

Axial velocities normalized to C$_0$
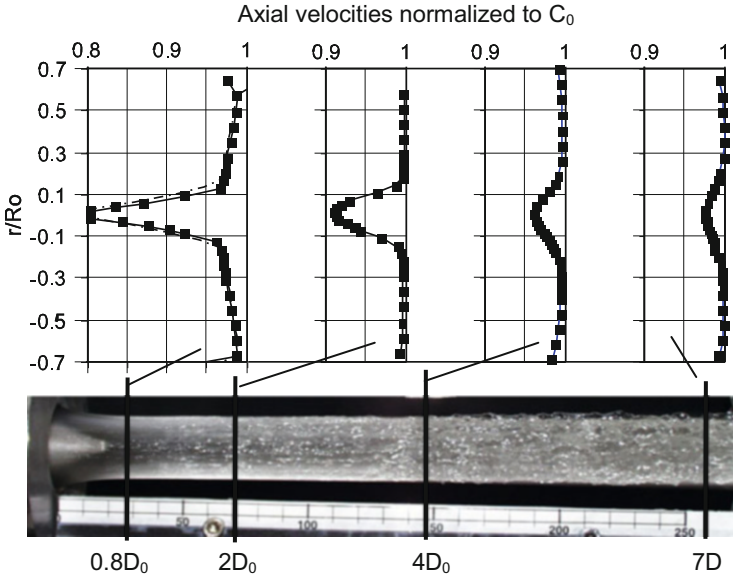
Fig. 4.2 Axial velocity distributions in a jet generated by an injector with straight inlet flow

Corresponding calculations on the second measurement section according to Fig. 4.2 show that the difference between the three mean velocities is negligibly small ($\overline{C}_I/\overline{C}_M = 1.0001$, $\overline{C_E^2}/\overline{C}_M^2 = 1.0004$). For this reason, it is practically not necessary to distinguish between three mean velocities.

2. In the first measurement section, the axial velocity increases linearly from the jet core to the jet surface. This nonconstant velocity profile indicates that the jet contracting has not yet completed up to here. Since as a consequence all streamlines are curved, there is a pressure increase towards the jet core. Accordingly, the flow velocity decreases, while the total pressure remains constant. This is also the reason why the normalized mean velocity at this jet section is obviously smaller than unity. It should be mentioned here that such a velocity distribution at the section with curved streamlines cannot be measured with a Pitot tube. The use of a Pitot tube requires that all streamlines there are straight and parallel. Obviously the accurate LDA measurements also enable the jet waist section to be located and identified.

3. According to the above points, the flow in the first measurement section of the jet is still found to operate under acceleration. The nonuniform velocity profile in the area outside the jet core is indicative of curved streamlines in the jet. It must be noted here that the corresponding streamline curvature can be calculated from the measured velocity profile.
   For this purpose the jet is considered in a cylindrical coordinate system. Since it does not possess any circumferential velocity component, the streamline is described simply by

$$r' = \frac{\mathrm{d}r}{\mathrm{d}z} = \frac{c_r}{c_z}. \tag{4.4}$$

Taking into account that the velocity components c_r and c_z in general are functions of the spatial coordinates, i.e., $r' = f(r, z)$, it further follows from Eq. (4.4) that

$$r'' = \frac{\mathrm{d}^2 r}{\mathrm{d}z^2} = \frac{1}{c_z^2} \left[c_z \left(\frac{\partial c_r}{\partial z} + \frac{\partial c_r}{\partial r} \frac{\mathrm{d}r}{\mathrm{d}z} \right) - c_r \left(\frac{\partial c_z}{\partial z} + \frac{\partial c_z}{\partial r} \frac{\mathrm{d}r}{\mathrm{d}z} \right) \right]. \tag{4.5}$$

Restricting ourselves to the streamlines in further considerations, the streamline equation $\mathrm{d}r/\mathrm{d}z = c_r/c_z$, according to Eq. (4.4), is inserted into the above equation. In addition, potential flow is also assumed so that $\partial c_r/\partial z = \partial c_z/\partial r$. With the assumption $c_r/c_z \ll 1$, Eq. (4.5) is then simplified to

$$r'' = \frac{1}{c_z} \frac{\partial c_z}{\partial r}, \tag{4.6}$$

and the curvature of the streamlines is given by

$$\frac{1}{R} = \frac{r''}{\left(1 + r'^2\right)^{3/2}} \approx r'' = \frac{1}{c_z} \frac{\partial c_z}{\partial r}. \tag{4.7}$$

Since the velocity gradient $\partial c_z/\partial r$ can be obtained from the measured velocity profile that has been shown in Fig. 4.2, the radius of curvature of the streamlines can be directly calculated. Table 4.1 shows some results of the exploited measurements at three pressure heads of 10, 20, and 30 m.

It can be confirmed that due to the almost equal radii of curvature of the streamlines at the measurement sections, all streamlines remain unchanged for different pressure heads. The jet flows are therefore similar.
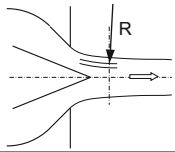
The curvature of streamlines in the jet has the additional consequence that the pressure increases towards the jet axis. The corresponding pressure gradient can be determined from the momentum equation. The Euler equation for the radial velocity component is given in this case by

$$-\frac{1}{\rho} \frac{\mathrm{d}p}{\mathrm{d}r} = c_r \frac{\partial c_r}{\partial r} + c_z \frac{\partial c_r}{\partial z}. \tag{4.8}$$

Assuming potential flow, which is free of rotation, one has $\frac{\partial c_r}{\partial z} - \frac{\partial c_z}{\partial r} = 0$. Due to $\frac{\partial c_z}{\partial r} = \frac{c_z}{R}$ from Eq. (4.7), one obtains

Table 4.1 Radii of curvature of streamlines while passing through the first measurement section according to Fig. 4.2 (Zhang and Casey 2007)

Hydraulic head	Needle stroke $s = 16$ mm		
	$\partial c_z / \partial r$	Curvature radius R (m)	
10 m	37.7	0.37	
20 m	54.0	0.37	
30 m	61.1	0.39	

$$\frac{\partial c_{\mathrm{r}}}{\partial z} = \frac{c_{\mathrm{z}}}{R}. \tag{4.9}$$

The pressure gradient in the jet at the considered measurement section is calculated from Eq. (4.8) with $c_{\mathrm{r}} \approx 0$; the result is

$$\frac{1}{\rho} \frac{\mathrm{d}p}{\mathrm{d}r} = -c_{\mathrm{z}} \frac{\partial c_{\mathrm{z}}}{\partial r} = -\frac{c_{\mathrm{z}}^2}{R}. \tag{4.10}$$

Such an expression of the pressure gradient is analogous to that of a *potential vortex* (see Sect. 6.1.2).

4. Except for the flow velocity in the surface region of the jet, the jet speed remains constant up to a distance $7D_0$. From the mass conservation law, it can be concluded that the jet diameter should remain unchanged as well. That this is realistic will be demonstrated in the next section.

Based on measurements of high-speed jet flows under the simplest flow conditions in the injector, the most important properties of the jet flow could be revealed in this section.

4.3 Jet Expansion

In the measurements shown in Fig. 4.2, it has been confirmed that the jet speed and thus the jet diameter remain almost unchanged over a distance of about $7D_0$. This property is a corroboration of the high quality of the jet flow with negligible energy loss. Based on the observations as well as the photographic recordings, however, it has often been reported that the jet usually suffers from an expansion of about 0.2° to 0.5°. Such an excessive jet expansion in reality cannot be correct. For this reason, the jet is assumed to have an expansion angle α (Fig. 4.3). Because of the constant flow rate $\dot{Q} = A\overline{C}$, the change in the mean speed along the jet is calculated to be

Fig. 4.3 Definition of the
jet expansion
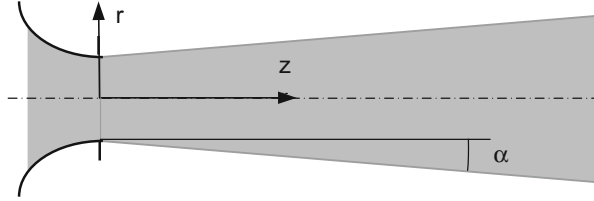
$$\frac{d\overline{C}}{dz} = -\frac{\overline{C}}{A}\frac{dA}{dz}. \tag{4.11}$$

The jet section is given by $A = \pi r^2$ from which it follows that

$$\frac{dA}{dz} = 2\pi r\frac{dr}{dz} = 2\pi r \tan\alpha. \tag{4.12}$$

The specific kinetic energy of the jet flow is given by $e = \overline{C}^2/2$. Its change along the jet is then obtained as

$$\frac{de}{e\,dz} = 2\frac{d\overline{C}}{\overline{C}\,dz}. \tag{4.13}$$

By substituting Eqs. (4.11) and (4.12) into Eq. (4.13) and with $d_0 = 2r_0$ for the jet diameter, one, finally, obtains the change in the specific kinetic energy along the jet in the form

$$\frac{\Delta e}{e} = -(8\tan\alpha)\frac{\Delta z}{d_0}. \tag{4.14}$$

For a typical distance of the jet flow path, say $\Delta z/d_0 = 4$, and a jet expansion angle of $0.2°$, the energy loss according to Eq. (4.14) is estimated to be 11%. Such an extent of the energy loss is actually by no means realistic. According to Eq. (4.14), a loss in kinetic energy of about 1% within a distance of $\Delta z/d_0 = 4$ corresponds to a jet expansion of only $0.02°$. From this assessment it can be concluded that the apparent jet expansion observed in practice is obviously only limited to the jet surface and is, therefore, insignificant in terms of the energy loss. The apparent jet expansion arises most likely only from the turbulent momentum exchange with the ambient air.

4.4   Secondary Flows in the Jet and the Jet Stability

In practice, the injector of a Pelton turbine is usually found downstream of a bend of a pipe (Fig. 2.3) which may be part of the distributor. A fully developed turbulent flow in a long straight pipe is no longer available. This is always the case at a vertical turbine with more than two injectors which are distributed around the Pelton wheel. The inflow to each injector is strongly influenced by the distributor design and is no longer axially symmetric but possesses secondary flow structure. In principle, all axial irregularities or disturbances in the flow can be effectively diminished when the flow is accelerated while passing through the injector. This could be confirmed by an arranged measurement of the jet flow. Despite the interferences of the needle supporting ribs or artificially enhanced disturbances in the injector, no notable change in the jet flow could be identified (Zhang et al. 2000b). However, the existing vortex cells in the flow behave differently. According to the conservation law of angular momentum for frictionless flow, the rotation retains undiminished in the jet. Figure 4.4 shows the corresponding secondary flows which were measured in two sections: downstream of a 90° bend of the pipe and in the jet, respectively. The same model injector as in Fig. 4.2 was used. The high measurement resolution for very small secondary flow velocities in the considered jet section was achieved by means of the dual measurement method (DMM) which was developed by Zhang (2005).

In Fig. 4.4, two well-structured rotating flow zones within the jet section can be confirmed. They are similar to the structure of the secondary flow at the injector inlet. Although such a secondary flow in the jet is sufficiently low against the axial flow, it can influence the jet nature decisively. The secondary flow in the jet takes a form so that two streams meet together on that jet side which corresponds to the inside of the pipe bend. Due to the free surface of the jet, the merger of two streams brings about the water to locally escape from the jet. The direct visible outcome is the formation of a string of longitudinal water droplets on the surface of the jet. Such water droplets behave as a disruptive factor for the mechanical parts of the turbine. By reaching the Pelton bucket, they could cause local damage to the bucket material. In a multi-jet Pelton turbine, the next injector must be protected against the impingement of such water droplets. The protection shelter which is commonly used in practice directly suffers from the strong droplet impingement and thus damage (Fig. 4.5).

In order to improve the jet quality in Pelton turbines, the formation of the water-droplet string on the jet surface has to be effectively suppressed. Since the cause of such an undesirable phenomenon is located upstream of the injector inlet, i.e., downstream of the pipe bend, the application of sharp pipe bends should be avoided if possible. The installation of a flow-straightening grid before or within the injector to break down the secondary flow structure is not always realistic, as this could cause additional head losses and enhance the risk of nozzle clogging. For this reason, it is rather difficult to reduce the swirling flow structure in the jet.
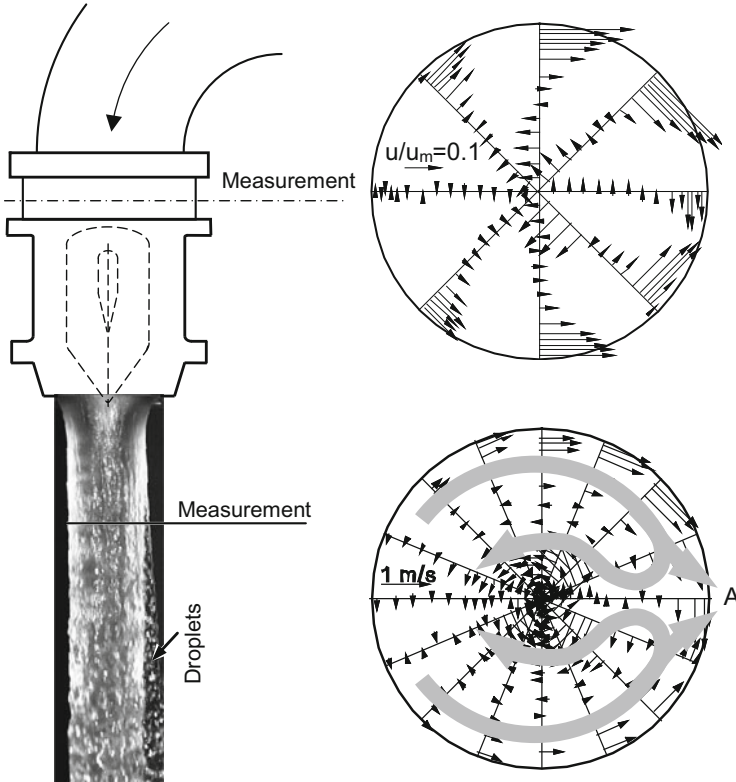
Fig. 4.4 Secondary flow structures in the flow after a 90° bend and in the jet, respectively, and the formation of the water-droplet string on the jet surface, from Zhang and Casey (2007)

Fig. 4.5 Protection shelter in the form of a washbasin and the material damage because of the impingement of water-droplet strings

References

Albrecht, H., Borys, M., Damaschke, N., & Tropea, C. (2003). *Laser doppler and phase doppler measurement techniques*. Berlin: Springer.

Berntsen, G., Brekke, H., Haugen, J., & Risberg, S. (2001). Analysis of the free surface non-stationary flow in a Pelton turbine. *Hydro 2001*, Riva del Garda, Italy.

Brekke, H. (2005). State of the art of small hydro turbines versus large turbines. Hydro 2005, Villach, Austria.

Durst, F., Melling, A., & Whitelaw, J. (1987). *Theorie und Praxis der Laser-Doppler-Anemometrie*. Karlsruhe: Verlag und Gesamtherstellung Braun.

Hüttmann, F., Leder, A., Michael, M., & Majohr, D. (2007). Wechselwirkungen runder Düsenfreistrahlen mit ebenen Wänden bei verschiedenen Auftreffwinkeln. 15. GALA-Tagung, Lasermethoden in der Strömungsmesstechnik, Rostock, Deutschland, Seite 7.1–7.6.

Richter, F., & Leder, A. (2006). Wechselwirkungen runder Düsenfreistrahlen mit ebenen Wänden. 14. GALA-Tagung, Lasermethoden in der Strömungsmesstechnik, Braunschweig, Deutschland, Seite 13.1–13.7.

Ruck, B. (1987). *Laser-Doppler-Anemometrie*. Stuttgart: AT-Fachverlag.

Zhang, Zh. (2010). *LDA application methods*. Berlin: Springer.

Zhang, Zh. (2004a). Optical guidelines and signal quality for LDA applications in circular pipes. *Experiments in Fluids, 37*, 29–39.

Zhang, Zh. (2004b). LDA-Methoden in Messungen aller drei Geschwindigkeitskomponenten in Rohrströmungen. 12. GALA-Tagung, Lasermethoden in der Strömungsmesstechnik, Karlsruhe, Deutschland, Seite 8.1–8.8.

Zhang, Zh. (2005). Dual-Measurement-Method and its extension for accurately resolving the secondary flows in LDA applications. *Flow Measurement and Instrumentation, 16*, 57–62.

Zhang, Zh., Bissel, C., & Parkinson, E. (2003). LDA-Anwendung zu Freistrahlmessungen bei einem Pelton-Turbine-Modell mit der Fallhöhe von 90 Metern. 11. GALA-Tagung, Lasermethoden in der Strömungsmesstechnik, Braunschweig, Deutschland, Seite 13.1–13.6.

Zhang, Zh., & Casey, M. (2007). Experimental studies of the jet of a Pelton turbine. *Proceeding of the IMechE Vol. 221, Part A: Journal of Power and Energy*, pp. 1181–1192.

Zhang, Zh., Eisele, K., & Geppert, L. (2000a). Untersuchungen am Freistrahl aus einer Modelldüse von Pelton-Turbinen mittels LDA. 8. GALA-Tagung, Lasermethoden in der Strömungsmesstechnik, Freising/München, Deutschland, Seite 15.1–15.6.

Zhang, Zh., Muggli, F., Parkinson, E., & Schärer, C. (2000b). Experimental investigation of a low head jet flow at a model nozzle of a Pelton turbine. *11th International Seminar on Hydropower Plants* (pp. 181–188), Vienna, Austria.

Zhang, Zh., & Parkinson, E. (2001). Strömungsuntersuchungen am Freistrahl der Pelton-Turbine und Anpassen des LDA-Verfahrens. 9. GALA-Tagung, Lasermethoden in der Strömungsmesstechnik, Winterthur, Schweiz, Seite 43.1–43.7.

Zhang, Zh., & Parkinson, E. (2002). LDA application and the dual-measurement-method in experimental investigations of the free surface jet at a model nozzle of a Pelton turbine. *11th International Symposium on Applications of Laser Anemometry to Fluid Mechanics*, Lisbon, Portugal.

Chapter 5
Interaction Between the Jet and Pelton Wheel

5.1 Jet Impingement on a Flat Plate

The impingement of a round jet on a flat plate at an angle θ represents a basic model of jet mechanics (Fig. 5.1). To calculate the spreading of the water sheet on the plate surface, the mass, momentum, and energy conservation laws need to be used. Under the assumptions of frictionless deflection of the jet and frictionless spreading of the water sheet, it can be deduced from the conservation law of energy that the spreading speed of the water sheet on the plate surface is equal to the jet speed. The flow distribution along a periphery circle as well as in the radial extent can then be calculated by means of the law of momentum. The mass conservation law determines that the integrated mass flow along each periphery circle should reflect the mass flow of the jet. The first accurate calculation of such a flow distribution was conducted by Hasson and Peck (1964). The distribution of the water-sheet height along the periphery of an arbitrary circle is given by

$$\frac{2r \cdot h}{R^2} = \frac{\sin^3\theta}{(1 - \cos\theta\cos\varphi)^2}.$$

(5.1)

The center of the arbitrary circle coincides with the stagnation point of the round jet on the flat plate and is eccentric to the jet axis at a distance s which is given by

$$\frac{s}{R} = \cos\theta.$$

(5.2)

The interaction force between the jet at a speed C and the flat plate can be determined again by the law of momentum. Since the flow is assumed to be free of friction and hence no force component in the plane of the plate exists, the resulting interaction force is perpendicular to the flat plate. Using the momentum law in the normal direction of the flat plate, then it is calculated as

Fig. 5.1 Impact of a round
jet on a flat plate and the
spreading of the water sheet
on the plate surface
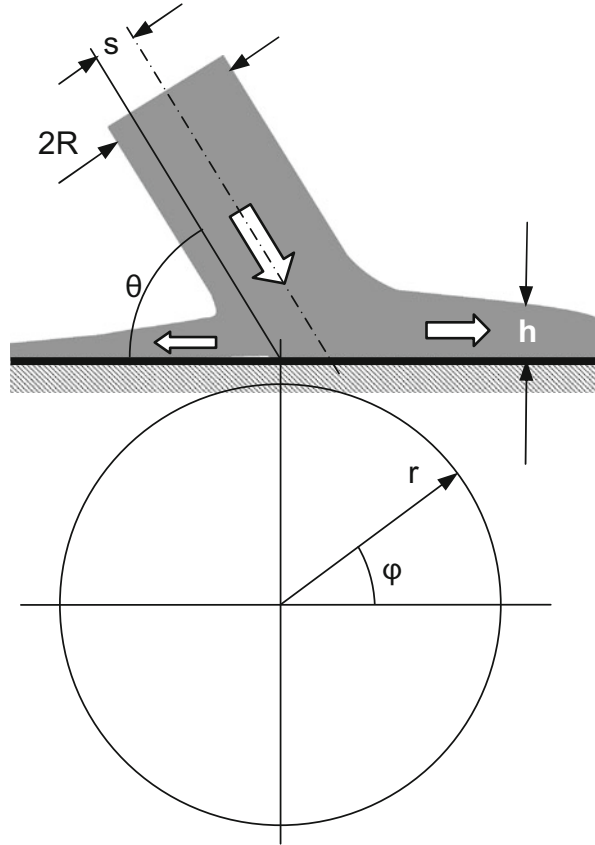
$$F_{jet} = \pi R^2 \cdot \rho C^2 \sin \theta. \tag{5.3}$$

This force is referred to as *jet impact force*. Near the stagnation point beneath the
water sheet, some overpressure exists. Its integration over the plate must be equal to
the jet impact force from Eq. (5.3). The pressure distribution in the immediate
vicinity of the stagnation point has been determined in a study by G.I. Taylor
(1960), among others.

5.2   Minimum Number of Pelton Buckets

A basic concept in the design of a Pelton turbine is the determination of the
minimum number of Pelton buckets so that no water in the jet will bypass unused
the Pelton wheel. The precondition for determining the minimum number of
buckets is that the turbine is operating under the nominal flow rate. According to

Fig. 5.2 Determination of the smallest bucket number by considering the outermost jet layer
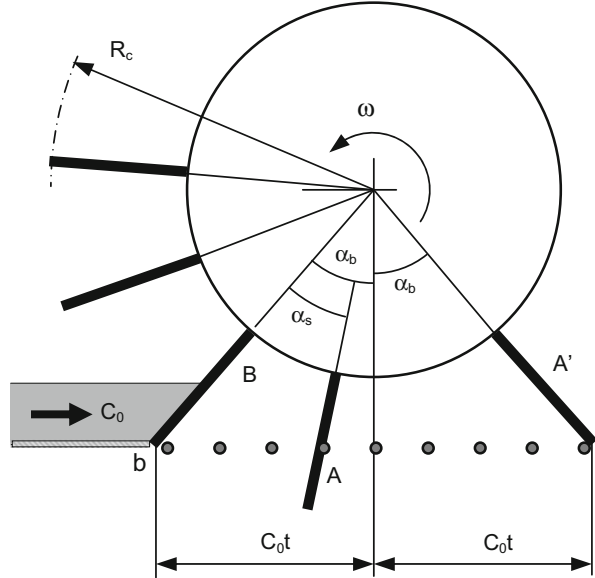
Fig. 5.2, the outermost jet layer has the greatest probability, partly to bypass the rotating buckets. It should be, thus, accounted for to determine the minimum bucket number of a given Pelton wheel.

The last droplet of water (at point b) which might escape from the bucket B must reach the leading bucket A at the latest at position A′. The necessary time is given by

$$2t = 2 \cdot \frac{R_c \cdot \sin \alpha_b}{C_0}. \tag{5.4}$$

Since this is the maximum time allowed, the corresponding rotation of the bucket A must meet the condition

$$2t \cdot \omega < 2\alpha_b - \alpha_s. \tag{5.5}$$

With $\alpha_s = 2\pi/N$ as the bucket distribution angle, this condition is also expressible as

$$2t \cdot \omega < 2\alpha_b - \frac{2\pi}{N}. \tag{5.6}$$

Together with Eq. (5.4) and for $\omega R_c = U_c$, the minimum required number of Pelton buckets is determined by

$$N_{\min} = \frac{\pi}{\alpha_{\mathrm{b}} - \frac{U_{\mathrm{c}}}{C_0} \sin \alpha_{\mathrm{b}}.} \tag{5.7}$$

With the condition that $2U_{\mathrm{c}} \approx C_0$ under nominal operation, this last equation is further simplified to

$$N_{\min} \approx \frac{2\pi}{2\alpha_{\mathrm{b}} - \sin \alpha_{\mathrm{b}}}. \tag{5.8}$$

A similar calculation can also be found in Raabe (1989). In practice, the number of employed buckets is much higher than the necessary minimum according to Eq. (5.8). If the minimum bucket number, for instance, is calculated from the above equation to be $N_{\min} = 14$, the number of buckets realistically used is often 20 or 21. The optimum number of buckets of a Pelton turbine has always been selected for the maximum efficiency and thus depends also on many other operation parameters, not just simply that from condition of Eq. (5.6). A well-proven criterion to practically determining the optimum number of Pelton buckets will be described in Sect. 5.5.

5.3   Water-Jet-Bucket Interaction and Its Specification

Rotating buckets of a Pelton turbine are subjected to the periodic impingement by the jet. For the design of the bucket profiles and the optimization of the turbine operations, the jet piece which interacts with a bucket each time should be determined. To this end and according to Fig. 5.3, the leading edge of the bucket cutout is approximated by a straight edge on the periphery of the diameter D_{c}. It starts cutting the jet at point a on the upper side of the jet. The corresponding bucket position is marked by α_{a} and calculated as

$$\cos \alpha_{\mathrm{a}} = \frac{R_{\mathrm{m}} - d_0/2}{R_{\mathrm{c}}} = \frac{D_{\mathrm{m}} - d_0}{D_{\mathrm{c}}}. \tag{5.9}$$

Analogously to Eq. (2.30), the bucket-position angel α_{a} in the above equation can also be expressed as a function of the specific speed. Under nominal operation conditions given on average by $k_{\mathrm{m,N}} = 0.47$ and $\varphi_{\mathrm{B,N}} = 0.11$, it can be expressed in terms of the specific speed, viz.,

$$\cos \alpha_{\mathrm{a}} = \frac{1 - 0.81 n_{\mathrm{q}}}{1 + 2n_{\mathrm{q}}}. \tag{5.10}$$

Subsequently and at time t_{b}, the same bucket cuts off the jet at point b on its lower side (Fig. 5.3). This means that the water particle which at the time $t = 0$ is located
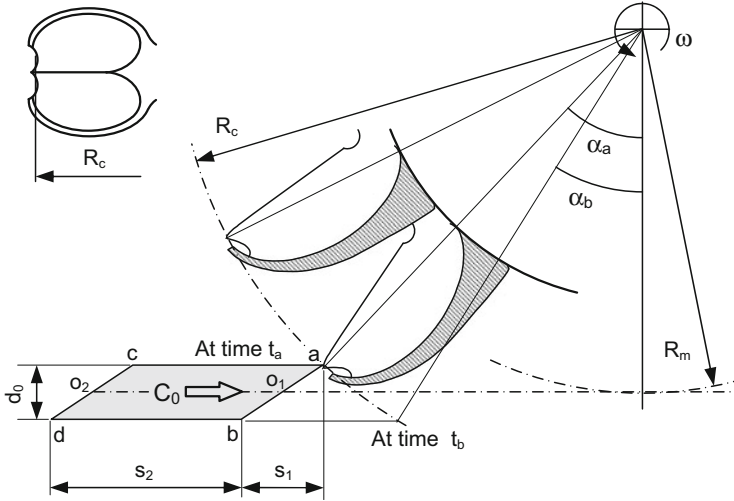
Fig. 5.3 Definition of the jet piece *abcd* and particular bucket positions

at position b will at time $t = t_b$ reach the bucket. The corresponding bucket position is calculated as

$$\cos \alpha_b = \frac{D_m + d_0}{D_c}.$$

(5.11)

For nominal operation conditions and following the same calculation as above, one obtains

$$\cos \alpha_b = \frac{1 + 0.81 n_q}{1 + 2 n_q}.$$

(5.12)

The bucket position α_{o1} at which the bucket intersects the jet axis has already been given in Chap. 2 as a special case; see Eq. (2.30).

Figure 5.4 shows computational results of the bucket positions α_a, α_{o1}, and α_b as functions of the specific speed. At Pelton turbines with higher specific speeds, the bucket cuts off the jet significantly earlier than at Pelton turbines with lower specific speeds. The related operation problems in the initiation of the jet-bucket interaction will be treated in Sects. 5.7 and 5.8.

The jet piece, which enters a bucket each time, is specified by the parallelogram *abcd* in Fig. 5.3. The cutting line *ab* can be regarded as a straight line (Appendix D), while the size of the jet piece is specified by the geometric lengths s_1 and s_2. According to the detailed calculations in Appendix D, these lengths are, respectively, given by

Fig. 5.4 Special bucket-position angles plotted against the specific speed of the Pelton turbine ($k_m = 0.47$, $\varphi_B = 0.11$)
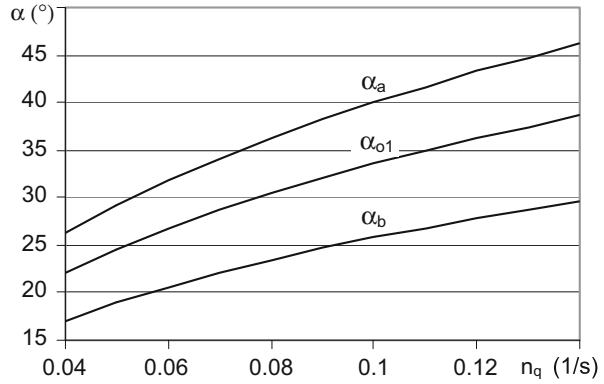
$$\frac{s_1}{D_m} = \frac{d_0}{D_m} \frac{1}{\sqrt{(D_c/D_m)^2 - 1}} \left(\frac{1}{k_m} - 1\right) \tag{5.13}$$

and

$$\frac{s_2}{D_m} = \frac{1}{k_m} \cdot \frac{\pi}{N}. \tag{5.14}$$

The aspect ratio s_1/s_2 is accordingly approximately given by

$$\frac{s_1}{s_2} \approx \frac{0.5}{1 + n_q}. \tag{5.15}$$

It lies normally between 0.43 and 0.46.

The last water particles at c and d on the jet piece $abcd$ reach the bucket at the bucket positions which are described by the angles α_c and α_d, respectively. As shown in Appendix E, these two position angles are given by

$$\alpha_c = \alpha_a - \frac{k_m(\tan\alpha_{o1} - \alpha_{o1}) + 2\pi/N}{1 - k_m} \tag{5.16}$$

and

$$\alpha_d = \alpha_b - \frac{k_m(\tan\alpha_{o1} - \alpha_{o1}) + 2\pi/N}{1 - k_m}. \tag{5.17}$$

Figure 5.5 shows four calculated bucket positions for a Pelton turbine ($n_q = 0.1\,1/s$). Whereas the angle α_a varies between 30° and 45° as shown in Fig. 5.4, the last two bucket positions (α_c and α_d) are practically found symmetrically to the 0-position ($\alpha = 0$). This indicates that the last water particle in the middle jet layer (on the jet

Fig. 5.5 Special bucket
positions, at which water
particles at positions a, b, c,
and d on the jet (see
Fig. 5.3), respectively, enter
the bucket for $n_q = 0.1\,1/s$
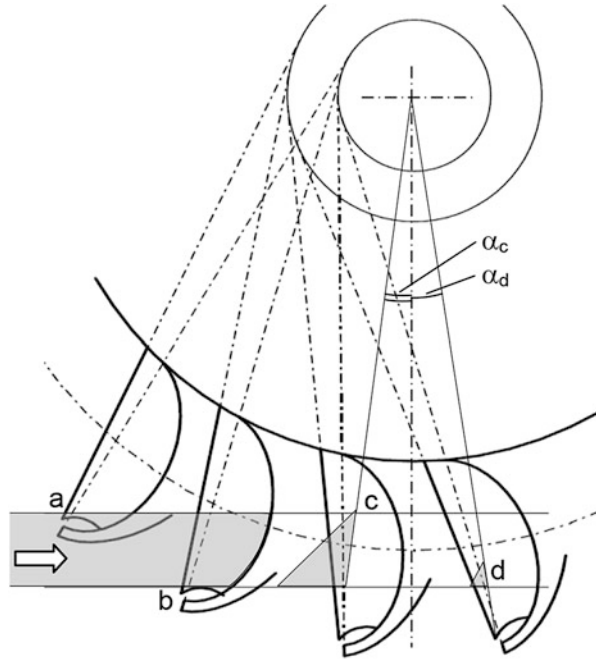
axis) will reach the bucket approximately at the vertical position ($\alpha = 0$) of the
bucket. This knowledge will be utilized to determine the appropriate number of
buckets of a Pelton wheel as a function of the specific speed (Sect. 5.5).

When a specified jet piece approaches and enters the bucket, the bucket sweeps
over an angular range of $\Delta\alpha = \alpha_d - \alpha_a$. This angular range must be given special
attention when a Pelton turbine with two or more injectors is designed. To avoid
interference between two jets in the same bucket, the offset angle between two
injectors must be larger than $\Delta\alpha$. For safe operations it normally measures at least
40° to 55°. For Pelton turbines with six injectors, therefore, precaution should
always be observed. The mutual interference between two jets will not only cause
additional loss in the hydraulic efficiency but also lead to local mechanical damage
of materials. Criteria for determining the smallest offset angle between two injec-
tors will be discussed in detail in Chap. 19.

According to Figs. 5.3 and 5.5, each bucket undergoes the full impingement of
the jet only in the angular range from α_b to α_c. The average angle $(\alpha_b + \alpha_c)/2$ can be
used when the interaction between the jet and the rotating buckets must be esti-
mated. The ideal jet-bucket interaction is achieved when the main part of the jet
enters approximately perpendicularly to the bucket (Fig. 5.6). This ensures ideal
spreading of the water in the rotating bucket. The flow then passes along the bucket
surface with almost constant circumferential speed. This corresponds to the condi-
tion for obtaining the maximum hydraulic efficiency.

Fig. 5.6 Spreading of water in the bucket
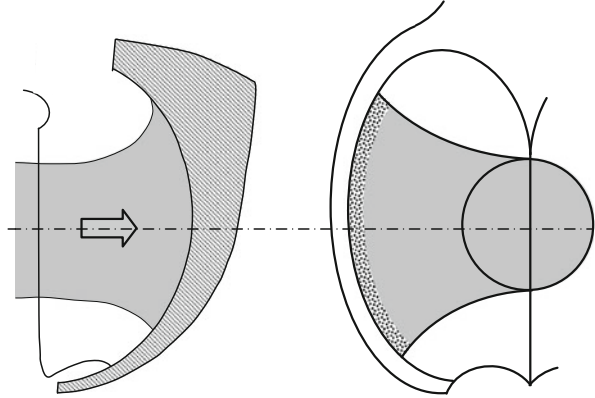
5.4   Coincidence and Symmetry Conditions

In practical applications of Pelton turbines, the peripheral speed coefficient k_m has been selected in the range between 0.45 and 0.48 at which maximum efficiencies can be achieved. To illustrate the possible background of this practical procedure, a thin jet layer is considered which is found at the height of the jet axis, as shown in Fig. 5.7. In Appendix E, the bucket-position angles α_{o1} and α_{o2} as well as their difference are derived. According to Eq. (E.9), the following relation holds:

$$\alpha_{o1} - \alpha_{o2} = \frac{2\pi}{N} + k_m(\tan\alpha_{o1} - \tan\alpha_{o2}). \qquad (5.18)$$

In order to achieve stable interaction between the jet and the rotating buckets, on average two buckets should simultaneously react with a full jet (Fig. 5.7). In other words, when a bucket begins to cut off a certain jet layer, another bucket, which is in advance of two buckets, should be relieved from the impingement of water of the same jet layer. The corresponding impingement and relief points are assumed to be found on the line which connects the tip of the main splitter and the wheel axis according to Fig. 5.7. For the jet layer on the jet axis, these points are denoted by o_1 and o_2, respectively. By observing this middle jet layer, the condition of two buckets subjected on average to the load of a full jet implies that the angle $\Delta\alpha_o = \alpha_{o1} - \alpha_{o2}$ must be twice the bucket distribution angle. This requirement can be formulated by the following equation with $\lambda = 1$:

$$\alpha_{o1} - \alpha_{o2} = 2\lambda \cdot \frac{2\pi}{N}. \qquad (5.19)$$

The factor λ is provisionally used as a placeholder, in order to later be able to consider real operation conditions at which not exactly two buckets are simultaneously found under the impingement of a full jet.

Fig. 5.7 Coincidence condition for the interaction between the jet and the rotating buckets

α_{o1}

$4\pi/N$

O_1

O_2
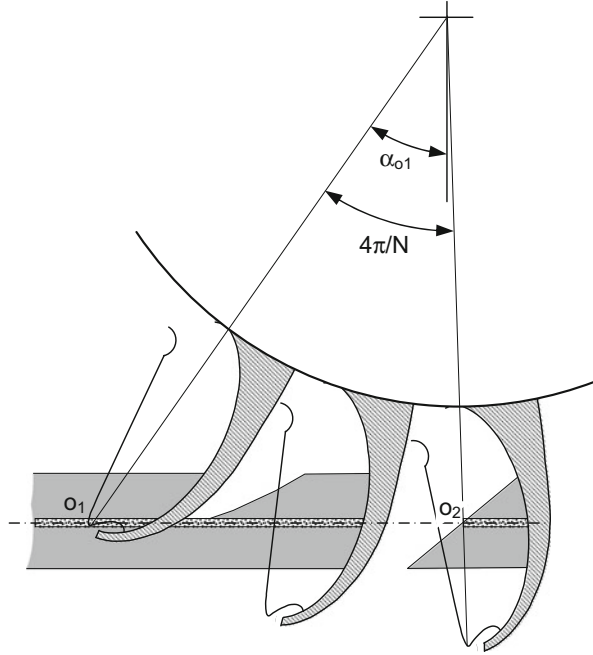
Now Eq. (5.19) is inserted into Eq. (5.18), from which the peripheral speed coefficient k_m is resolved to be

$$k_m = \frac{2\pi}{N} \frac{2\lambda - 1}{\tan \alpha_{o1} - \tan \alpha_{o2}}. \tag{5.20}$$

The angle α_{o2} in the equation is again replaced by Eq. (5.19). This finally results in

$$k_m = \frac{2\pi}{N} \frac{2\lambda - 1}{\tan \alpha_{o1} - \tan (\alpha_{o1} - 4\lambda\pi/N)}. \tag{5.21}$$

The selection $\lambda = 1$ means that, on average, two buckets are simultaneously under the impingement of a full jet, as has already been illustrated in Fig. 5.7. By applying this condition which is called *coincidence condition* to a concrete Pelton turbine, for instance, with 21 buckets and $\alpha_{o1} = 33.5°$ (for $n_q = 0.1$), the operation point of the turbine is expected to have the value $k_m = 0.44$. In most applications of Pelton turbines, the peripheral speed coefficient k_m is known to be within 0.45 to 0.48. The derivation presented above thus explains the mechanical connection to the practical operation point with $k_m < 0.5$. Because of the values of k_m that in actual turbines are practically larger than that expected above, more than two buckets on average actually take part in the exchange with a full jet. This fact can be confirmed, for instance, with the aid of Eq. (5.21). By assuming $\lambda = 1.05$, a peripheral speed coefficient of $k_m = 0.47$ is obtained which agrees well with an actual operation

point of a Pelton turbine. The factor λ is therefore referred to as *multi-bucket factor* and can be assumed to be $\lambda = 1.05$ for Pelton wheels with a middle specific speed $n_q = 0.1$. As will be shown in the next section, the multi-bucket factor is a function of both the peripheral speed coefficient and the specific speed of a Pelton wheel.

It has been mentioned in connection with Fig. 5.5 that the middle bucket position of α_c and α_d should be approximately zero. This simply means that

$$\alpha_{o2} = 0. \tag{5.22}$$

This condition is referred to as *symmetry condition*. It enables, for example, the bucket number of a Pelton wheel to be determined as a function of the specific speed of the turbine.

5.5   Number of Buckets of a Pelton Wheel

The *symmetry condition* introduced in the last section can be applied for the determination of the bucket number. To this end, Eq. (5.22) is applied to Eq. (5.19). The number of buckets is then obtained as

$$N = \frac{4\pi\lambda}{\alpha_{o1}}. \tag{5.23}$$

On the other hand, Eq. (5.20) implies with $\alpha_{o2} = 0$

$$k_m = \frac{2\pi}{N} \frac{2\lambda - 1}{\tan \alpha_{o1}}. \tag{5.24}$$

From these two equations, the multi-bucket factor λ can be eliminated. The bucket number is then obtained as

$$N = \frac{2\pi}{\alpha_{o1} - k_m \tan \alpha_{o1}} = f\left(k_m, n_q\right), \tag{5.25}$$

in which for the identification of the function $f(k_m, n_q)$, Eq. (2.30) has been employed. Comparison with Eq. (5.8) for the minimum number of buckets confirmed the similar structure of the two calculations. The number of buckets according to Eq. (5.25) shows its clear dependence on the peripheral speed coefficient and the specific speed of the Pelton wheel.

The *multi-bucket factor* is determined from Eqs. (5.23) to (5.25) as

$$\lambda = \frac{1}{2}\frac{1}{1 - k_{\mathrm{m}}\frac{\tan\alpha_{\mathrm{o}1}}{\alpha_{\mathrm{o}1}}} = f\left(k_{\mathrm{m}}, n_{\mathrm{q}}\right). \tag{5.26}$$

With this multi-bucket factor, the bucket number can also be directly determined from Eq. (5.23). Furthermore, from the expression $\cos\alpha_{\mathrm{o}1}$ in Eq. (2.30), the expression $\tan\alpha_{\mathrm{o}1}$ can be formulated and then inserted into Eq. (5.24). This results in another formula for calculating the number of buckets, as given by

$$N = \frac{\pi}{k_{\mathrm{m}}}\frac{2\lambda - 1}{\sqrt{n_{\mathrm{q}}\left(1 + n_{\mathrm{q}}\right)}}. \tag{5.27}$$

The number of buckets in this form connects the peripheral speed coefficient, the specific speed, and the multi-bucket factor. For each given Pelton wheel (N, n_{q}) under nominal operation conditions ($k_{\mathrm{m,N}}$), the real multi-bucket factor can thus be determined and used to evaluate the interaction between the jet and the rotating buckets.

Figures 5.8 and 5.9, respectively, show the multi-bucket factor and the number of buckets as functions of the specific speed for different peripheral speed coefficients. For a specific speed of $n_{\mathrm{q}} = 0.11$ on average and a peripheral speed coefficient of $k_{\mathrm{m}} = 0.47$, for instance, the bucket number of $N = 22$ is obtained, which agrees quite well with practical realities. The multi-bucket factor is found to be $\lambda = 1.08$. For Pelton wheels with low specific speeds and operation point k_{m} close to 0.5, the multi-bucket factor tends to unity. In particular, for $n_{\mathrm{q}} \to 0$ and $k_{\mathrm{m}} = 0.5$, there follows $\lambda = 1$. The coincidence condition is then completely fulfilled, and the interaction between the jet and the rotating buckets is comparable to the interaction between the jet and a linearly translating bucket.

The above calculations were carried out under the symmetry condition $\alpha_{\mathrm{o}2} = 0$. Under certain circumstances, the use of the calculated bucket number for a Pelton wheel with high specific speeds may cause problems in the mechanical manufacturing when the clearance between two adjacent buckets is a bit too narrow. In such cases, a lower bucket number is usually selected than calculated. For instance, if from $n_{\mathrm{q}} = 0.13$ and $k_{\mathrm{m}} = 0.47$, the number of buckets is calculated as $N = 21$, one will select in practice $N = 19$. According to Eq. (5.21), this implies a small change of the multi-bucket factor from $\lambda = 1.11$ to $\lambda = 1.10$. The bucket-position angle $\alpha_{\mathrm{o}2}$ changes according to Eq. (5.19) from $\alpha_{\mathrm{o}2} = 0°$ to $\alpha_{\mathrm{o}2} = -4°$. Since this angle change is not particularly large, the number of buckets, $N = 19$ instead of $N = 21$, is anyhow acceptable. The slightly lower numbers of buckets found in practical applications can always be justified with the maximization of the system efficiency. In so doing other influence factors, in particular the friction effect according to Chaps. 10–12, may play a far larger role. Based on experimental studies, an empirical equation for determining the number of Pelton buckets was proposed by Taygun (1946); it reads

Fig. 5.8 Multi-bucket factor plotted against the specific speed (n_q) for different peripheral speed coefficients (k_m)
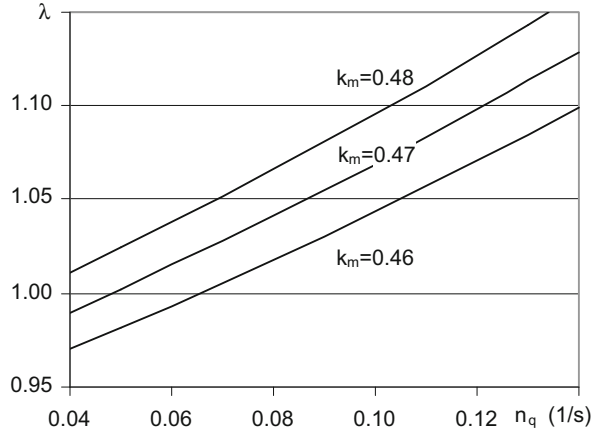
Fig. 5.9 Bucket number plotted against the specific speed and the peripheral speed coefficient under symmetry conditions. Comparison with the empirical calculations according to Taygun (1946) for $k_m = 0.47$, Eq. (5.30)
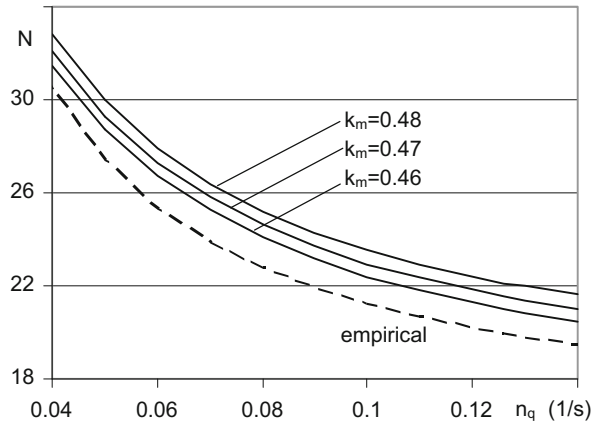
$$N = 15 + \frac{1}{2}\frac{D_m}{d_0}. \tag{5.28}$$

In connection with Eq. (2.26), this empirical equation can be further represented as a function of the peripheral speed coefficient and the specific speed:

$$N = 15 + 1.3\frac{k_m}{n_q}. \tag{5.29}$$

It can further be demonstrated that the rounded bucket number only very slightly depends on the peripheral speed coefficient. Thus, for a mean peripheral speed coefficient of $k_m = 0.47$, one obtains

$$N = 15 + \frac{0.62}{n_{\mathrm{q}}}, \tag{5.30}$$

which is of purely geometric nature because of the specific speed n_{q}. For comparison reasons, the bucket number, calculated in this way, has also been shown in Fig. 5.9 as a function of the specific speed. It confirms a very good similarity between the high empirical and theoretical values. The relevant equation (5.27), which is derived by the use of the coincidence and symmetry conditions, clearly reveals the mechanical connection of these conditions to the optimum number of buckets of a Pelton wheel. With it, it is now also clarified why the peripheral speed coefficient of a Pelton turbine is always found in the range 0.45 to 0.48, i.e., less than 0.5.

5.6   Relative Track of the Jet

The real interaction between the jet and a Pelton bucket can be well illustrated when the relative velocity of the jet before and at the entrance of the bucket is considered. For this purpose, the relative track of a water particle that enters a rotating bucket should be considered first. The water particle is found on its trajectory on the jet layer which, according to Fig. 5.10, is a distance h away from the wheel axis. With respect to the coordinate system in the figure, the components of the relative flow velocity $\vec{W}_0$ of a water particle before entering the bucket are given by

$$W_{0\mathrm{x}} = C_{0\mathrm{x}} - U_{\mathrm{x}} = C_0 - \omega \cdot h, \tag{5.31}$$

$$W_{0\mathrm{y}} = 0 - U_{\mathrm{y}} = -\omega \cdot R \cdot \sin \alpha. \tag{5.32}$$

The water particle is assumed to enter at time $t = 0$ the bucket at the bucket position α_{e}, i.e., at the radial position $R_{\mathrm{e}} = h/\cos \alpha_{\mathrm{e}}$ with $x = x_{\mathrm{e}}$ and $y = h$. The relative track of the water particle before entering the bucket will thus be characterized by negative times.

Since the water particle before entering the bucket is found at $h = $ const, i.e., $R \cdot \cos \alpha = $ const, one also has in steady rotation $W_{0\mathrm{x}} = $ const according to Eq. (5.31). The relative track of the water particle in the relative system is then described by

$$x = x_{\mathrm{e}} + \int_0^t W_{0\mathrm{x}} \mathrm{d}t = x_{\mathrm{e}} + (C_0 - \omega \cdot h) \cdot t, \tag{5.33}$$

$$y = h + \int_0^t W_{0\mathrm{y}} \mathrm{d}t = h - \omega \int_0^t R \cdot \sin \alpha \mathrm{d}t. \tag{5.34}$$

Because $R \cdot \sin \alpha = -x_{\mathrm{e}} - C_0 \cdot t$, Eq. (5.34) may also be written as

Fig. 5.10 Relative track of a water particle which enters the bucket at the bucket-position angle α_e
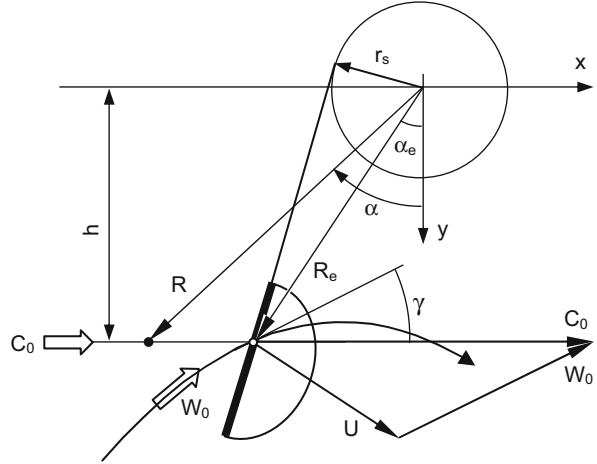
$$y = h + \omega \int_0^t (x_e + C_0 \cdot t)\mathrm{d}t = h + \omega\left(x_e t + \frac{1}{2}C_0 t^2\right). \tag{5.35}$$

Eliminating the time between Eqs. (5.33) and (5.35), the relative track of the observed water particle is expressible as

$$y = h + \omega \frac{x - x_e}{C_0 - \omega \cdot h}\left(x_e + \frac{1}{2} \cdot \frac{x - x_e}{1 - \omega \cdot h/C_0}\right). \tag{5.36}$$

This relative track relation only applies to water particles that enter the bucket at the position with $x = x_e$ and $y = h$. There, the tangent of the relative track coincides with the slope of the relative velocity W_0, as shown in Fig. 5.10. The angle γ, at which the observed water particle enters the bucket, is calculated from the relation

$$\tan\gamma = -\left(\frac{W_{0y}}{W_{0x}}\right)_e = \frac{\omega x_e}{C_0 - \omega h}. \tag{5.37}$$

For water particles on the jet axis, one has $\omega h = U_m$. Moreover, because of $k_m = U_m/C_0$, it further follows from the above equation that

$$\tan\gamma_o = \frac{k_m}{1 - k_m}\frac{x_o}{h} = \frac{k_m}{1 - k_m}\tan\alpha_o \approx 0.9\tan\alpha_o, \tag{5.38}$$

in which the subscript "e" has been altered to "o." For small values of α_o and γ_o, this can be approximated by

$$\gamma_o \approx 0.9\alpha_o. \tag{5.39}$$

The connection between $\tan \gamma_o$ and $\tan \alpha_o$ by the parameter k_m can also be directly obtained by applying the velocity triangle. The approximation in the above equation is made only for $k_m = 0.475$.

If the relative motion of the water particle is further considered for the period $t > 0$ and supposed to be unaffected by the bucket, then the water particle will reach the peak of the relative track (Fig. 5.10), at which there is $W_y = 0$. In the absolute system, the water particle is found on the y-axis because, according to Eq. (5.32), there is $\alpha = 0$.

5.7   Flow Detachment at the Cutting Edge of Bucket Cutout

It has already been shown in Sect. 5.3, and was illustrated in Fig. 5.4, that for Pelton turbines with high specific speeds, the bucket starts to cut off the jet relatively early. This has as a consequence that the relative flow velocity in the velocity triangle, according to Fig. 5.11, may be too "steeply" oriented towards the bucket; the flow will then get separated at the cutout edge. The water that passes the bucket cutout edge follows the relative track that has already been calculated in Sect. 5.6 and subsequently quickly strikes the inner surface of the bucket. The impact position, denoted by a, can be determined from Fig. 5.11 by following the water particle within a short time, during which the bucket sweeps over an angle $\Delta \alpha = \omega t$, and the water particle moves a distance $\Delta x = C_0 t$.

The immediate consequence of this impulsive action is abrasion damage on the bucket surface. Such damages have already been observed in practice for Pelton turbines with high specific speeds. Figure 5.12 shows the systematic breakdown of the wear coating on the bucket surface, just in the zone where the separated flow gets reattached and strikes with a hammer effect. The high periodic beating, in the illustrated example at 30 Hz, deteriorates the adhesion of the wear coating and leads to its breakdown after a short operation time. For this reason, the bucket profile in the region of bucket cutout must be carefully designed, especially for Pelton wheels with high specific speeds.

5.8   Shockless Condition on the Bucket Rear Side

At the instance of cutting off the jet by the bucket cutout, the jet is split into two parts. One part enters the bucket; the other part bypasses it. In the case of unfavorable design of the bucket cutout, the second part of the jet may partly impinge on the rear side of the bucket. The situation becomes worse particularly for a Pelton wheel with high specific speeds at which the slope of the relative velocity at the bucket cutout is relatively "steep," as already shown in Fig. 5.11. The impingement of the

Fig. 5.11 Flow separation
and reattachment for Pelton
wheels with large specific
speeds
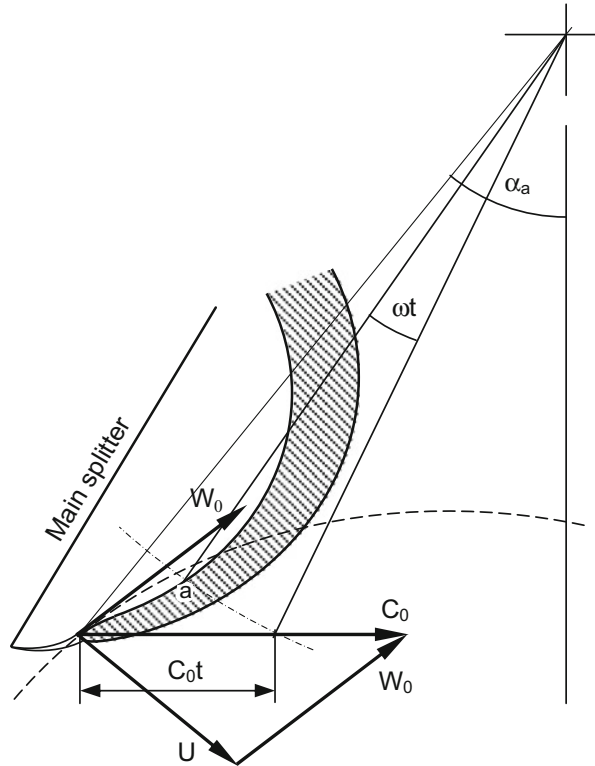
Fig. 5.12 Systematic
breakdown of the wear
coating on the bucket inside
of a Pelton turbine
($n_q = 0.13$), caused by the
hammer effect of water
droplets
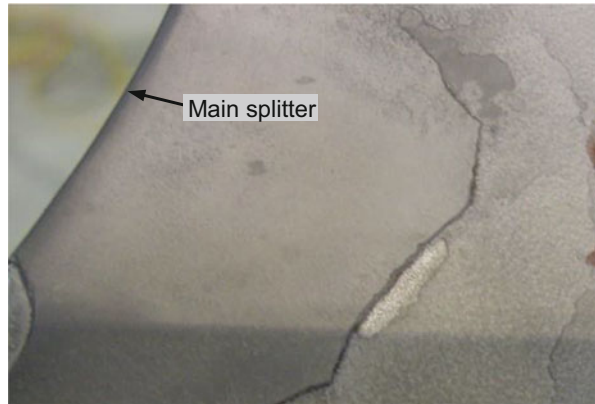
jet on the rear side of the bucket will primarily cause an efficiency drop and thus should be avoided whenever possible. To this end, a criterion should be worked out.

The criterion of designing the profile of the bucket cutout is the velocity relation in the rotating frame. It has already been shown in the last section that the steepest relative velocity and therefore the most critical flow angle are found at the

Fig. 5.13 Condition for flows avoiding jet impingement on the rear side of the bucket at the bucket cutout zone, $\psi < \varphi_a$ with $\varphi_a = \pi/2 - \beta_a$
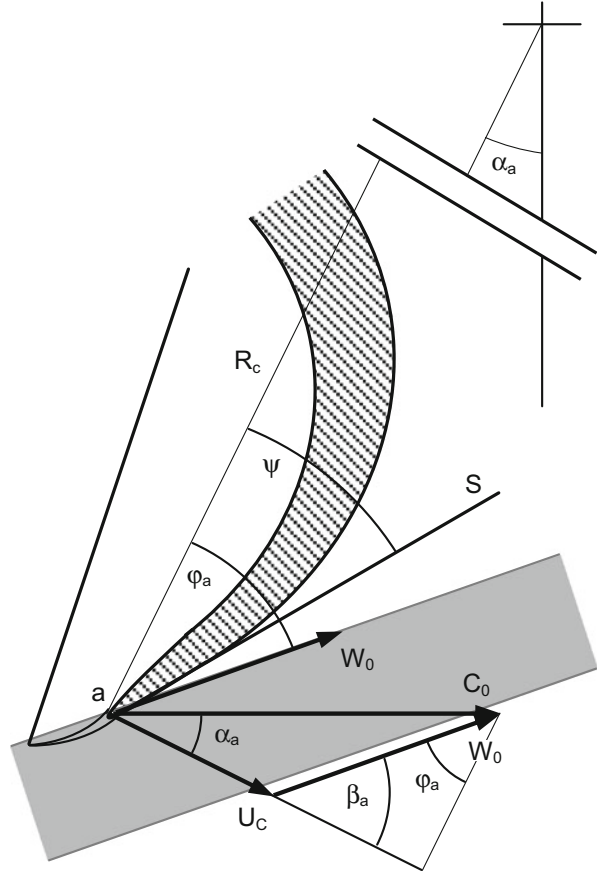
beginning of cutting off the jet. The corresponding bucket position is given by α_a, and the corresponding velocity relation is shown in Fig. 5.13. The relative velocity points in the direction that is given by the angle φ_a. The surface profile on the rear side of the bucket is indicated by S which has a fixed inclination angle ψ relative to the radial direction. The condition of the jet flow without touching the bucket rear side is simply given by $\psi < \varphi_a$.

The flow angle φ_a of the relative flow is calculated from the velocity triangle at the bucket entry. After Fig. 5.13 by employing the law of sines, it is determined by

$$\cos \varphi_a = \frac{C_0 \cdot \sin \alpha_a}{W_0}. \tag{5.40}$$

In this equation, the relation $\sin(\pi - \beta_a) = \sin \beta_a = \cos \varphi_a$ has been applied.

The relative flow velocity is calculated according to the law of cosines:

$$W_0^2 = U_c^2 + C_0^2 - 2U_c C_0 \cos \alpha_a, \tag{5.41}$$

which can also be given in the form

$$\frac{W_0^2}{C_0^2} = \frac{U_c^2}{C_0^2} + 1 - 2\frac{U_c \cos \alpha_a}{C_0}. \tag{5.42}$$

Inserting this relation into Eq. (5.40) yields

$$\cos^2 \varphi_a = \frac{\sin^2 \alpha_a}{(U_c/C_0)^2 + 1 - 2(U_c/C_0) \cdot \cos \alpha_a}. \tag{5.43}$$

This equation may also be represented as a function of the specific speed. To this end Eq. (5.10) for α_a and Eq. (2.33) with $k_m = 0.47$ are taken into account. Then there follows from Eq. (5.43)

$$\cos^2 \varphi_a = \frac{1 - \left(\frac{1 - 0.81 n_q}{1 + 2n_q}\right)^2}{0.22(1 + 2n_q)^2 + 0.76 n_q + 0.06}. \tag{5.44}$$

The dependence of the relative flow angle φ_a on the specific speed n_q has thus been derived. A graphical relation is shown in Fig. 5.14. Obviously, the relative flow angle φ_a decreases rapidly with the increase of the specific speed of the Pelton wheel. This circumstance highly complicates the design of the rear side profile of the bucket cutout for being free of impingement ($\psi < \varphi_a$). Since almost inevitable jet impingement on the rear side of Pelton buckets is always associated with a counterforce to the bucket rotation, an additional loss in the system efficiency must be expected. Furthermore, increasing material abrasion will occur. It also shows that the flow angle φ_a is practically independent of the peripheral speed coefficient k_m.

For practical applications, the flow angle φ_a as a function of the specific speed can be approximated by fitting the curve in Fig. 5.14 to a quadratic polynomial. The result is

$$\varphi_a = 1500 n_q^2 - 610 n_q + 63. \tag{5.45}$$

A reference criterion for designing Pelton buckets with $\psi < \varphi_a$ is thus available.

Fig. 5.14 Flow angle at the bucket rear side plotted against the specific speed n_q
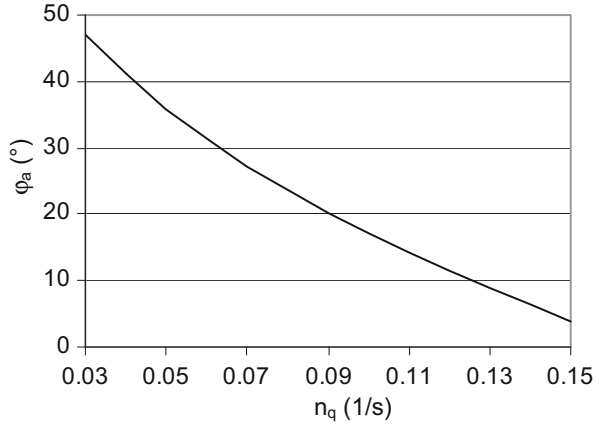
5.9   Shock Load Force and Related Power at Bucket Entries

The high-speed jet enters a bucket both at the bucket cutout and along the main splitter. For Pelton wheels of high specific speeds, the flow separation at the bucket cutout edge often occurs, as has already been revealed in Sect. 5.7. Apart from this undesirable flow, the entering of the jet both at the bucket cutout and along the main splitter is always related with a "sudden" deflection of the flow and thus with a shock load. While in closed channel flows, the flow separation due to a sudden change in the flow state always generates a shock loss, the shock effect in the current case at entries of Pelton buckets can be regarded to be free of any losses. The related flow mechanism is quite simple. During the quasi-sudden deflection of the flow at the bucket edges, the kinetic energy of the high-speed jet is partially converted into the pressure energy which shortly thereafter is converted back again. The energy conversion in this form occurs without any spatial restriction and is thus not related to any flow separation. The comparable flow deflection has already been shown in Sect. 5.1 (see Fig. 5.1).

In the following, the shock effects at both the main splitter and the cutout edge of Pelton turbines will be separately considered.

5.9.1   Deflection of the Flow at the Bucket Main Splitter

The bucket main splitter of Pelton turbines is mostly configured to have an angle 2ε of 25° to 40° (Fig. 5.15). It receives the jet generally at a non-perpendicular angle to the jet axis as well as to the relative flow velocity (Sect. 5.6). For simplicity, here only the case is considered in which the bucket main splitter is just perpendicular to the jet axis. The sudden deflection of the flow by the angle ε results in a shock load of the bucket. The associated *shock load force* acts on the moving bucket and

Fig. 5.15 Flow deflection
at the main splitter
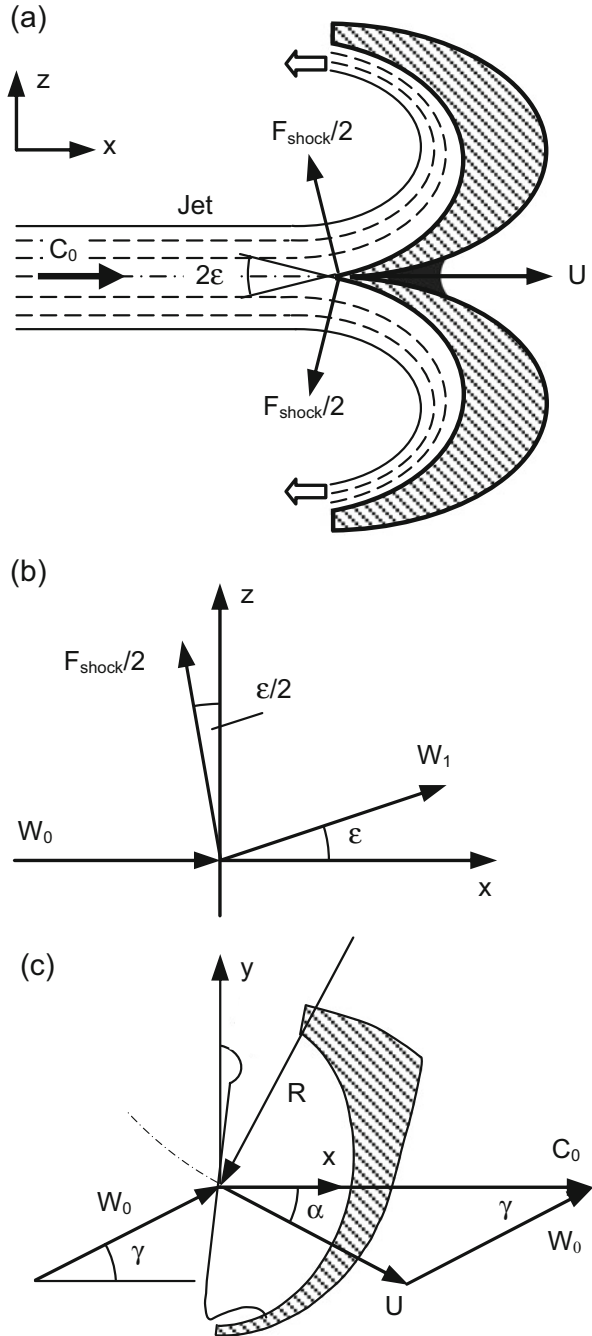
therefore contributes to the shaft power. Its determination is simply based on the law of momentum. For this reason, an x-y-z coordinate system, as shown in Fig. 5.15, is introduced. The x-y plane is found in the plane which is spanned by the jet axis and the bucket main splitter. The x- and y-axes are parallel to the jet axis and the bucket main splitter. In addition, the relative velocity is found at an inclination angle γ to the jet axis.

For the use of the momentum law, the flow in the upper half of the bucket (Fig. 5.15a) is considered. The relative flow rate and the shock load force are given by $\dot{Q}_w/2$ and $F_{shock}/2$, respectively. In the relative frame, the momentum flow rate before the jet deflection is a vector quantity having three components as

$$\vec{I}_0 = \left(\frac{1}{2}\rho\dot{Q}_w W_0 \cos\gamma, \ \frac{1}{2}\rho\dot{Q}_w W_0 \sin\gamma, \ 0 \right). \tag{5.46}$$

The relative velocity in this equation is found in the x-y plane.

After the deflection of the jet, the momentum flow rate is given by the momentum vector $\vec{I}_1 = (I_{1x}, I_{1y}, I_{1z})$.

The shock load force is restricted to the x-z plane. This is so because at the jet impact point and along the y-axis, the velocity component W_y remains constant, and thus the corresponding force component disappears. The shock load force on the main splitter is then given in vector form by

$$\frac{1}{2}\vec{F}_{shock} = \left(-\frac{1}{2}F_{shock}\sin\frac{\varepsilon}{2}, \ 0, \ \frac{1}{2}F_{shock}\cos\frac{\varepsilon}{2} \right). \tag{5.47}$$

Consequently, from the law of momentum in the form $\frac{1}{2}\vec{F}_{shock} = \vec{I}_1 - \vec{I}_0$, the following component relations for the momentum after the shock load incident can be obtained:

$$I_{1x} = \frac{1}{2}\left(\rho\dot{Q}_w W_0 \cos\gamma - F_{shock}\sin\frac{\varepsilon}{2} \right), \tag{5.48}$$

$$I_{1y} = \frac{1}{2}\rho\dot{Q}_w W_0 \sin\gamma, \tag{5.49}$$

$$I_{1z} = \frac{1}{2}F_{shock}\cos\frac{\varepsilon}{2}. \tag{5.50}$$

In order to resolve the shock load force from these relations, the energy law must also be applied. Because the flow deflection is free of loss, the kinetic energy in the flow must remain constant; it is represented by

$$I_{1x}^2 + I_{1y}^2 + I_{1z}^2 = I_{0x}^2 + I_{0y}^2 + I_{0z}^2. \tag{5.51}$$

Substituting all the related expressions derived above, the magnitude of the shock load force $F_{shock}/2$ is deducible as

$$\frac{F_{\text{shock}}}{2} = \rho \dot{Q}_{\text{w}} W_0 \cos\gamma \cdot \sin\frac{\varepsilon}{2}. \qquad (5.52)$$

It is directed perpendicular to the flow (Fig. 5.15a). The force which is directed towards the bucket is given by the same value.

The circumferential speed of the bucket is expressible as $\vec{U} = (U\cos\alpha, \ -U\sin\alpha, \ 0)$. With respect to the flow deflection at two bucket halves, the total power of working provided by the shock load force at a full bucket is calculated to

$$P_{\text{shock}} = -\vec{U} \cdot \vec{F}_{\text{shock}} = 2\rho \dot{Q}_{\text{w}} W_0 U \cos\alpha \cos\gamma \cdot \sin^2\left(\frac{\varepsilon}{2}\right), \qquad (5.53)$$

or, since $\sin^2(\varepsilon/2) = (1 - \cos\varepsilon)/2$,

$$P_{\text{shock}} = \rho \dot{Q}_{\text{w}} W_0 U \cos\alpha \cos\gamma \cdot (1 - \cos\varepsilon). \qquad (5.54)$$

The specific work that is done by the shock load force is, from its definition, given by

$$e_{\text{shock}} = \frac{P_{\text{shock}}}{\rho \dot{Q}_{\text{w}}} = W_0 U \cos\alpha \cos\gamma \cdot (1 - \cos\varepsilon). \qquad (5.55)$$

If related to the specific kinetic energy $C_0^2/2$ of the jet, one obtains

$$\eta_{\text{shock}} = \frac{e_{\text{shock}}}{\frac{1}{2}C_0^2} = 2\frac{W_0}{C_0}\frac{U}{C_0} \cos\alpha \cos\gamma \cdot (1 - \cos\varepsilon). \qquad (5.56)$$

This is called the partial efficiency of the shock load force. A special case is given for $\alpha = 0$ which also means $\gamma = 0$ and $W_0 = C_0 - U_{\text{m}}$. This corresponds to the vertical alignment of the relative flow to the bucket main splitter and is therefore equivalent to the case of a linearly translating bucket. With $k_{\text{m}} = U_{\text{m}}/C_0$, Eq. (5.56) leads to

$$\eta_{\text{shock}} = 2k_{\text{m}}(1 - k_{\text{m}})(1 - \cos\varepsilon). \qquad (5.57)$$

This result is formally identical to Eq. (2.16) or Eq. (2.40). Numerically, for instance, for $k_{\text{m}} = 0.5$ and $\varepsilon = 15°$, the related partial efficiency is given by $\eta_{\text{shock}} = 1.7\%$. Recall that this partial efficiency is solely due to the sudden change of the flow direction at the main splitter of the bucket and not due to the flow process.

The exclusive analysis of the shock load force and its effect aids to divide the power conversion between the jet and the rotating buckets into two mechanical forms: (1) the shock form at the bucket main splitter and (2) the continuous form of

the flow inside the rotating bucket towards the bucket exit. The hydraulic efficiency achieved by the continuous flow process is determinable by

$$\eta_{\text{continuity}} = 2k_{\text{m}}(1 - k_{\text{m}}) \cdot (\cos \varepsilon - \cos \beta_2). \qquad (5.58)$$

Together with the partial efficiency η_{shock}, the overall efficiency can be obtained; it agrees exactly with Eq. (2.40).

The separation of the entire power conversion process into two subforms has the practical significance when the conversion performances like the power, efficiency, etc. have to be determined from the integration of the flow along the bucket surface. In so doing, the lower bound of the integration must obviously be located at the bucket entry with the real flow angle ε which is nonzero. A comparable computational example which concerns a similar flow will be shown in Chap. 12. There, the flow friction effect in the relative flow within a rotating bucket has also been considered by integration.

5.9.2   Deflection of the Flow at the Bucket Cutout Edge

To calculate the shock load force at the bucket cutout edge, the cutting edge is assumed to be straight in the z direction, as shown in Fig. 5.16. The x-coordinate is selected to be parallel to the jet axis. Since the case with $\gamma > \gamma_{\text{c}}$ implies flow separation, which, according to Sect. 5.7, should not occur, only the case of $\gamma < \gamma_{\text{c}}$ will be considered here.

Apart from the singularity of the flow at the cutting edge, the shock load force associated with the sudden change of the flow direction is perpendicular to the bucket surface. This implies that that part of the water which depends on the angle difference $\Delta\gamma = \gamma_{\text{c}} - \gamma$ will flow backwards. For calculating the flow within the bucket, one is tempted to take into account only the forward moving flow rate. Indeed, since the angle difference $\Delta\gamma$ in effect is very small, the back flow can be neglected. This, however, has the consequence that, according to the law of momentum, the direction of the shock load force will slightly deviate from the normal direction of the bucket surface. Instead of being perpendicular to the bucket surface, it is then in line with the bisector of the deflection angle. Such a situation has already been encountered in Fig. 5.15 where the shock load force deviated from the normal of the bucket surface by $\varepsilon/2$.

In the rotating frame, the momentum flow rate of the jet before deflection (index 0) is represented by its components:

$$I_{0x} = \rho \dot{Q}_{\text{w}} W_0 \cos \gamma, \qquad (5.59)$$

$$I_{0y} = \rho \dot{Q}_{\text{w}} W_0 \sin \gamma. \qquad (5.60)$$

Here, the relative flow rate can be determined from calculations in Sect. 7.1.

Fig. 5.16 Shock load force
at the bucket cutout
cutting edge
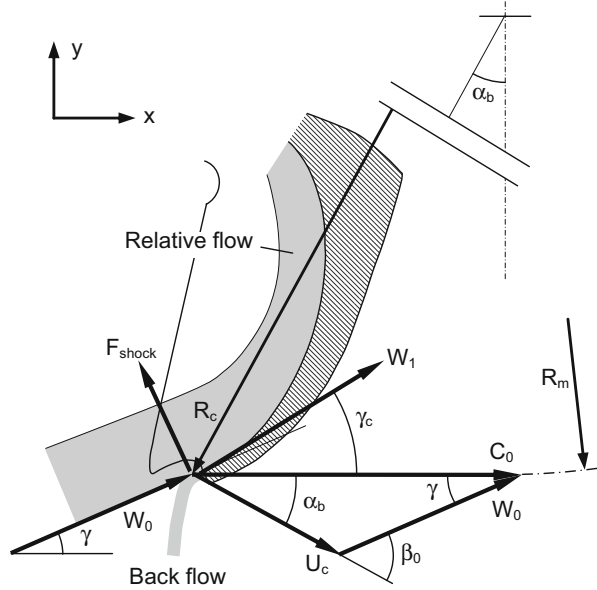
After deflection of the jet, the momentum flow rate is given by (with $W_1 = W_0$)

$$I_{1x} = \rho \dot{Q}_w W_0 \cos \gamma_c, \tag{5.61}$$

$$I_{1y} = \rho \dot{Q}_w W_0 \sin \gamma_c. \tag{5.62}$$

According to the balance law of momentum, the shock load force acting on the flow
is given by

$$F_{shock,x} = I_{1x} - I_{0x}, \tag{5.63}$$

$$F_{shock,y} = I_{1y} - I_{0y}. \tag{5.64}$$

The jet deflection at the bucket cutout edge happens at the bucket-position angle α_b,
which has already been clearly defined in Figs. 5.2 and 5.3. The related components
of the peripheral speed of the bucket cutout edge are thus given by

$$U_x = U_c \cos \alpha_b, \tag{5.65}$$

$$U_y = -U_c \sin \alpha_b. \tag{5.66}$$

The power provided by the shock load force is calculated from the corresponding
scalar product:

$$P_{shock} = -\vec{F}_{shock} \cdot \vec{U}_c = -\left(F_{shock,x} U_x + F_{shock,y} U_y\right). \tag{5.67}$$

With reference to Eqs. (5.59) to (5.66) and because $\alpha_b + \gamma = \beta_0$, the above equation is also representable in the form

$$P_{shock} = \rho \dot{Q}_w W_0 U_c [\cos \beta_0 - \cos (\alpha_b + \gamma_c)]. \qquad (5.68)$$

The related specific work is then obtained in the form

$$e_{shock} = \frac{P_{shock}}{\rho \dot{Q}_w} = W_0 U_c [\cos \beta_0 - \cos (\alpha_b + \gamma_c)]. \qquad (5.69)$$

According to Fig. 5.16, the angle $\alpha_b + \gamma_c$ represents a geometric angle at the bucket cutout and will be referred to β_1. By relating Eq. (5.69) to the specific kinetic energy $C_0^2/2$ of the jet, the related partial efficiency is then obtained in the form

$$\eta_{shock} = \frac{e_{shock}}{C_0^2/2} = 2 \frac{W_0 U_c}{C_0^2} (\cos \beta_0 - \cos \beta_1). \qquad (5.70)$$

With $k_m = U_m/C_0$, one further obtains

$$\eta_{shock} = 2 k_m^2 \frac{W_0}{U_m} \frac{R_c}{R_m} (\cos \beta_0 - \cos \beta_1). \qquad (5.71)$$

For $\beta_1 = \beta_0$, both the shock load force and the related partial efficiency are zero.

   As already indicated in Sect. 5.9.1, the exclusive analysis of the shock load force at the bucket entry is necessary, because its contribution to the shaft power cannot be detected by performing the integration of the flow from the bucket entry to the exit. A sample calculation will be shown in Chap. 12.

5.10   Effect of Eroded Main Splitters on Turbine Efficiency

In Sect. 5.9, when calculating the shock load force, it has been assumed that the quasi-sudden deflection of the jet flow does not lead to any efficiency loss. This is true as long as the main splitters keep their initial form or are kept sufficiently sharp. In practice, however, it is common that main splitters of Pelton buckets are eroded after a period of operation (Fig. 5.17). The period may be significantly shorter, when the water is highly loaded with suspended sediment particles. This phenomenon is called *hydroabrasive wear* or *hydroabrasive erosion*. It often occurs when the water from glaciers or river water during/after floods, for instance, is routed to Pelton turbines without passing a lake, where particles could settle (Boes et al. 2013; Felix et al. 2012, 2013). Further information about the sand erosion problems in Pelton turbines and related investigations will be presented in Chap. 22 for special consideration of the motion of particles in the water-sheet flow within the bucket.

Fig. 5.17 Wear of main splitters and inner surface of Pelton buckets (photo: TIWAG)
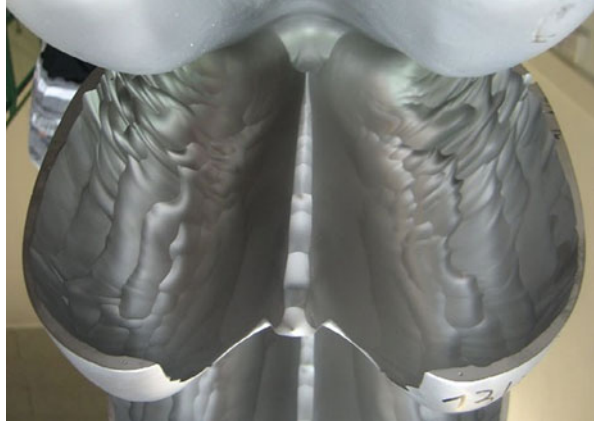
In general, the increase of splitter width due to erosion has been related to suspended sediment load (e.g., Boes 2009). The wear on main splitters leads to significant efficiency drops in Pelton turbines, as reported, e.g., by Brekke et al. (2002), Maldet (2008), and Abgottspon et al. (2013). According to Brekke et al. (2002), an increase in the splitter width by 1 % of the inner bucket width B causes approximately a 1 % efficiency drop at full load. Although this statement is based on practical measurements, the dependence of efficiency drop on the eroded splitter width, however, has not yet been generalized. There exists still no explanation to the related dependence and generating mechanism.

As will be presented in this section, a model of the mechanism causing efficiency losses at eroded splitters has been proposed, quantified, and verified by available measurements. The method is basically restricted to the plane form of eroded splitters. Nevertheless, it provides a possibility to predict the order and tendency of efficiency losses as a function of the relative width of eroded main splitters.

5.10.1   Basic Model and Mechanism of Losses

The hydraulic mechanism of efficiency loss caused by eroded splitters of Pelton buckets is flow detachment. The occurrence and extent of such local flow detachment depend on the ratio of the eroded splitter width to the jet diameter. For simplicity, the approaching flow of the jet is assumed to be perpendicular to the two-dimensional splitter crest profile, as shown in Fig. 5.18. A jet layer of a distance y to the jet axis is considered. For a small value of y, the jet layer width s is significantly larger than the width b of the eroded splitter. The jet layer, after reaching the bucket splitter, flows attached along the bucket surface (Fig. 5.18a). For a jet layer at a large distance of y (approaching half jet diameter), substantial flow detachment occurs at the splitter because of the relatively small ratio s/b (Fig. 5.18b). The detached jet layer then hits the bottom of the bucket or even
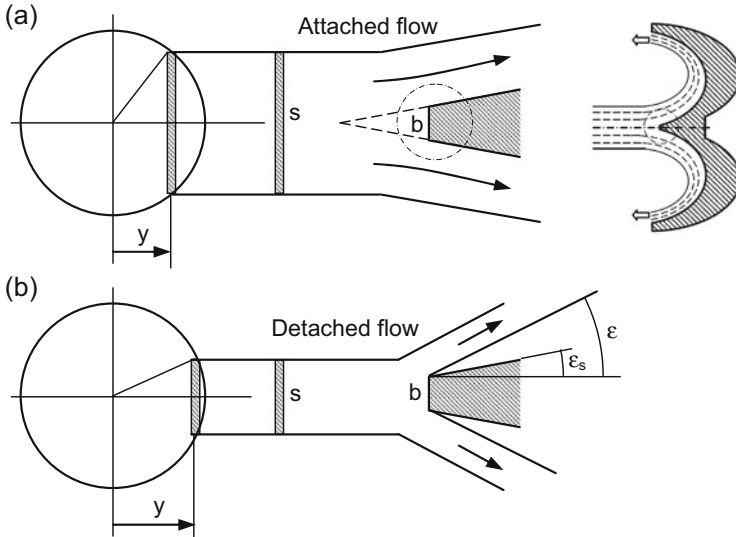
Fig. 5.18 Model of the flow at an eroded splitter of width b with (**a**) attached flow and (**b**) detached flow

flows towards the bucket exit. In this case, the amount of water involved in the jet layer is assumed to be lost for the momentum and energy transfer.

For flow detachments at small angle, the detached fluid reattaches to the flanks of the splitter (Fig. 5.19). The related flow disturbance is minute and can be neglected.

Obviously, the amount of water loss and thus the efficiency drop depend on the relative width of the splitter to the jet thickness. The critical width ratio s/b is defined as that at which the deflection angle ε_{cr} of the flow (Fig. 5.19) is just equal to or slightly greater than the geometrical splitter angle. Thus the critical deflection angle of the jet flow is given by $\varepsilon_{cr} = \varepsilon_s + \Delta\varepsilon$, typically with $\Delta\varepsilon \approx 5°$. For common designs of Pelton buckets, the angle of main splitters is about $2\varepsilon_s = 25° - 40°$.

Corresponding to each splitter angle, i.e., the critical angle ε_{cr}, there exists a critical width ratio $(s/b)_{cr}$ and thus a critical y_{cr}-value according to Fig. 5.19. All water in the jet that lies beyond y_{cr} on both sides ($\pm y_{cr}$) must be considered ineffective for the energy conversion. This consideration is actually only an approximation. At large deflection angle, the detached fluid hits the bucket bottom. The contribution of the associated impact force to the energy conversion may be elsewhere accounted for, for instance, by selecting an appropriate excessive angle $\Delta\varepsilon$ for ε_{cr}. This means that the critical deflection angle ε_{cr}, as a variable, has to be selected so that the estimated efficiency loss approximately agrees with the measurements. The point to be emphasized here is that the current calculation aims to physically model the mechanism of splitter width causing the efficiency drop rather than to accurately quantify the drop of the turbine efficiency.
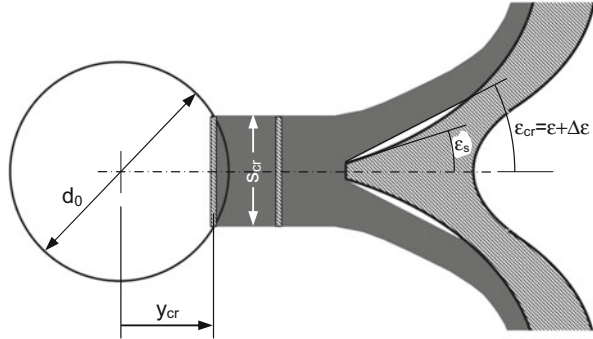
5.10.2   Critical Width Ratio for Flow Detachment

The critical width ratio s/b at the main splitter of a Pelton bucket corresponds to the
determination of the dependence of the deflection angle ε on the width ratio s/b. For
this purpose, a flow model according to Fig. 5.20 is considered. A two-dimensional
jet of a thickness s is split by a central block of width b into two partial flows. The
deflection angle of each partial flow from the approaching flow, ε, is a function of
the size ratio s/b. This function can be obtained by applying the conservation law of
linear momentum in the direction of the approaching jet. The unique force exerted
on the flow is the pressure force on the block surface. At the center point of the
block face, i.e., the stagnation point of the jet flow, the pressure is equal to the
dynamic pressure $\frac{1}{2}\rho c^2$ of the approaching flow. The pressure at the edges of the
block corresponds to the ambient pressure p_0. The pressure distribution on the block
surface is not linear. Strictly speaking, it depends on the size ratio s/b. For not too
small size ratios s/b, say $s/b > 1$, the mean pressure on the block surface is
approximated as one third of the dynamic pressure

$$\bar{p} \approx \frac{1}{3}\left(\frac{1}{2}\rho c^2\right). \tag{5.72}$$

For a unit length of the block, the z-component of the pressure force exerted on the
fluid is given by

$$F_z = \bar{p}b = \frac{1}{6}b\rho c^2. \tag{5.73}$$

The deflection of the flow caused by this force component is considered to be free of
energy losses. This implies that the deflected flow has the same speed as the
approaching flow. The z-component of the velocity of the deflected flows is thus
$c\cos\varepsilon$. The conservation law of momentum then implies

Fig. 5.20 Symmetrical splitting and deflection of a two-dimensional jet
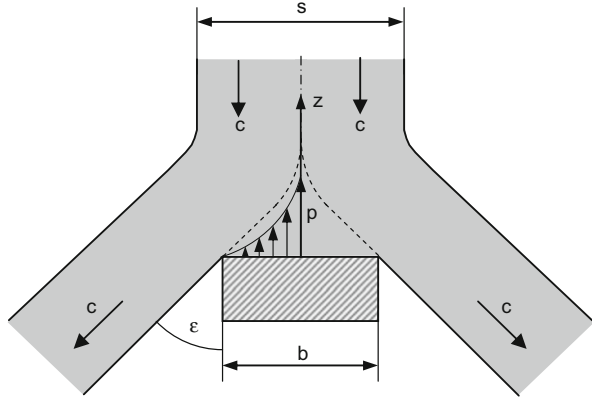
$$F_z = s\rho c^2 - s\rho c^2 \cos \varepsilon. \tag{5.74}$$

By considering the force component given in Eq. (5.73), the deflection angle ε of the flow is obtainable from

$$\cos \varepsilon = 1 - \frac{1}{6}\frac{b}{s}. \tag{5.75}$$

As mentioned before, this equation generally applies with $s/b > 1$.

The relation of Eq. (5.75) is applied to the eroded splitter of Pelton buckets. With respect to the reattachment of the detached fluid according to Fig. 5.19 and to the selected critical deflection angle $\varepsilon_{cr} = \varepsilon_s + \Delta\varepsilon$, the critical width ratio $(s/b)_{cr}$ is then deducible from Eq. (5.75) as

$$\left(\frac{s}{b}\right)_{cr} = \frac{1}{6(1 - \cos \varepsilon_{cr})}. \tag{5.76}$$

For a given angle ε_s (or ε_{cr}) and a width b of eroded bucket splitters, the critical width s_{cr} of the approaching flow (see Fig. 5.19 for a round jet) can be determined. The water outside this chord flows detached from the splitter and must be considered to be ineffective for torque generation. For a typical splitter angle $\varepsilon_{cr} = 15°$, for instance, the critical value of s/b according to Eq. (5.76) is calculated as $(s/b)_{15°} = 5$. The meaning of this critical length ratio is evident. If the jet layer width s is less than five times the width of the eroded splitter, fluid detachment with efficiency losses occurs. To determine the related reduction in turbine efficiency, thus, one must only consider the jet part with $s/b < 5$.

The width of the eroded splitter is often given in terms of the ratio b/B, where B denotes bucket inner width. When related to the jet diameter d_0, Eq. (5.76) is rewritten as

$$\frac{s_{cr}}{d_0} = \frac{1}{6(1 - \cos \varepsilon_{cr})} \frac{d_{0,N}}{d_0} \frac{B}{d_{0,N}} \frac{b}{B}. \tag{5.77}$$

The jet diameter at the nominal flow rate is denoted by $d_{0,N}$. According to Eq. (2.21), with φ_B varying between 0.09 and 0.11, there is $B/d_{0,N} \approx 3$. The diameter ratio $d_0/d_{0,N}$ in the above equation, indeed, implies the partial load of injectors, as given by $d_0/d_{0,N} = \sqrt{\dot{Q}/\dot{Q}_N}$ for constant jet speed. Eq. (5.77) can then further be written as

$$\frac{s_{cr}}{d_0} = \frac{0.5}{1 - \cos \varepsilon_{cr}} \frac{b}{B} \sqrt{\frac{\dot{Q}_N}{\dot{Q}}}. \tag{5.78}$$

To more accurately model the flow at the eroded splitters of the Pelton buckets, the critical deflection angle ε_{cr} in the above equation must be considered to depend on the relative splitter width b/B. This is evident, when considering Fig. 5.19. With increased wear of the bucket splitter, both the relative splitter width b/B and the geometrical splitter angle ε_s increase. The corresponding relation can be formulated as

$$\varepsilon_{cr} = \varepsilon_{cr0} + k\frac{b}{B}. \tag{5.79}$$

Here, ε_{cr0} is related to the critical angle based on the initial design of the bucket splitter ($b = 0$). The constant k, as will be shown below, can be set equal to $k = 100°$.

5.10.3 Water Loss Related to Flow Deflection at Bucket Splitters

It was shown that the critical chord length s_{cr} of the approaching jet is a function of the width b and the angle ε_{cr} of the eroded main splitters. Since all water in the segment outside the critical chord (s_{cr}) is considered to be ineffective, its ratio to the total jet flow rate represents the dependent efficiency drop. For a jet of thickness d_0 and by considering two segments lying symmetrically ($\pm y$) to the center line (Fig. 5.21), the associated efficiency drop amounts to

$$\Delta\eta_{splitter} = \frac{A_{cr}}{A_0} = \frac{2}{\pi}\left(\arccos\sqrt{1 - \frac{s_{cr}^2}{d_0^2}} - \frac{s_{cr}}{d_0}\sqrt{1 - \frac{s_{cr}^2}{d_0^2}}\right). \tag{5.80}$$

Because the incorporation of Eq. (5.79) into Eq. (5.78) results in $s_{cr} = f(b/B)$, it follows from Eq. (5.80) the following general functional relation:

Fig. 5.21 Portion of water jet suffering from deflection at the eroded bucket splitters
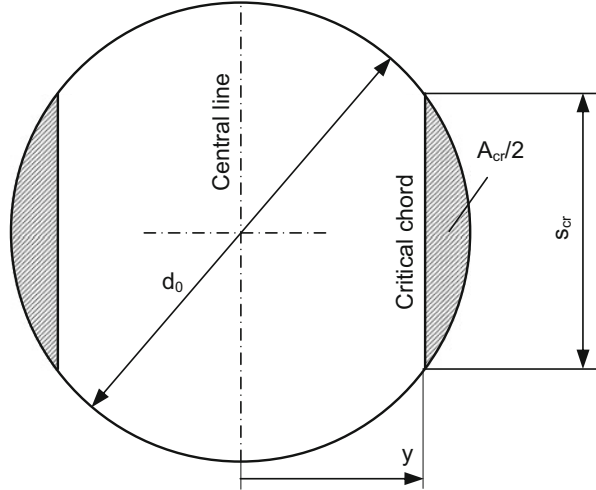
$$\Delta\eta_{\text{splitter}} = f\left(\frac{b}{B}, \frac{\dot{Q}}{\dot{Q}_N}\right). \tag{5.81}$$

At partial load operation ($\dot{Q}/\dot{Q}_N < 1$), one has $d_0/s_{\text{cr}} < d_{0,N}/s_{\text{cr}}$, as obtained from Eq. (5.78) for a given width of the eroded splitter and thus a given critical chord length s_{cr}. Equation (5.80) then implies, because of the area ratio A_{cr}/A_0, that the associated efficiency loss at partial load is higher than at full, i.e., nominal load. Figure 5.22 shows the computational results from Eq. (5.81) for a given initial splitter angle ($\varepsilon_{\text{cr}0} = 13°$) at full and 75 % partial load. The efficiency drop progressively increases with the relative width of eroded splitters.

5.10.4   Comparison with Measurements

The analyses completed in the above sections are based on the flow model according to Figs. 5.19 and 5.20. To show the applicability of the constructed flow model, calculations as shown in Fig. 5.22 are compared with field measurements, which were reported by Maldet (2008). This comparison is displayed in Fig. 5.23 with the splitter width b as the abscissa. A quite satisfactory agreement between the calculations and the measurements has been achieved. As for the measurements displayed in the figure, the operation condition of the Pelton turbines should be mentioned. At each Pelton wheel, the flow-rate range from 50 to 100 % of the nominal flow rate was effective. In addition, the geometric form of the eroded splitters is certainly not exactly of plane form as supposed in the applied computational model (Fig. 5.20).
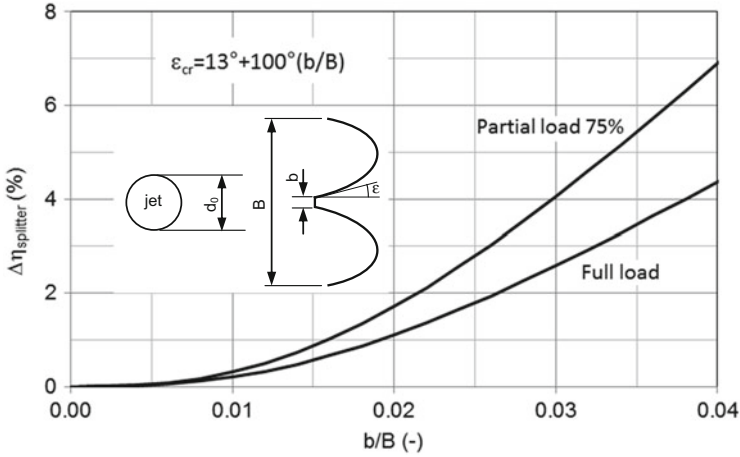
Fig. 5.22 Calculated efficiency drops caused by eroded main splitters of Pelton buckets
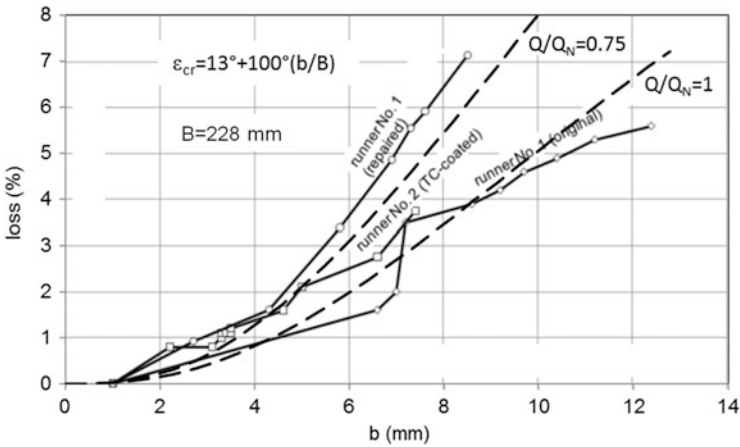
Fig. 5.23 Comparison of calculated efficiency drops caused by eroded main splitters of Pelton buckets (*dashed lines* copied from Fig. 5.22) and measurements (*solid lines*) reported by Maldet (2008)

5.10.5 Negligible Impact Force on the Eroded Splitter Plane

In the above considerations, the detached flow with large detachment angle at the bucket splitters has been assumed to be ineffective for the energy conversion. The amount of the related water, as a portion of the total jet flow, increases with the increase of the eroded splitter width. This implies, according to Eq. (5.73), that the impact force F_z, which acts as a positive driving force for the bucket rotation, also increases. It, thus, positively contributes to the energy conversion. In the frame of

evaluating the constructed model for the flow at the eroded bucket splitters, it seems to be significant that this contribution is negligible.

To this end, Eq. (5.73) is applied to the interaction between the jet and the eroded bucket splitter. Instead of the unit length assumed in that equation, the jet diameter d_0 must be applied as length scale. In addition, the relative velocity between the jet and the moving bucket must be used. For simplicity, the operation condition $k_m = 0.5$ is assumed, which implies that the relative velocity is equal to half of the jet speed (C_0). Thus, it follows from Eq. (5.73) that

$$F_z = \frac{1}{6} b d_0 \rho \left(\frac{C_0}{2}\right)^2. \tag{5.82}$$

The operation condition of $k_m = 0.5$ also means that the peripheral speed of the pitch circle of the bucket (U_m) also equals the half of the jet speed. The power provided by the impact force F_z is then given by

$$P_{b/B} = F_z \frac{C_0}{2} = \frac{1}{6} b d_0 \rho \left(\frac{C_0}{2}\right)^3. \tag{5.83}$$

This power is normalized by the power of the jet; this yields the effective contribution of the impact force F_z to the turbine efficiency. With $B \approx 3d_0$, one obtains

$$\eta_{b/B} = \frac{P_{b/B}}{\frac{1}{4}\pi d_0^2 C_0 \frac{1}{2}\rho C_0^2} = \frac{1}{6\pi}\frac{b}{d_0} = \frac{1}{2\pi}\frac{b}{B}. \tag{5.84}$$

For $b/B = 0.04$, one obtains $\eta_{b/B} = 0.6\,\%$. Obviously, this value is negligibly small against the efficiency loss $\Delta\eta_{splitter} = 4.4\,\%$, which can directly be read from Fig. 5.22.

References

Abgottspon, A., Stern, P., Staubli, T., Felix, D., & Winkler, K. (2013). Measuring turbine abrasion and efficiency decrease: First results of the case study at HPP Fieschertal. Hydro 2013, Innsbruck, Austria.

Boes, R. (2009). Real-time monitoring of SSC and PSD in the headwater way of a high-head hydropower plant. *Proceedings of the 33rd IAHR Congress* (pp. 4037–4044), Vancouver, Canada.

Boes, R., Felix, D., & Albayrak, I. (2013). Schwebstoffmonitoring zum verschleissoptimierten Betrieb von Hochdruck-Wasserkraftanlagen. *Wasser Energie Luft, 105*(1), 35–42.

Brekke, H., Wu, Y., & Cai, B. (2002). Design of hydraulic machinery working in sand laden water. In C. Duan & V. Karelin (Eds.), *Abrasive erosion and corrosion of hydraulic machinery* (Vol. 2). London: Imperial College Press.

Felix, D., Albayrak, I., Abgottspon, A., Boes, R., & Gruber, P. (2012), Suspended sediment and Pelton turbine wear monitoring: Experimental investigation of various optical and acoustic

devices and beginning of the case study at HPP Fieschertal. *17th International Seminar on Hydropower Plants* (pp. 483–494), Vienna, Austria.

Felix, D., Albayrak, I., Boes, R., Abgottspon, A., Deschwanden, F., & Gruber, P. (2013). Measuring suspended sediment: Results of the first year of the case study at HPP Fieschertal in the Swiss Alps. Hydro 2013, Innsbruck, Austria.

Hasson, D., & Peck, R. (1964). Thickness distribution in a sheet formed by impinging jets. *American Institute of Chemical Engineers Journal, 10*(5), 752–754.

Maldet, R. (2008). Pelton runner with high erosion caused by glacier sediment: assessment and measures. *15th International Seminar on Hydropower Plants* (pp. 639–646), Vienna, Austria.

Raabe, J. (1989). *Hydraulische Maschinen und Anlagen*. VDI Verlag.

Taygun, F. (1946). Untersuchungen über den Einfluss der Schaufelzahl auf die Wirkungsweise eines Freistrahlrades. Diss., Eidgenössische Technische Hochschule in Zürich.

Taylor, G. (1960). Formation of thin flat sheets of water. *Proceedings of the Royal Society Series A, 259*, 1–17.

Chapter 6
Fluid Mechanics in the Rotating Bucket

6.1 Basic Equations

Water flow in rotating buckets is a complex hydro-mechanical process, which is characterized by the presence of a free surface and the influences of centrifugal and Coriolis forces as well as of friction, inertial, and pressure forces in the flow. These forces affect the spreading of water in the bucket and, finally, the hydraulic efficiency of the turbine system. For simplicity, frictionless flow is considered first. The frictional flow and the influence of friction on the hydraulic efficiency will be discussed in Chaps. 10–12.

6.1.1 Equation of Motion

Both the centrifugal and Coriolis forces associated with the rotation of the Pelton wheel affect the spreading of water flow in Pelton buckets. They are given for the unit mass of flow, respectively, by

$$\vec{F}_{ct} = -\vec{\omega} \times \left(\vec{\omega} \times \vec{R} \right) \tag{6.1}$$

and

$$\vec{F}_{Co} = -2\vec{\omega} \times \vec{W}. \tag{6.2}$$

In further calculations, the unit mass is interpreted as the mass which has a height equal to the height of the water sheet in the Pelton bucket (Fig. 6.1). This treatment has the advantage that the unit mass is found under constant atmospheric pressure and can therefore be regarded as a free solid particle. The calculation of the particle motion can then be carried out simply by applying the laws of solid mechanics.

Fig. 6.1 Flow forces and the coordinate system for the motion of a water particle in a rotating bucket
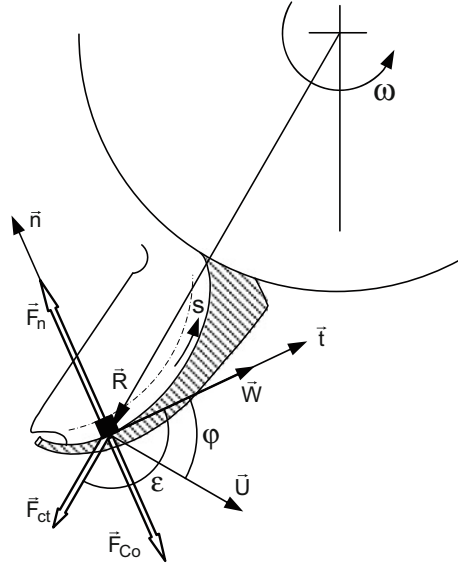
The movement of the unit mass of the flow in the rotating bucket is three-dimensional and subjected to the influences of centrifugal and Coriolis forces as well as the force exerted from the bucket surface towards the flow (supporting force). According to the law of momentum, the temporal change in the momentum flow rate is equal to the sum of all external active forces. For the unit mass, this is expressed as

$$\frac{\mathrm{d}\vec{W}}{\mathrm{d}t} = \frac{\mathrm{d}W_{\mathrm{t}}}{\mathrm{d}t}\vec{t} + \frac{W^2}{r_{\mathrm{b}}}\vec{n} = \vec{F}_{\mathrm{ct}} + \vec{F}_{\mathrm{Co}} + \vec{F}_{\mathrm{n}}. \tag{6.3}$$

Here, $\vec{t}$ and $\vec{n}$ are unit vectors parallel and orthogonal to the bucket surface. The supporting force $\vec{F}_{\mathrm{n}}$ that is directed from the bucket surface onto the flow is perpendicular to the bucket surface. According to Eq. (6.3), the time rate of change of the relative flow velocity, or the flow acceleration, comprises the flow acceleration along the bucket surface in the direction of the flow (tangential) and the acceleration normal to the bucket surface. The latter occurs as a result of the change in the flow direction by following the bucket inner surface. According to Fig. 6.1, the unit normal vector of the bucket surface is represented by the vector $\vec{n}$ which is directed towards the center of surface curvature. The corresponding radius of curvature is designated by r_{b}.

Equation (6.3) is the fundamental equation of fluid dynamics in a rotating bucket. On this basis, both the relative motion of the water sheet in the rotating bucket and the power of respective forces can be calculated.

6.1.2   Water Film Rotation and Pressure Distribution Through the Sheet Height

In Eq. (6.3), the normal component of acceleration of a water particle due to the surface curvature is expressed by W^2/r_b. The relative motion of the water sheet in a Pelton bucket is congruent to the bucket form and, thus, continuously undergoes a change in the flow direction. According to the law of momentum, a force must result from such a direction change which acts perpendicular to the flow direction. It is indeed nothing else than the pressure force below the water sheet. To illustrate the pressure force and flow conditions in such flows, a two-dimensional rotating flow as shown in Fig. 6.2a is considered. The water sheet of height h circles on the inside of the circular tube with a radius r_b. The flow is characterized by the fact that the circulation velocity at the surface of the water sheet is W_o and the flow does not have any radial velocity components.

According to the Euler equation for frictionless flow in cylindrical coordinates, the pressure gradient beneath the water sheet is given by

$$\frac{\partial p}{\partial r} = \rho \frac{W^2}{r}. \tag{6.4}$$

Additionally, the total pressure in the water sheet is assumed to be constant. The Bernoulli equation is then written as

$$\frac{p}{\rho} + \frac{1}{2} W^2 = \text{const.} \tag{6.5}$$

By eliminating the pressure term from the last two equations, one obtains the differential equation of the related flow field:

$$\frac{W}{r} + \frac{dW}{dr} = 0. \tag{6.6}$$

The velocity distribution in the water sheet is then obtained from the integration

Fig. 6.2 Potential flow and the pressure distribution beneath the water sheet
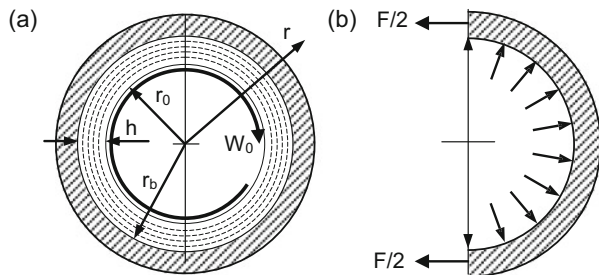
$$W = W_0 \frac{r_0}{r}.\tag{6.7}$$

It corresponds to the velocity field of a potential vortex which satisfies the irrotational flow condition. In reality, this result is also expected when the Bernoulli equation (6.5) is applied to the whole flow field rather than merely along the streamlines.

The flow velocity on the surface of the circular pipe is given by $r = r_b$. With $r_0 = r_b - h$, thus, one obtains from Eq. (6.7)

$$W_b = W_0 \left(1 - \frac{h}{r_b}\right),\tag{6.8}$$

or with $h/r_b \ll 1$ by Taylor series expansion truncated at the linear terms,

$$W_b^2 \approx W_0^2 \left(1 - \frac{2h}{r_b}\right).\tag{6.9}$$

When the pressure in the pipe is assumed to be p_0, then, according to Eq. (6.5), the overpressure on the pipe surface is given by

$$p_b - p_0 = \frac{1}{2}\rho\left(W_0^2 - W_b^2\right) = \rho W_0^2 \frac{h}{r_b}.\tag{6.10}$$

The total pressure force acting on half of a pipe of unit length, as shown in Fig. 6.2b, is obtained as

$$F = 2p_b r_b = 2r_b \left(p_0 + \rho W_0^2 \frac{h}{r_b}\right).\tag{6.11}$$

The present consideration of the pressure force acting on the half perimeter of a pipe corresponds to the case in a Pelton bucket at which the flow is deflected by approximately 180°.

6.2   Relative Fluid Flow and Invariance Equation

To track the motion of water in a rotating bucket, Eq. (6.3) must be solved. From Sect. 6.1 it is known that the Coriolis force always acts perpendicular to the flow direction. This means that this force affects only the flow direction but not the velocity values of water particles or the water sheet. If the equation of motion, i.e., Eq. (6.3), is multiplied by the tangential unit vector $\vec{t}$ (shown in Fig. 6.1 along the streamline), then the terms for both Coriolis and supporting forces will fall off this momentum balance, and it follows that

$$\frac{dW_t}{dt} = \vec{F}_{ct} \cdot \vec{t}. \tag{6.12}$$

This equation indicates that the relative velocity of a water particle in the rotating bucket is affected only by the centrifugal force.

Both sides of the above equation are multiplied by $W_t dt = d\vec{s} \cdot \vec{t}$ which is obtained from the relative velocity $\vec{W} = d\vec{s}/dt$. This then results in

$$W_t \cdot dW_t = \left(\vec{F}_{ct} \cdot \vec{t}\right)\left(d\vec{s} \cdot \vec{t}\right) = \vec{F}_{ct} \cdot d\vec{s}. \tag{6.13}$$

Here, $d\vec{s}$ is the infinitesimal movement of the water particle in the rotating bucket.

Due to $W_t^2 = W^2$, the above equation is reformulated as

$$d\left(\frac{1}{2}W^2\right) = \vec{F}_{ct} \cdot d\vec{s}. \tag{6.14}$$

This equation shows that the change in kinetic energy of the flow along the bucket surface is equal to the work which is done by the centrifugal force. This is self-evident because the centrifugal force is the only one that affects the value of the flow velocity in the rotating frame.

The vector product $\vec{F}_{ct} \cdot d\vec{s}$ in the above equation can be calculated by taking account of the angle ε between the vectors $\vec{F}_{ct}$ and $d\vec{s}$ as shown in Fig. 6.1. From Eq. (6.14) one obtains

$$d\left(\frac{1}{2}W^2\right) = F_{ct} ds \cos \varepsilon. \tag{6.15}$$

From Fig. 6.1 it can be seen that $ds \cos \varepsilon = dR$ is the projection of the infinitesimal movement $d\vec{s}$ of the particle in the radial direction $\vec{R}$. Thus, Eq. (6.15) becomes

$$d\left(\frac{1}{2}W^2\right) = R\omega^2 dR. \tag{6.16}$$

In this equation, the modulus of the centrifugal force, $F_{ct} = R\omega^2$, obtained from Eq. (6.1) has been applied.

Integration of the above equation from R_1 to R_2 results in

$$W_2^2 - W_1^2 = \omega^2\left(R_2^2 - R_1^2\right). \tag{6.17}$$

With $U = \omega R$, as the local peripheral speed of the bucket, it finally follows from the above equation

$$W^2 - U^2 = W_1^2 - U_1^2 = W_2^2 - U_2^2 = E. \tag{6.18}$$

This equation has been referred by Zhang (2007) as the *invariance equation*, with E as the *energy invariance*. According to Eq. (6.18), the relative velocity of a water particle in the rotating bucket will only change when along the streamlines the local peripheral speed (U) of the bucket changes. The practical significance of the invariance equation is obvious: when the flow (W and U) at the bucket entry (index 1) is known, then the flow both within the rotating bucket and at the bucket exit (index 2) can be immediately calculated, when the corresponding peripheral speed is known.

The invariance equation (6.18) has been obtained from the assumption of constant pressure in the water sheet. This assumption is justified if the invariance equation is applied to the flow at the bucket exit where all streamlines are straight. Otherwise, the assumption of constant pressure is not entirely correct. Due to the curvature of the bucket inner surface and, thus, of the streamlines, a pressure increase normal to the bucket surface is present according to Eq. (6.4). The relative velocity decreases according to Eq. (6.7). Taking into account this pressure effect, Eq. (6.18) is generalized to

$$\frac{p}{\rho} + \frac{1}{2}\left(W^2 - U^2\right) = \text{const.} \tag{6.19}$$

In the field of turbomachinery, this equation is called Bernoulli equation in the relative system or occasionally as the *rothalpy equation*. For Pelton turbines which are also called "impulse turbines" and operate under constant pressure, Eq. (6.19) is reduced to Eq. (6.18).

At this point it should be noted that the water-sheet flow in a rotating Pelton bucket is a type of open channel flow. Such a sheet flow of depth h is a type of the shooting flow as the Froude number is much greater than one according to the definition $\text{Fr} = W/\sqrt{gh}$. With respect to the invariance equation, i.e., Eq. (6.18), the condition $\text{Fr} > 1$ and, thus, $W^2 > gh$ can be expressed by

$$E_1 + (R\omega)^2 > gh. \tag{6.20}$$

For flows in a rotating bucket, this condition should only be checked when $E_1 < 0$. This is a quite realistic case in Pelton turbines, as will be shown in Chap. 8.

6.2.1 Influence of the Pressure Gradient Due to the Surface Curvature

The *invariance equation*, i.e., Eq. (6.18), was derived under the assumption of constant pressure in the flow. However, overpressure below the free surface of the

Fig. 6.3 Radius of
curvature of the bucket
inner surface at the lowest
point of the bucket
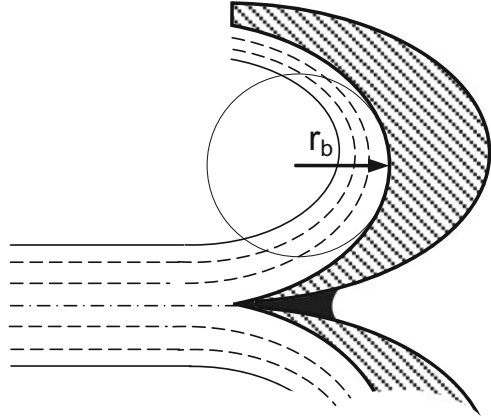
water sheet is actually present because of the curved streamlines; see Eq. (6.4) for
the pressure gradient. The influence of the pressure gradient within the water sheet
on the corresponding velocity distribution is greatest at the lowest point of the
bucket (Fig. 6.3) because, there, the largest streamline curvature is present. To
estimate the curvature effect, Eq. (6.19) is considered, which completely accounts
for the streamline curvature effects. If the maximum overpressure on the bucket
surface is estimated with Eq. (6.10) and the result is inserted into Eq. (6.19), then

$$\frac{1}{2}\left(W^2 - U^2\right) + W_0^2\frac{h}{r_{\mathrm{b}}} = \text{const.} \tag{6.21}$$

is obtained. As long as the depth of the water sheet is sufficiently small compared to
the radius of curvature of the bucket inner surface, the second term on the left side
in the above equation (6.21) is negligible. The flow in the entire bucket, from entry
to exit, can then be easily calculated by using the invariance equation, i.e.,
Eq. (6.18).

More details on the streamline curvatures and the thickness of the water sheet
can be found in Chap. 22, where, based on a concrete computational example,
accurate calculations have been completed.

6.2.2   Jet Layer Method

The interaction between the jet and rotating buckets is unsteady. This means that
the invariance equation, i.e., Eq. (6.18), is only applicable for tracking each
individual water particle with its own velocity values U and W. For a full jet of
length s_2 (Fig. 5.3), large computational efforts would be needed. Extensions of the
applicability of the invariance equation have been derived by Zhang (2007). They
concern the so-called jet layer method, as presented below.

Fig. 6.4 Jet layer method
to extend the applicability
of the invariance equation
(6.18)
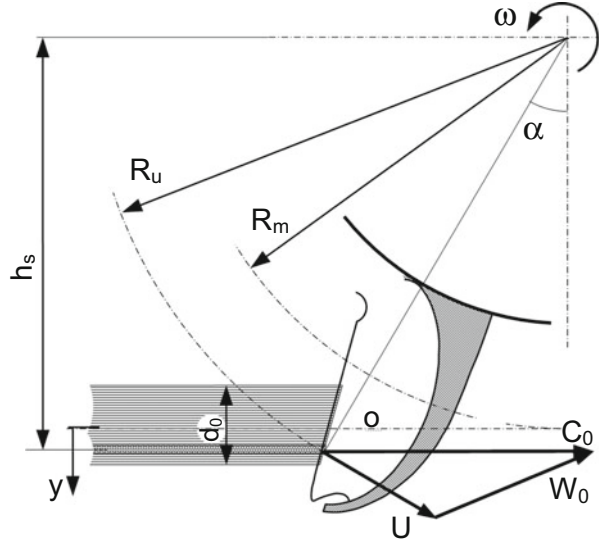
According to Fig. 6.4, the jet is divided into n thin layers. In a certain jet layer which has a distance h_s from the axis of the Pelton wheel, each water particle will reach the bucket at its particular time. This also means that each water particle has its individual entry point at the bucket and, therefore, individual velocity triangle with individual circumferential and relative velocities. In considering the velocity triangle at the main splitter of the bucket and by applying the cosine law, one has

$$W_0^2 = C_0^2 + U^2 - 2C_0 U \cos \alpha. \tag{6.22}$$

With $U \cos \alpha = \omega R_u \cos \alpha = \omega h_s$, the invariance equation is formulated with the aid of the above equation as

$$E = W_0^2 - U^2 = C_0^2 - 2\omega h_s C_0. \tag{6.23}$$

This equation states that all water particles in a same jet layer with $h_s = $ const (geometric constant) possess a unique constant value $E = W_0^2 - U^2$, even though W_0 and U are not constant. For this reason, a small number (equal to the jet layer number) of constant E will, finally, suffice in order to completely describe the flows both in and out of a rotating bucket. The *energy invariance E*, as from Eq. (6.23), is only restricted to a jet layer. It varies in reality from layer to layer owing to the variation of the distance h_s. This can be determined with the aid of Fig. 6.4. For the jet layer at distance y from the jet axis, the invariance equation, i.e., Eq. (6.23), is formulated in the form[1]

---

[1] The subscript y in Eq. (6.24) is to identify the y-coordinate, so that W_y, for instance, indicates the relative flow velocity W at y. It should not be considered to be the y-component of the velocity W.

$$E_y = W_y^2 - U_y^2 = C_0^2 - 2\omega(R_m + y)C_0. \tag{6.24}$$

Taking into consideration the peripheral speed coefficient $k_m = \omega R_m / C_0$, already defined in Eq. (2.18), one obtains from Eq. (6.24)

$$\frac{E_y}{C_0^2} = 1 - 2k_m\left(1 + \frac{y}{R_m}\right). \tag{6.25}$$

The energy invariance (only for a given layer), thus, varies linearly from layer to layer. On the jet axis at $y = 0$, one has

$$\frac{E_o}{C_0^2} = 1 - 2k_m. \tag{6.26}$$

In the lowest, i.e., the outermost jet layer ($y \approx d_0/2$), the energy invariance is calculated to be

$$\frac{E_b}{C_0^2} = 1 - 2k_m\left(1 + \frac{d_0}{2R_m}\right). \tag{6.27}$$

Since the expression in parentheses represents a value which is clearly greater than unity, it will often happen that the energy invariance E_b may be smaller than zero. This negative value then remains constant till the bucket exit.

Under the application of Eq. (2.26), for replacing the term $d_0/2R_m$, the energy invariance in the above equation can also be represented as a function of the specific speed:

$$\frac{E_b}{C_0^2} = (1 - 2k_m) - 0.76n_q. \tag{6.28}$$

The possible negative values of the energy invariance, which means that $W < U$, are given at large peripheral speed coefficients and high specific speeds. This condition may cause problems in some cases associated with the exit flow out of the bucket, as will be discussed in detail in Chap. 8.

It should be noted that on the intersection line ab (Fig. 5.3), one simply has $U_c = R_c\omega = $ const. With this condition the following difference is formed from Eq. (6.24):

$$E_y - E_{o1} = W_y^2 - W_{o1}^2 = -2\omega C_0 y. \tag{6.29}$$

Therefore, the relative velocity is given by

$$W_{\mathrm{y}}^2 = W_{\mathrm{o}1}^2 - 2\omega C_0 y \tag{6.30}$$

or, when normalized by the jet velocity,

$$\frac{W_{\mathrm{y}}^2}{C_0^2} = \frac{W_{\mathrm{o}1}^2}{C_0^2} - 2k_{\mathrm{m}}\frac{y}{R_{\mathrm{m}}}. \tag{6.31}$$

This relation shows that starting from the relative velocity at location o_1 on the jet axis (Fig. 5.3), the relative velocities of all water particles on the cutting line ab can be calculated. For water particles at the point a ($y = -d_0/2$) and b ($y = d_0/2$), respectively, the corresponding relative velocities can be expressed as

$$\frac{W_{\mathrm{a}}^2}{C_0^2} = \frac{W_{\mathrm{o}1}^2}{C_0^2} + k_{\mathrm{m}}\frac{d_0}{R_{\mathrm{m}}} \tag{6.32}$$

and

$$\frac{W_{\mathrm{b}}^2}{C_0^2} = \frac{W_{\mathrm{o}1}^2}{C_0^2} - k_{\mathrm{m}}\frac{d_0}{R_{\mathrm{m}}}. \tag{6.33}$$

The previous analyses concerning the invariance equation are based on the conservation law of energy by assuming frictionless flows. Since viscous friction between the water sheet and the bucket surface does not cause any significant change in the relative flow velocity, the reliability of all derived relations can be mathematically verified.

6.2.3   Invariance Equation and Euler Equation

The *invariance equation* describes the relative flow of the water sheet in a rotating system, i.e., in a rotating bucket of a Pelton turbine. On the other hand, the well-known *Euler equation* is generally used to calculate the specific work in all types of turbomachinery. It is expected that between the invariance equation and the Euler equation, a relation may exist, with the aid of which one equation can be derived from the other. For assumed frictionless flows in a Pelton turbine, the converted specific hydraulic energy is calculated as the difference of the specific kinetic energies evaluated at the entry and the exit, viz.,

$$e = \frac{1}{2}\left(C_1^2 - C_2^2\right). \tag{6.34}$$

The Euler equation, which applies to all types of turbomachinery for calculating the specific work, is given by

Fig. 6.5 Velocity triangle
to explain the relation
between the invariance and
Euler equations
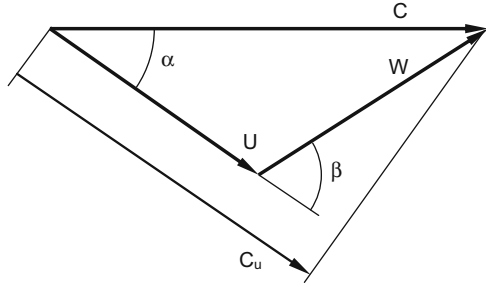
$$e = U_1 C_{1u} - U_2 C_{2u}. \tag{6.35}$$

Here, C_{1u} and C_{2u} are circumferential components of the absolute velocity C, respectively, at the bucket entry and exit (Fig. 6.5). With $C_u = C \cos \alpha$, it follows from Eq. (6.35) that

$$e = U_1 C_1 \cos \alpha_1 - U_2 C_2 \cos \alpha_2. \tag{6.36}$$

Equalizing Eqs. (6.34) and (6.36) leads to

$$C_2^2 - 2U_2 C_2 \cos \alpha_2 = C_1^2 - 2U_1 C_1 \cos \alpha_1. \tag{6.37}$$

Subsequently, the cosine law in the form $W^2 = C^2 + U^2 - 2CU \cos \alpha$ (see Fig. 6.5) is used in the above equation, yielding

$$W_2^2 - U_2^2 = W_1^2 - U_1^2, \tag{6.38}$$

which corresponds to the invariance equation given by Eq. (6.18), as derived before.

At this point, the specific work in Pelton turbines should be considered in more details. The greater part of the jet enters the Pelton bucket approximately perpendicular to the main splitter (Fig. 5.6). Under this condition, water particles spread along the bucket surface with constant circumferential speed (U). According to the invariance equation, the relative velocity W must remain constant during the whole flow process in the bucket. Because $UC_u = U(U + W \cos \beta)$, as obtained from Fig. 6.5, Eq. (6.35) is converted for $\beta_1 = 0$ into the following form:

$$e = U_1 W_1 (1 - \cos \beta_2). \tag{6.39}$$

This equation is equivalent to Eq. (2.9). The specific energy that is transferred from the jet to the rotating buckets is, finally, only a function of the exit flow angle β_2 of the relative velocity and is independent of the path traversed by the water. In the practical design of Pelton buckets, the exit flow angle β_2 has usually been set to

about 170°. The criterion for determining this angle will be explained in detail in Sect. 8.2.

6.2.4 Example: Relative Flow in a Semicircular Bucket

The invariance equation indicates that the relative flow velocity of a water particle in a rotating bucket depends on the particle position. When a water particle is found on a trajectory of constant circumferential speed, then the relative velocity also remains constant. This simplest case does not require any further consideration.

Therefore, the general case of variable relative velocity of a water particle in the rotating bucket should be considered in more details by a concrete calculation of an example. For simplicity a two-dimensional semicircular bucket according to Fig. 6.6 is looked at. The motion of the water particle in the bucket as shown in Fig. 6.6a corresponds approximately to the flow form in a Pelton bucket, at which the jet is intercepted by the bucket cutout edge and subsequently flows towards the bucket root (see Fig. 5.16). In order to show that the relative motion of water particles in a rotating bucket also depends on the direction of the particle motion, the case illustrated in Fig. 6.6b is also considered for comparison.

The relative velocity of a water particle in the rotating bucket is calculated, according to Eq. (6.18), from the known constant $E = E_1$ at the bucket entry; it is given by

$$W = \sqrt{E_1 + U^2} = \sqrt{E_1 + (\omega R)^2}. \tag{6.40}$$

The radial position of the water particle in the bucket is designated by R. By applying the cosine law in the form $R^2 = R_o^2 + r_b^2 \pm 2r_b R_o \cos\tau$ to both flow forms in Fig. 6.6, one obtains from Eq. (6.40)

Fig. 6.6 Examples of flows in a semicircle bucket. Case (**a**): water particle motion along the positive t-direction. Case (**b**): water particle motion along the negative t-direction
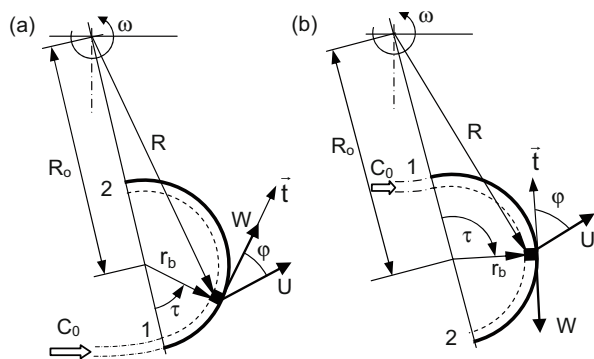
$$\frac{W}{\omega R_o} = \sqrt{\frac{E_1}{\omega^2 R_o^2} + \left(1 + \frac{r_b^2}{R_o^2} \pm 2\frac{r_b}{R_o} \cos \tau\right)}. \qquad (6.41)$$

In this equation, the upper (lower) sign is for the motion of the water particle in the positive (negative) $\vec{t}$-direction (Fig. 6.6a). The angle $\tau = 0$ is agreed to denote the initial position of the water particle when the particle enters the bucket.

Insertion of the relative velocity in the form $W = r_b d\tau/dt$ into Eq. (6.41) yields

$$\frac{r_b}{\sqrt{E_1 + \omega^2 \left(R_o^2 + r_b^2 \pm 2r_b R_o \cos \tau\right)}} d\tau = dt. \qquad (6.42)$$

Integration of this equation leads to

$$r_b \int_0^\tau \frac{1}{\sqrt{E_1 + \omega^2 \left(R_o^2 + r_b^2 \pm 2r_b R_o \cos \tau\right)}} d\tau = t. \qquad (6.43)$$

This equation describes t as a function of τ or τ as a function of t. The function $\tau = f(t)$ represents the time-dependent motion of a water particle in the rotating bucket. For a given flow at the bucket entry (E_1), the integration can be converted into summation form and then computed numerically.

To show a comparison between the two cases in Fig. 6.6, the same entry condition is assumed for the two water particles: the jet speed is twice as high as the local peripheral speed U_o of the bucket center, that is, $C_0 = 2\omega R_o$. Under these conditions the energy invariance at the bucket entry is given by

$$E_1 = W_1^2 - U_1^2 = (C_0 - \omega R_1)^2 - (\omega R_1)^2 = C_0(C_0 - 2\omega R_1). \qquad (6.44)$$

For the given condition, $C_0 = 2\omega R_o$, Eq. (6.44) is simplified for both cases with $R_1 = R_o + r_b$ and $R_1 = R_o - r_b$, respectively, to

$$E_1 = 4\omega^2 R_o(R_o - R_1) = \mp 4\omega^2 R_o r_b. \qquad (6.45)$$

This equation is now inserted into Eq. (6.43). One obtains

$$\int_0^\tau \frac{1}{\sqrt{\left(\frac{R_o}{r_b}\right)^2 + 1 \pm 2\frac{R_o}{r_b}\left(\cos \tau - 2\right)}} d\tau = \omega t. \qquad (6.46)$$

The position of the water particle (τ) in the bucket has, thus, been represented as a function of the time or of the bucket rotation angle ωt. Under the specified condition of $\omega R_o/C_0 = 0.5$, the position angle τ together with the respective relative velocity as calculated from Eq. (6.41) is shown in Fig. 6.7. Obviously the time required for a water particle passing through the bucket is quite different in the two cases. The
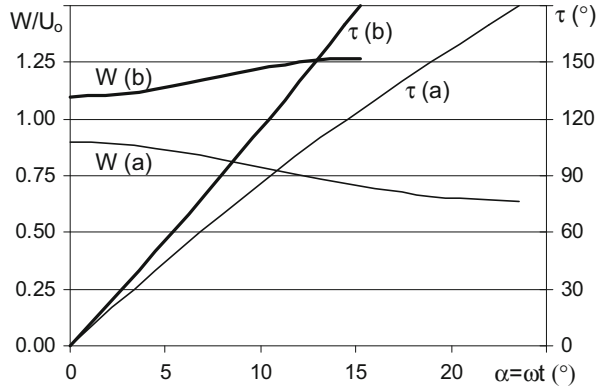
water particle that travels through the bucket from a small to a large radius possesses already at the beginning a relatively greater relative velocity $W(b)$ than in the reverse flow case. According to the invariance equation, this particle will be further accelerated during its motion in the bucket, as can be well seen in Fig. 6.7.

In the mentioned example of the flow according to Fig. 6.6a, the energy invariance at the bucket entry is negative, as confirmed from Eq. (6.45). Since the water particle in the bucket should not come to a standstill (hydraulic jump), the condition stated in Eq. (6.20) for the flow at the bucket exit must be satisfied. Accordingly, it follows with $h \approx 0$

$$R_2^2 > 4 r_b R_o. \tag{6.47}$$

Moreover, with $R_2 = R_o - r_b$, this implies

$$\frac{r_b}{R_o} < 3 - 2\sqrt{2} \approx 0.17. \tag{6.48}$$

In the example shown in Fig. 6.7, $r_b/R_o = 0.1$ has been applied.

6.3 Effective Driving Forces and Related Powers

Apart from viscous friction, the interaction force between the water flow and the rotating bucket is the pressure force $\vec{F}_n$ which is directed normal to the bucket surface; see Fig. 6.1. It is indeed equal to the sum of normal components of all volume forces in the rotating system and therefore represents the effective driving force for the rotation of the Pelton wheel. For estimating the contribution of each volume force to the power of the shaft, only the force components normal to the bucket surface should be considered. Scalar multiplication of the force expression, Eq. (6.3), with $\vec{n}$ results in

$$F_{\mathrm{n}} = \frac{W^2}{r_{\mathrm{b}}} - \vec{F}_{\mathrm{ct}} \cdot \vec{n} - \vec{F}_{\mathrm{Co}} \cdot \vec{n}. \tag{6.49}$$

It represents the force that exists in the form of the overpressure below the water sheet. The pressure force is hence deemed to be the interaction force between the flow and the rotating buckets. Since this force is always perpendicular to the bucket surface and generally does not agree with the direction of the motion of the bucket, i.e., the direction of the peripheral speed, only its component in the circumferential direction of the bucket rotation is effective for the power generation. For unit mass of water, the power of the pressure force is accordingly given by

$$\dot{e} = \frac{\mathrm{d}e}{\mathrm{d}t} = F_{\mathrm{n}}(-\vec{n}) \cdot \vec{U} = -\frac{W^2}{r_{\mathrm{b}}} \vec{n} \cdot \vec{U} + \left(\vec{F}_{\mathrm{ct}} \cdot \vec{n}\right)\vec{n} \cdot \vec{U} + \left(\vec{F}_{\mathrm{Co}} \cdot \vec{n}\right)\vec{n} \cdot \vec{U}. \tag{6.50}$$

It is composed of three contributions which will individually be considered below. The expression of the partial power provided by each volume force (centrifugal and Coriolis) in the above equation is easily comprehensible if one recognizes that the bucket only supports the normal component of that volume force of the flow. This normal force component contributes to the shaft power only through its component in the direction of the bucket motion (U).

The work that is done by the pressure force F_{n} over time is calculated from the following integration:

$$e = \int_0^t \dot{e}\,\mathrm{d}t. \tag{6.51}$$

The total specific work done by the water particles of unit mass while passing through the bucket is calculated by the above integration; with $t = t_2$, then $e = e_2$ is obtained, in which the subscript 2 refers to the bucket exit. For a mass flow rate $\dot{m}_{\mathrm{jet}}$ of a jet, measured in the absolute system, the contribution to the shaft power is $P_{\mathrm{jet}} = \dot{m}_{\mathrm{jet}}e_2$.

6.3.1   Centrifugal Force

The centrifugal force per unit mass has been given in Eq. (6.1). Its component in the $-\vec{n}$ direction (towards the bucket surface) is considered to be effective for the bucket motion and calculated as follows:

$$F_{\mathrm{ct},-\mathrm{n}} = -\vec{\omega} \times \left(\vec{\omega} \times \vec{R}\right) \cdot (-\vec{n}). \tag{6.52}$$

The power provided by this force component is calculated according to Eq. (6.50) to

$$\dot{e}_{\text{ct}} = -\vec{\omega} \times \left(\vec{\omega} \times \vec{R} \right) \cdot \vec{n} \left(\vec{n} \cdot \vec{U} \right). \tag{6.53}$$

For simplicity and to show the mechanism of power generation in a rotating system, the centrifugal force and its effects are considered here only in a two-dimensional bucket with two-dimensional flow, which lies in the drawing plane of Fig. 6.1. The third coordinate coincides with the axis of the wheel.

For calculating vector products, a local coordinate system (t, n, z) according to Fig. 6.1 is applied. The z-axis is perpendicular to the drawing plane. In this coordinate system, the respective vectors in Eqs. (6.52) and (6.53) are represented as

$$\begin{aligned}
\vec{n} &= (0, 1, 0), \\
\vec{R} &= (-R\sin\varphi, \ -R\cos\varphi, 0), \\
\vec{\omega} &= (0, 0, \omega), \\
\vec{U} &= (\omega R\cos\varphi, \ -\omega R\sin\varphi, 0), \\
\vec{W} &= (W_{\text{t}}, 0, 0).
\end{aligned} \tag{6.54}$$

Here, φ is the angle between $\vec{U}$ and $\vec{t}$. It is independent of the flow direction.

From corresponding vector expressions, Eqs. (6.52) and (6.53) are calculated, respectively, to

$$F_{\text{ct},-\text{n}} = R\omega^2 \cos\varphi \tag{6.55}$$

and

$$\dot{e}_{\text{ct}} = R^2\omega^3 \sin\varphi \cos\varphi. \tag{6.56}$$

These results indeed may also be obtained directly from Fig. 6.1, when the centrifugal force $F_{\text{ct}} = R\omega^2$ is directly applied there.

In the bucket area where $\varphi < 90°$ is given, one has $\dot{e}_{\text{ct}} > 0$. This indicates that the centrifugal force contributes to a positive power. The work done by the centrifugal force between time $t = 0$ and $t > 0$ is, in view of Eqs. (6.51) and (6.56), given by

$$e_{\text{ct}} = \omega^3 \int_0^t R^2 \sin\varphi \cos\varphi \, \mathrm{d}t. \tag{6.57}$$

The influence of the relative flow velocity on the calculations is not explicitly given in this equation, however, remains present because of the dependence $\varphi = f(W, t)$. With $\mathrm{d}s = W\mathrm{d}t$ as the infinitesimal motion of the water particle in the flow, Eq. (6.57) takes the form

$$e_{\text{ct}} = \omega^3 \int_0^s R^2 \sin \varphi \cos \varphi \frac{1}{W} \mathrm{d}s. \tag{6.58}$$

The relative velocity W in the rotating bucket is determined by the invariance equation. Starting from the energy invariance $E_1 = W_1^2 - U_1^2$ at the bucket entry, the relative velocity at other times is calculated with the local circumferential speed $U = R\omega$ to $W = \sqrt{E_1 + (R\omega)^2}$. Accordingly, Eq. (6.58) becomes

$$e_{\text{ct}} = \omega^3 \int_0^s R^2 \sin \varphi \cos \varphi \frac{1}{\sqrt{E_1 + (R\omega)^2}} \mathrm{d}s. \tag{6.59}$$

For further evaluation of the integral, it should be distinguished between the flows in the positive and negative $\vec{t}$-directions. After Fig. 6.1 $\sin \varphi \mathrm{d}s = \mp \mathrm{d}R$ applies with the upper sign for the flow in the positive $\vec{t}$-direction (see also Fig. 6.6a). Thus, it follows from Eq. (6.59) that

$$e_{\text{ct}} = \mp\omega^3 \int_{R_1}^R R^2 \cos \varphi \frac{1}{\sqrt{E_1 + (R\omega)^2}} \mathrm{d}R. \tag{6.60}$$

The integration can be performed analytically, when the angle φ is given as a function of the coordinate R, else, the integration must be performed numerically.

6.3.1.1 Special Case 1: Semicircular Bucket

To simplify the calculation in Eq. (6.60), the flow in a semicircular rotating bucket displayed in Fig. 6.6 is again considered. According to the cosine law for the triangle in Fig. 6.6a, one has

$$R_{\text{o}}^2 = R^2 + r_{\text{b}}^2 - 2Rr_{\text{b}} \cos \varphi. \tag{6.61}$$

This may be rewritten as

$$R \cos \varphi = \frac{1}{2r_{\text{b}}} R^2 + \frac{1}{2}\left(r_{\text{b}} - \frac{R_{\text{o}}^2}{r_{\text{b}}}\right). \tag{6.62}$$

Substitution into Eq. (6.60) yields

$$e_{ct} = \mp \frac{1}{2}\omega^3 \int_{R_1}^{R} \left[\frac{R^3}{r_b} + \left(r_b - \frac{R_o^2}{r_b} \right) R \right] \frac{1}{\sqrt{E_1 + (R\omega)^2}} dR. \tag{6.63}$$

The integration can explicitly be performed which leads to

$$e_{ct}$$
$$= \pm \frac{1}{2}\omega \left[\left(\frac{r_b^2 - R_o^2}{r_b} + \frac{\omega^2 R_1^2 - 2E_1}{3r_b\omega^2} \right) \sqrt{E_1 + \omega^2 R_1^2} - \left(\frac{r_b^2 - R_o^2}{r_b} + \frac{\omega^2 R^2 - 2E_1}{3r_b\omega^2} \right) \sqrt{E_1 + \omega^2 R^2} \right]. \tag{6.64}$$

If the flow at the bucket entry (R_1) is known (E_1), the specific work of the centrifugal force can be calculated; it depends on the position R of the unit mass in the bucket. It should also be noted that E_1 and $\omega^2 R_1^2$ in this equation should not be considered as two independent variables. According to its definition, the energy invariance at the bucket entry can be expressed as

$$E_1 = W_1^2 - U_1^2 = (W_1 - U_1)(W_1 + U_1) = (C_0 - 2U_1)C_0$$
$$= \left(1 - \frac{2\omega R_1}{C_0} \right) C_0^2. \tag{6.65}$$

To non-dimensionalize Eq. (6.64), the following abbreviations are introduced:

$$\bar{r}_b = \frac{r_b}{R_o}, \bar{R} = \frac{R}{R_o}, \bar{R}_1 = \frac{R_1}{R_o}, k_o = \frac{\omega R_o}{C_0}, e^* = \frac{e}{C_0^2/2}, \bar{E}_1 = \frac{E_1}{\omega^2 R_o^2}. \tag{6.66}$$

In these expressions, the specific work (e) is scaled with the kinetic energy of water particles at the bucket entry, i.e., in the jet. It can therefore be interpreted as the partial efficiency of the centrifugal force.

To avoid confusion in the use of symbols, the peripheral speed coefficient $\omega R_o / C_0$ is denoted here by k_o instead of k_m because according to Eq. (2.18), the symbol k_m has a clearly defined meaning in Pelton turbines.

With Eq. (6.66), then Eqs. (6.64) and (6.65) are simplified to

$$e_{ct}^*$$
$$= \pm k_o^2 \frac{1}{\bar{r}_b} \left\{ \left[\bar{r}_b^2 - 1 + \frac{1}{3} \left(\bar{R}_1^2 - 2\bar{E}_1 \right) \right] \sqrt{\bar{E}_1 + \bar{R}_1^2} - \left[\bar{r}_b^2 - 1 + \frac{1}{3} \left(\bar{R}^2 - 2\bar{E}_1 \right) \right] \sqrt{\bar{E}_1 + \bar{R}^2} \right\}, \tag{6.67}$$

with

$$\overline{E}_1 = \frac{1}{k_o^2}\left(1 - 2k_o\overline{R}_1\right). \tag{6.68}$$

In general form, it is expressible as

$$e_{ct}^* = f\left(\overline{r}_b, k_o, \overline{R}_1, \overline{R}\right). \tag{6.69}$$

For given values of $\overline{r}_b$, k_o, and $\overline{R}_1$, the work e_{ct}^* done by the centrifugal force can be calculated as a function of $\overline{R}$. Because of the relationship $R^2 = R_o^2 + r_b^2 \pm 2r_bR_o \cos \tau$ from Fig. 6.6, the work done can also be represented as a function of the particle position angle τ, which is again associated with the time by Eq. (6.43). For $E_1 = 0$, a computational example will be given below.

The specific work which is done by the centrifugal force during the flow throughout the rotating bucket is calculated by simply setting $\overline{R} = \overline{R}_2 = 1 \mp \overline{r}_b$.

6.3.1.2 Special Case 2: Semicircular Bucket for $E_1 = 0$

A further simplification is considered here for $E_1 = 0$ which means that at the bucket entry (subscript 1), the relative flow velocity W_1 is equal to the local peripheral speed U_1 of the bucket. According to the invariance equation with $E = E_1 = 0$, the relative flow velocity must be equal to the local circumferential speed $W = R\omega$ also to other times.

With $E_1 = 0$, Eq. (6.68) implies $k_o = 1/(2\overline{R}_1)$. Accordingly, Eq. (6.67) can be simplified to

$$e_{ct}^* = \pm\frac{1}{4\overline{R}_1^2}\frac{1}{\overline{r}_b}\left[\left(\overline{r}_b^2 - 1\right)\left(\overline{R}_1 - \overline{R}\right) + \frac{1}{3}\left(\overline{R}_1^3 - \overline{R}^3\right)\right]. \tag{6.70}$$

As a result of the relation $R^2 = R_o^2 + r_b^2 \pm 2r_bR_o \cos \tau$ and thus $\overline{R}^2 = 1 + \overline{r}_b^2 \pm 2\overline{r}_b \cos \tau$ (Fig. 6.6), the normalized specific work according to Eq. (6.70) can be represented as a function of the position angle τ of a water particle in the rotating bucket and, because of Eq. (6.43), also as a function of time. Figure 6.8 shows a computational example for the motion of a water particle in the positive $\vec{t}$-direction in a semicircular bucket of $r_b/R_o = 0.1$. At the time of a rotation angle $\omega t \approx 9°$, the water particle is found at the position $\tau_m \approx 96°$. Beyond this position, the work done again decreases. This is explained by the fact that beyond $\tau_m \approx 96°$ the angle φ will be $\varphi > 90°$; furthermore, $\dot{e}_{ct} < 0$ according to Eq. (6.56). This can be determined by

$$\frac{de_{ct}^*}{d\tau} = \frac{de_{ct}^*}{d\overline{R}}\frac{d\overline{R}}{d\tau} = 0. \tag{6.71}$$

It follows then from Eq. (6.70) with $\overline{R}^2 = 1 + \overline{r}_b^2 + 2\overline{r}_b \cos \tau$ that
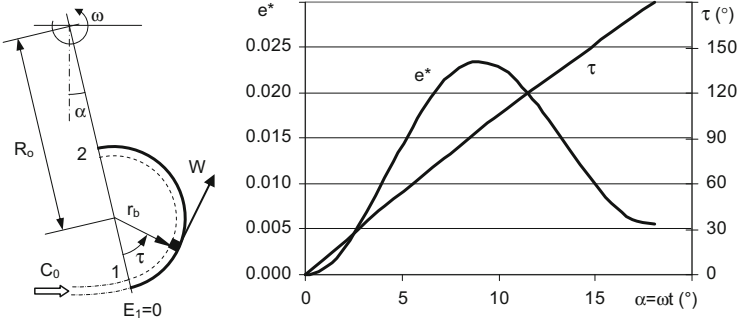
Fig. 6.8 Movement of a water particle in a rotating semicircular bucket and the work done by the centrifugal force, normalized by the kinetic energy of the inlet flow, $r_b/R_o = 0.1$ and $E_1 = 0$

$$\cos \tau_m = -\overline{r}_b. \tag{6.72}$$

For $\overline{r}_b = 0.1$, thus $\tau_m = 96°$ arises.

The flow of a water particle throughout the semicircular bucket should be considered now. The work done by the centrifugal force is determined by setting $\overline{R} = \overline{R}_2 = 1 - \overline{r}_b$. From Eq. (6.70) with $\overline{R}_1 = 1 + \overline{r}_b$, it then accordingly follows

$$e_{ct,2}^* = \frac{2}{3}\left(\frac{\overline{r}_b}{\overline{R}_1}\right)^2 = \frac{2}{3}\left(\frac{r_b}{R_1}\right)^2 \tag{6.73}$$

and with $C_0 = 2\omega R_1$ (from $E_1 = 0$) in explicit form

$$e_{ct,2} = \frac{4}{3}\omega^2 r_b^2. \tag{6.74}$$

Equation (6.73) represents the specific work normalized by the specific kinetic energy of the jet. It is evident that the specific work done by the centrifugal force $e_{ct,2}$ has a very small value compared to the kinetic energy of the jet, $C_0^2/2$, since r_b/R_1 is generally very small for a Pelton turbine.

It can be demonstrated that the same result as Eq. (6.74) can be obtained for the flow according to Fig. 6.6b. In this case, the negative sign in Eq. (6.70) has to be applied. Correspondingly, one now has $\overline{R}_1 = 1 - \overline{r}_b$. With the entry condition $E_1 = 0$ in this case, $C_0 = 2\omega R_1$ is still applicable, but with $R_1 = R_o - r_b$.

6.3.2   Coriolis Force

The Coriolis force per unit mass has been defined in Eq. (6.2). Analogously to Eq. (6.52), the force component in the $-\vec{n}$-direction (towards the bucket surface) is given by

$$F_{\text{Co},-\text{n}} = -2\left(\vec{\omega} \times \vec{W}\right) \cdot (-\vec{n}). \tag{6.75}$$

The power provided by this force component is calculated according to Eq. (6.50) by

$$\dot{e}_{\text{Co}} = -2\left(\vec{\omega} \times \vec{W}\right) \cdot \vec{n}\left(\vec{n} \cdot \vec{U}\right). \tag{6.76}$$

Two-dimensional flow in a two-dimensional bucket is again considered here. The flow lies in the drawing plane of Fig. 6.1. In the coordinate system (t, n, z) as shown in Fig. 6.1 and with corresponding vector expressions in Eq. (6.54), the above two equations are easily evaluated as

$$F_{\text{Co},-\text{n}} = 2\omega W_{\text{t}} \tag{6.77}$$

and

$$\dot{e}_{\text{Co}} = 2R\omega^2 W_{\text{t}} \sin\varphi = -2R\omega^2 W_{\text{r}}. \tag{6.78}$$

Here $W_{\text{t}} \sin\varphi = -W_{\text{r}}$ represents the component of the velocity vector $\vec{W}$ in the radial direction $(\vec{R})$.

Equation (6.78) also establishes the link with the centrifugal force $(R\omega^2)$.

The work done by the Coriolis force per unit mass is obtained as follows:

$$e_{\text{Co}} = \int_0^t \dot{e}_{\text{Co}}\mathrm{d}t = -2\omega^2 \int_0^t R \cdot W_{\text{r}}\mathrm{d}t. \tag{6.79}$$

With $W_{\text{r}} = \mathrm{d}R/\mathrm{d}t$, it can, finally, easily be evaluated as

$$e_{\text{Co}} = -2\omega^2 \int_{R_1}^R R \cdot \mathrm{d}R = \omega^2\left(R_1^2 - R^2\right) = U_1^2 - U^2. \tag{6.80}$$

With the variables of Eq. (6.66), one obtains its dimensionless form:

$$e_{\text{Co}}^* = 2k_{\text{o}}^2\left(\overline{R}_1^2 - \overline{R}^2\right). \tag{6.81}$$

Eq. (6.80) or Eq. (6.81) shows that the Coriolis force for radial flows towards the wheel axis $(R < R_1)$ performs positive work. This result will be needed later to

completely understand the fluid mechanics of a special flow model which will be presented in Sect. 6.3.5.

By contrast to Eq. (6.60) for the work done by the centrifugal force, the work done by the Coriolis force only depends on the initial and the current radial positions of the flow in the rotating bucket, but not on the traveled path. Furthermore, it is independent of the flow velocity.

For the through flow through the bucket (not necessarily of circular form), one sets $R = R_2$ in Eq. (6.80) and obtains

$$e_{\mathrm{Co},2} = \omega^2\left(R_1^2 - R_2^2\right) = U_1^2 - U_2^2. \tag{6.82}$$

It should be noted that computational results of Eq. (6.80) to Eq. (6.82) only apply for the simplified flows in the drawing plane of Fig. 6.1, where the bucket is assumed to be two-dimensional. This condition has already been specified by the normal vector $\vec{n} = (0,\ 1,\ 0)$ in the local coordinate system $(t,\ n,\ z)$. Therefore, no conclusion for the case $U_1 = U_2$ can be generally made from Eq. (6.82), because this is not possible in the two-dimensional flow according to Fig. 6.1.

6.3.2.1 Special Case 1: Semicircular Bucket

The semicircular bucket shown in Fig. 6.6 is considered again. Water particles are assumed to move again in two different directions with the entry at $R_1 = R_\mathrm{o} \pm r_\mathrm{b}$ and the exit at $R_2 = R_\mathrm{o} \mp r_\mathrm{b}$. Equation (6.82) is then simplified to

$$e_{\mathrm{Co},2} = \pm 4 r_\mathrm{b} R_\mathrm{o} \omega^2. \tag{6.83}$$

If this is normalized with the initial kinetic energy of the jet flow, one obtains

$$e_{\mathrm{Co},2}^* = \frac{e_{\mathrm{Co},2}}{\frac{1}{2}C_0^2} = \pm 8 k_\mathrm{o}^2 \frac{r_\mathrm{b}}{R_\mathrm{o}}. \tag{6.84}$$

6.3.2.2 Special Case 2: Semicircular Bucket for $E_1 = 0$

A further simplification is possible for $E_1 = 0$, from which $W_1 = U_1 = C_0/2$ and $k_\mathrm{o} = U_\mathrm{o}/C_0 = 0.5 R_\mathrm{o}/R_1$ are obtained. Equation (6.81) then implies

$$e_{\mathrm{Co}}^* = \frac{1}{2}\left(1 - \frac{\overline{R}^2}{\overline{R}_1^2}\right). \tag{6.85}$$

Similarly for Eq. (6.84),

$$e_{Co,2}^* = \pm 2 \frac{R_o\, r_b}{R_1\, R_1}. \tag{6.86}$$

For positive work and by the comparison with Eq. (6.73), it is noticeable that the work done by the Coriolis force is significantly larger than the work done by the centrifugal force. From Eq. (6.73) and Eq. (6.86), one obtains, for instance,

$$\frac{e_{ct,2}^*}{e_{Co,2}^*} = \frac{e_{ct,2}}{e_{Co,2}} = \pm \frac{1}{3} \frac{r_b}{R_o}. \tag{6.87}$$

For comparison between the centrifugal and Coriolis forces, see also Sect. 6.3.5 for computational examples.

6.3.3 Impulsive Force Inferred from Streamline Curvature

Water flow along the bucket surface continuously changes its direction. The related streamline curvature then leads to the change in the momentum flow rate (as a vector quantity) and thus to an impulsive force which is perpendicular to the streamlines and acts on the bucket surface. According to Eq. (6.49), such an impulsive force per unit mass is formulated as

$$F_I = \frac{W^2}{r_b}. \tag{6.88}$$

Here, r_b is referred to as the radius of curvature of the local streamlines which are congruent with the bucket surface.

The power provided by the impulsive force is calculated according to Eq. (6.50) by

$$\dot{e}_I = -\frac{W^2}{r_b}\, \vec{n} \cdot \vec{U}. \tag{6.89}$$

Next, consider again the two-dimensional flow in a two-dimensional bucket according to Fig. 6.1. With respect to relation $\vec{n} \cdot \vec{U} = -\omega R \sin\varphi$, it then follows from Eq. (6.89)

$$\dot{e}_I = \frac{W^2}{r_b}\, \omega R \sin\varphi. \tag{6.90}$$

The specific work done during the flow is accordingly

$$e_{\mathrm{I}} = \int_0^t \dot{e}_{\mathrm{I}} \mathrm{d}t = \int_0^t \frac{W^2}{r_{\mathrm{b}}} \omega R \sin \varphi \mathrm{d}t. \tag{6.91}$$

To perform the integration, again Eq. (6.12) is considered. Taking into account the centrifugal force $\left|\vec{F}_{\mathrm{ct}}\right| = R\omega^2$, one obtains by considering Fig. 6.1

$$\frac{\mathrm{d}W_{\mathrm{t}}}{\mathrm{d}t} = \vec{F}_{\mathrm{ct}} \cdot \vec{t} = R\omega^2 \cos\left(\frac{\pi}{2} + \varphi\right) = -R\omega^2 \sin \varphi. \tag{6.92}$$

This equation is inserted into Eq. (6.91) to eliminate dt. With $W^2 = W_{\mathrm{t}}^2$, this results in

$$e_{\mathrm{I}} = -\frac{1}{\omega} \int_{W_{\mathrm{t1}}}^{W_{\mathrm{t}}} \frac{1}{r_{\mathrm{b}}} W_{\mathrm{t}}^2 \mathrm{d}W_{\mathrm{t}}. \tag{6.93}$$

In this equation, W_{t} is positive if the flow direction agrees with the orientation of the tangent vector $\vec{t}$ in Fig. 6.1, else W_{t} is negative.

6.3.3.1   Special Case 1: Bucket of Circular Form

A bucket of circular form with $r_{\mathrm{b}} = $ const is considered. From Eq. (6.93) it follows straightforwardly that

$$e_{\mathrm{I}} = \frac{1}{3\omega r_{\mathrm{b}}} \left(W_{\mathrm{t1}}^3 - W_{\mathrm{t}}^3\right). \tag{6.94}$$

To determine the relative flow velocity, again the invariance equation is applied. One obtains $W_{\mathrm{t}} = \pm\sqrt{E_1 + (\omega R)^2}$. Then Eq. (6.94) takes the form

$$e_{\mathrm{I}} = \pm\frac{1}{3\omega r_{\mathrm{b}}} \left\{ \left[E_1 + (R_1\omega)^2\right]^{3/2} - \left[E_1 + (R\omega)^2\right]^{3/2} \right\} \tag{6.95}$$

and, when non-dimensionalized,

$$e_{\mathrm{I}}^* = \pm\frac{2k_{\mathrm{o}}^2}{3\bar{r}_{\mathrm{b}}} \left[\left(\bar{E}_1 + \bar{R}_1^2\right)^{3/2} - \left(\bar{E}_1 + \bar{R}^2\right)^{3/2} \right]. \tag{6.96}$$

According to the flow models shown in Fig. 6.6a, the positive sign in this equation is for a motion of water particles co-parallel to the tangent vector $\vec{t}$. It should be noted that $\bar{E}_1$ and $\bar{R}_1$ are not independent of each other, but are linked by Eq. (6.68).

6.3.3.2 Special Case 2: Semicircular Bucket for $E_1 = 0$

Under the entry condition $E_1 = 0$, Eq. (6.95) is simplified to

$$e_{\mathrm{I}} = \pm \frac{\omega^2}{3r_{\mathrm{b}}}\left(R_1^3 - R^3\right). \tag{6.97}$$

Because of the condition $E_1 = 0$, which also means $W_1 = U_1 = C_0/2$ and $\omega R_1 = C_0/2$, the above equation takes the dimensionless form

$$e_{\mathrm{I}}^* = \pm \frac{1}{6\overline{r}_{\mathrm{b}}\overline{R}_1^2}\left(\overline{R}_1^3 - \overline{R}^3\right). \tag{6.98}$$

For the flow through the bucket ($R = R_2$), the specific work done by the impulsive force due to the streamline curvature is obtained as

$$e_{\mathrm{I},2} = \pm \frac{1}{3r_{\mathrm{b}}}\omega^2\left(R_1^3 - R_2^3\right). \tag{6.99}$$

According to Fig. 6.6b for the flow model of a semicircular bucket, the flow is directed in the negative $\vec{t}$-direction. Both the entry and exit positions are given by $R_1 = R_{\mathrm{o}} - r_{\mathrm{b}}$ and $R_2 = R_{\mathrm{o}} + r_{\mathrm{b}}$, respectively. With the negative sign in Eq. (6.99), one obtains

$$e_{\mathrm{I},2} = 2\omega^2\left(R_{\mathrm{o}}^2 + \frac{1}{3}r_{\mathrm{b}}^2\right). \tag{6.100}$$

It can be shown that the same result will be obtained if the flow as shown in Fig. 6.6a follows the positive $\vec{t}$-direction. Equation (6.100) is therefore independent of the flow direction in the assumed semicircular bucket. It should be noted that the condition $E_1 = 0$ which has led to Eq. (6.100) for both flow arrangements requires a different jet speed. Although in both cases the condition $C_0 = 2\omega R_1$ holds, the relations $R_1 = R_{\mathrm{o}} + r_{\mathrm{b}}$ and $R_1 = R_{\mathrm{o}} - r_{\mathrm{b}}$, respectively, must separately be applied.

6.3.4 Total Effect of Impulsive, Centrifugal, and Coriolis Forces

All volume forces in the frictionless flow in a rotating bucket, as shown in Sect. 6.1.1, include centrifugal and Coriolis forces as well as the impulsive force due to changes of streamline curvatures. All these forces, with their respective components perpendicular to the bucket surface, are united to a pressure force on the bucket surface. The contribution of each single force performing the mechanical

work has all been scrutinized in previous sections. The current section describes the overall effect in more details. For obtaining the explicit and simple results, the following assumptions will be again applied:

- Semicircular bucket
- Entry condition $E_1 = 0$

First, all three partial works that have been given in Eqs. (6.70), (6.85), and (6.98), respectively, can be summarized in a single formula, namely,

$$e^* = e^*_{ct} + e^*_{Co} + e^*_I$$
$$= \pm \frac{1}{4\overline{R}_1^2} \frac{1}{\overline{r}_b} \left[\left(\overline{r}_b^2 - 1 \right) \left(\overline{R}_1 - \overline{R} \right) + \left(\overline{R}_1^3 - \overline{R}^3 \right) \right] + \frac{1}{2\overline{R}_1^2} \left(\overline{R}_1^2 - \overline{R}^2 \right). \quad (6.101)$$

To simplify this equation further, the positive sign is first considered. This corresponds to the case shown in Fig. 6.6a with $\overline{R}_1 = 1 + \overline{r}_b$. From the above equation, it then follows

$$e^*_+ = 1 - \frac{1}{4(1 + \overline{r}_b)^2} \frac{\overline{R}}{\overline{r}_b} \left[\left(\overline{r}_b + \overline{R} \right)^2 - 1 \right]. \quad (6.102)$$

Similarly, Eq. (6.101) with the negative sign for the case of Fig. 6.6b with $\overline{R}_1 = 1 - \overline{r}_b$ implies

$$e^*_- = 1 - \frac{1}{4(1 - \overline{r}_b)^2} \frac{\overline{R}}{\overline{r}_b} \left[1 - \left(\overline{r}_b - \overline{R} \right)^2 \right]. \quad (6.103)$$

For the flow throughout the semicircular bucket, one has $\overline{R} = \overline{R}_2 = 1 - \overline{r}_b$ for the case of Fig. 6.6a and $\overline{R} = \overline{R}_2 = 1 + \overline{r}_b$ for the case of Fig. 6.6b. From Eqs. (6.102) and (6.103), one obtains equally

$$e^*_+ = e^*_- = 1 \quad (6.104)$$

or

$$e_+ = e_- = \frac{1}{2} C_0^2. \quad (6.105)$$

This result fully agrees with the expectation. For the entry condition $E_1 = 0$, the kinetic energy in the jet has been completely transferred to the rotating buckets, and the hydraulic efficiency in both cases is 100 %. The conversion of kinetic into mechanical energy is thus in both cases perfect. This statement can also be obtained directly from the invariance equation. Because of the equality $E_2 = E_1 = 0$, there is $\vec{U}_2 = -\vec{W}_2$ and, thus, $\vec{C}_2 = 0$ at the exit of the semicircular bucket. The absolute

velocity and, therefore, the kinetic energy of the flow after leaving the bucket are zero in both cases. The energy conversion is complete.

6.3.5 Examples

After the relative flow in the rotating bucket has been analyzed in detail, two examples will be shown to illustrate calculations and computational results of such a combined flow.

Example 1: Individual Forces and Specific Works
In the above sections, significances of both the centrifugal and Coriolis forces as well as the impulsive force due to the streamline curvature have been examined. The specific works done by each individual force in a two-dimensional semicircular bucket and under the general entry condition $E_1 \neq 0$ are given, respectively, by Eqs. (6.67), (6.81), and (6.96). For ease of use, these equations are again summarized here as follows:

$$e_{ct}^{*} = \pm k_o^2 \frac{1}{\overline{r}_b} \left\{ \left[\overline{r}_b^2 - 1 + \frac{1}{3} \left(\overline{R}_1^2 - 2\overline{E}_1 \right) \right] \sqrt{\overline{E}_1 + \overline{R}_1^2} - \left[\overline{r}_b^2 - 1 + \frac{1}{3} \left(\overline{R}^2 - 2\overline{E}_1 \right) \right] \sqrt{\overline{E}_1 + \overline{R}^2} \right\},$$
(6.67)

$$e_{Co}^{*} = 2k_o^2 \left(\overline{R}_1^2 - \overline{R}^2 \right),$$
(6.81)

$$e_I^{*} = \pm \frac{2k_o^2}{3\overline{r}_b} \left[\left(\overline{E}_1 + \overline{R}_1^2 \right)^{3/2} - \left(\overline{E}_1 + \overline{R}^2 \right)^{3/2} \right].$$
(6.96)

The entry condition according to Eq. (6.68) is also rewritten here:

$$\overline{E}_1 = \frac{1}{k_o^2} \left(1 - 2k_o \overline{R}_1 \right).$$
(6.68)

The positive sign in the above equations is for positive flow according to Fig. 6.6a and the negative sign for negative flow according to Fig. 6.6b. The overall specific work per unit mass for the general case $E_1 \neq 0$ is given by

$$e^{*} = e_{ct}^{*} + e_{Co}^{*} + e_I^{*}.$$
(6.106)

Apart from this overall work, one is also interested in a comparison between the three individual specific works. Obviously one has to distinguish between two flow models in Fig. 6.6. For simplicity the two-dimensional jet speed is twice as high as the peripheral speed of the bucket center point, i.e., $C_0 = 2\omega R_o$ or $k_o = 0.5$.

According to Eq. (6.68), this condition simply means for both flow models in Fig. 6.6 that

$$\overline{E}_{1+} = 4(1 - \overline{R}_1) = -4\overline{r}_b, \tag{6.107}$$

$$\overline{E}_{1-} = 4(1 - \overline{R}_1) = 4\overline{r}_b. \tag{6.108}$$

Figure 6.9 shows the computational results regarding the respective specific works as functions of the bucket-position angle. The overall work has also been shown in the figure. This type of the presentation with ωt as the variable has already been applied in Figs. 6.7 and 6.8.

As can be seen, the contribution of the impulsive force arising from the streamline curvature to the total power exchange dominates. While the effect of the centrifugal force in both cases is negligible, the Coriolis force makes a significant contribution in either a positive or a negative sense, depending on the flow direction. By reaching the exit of semicircular buckets, the flows perform the overall work $e_+^* = 0.983$ for the positive flow and $e_-^* = 0.993$ for the negative flow, respectively. Both values in reality represent the hydraulic efficiencies of the energy conversion in the respective flow processes.

Example 2: KWO Gedanken Model, a Technical Conundrum

To show the significance of the invariance equation, a conceptual flow model has been designed by the author during his time at the Oberhasli Hydroelectric Power Company (KWO). It deals with a fictitious turbine with two-dimensional buckets as shown in Fig. 6.10. For a two-dimensional jet of a speed ratio $U_1/C_0 = 0.5$ at the bucket entry, the question arises as to whether both bucket halves A and B have the same energy exchange with the jet and thus the same efficiency when the jet is deflected to 180° and the flow is frictionless.

The given condition of $U_1/C_0 = 0.5$ in reality implies the condition $U_1 = W_1$ at the bucket entry. According to the invariance equation $W^2 - U^2 = $ const, which in the current case simply means $W^2 - U^2 = 0$, there has to be $U_2 = W_2$ at the bucket
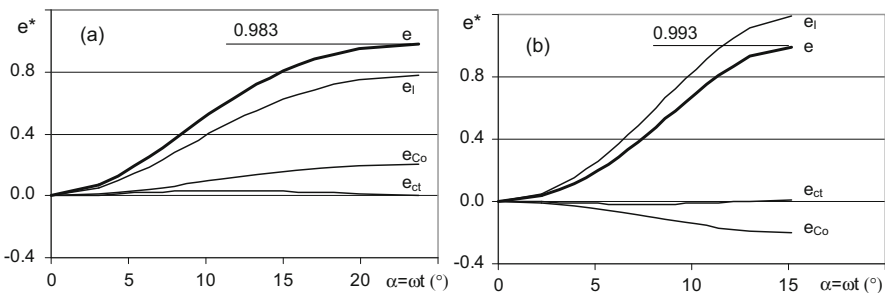
Fig. 6.9 Effectiveness of the centrifugal, Coriolis, and impulsive forces in a rotating semicircular bucket with parameter settings $C_0 = 2\omega R_o$ and $r_b/R_o = 0.1$. The overall effect is $e = e_{ct} + e_{Co} + e_I$. (**a**) Positive flow according to Fig. 6.6a. (**b**) Negative flow according to Fig. 6.6b
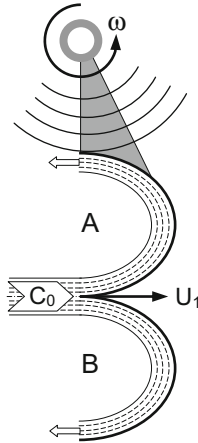
Fig. 6.10 KWO fictitious Pelton turbine flow model with two-dimensional inviscid flow
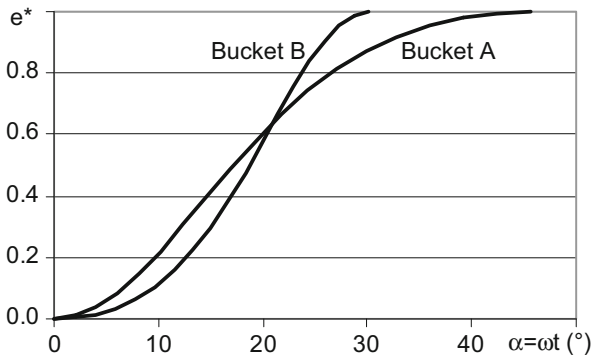
Fig. 6.11 Specific work done in the buckets A and B in the flow model shown in Fig. 6.10 with $E_1 = 0$ and $r_b/R_1 = 0.2$

exit for both bucket halves A and B. This means, in turn, that the absolute velocity at the bucket exit must be equal to zero $C_2 = 0$ in both cases with the jet deflection of $180°$. With other words, the kinetic energy of the jet is completely transferred to the rotating bucket. The conversion rate of the energy in both bucket halves is therefore equal. In fact, this result has already been demonstrated in Sect. 6.3.4 by Eq. (6.104) for the flow in a semicircular bucket.

The conclusion of equal power exchange in the presented flow model with two bucket halves can be proved by yet another calculation, as shown in Fig. 6.11. It demonstrates that at the bucket half A, the work done by the flow gently increases over the time with the bucket rotation. Because of the low value of the relative velocity, the flow reaches the bucket exit only after a bucket rotation of about $45°$. By contrast, the flow at the bucket half B has almost no reaction with the bucket at

the beginning. After the flow has reached the bucket bottom, the work done by the flow rapidly increases. Since the relative flow velocity here is higher than that in the bucket half A, the flow reached the bucket exit already after a bucket rotation of about 30°.

For a better understanding of such flows in the rotating bucket, the effect of the Coriolis force needs to be considered in more details. In the bucket half A, the Coriolis force is directed to the bucket surface so that this force performs a positive work. In contrast, the Coriolis force in the bucket half B is directed away from the bucket surface and therefore does a negative work (see also Fig. 6.9b). Taking into account the different impulsive forces due to the different relative flow velocities, the same power exchange in two bucket halves has been finally obtained.

The flow model shown in Fig. 6.10 can be extended to the general mechanics when two solid balls of equal mass are considered in place of the jet flow. The model can be further extended to two buckets of different size under the same condition.

Reference

Zhang, Zh. (2007). Flow interactions in Pelton turbines and the hydraulic efficiency of the turbine system. *Proceedings of the IMechE Vol. 221, Part A: Journal of Power and Energy*, pp. 343–357.

Chapter 7
Water Spreading in the Rotating Bucket

7.1 Relative Flow Rate

Water spreading in Pelton buckets is three-dimensional and obeys Newton's second law of motion. As it has already been derived in Sect. 6.2 by applying this law, the relative flow of water in a rotating bucket can be described by the *invariance equation*. According to Eq. (6.23), all water particles in a given jet layer retain the same value of energy invariance. This so-called jet layer method will be applied here to determine the relative flow rate in the rotating system.

Consider first the peripheral speeds and velocity triangles at the bucket entry (main splitter) for three different water particles in a given jet layer, as shown in Fig. 7.1 with three positions of an idealized bucket at consecutive time slices. The particle speed is equal to C_0. Because the particles will reach the bucket at different times, their entry points at the bucket must have different circumferential velocities U. The x-components of these velocities, however, are equal to each other, i.e., independent of the particle entry point, as given by $U_x = U \cos \alpha = \omega h_s = $ const; see also Eq. (6.23). Because of this relation, the x-components of the relative velocities of all particles are obtained as

$$W_{0x} = C_0 - U_x = \text{const.} \tag{7.1}$$

This equation states that all water particles in a given jet layer before entering the bucket (subscript 0) have the same constant velocity component W_{0x} (Fig. 7.1b). Since each jet layer has its own constant cross section ΔA, as shown in Fig. 7.2, the related flow rate in the relative system has its own value proportional to ΔA during the interaction between the jet layer and the rotating buckets. This is given by

$$\Delta \dot{Q}_w = W_{0x} \Delta A = \text{const.} \tag{7.2}$$
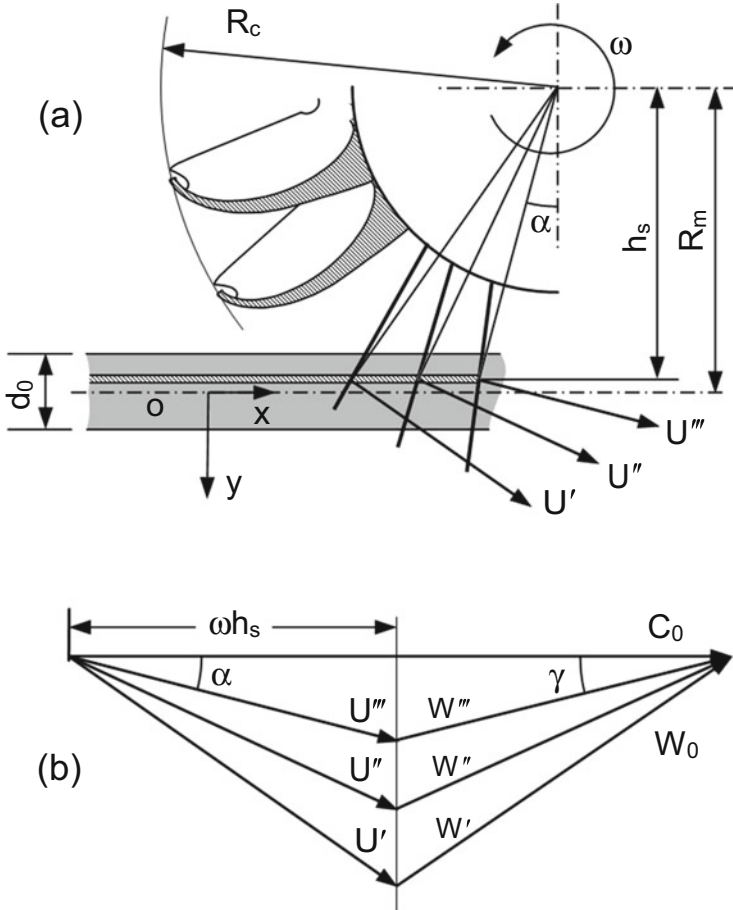
Fig. 7.1 Consecutive time slices for water particles in the same jet layer when entering the bucket. (**a**) Circumferential velocities and (**b**) velocity triangles with constant components of the circumferential velocities

Moreover, the value of the constant also depends on the position h_s of the jet layer within the jet. The flow rate specified in this equation also remains constant in the rotating bucket. Since the relevant flow parameter in a rotating bucket is always the relative flow velocity, the flow rate in a half of the bucket is accordingly given by $\Delta \dot{Q}_w/2 = \Delta dhW$. Thus, the elementary section of the water sheet is calculated as the product of the water-sheet thickness h and the elementary water-sheet width Δd, according to Fig. 7.2 given by

$$\Delta dh = \frac{1}{2} \Delta A \frac{W_{0x}}{W}. \tag{7.3}$$

Fig. 7.2 General spreading form of the jet in the Pelton bucket. Δd is the width of the contribution of the jet layer, and W the depth averaged velocity as it spreads in the bucket
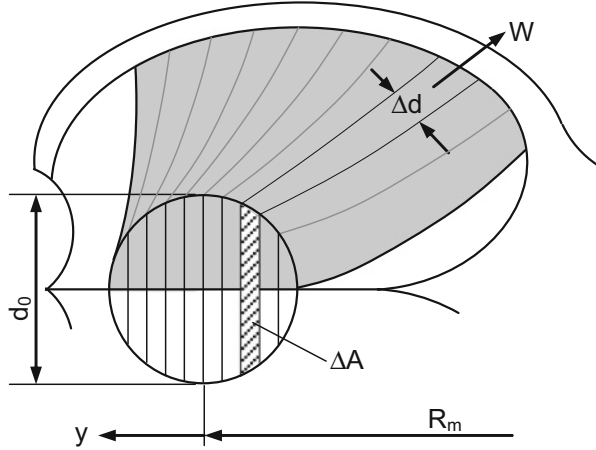
It should be noted that the relative flow velocity W in the rotating bucket depends on the varying relative flow velocity W_0 before entering the bucket (see Fig. 7.1b). It further changes, according to the invariance equation, with the local peripheral speed and is therefore generally not constant.

According to Eq. (7.2), the relative flow rate varies from layer to layer of the jet, not only because of the change of the cross section ΔA but also because of the variation of the velocity component W_{0x}. The relative flow rate related to a half jet is obtained from the integration of Eq. (7.2) to

$$\frac{\dot{Q}_w}{2} = \frac{1}{2} \int_0^{A_0} W_{0x} dA = \frac{1}{2} \int_{-d_0/2}^{d_0/2} (C_0 - \omega h_s) \frac{dA}{dy} dy. \tag{7.4}$$

With $h_s = R_m + y$ and $dA = 2\sqrt{(d_0/2)^2 - y^2} \cdot dy$ as the cross section of an infinitesimally thin jet layer, shown in Fig. 7.2, the overall relative flow rate in the rotating system can be calculated; the result of the integration is

$$\frac{\dot{Q}_w}{2} = \frac{1}{8} \pi d_0^2 (C_0 - \omega R_m) = \frac{1}{8} \pi d_0^2 W_{0x,o}, \tag{7.5}$$

in which $W_{0x,o}$ is the x-component of the relative velocity of particles at the jet axis. Because this unique representative velocity is independent of the bucket position, the relative flow rate given in Eq. (7.5) is constant and thus valid for all positions of the bucket when intersecting the jet. At this point the reader should be alerted that the relative flow rate is not simply the product of the relative velocity (W) and the jet section, but according to Eq. (7.5), it is the product of the velocity component $W_{0x,o}$ and the jet section.

The relative flow rate, according to Eq. (7.5), also maintains its value in the rotating bucket. As in Eq. (7.3), the flow in a Pelton bucket is always considered by

the relative flow velocity which is obtained by averaging velocities over all jet layers. The mean section of the water-sheet flow is then given by the product of the water-sheet width d and the sheet height h:

$$h \cdot d = \frac{\dot{Q}_w}{2W} = \frac{1}{8}\pi d_0^2 \frac{W_{0x,o}}{W}. \tag{7.6}$$

As mentioned before, the relative flow velocity W changes with the relative flow velocity W_0 of the jet before entering the bucket (Fig. 7.1b). It also changes with the local peripheral speed according to the invariance equation. This change becomes more sensible, the greater the specific speed of a Pelton turbine is. This is justified by the fact that according to Fig. 5.4 the first full jet cutoff at the bucket position α_b begins rather early. Large variation of the bucket-position angle α then leads to a large variation of the angle γ in Fig. 7.1b and thus to a large variation of the relative flow velocity W_0.

If the ratio $\dot{Q}_c/\dot{Q}_w$ of the absolute flow rate in the jet to the relative flow rate in a rotating bucket is formed, then with $\dot{Q}_c = \pi d_0^2/4 \cdot C_0$ and $\dot{Q}_w$ from Eq. (7.5), one obtains

$$2\lambda = \frac{\dot{Q}_c}{\dot{Q}_w} = \frac{C_0}{C_0 - \omega R_m} = \frac{1}{1 - k_m}. \tag{7.7}$$

This can be considered as the number of buckets that simultaneously react with a jet. It is just of the same form as the flow-rate ratio κ in Eq. (2.8) for the linearly translating bucket. The factor λ is, as in Chap. 5, likewise denoted *multi-bucket factor*. It is calculated according to Eq. (7.7) from the ratio of two volume flow rates, while the multi-bucket factor according to Eq. (5.26) was derived from the geometric relation between the jet and the rotating bucket. Since the peripheral speed coefficient under the nominal operation point of a Pelton turbine is smaller than 0.5 i.e., $k_m < 0.5$, the value for λ must be smaller than 1. For Pelton wheels with very low specific speed, the bucket-position angle α_{o1} tends to zero according to Eq. (2.30). Then Eq. (5.26) is equal to Eq. (7.7). The interaction between the jet and the bucket is then equivalent to the case of a linearly translating bucket.

7.2   Width and Height of the Water Sheet in the Bucket

For the purpose of computing the energy exchange in the relative flow in a rotating bucket (see Chap. 10), most part of the water in the jet can be considered as vertically entering into the bucket according to Fig. 7.3. In a first approximation, the *water-sheet width* in the bucket can be assumed to linearly increase with the distance covered by the flow, that is,

Fig. 7.3 Cross spreading of the jet in a Pelton bucket
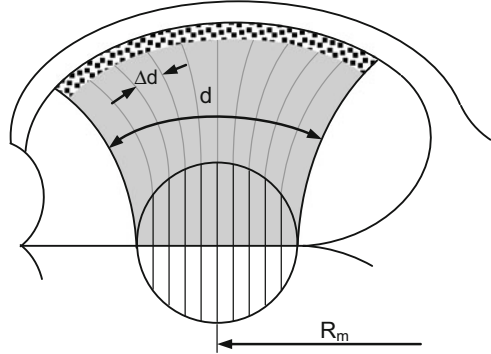
$$d = d_0 + \frac{d_2 - d_0}{S} s, \tag{7.8}$$

where d_2 and S are the water-sheet width at the bucket exit and the trajectory length of the flow from the bucket entry to its exit. At the bucket entry, the water-sheet width is equal to the jet diameter d_0. At the bucket exit, it can be assumed to be 85 % of the bucket width B at the nominal flow rate ($d_{0,\mathrm{N}} \approx B/3$). This assumption results in

$$d_{2,\mathrm{N}} = 0.85B = 0.85 \times 3d_{0,\mathrm{N}} \approx 2.5d_{0,\mathrm{N}}. \tag{7.9}$$

The *water-sheet height h* along the sheet width d, as outlined in Fig. 7.3, can be assumed to be uniform and thus constant. From Eq. (7.6) it follows then that

$$h = \frac{1}{8}\pi d_0^2 \frac{1}{d}\frac{W_{0x,\mathrm{o}}}{W}. \tag{7.10}$$

By assuming perpendicular entry flow, the flow in the bucket approximately follows the path of constant peripheral speed toward the bucket exit. According to the invariance equation and by assuming frictionless flow (Chap. 6), the relative flow velocity W in the rotating bucket remains unchanged, so that $W = W_{0x,\mathrm{o}}$. Equation (7.10) is then simplified as

$$h = \frac{1}{8}\pi d_0^2 \frac{1}{d}. \tag{7.11}$$

For the nominal flow rate with $d_{2,\mathrm{N}} \approx 2.5d_0$, the water-sheet height at the bucket exit is obtained as

$$h_{2,\mathrm{N}} = \frac{\pi}{20} d_0. \tag{7.12}$$

Because the nominal flow rate is also interpreted by $d_0/B = \sqrt{\varphi_B} = \sqrt{0.11}$, see Eq. (2.21), the height of the water sheet at the bucket exit can be expressed as

$$h_{2,N} \approx 0.05B. \tag{7.13}$$

In reality, the water sheet in the center along the sheet width is the thickest. Due to viscous friction, the relative flow velocity along the bucket surface is additionally slowed down by up to 10 % (Chap. 11), so that the water-sheet height correspondingly increases. The real height of the water sheet must be taken into account in order to ensure sound exit flows out of rotating buckets by correctly setting the bucket exit angle. Details about such exit flow conditions will be discussed in Chap. 8.

7.3　Overpressure in the Water Sheet

It has often been indicated that curved streamlines in the bucket flow lead to a pressure increase beneath the water sheet and on the bucket surface. Such a pressure increase can be estimated if the local radius of curvature (r_b) of the bucket surface is known. The pressure p_b on the bucket surface is then calculated according to Eq. (6.10). With respect to the peripheral speed coefficient, as defined in Eq. (2.18), the *overpressure coefficient* of the related overpressure is introduced as

$$c_p = \frac{p_b}{\frac{1}{2}\rho C_0^2} = 2(1 - k_m)^2 \frac{h}{r_b}. \tag{7.14}$$

For the derivation of this formula, the assumption $W = C_0 - U_m$ has been employed, which, basically, only applies for a perpendicular entry of the middle jet layer into the bucket. With the water-sheet height, which has been estimated by Eq. (7.11), the overpressure coefficient then takes the form

$$c_p = (1 - k_m)^2 \frac{\pi}{4} \frac{d_0^2}{r_b d}. \tag{7.15}$$

The orders of magnitude of c_p-values can be estimated in a bucket flow. The bucket form is initially designed for the nominal flow rate, which is given by the jet diameter $d_{0,N}$. At the bottom of the bucket surface, the radius of curvature of the surface profile can be assumed to be about $r_b = 0.55d_{0,N}$ (Fig. 6.3). The water-sheet width d is determined from Eq. (7.8). With $d_{2,N} \approx 2.5d_{0,N}$ and $s \approx S/2$, it then follows $d = 1.75d_{0,N}$. Moreover, with $k_m = 0.47$, the overpressure coefficient on the bucket surface at the bucket bottom is calculated as

$$c_{p,N} \approx 0.23. \tag{7.16}$$

This value corresponds very closely to the measured value by Angehrn (2000) and also to the value recalculated from the measurements of Perrig et al. (2006).

References

Angehrn, R. (2000). Safety engineering for the 423 MW-Pelton-runners at Bieudron. *Proceeding of the 20th IAHR Symposium*, Charlotte, NC.

Perrig, A., Avellan, F., Kueny, J., Farhat, M., & Parkinson, E. (2006). Flow in a Pelton turbine bucket: Numerical and experimental investigations. *Journal of Fluids Engineering, Transactions of the ASME, 128*, 350–358.

Chapter 8
Exit Flow Conditions

In the design of Pelton turbines, it is extremely important to arrange the flow out of the bucket to freely leave the buckets and the Pelton wheel. The exit flow thus contains the kinetic energy which cannot be further exploited and thus will be lost. This type of flow loss is called *swirling loss* (see Chap. 9). The associated exit flow conditions depend on the installation form, geometries, and the operation point of the turbine. They are, for instance, differently specified for horizontal and vertical Pelton turbines. At Pelton turbines with vertical axes, the water out of the upper bucket halves should not drop back onto the Pelton wheel. For this installation form of Pelton turbines, therefore, special exit conditions are required. Before this is discussed in detail, it should first be shown how the exit flow velocity and its distribution generally look like along the trailing edge of a bucket. This serves to derive the general exit flow condition.

8.1 Velocity Distribution at the Bucket Exit

Water flow across the bucket exit is considered here according to Fig. 8.1, where the flow is primarily assumed to laterally traverse the bucket. According to Eq. (6.25), the distribution of the energy invariance across the jet is given by

$$\frac{E_y}{C_0^2} = 1 - 2k_m \left(1 + \frac{y}{R_m} \right), \tag{6.25}$$

in which k_m is the peripheral speed coefficient. Depending on the geometry of the wheel and the operation point, it is possible that jet layers with large y-values have negative energy invariance ($E < 0$). Because, according to the invariance equation given in Eq. (6.18), this negative value must prevail up to the bucket exit, the local relative velocity at the bucket exit is smaller than the local peripheral speed (W_2

Fig. 8.1 General form of velocity distribution at the bucket exit. At sufficiently low peripheral speed coefficient, the condition $E > 0$ and thus $C_{2u} < 0$ can be achieved throughout the bucket exit area
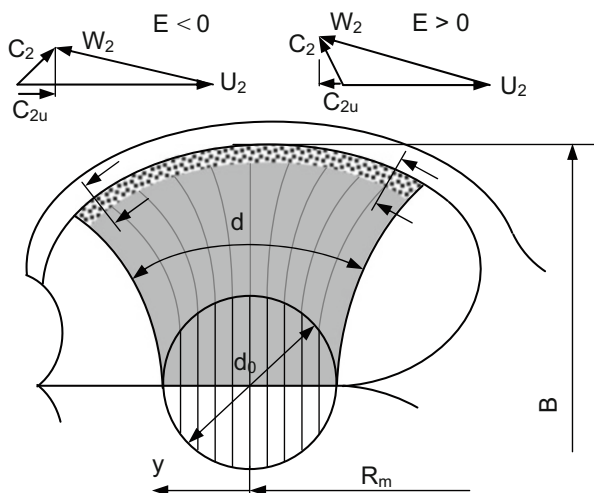
$< U_2$). The corresponding velocity triangle is shown in Fig. 8.1 (upper left). The negative energy invariance simply corresponds to a forward sloping exit flow ($C_{1u} > 0$). Only if the peripheral speed coefficient k_m is sufficiently small, one has $E_y > 0$ for all jet layers. Uniquely, backward sloping exit flow ($C_{2u} < 0$) is then guaranteed along the entire trailing edge of the bucket. That such an exit condition is necessary for Pelton turbines with vertical axes will be shown in Sect. 8.3.

8.2 General Exit Flow Condition

In order to ensure sound and free exit flows out of each bucket without disturbing other buckets, the exit flow velocity C_2 must possess a lateral, i.e., x-component according to Fig. 8.2. Within a limited time interval Δt, a water particle on the free surface of the water sheet then must travel to the side at least the distance of h_a, which is the sum of the water-sheet height and the bucket wall thickness. The *exit flow condition* can therefore be formulated as

$$C_{2x}\Delta t > h_a. \tag{8.1}$$

Since the water sheet is thickest when the turbine is operated at the point of maximum flow rate, the thickness h_a should always be referred to the full load.

Within the time interval Δt, the next bucket moves a distance T_u, whereas the considered water particle travels a distance T_c in the opposite direction. In the critical case, the time Δt in Eq. (8.1) has to be so large that the sum of these two distances is equal to the pitch length between two buckets, that is,

Fig. 8.2 Determination of the flow conditions at the bucket exit
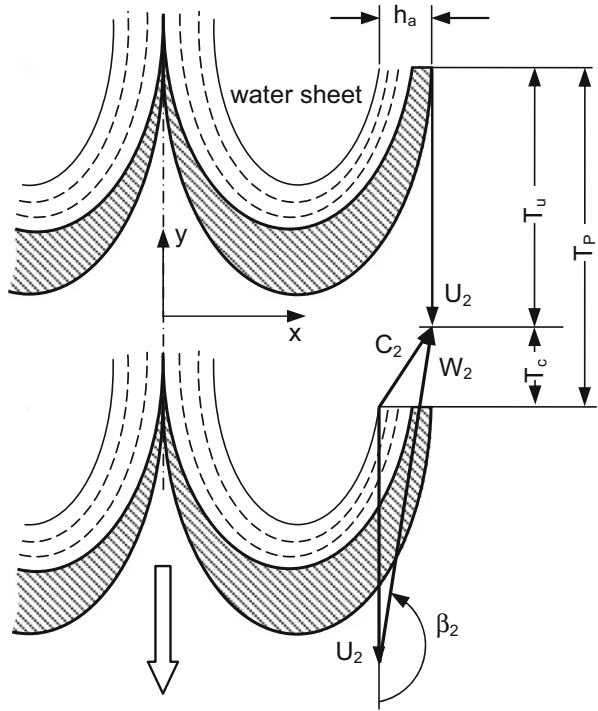
$$T_P = T_u + T_c = (U_2 + C_{2y})\Delta t, \qquad (8.2)$$

which means

$$\Delta t = \frac{T_P}{U_2 + C_{2y}}. \qquad (8.3)$$

According to the velocity triangle shown in Fig. 8.2, one obtains $C_{2y} = W_{2y} - U_2$. Thus, one obtains from Eq. (8.3)

$$\Delta t = \frac{T_P}{W_{2y}}. \qquad (8.4)$$

Inserting this result into Eq. (8.1) with $C_{2x} = W_{2x}$ leads to

$$\frac{h_a}{T_P} \frac{W_{2y}}{W_{2x}} < 1 \qquad (8.5)$$

and because $\tan \beta_2 = -W_{2x}/W_{2y}$ this, finally, yields

$$-\frac{h_{\mathrm{a}}}{T_{\mathrm{P}}}\frac{1}{\tan\beta_2} < 1. \tag{8.6}$$

This is the exit flow condition, which ensures the free flow of water out of each bucket. It can be demonstrated that this condition also applies when the exit flow is forward directed, i.e., $C_{2y} < 0$, according to Fig. 8.2.

The exit flow angle which can be determined from Eq. (8.6) depends on the specific speed of the Pelton turbine. For Pelton turbines of high specific speed (n_{q}), i.e., with relatively tight bucket distribution, the ratio $h_{\mathrm{a}}/T_{\mathrm{P}}$ is correspondingly large. The exit flow angle β_2 must be so configured that the water flow out of the bucket is deflected more to the sides. Quantitatively, this dependence is derived as follows.

Equation (5.30) provides a formula for the number N of Pelton buckets. Based on this, the bucket pitch length T_{P} in Eq. (8.6) is calculated by

$$T_{\mathrm{P}} = \frac{\pi D_{\mathrm{m}}}{N} = \frac{\pi D_{\mathrm{m}}}{15 + 0.62/n_{\mathrm{q}}}. \tag{8.7}$$

The height of the water sheet at the nominal operation point has already been determined by Eq. (7.13). With the assumption that the height of the water sheet is approximately equal to the bucket thickness, so that $h_{\mathrm{a}} = 2h_{2,\mathrm{N}} = 0.1B$, one may deduce from Eq. (8.6)

$$\tan\beta_2 > -\frac{0.1}{\pi}\frac{B}{D_{\mathrm{m}}}\left(15 + \frac{0.62}{n_{\mathrm{q}}}\right). \tag{8.8}$$

For further calculations, Eq. (2.27) is used to replace B/D_{m} by the specific speed n_{q}. Since the nominal flow rate is considered, one has again $\varphi_{\mathrm{B}} = 0.11$. Moreover, for $k_{\mathrm{m}} = 0.47$, one obtains

$$\tan\beta_2 > -(1.2n_{\mathrm{q}} + 0.05) \tag{8.9}$$

or

$$\beta_2 < \pi - \arctan(1.2n_{\mathrm{q}} + 0.05). \tag{8.10}$$

The calculated limits of the bucket exit angle as a function of the specific speed n_{q} are shown in Fig. 8.3. It is evident that for Pelton turbines with large specific speeds, the flow at the bucket exit needs to be more deflected than for Pelton turbines with small specific speeds. It should be noted that both the calculation according to Eq. (8.10) and the graphical presentation in Fig. 8.3 only apply to the bucket thickness which is approximately equal to the height of the water sheet. Thus, Eq. (8.10) only represents an approximation in the practical design of Pelton buckets. To accurately determine the bucket exit angle β_2, the condition of

Fig. 8.3 Bucket exit angle as a function of the specific speed, calculated under the assumption that the bucket thickness equals to the height of the water sheet
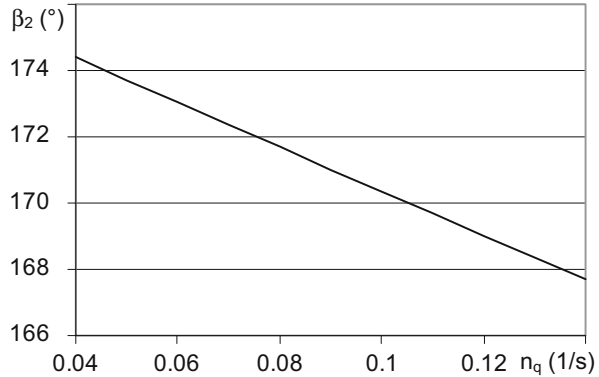
inequality (8.6) should be directly applied. For the height of the water sheet, the approximation $h_{2,N} = 0.06B$ should be used instead of the average value of Eq. (7.13). This is simply so, because the water sheet in the middle along the bucket trailing edge is thickest and the height of the water sheet will additionally get larger owing to the flow deceleration caused by viscous friction. On the other hand, the water leaves the bucket with a so-called exaggeration angle of about $5°$ to $8°$ (known as "Übertreibungswinkel" by Raabe 1989),[1] as compared to the geometric discharge angle $(180° - \beta_2)$. Such an exaggeration angle corresponds to an additional outward deflection of the exit flow and should be taken into account geometrically in the design process of Pelton buckets.

In the above calculations, β_2 is the exit flow angle that should always be measured from the direction of the peripheral speed. Under this condition, the calculations also hold for estimation of the exit flow angle in both the bucket root area and the area at the bucket cutout. According to Eq. (8.6), one must each time use the corresponding bucket pitch length T_P. It is obviously advantageous to show the exit angle relative to the bucket exit edge. For convenience, as shown in Fig. 8.4, the bucket exit edge is represented by a reference line which has a base circle of radius r_a. In this approach, the applied velocity triangles at the bucket cutout, as well as in the root zone, are significantly different from the velocity triangle in the bucket middle section (at D_m). If the inclination of the bucket trailing edge is denoted by δ, then the flow angle β_2' in the region of the bucket cutout is calculated to be

$$\beta_2' = 270° - \delta - \beta_2. \tag{8.11}$$

For example, with $\beta_2 = 173°$ and $\delta = 7°$, it follows $\beta_2' = 90°$. The exit flow in this case is approximately perpendicular to the bucket trailing edge.

In the bucket root area, the exit flow angle β_2' is obtained as

---

[1] This seems to be too large. An exaggeration angle up to $3°$ would be realistic.

Fig. 8.4 Determination of
the bucket exit angle
relative to the bucket
trailing edge
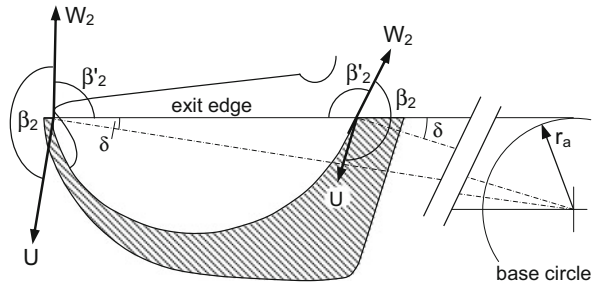
$$\beta_2' = 270° + \delta - \beta_2. \tag{8.12}$$

For $\beta_2 = 165°$ and $\delta = 10°$, one obtains $\beta_2' = 115°$. Relative to the bucket trailing edge, the exit flow is less steep.

8.3   Exit Flow Condition for Vertical Turbines

For vertical Pelton turbines, water in the upper bucket halves exits upwards. In the design and operation of turbines of such an installation form, one must ensure that the exit flow, after leaving the upper bucket halves, still owns sufficient energy to finally leave the Pelton wheel, as shown in Fig. 8.5. A minimum kinetic energy of the exit flow is required for a track distance T against the force of gravity. Two aspects need to be considered:

- Water from the root zone of the buckets has the greatest distance to be covered. This represents the most critical case.
- The exit flow in the vicinity of the bucket cutout must be reverse, i.e., directed against the direction of bucket rotation. This ensures rearward exit flows across the entire field along the bucket trailing edge.

Obviously, both aspects are connected with the peripheral speed coefficient (k_m) of the Pelton turbine. To ensure safe operation of a Pelton turbine, i.e., to fulfill the related exit flow conditions, the peripheral speed coefficient must be set sufficiently low (according to Sect. 8.1). Quantitatively, this will be outlined in the following sections.

8.3.1   Exit Flow Condition at the Bucket Root Zone

To ensure the exit flow to be able to fly over a track distance T, the minimum exit flow velocity C_2 out of a bucket must be determined. The free flight of water after leaving the bucket shall be calculated by taking into account the influence of
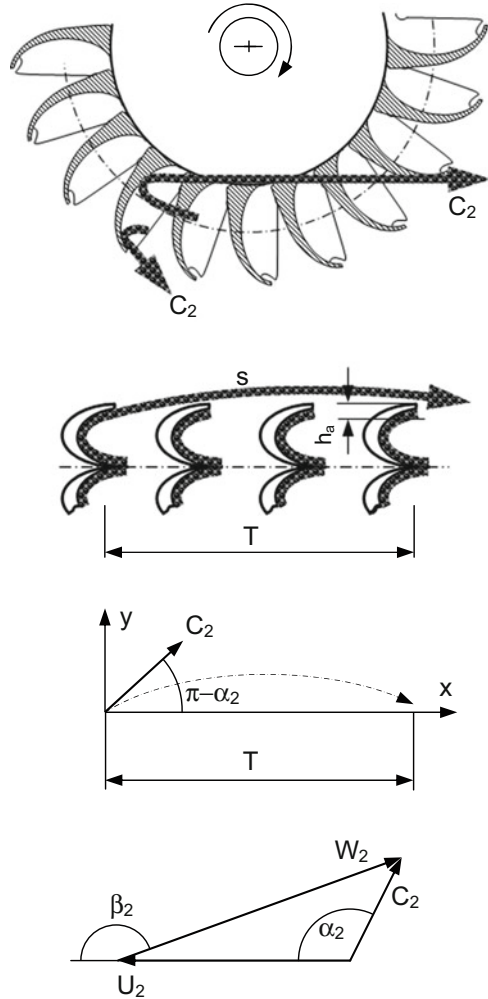
gravity. With respect to the specified coordinate system in Fig. 8.5, the two velocity components of the free flow are given by

$$C_{2x} = C_{2x,0}, \tag{8.13}$$

$$C_{2y} = C_{2y,0} - gt, \tag{8.14}$$

with $C_{2x,0}$ and $C_{2y,0}$ as the respective velocity components initially at the bucket exit.

The trajectory, i.e., the flight path of free flow as a function of time t, is obtained by integrating the above equations to

$$x = C_{2x,0}t, \tag{8.15}$$

$$y = C_{2y,0}t - \frac{1}{2}gt^2. \tag{8.16}$$

The trajectory is then given in the form $y = f(x)$. For the free flight of water over the distance $x = T$, the following condition must be fulfilled:

$$y = f(T) > h_a. \tag{8.17}$$

Here, according to Fig. 8.5, h_a represents the sum of the water-sheet height and the bucket wall thickness.

The condition specified in Eq. (8.17) is applied to Eqs. (8.15) and (8.16). It follows then that

$$T = C_{2x,0}t, \tag{8.18}$$

$$h_a = C_{2y,0}t - \frac{1}{2}gt^2. \tag{8.19}$$

Eliminating the time t, and with $\tan \alpha_2 = -C_{2y,0}/C_{2x,0}$, the velocity component $C_{2x,0}$ is determined by

$$C_{2x,0}^2 = -\frac{1}{2}\frac{gT}{\frac{h_a}{T} + \tan \alpha_2}. \tag{8.20}$$

It represents the minimum velocity component of the exit flow and should be applied to the bucket root zone because there, the maximum flight distance has to be covered.

On the other hand, one may raise the question how, according to Eq. (8.20), the smallest exit velocity can be reached at all. According to Sect. 8.1, the peripheral speed coefficient k_m has to be set sufficiently small. The actual exit velocity at the bucket root zone should then be compared with the required minimum value in Eq. (8.20). For this reason, the law of sines for the velocity triangle according to Fig. 8.5 is applied, so that

$$C_2 = \frac{\sin \beta_2}{\sin \alpha_2}W_2 \tag{8.21}$$

or in the form of velocity component as

$$C_{2x,0} = -C_2 \cos \alpha_2 = -\frac{\sin \beta_2}{\tan \alpha_2}W_2. \tag{8.22}$$

The related task is to determine the relative velocity in the region of the bucket root (W_2) as well as the flow angle α_2, both in Eq. (8.20) and Eq. (8.22) as functions of the peripheral speed coefficient. For this purpose, the invariance equation is again

applied. For the real flow, according to Fig. 8.1, it is assumed that the water in the jet layer $y = -d_0/2$ will reach the bucket root. The energy invariance of this jet layer is given, according to Eq. (6.25) with $D_m = 2R_m$, by

$$\frac{E_{-d_0/2}}{C_0^2} = 1 - 2k_m\left(1 - \frac{d_0}{D_m}\right).$$

(8.23)

Since the energy invariance $E_{-d_0/2}$ holds up to the bucket exit (subscript 2), one obtains from Eq. (8.23)

$$\frac{W_2^2 - U_2^2}{C_0^2} = 1 - 2k_m\left(1 - \frac{d_0}{D_m}\right).$$

(8.24)

The corresponding relative flow velocity is then given by

$$\frac{W_2^2}{C_0^2} = \frac{U_2^2}{C_0^2} + 1 - 2k_m\left(1 - \frac{d_0}{D_m}\right).$$

(8.25)

With the peripheral diameter D_2 at the bucket root and further because of $\frac{U_2}{C_0} = \frac{U_m}{C_0} \cdot \frac{U_2}{U_m} = k_m\frac{D_2}{D_m}$, this implies

$$\frac{W_2^2}{C_0^2} = k_m^2\left(\frac{D_2}{D_m}\right)^2 + 1 - 2k_m\left(1 - \frac{d_0}{D_m}\right).$$

(8.26)

Inserting this equation into Eq. (8.22), one obtains

$$\frac{C_{2x,0}}{C_0} = -\frac{\sin\beta_2}{\tan\alpha_2}\sqrt{k_m^2\left(\frac{D_2}{D_m}\right)^2 + 1 - 2k_m\left(1 - \frac{d_0}{D_m}\right)}.$$

(8.27)

This is the determining equation for the exit velocity at the bucket root zone, where only the flow in the jet layer $y = -d_0/2$ arrives (Fig. 8.1). It is shown above as a function of the peripheral speed coefficient. On the other hand, in order to determine the required peripheral speed coefficient under the condition of Eq. (8.20), the exit flow angle α_2, both in Eq. (8.20) and Eq. (8.27), should also be shown as a function of the peripheral speed coefficient. For this purpose, the law of sines is applied to the velocity triangle in Fig. 8.5:

$$\frac{W_2}{\sin\alpha_2} = \frac{U_2}{\sin(\beta_2 - \alpha_2)} = \frac{U_2}{\sin\beta_2\cos\alpha_2 - \cos\beta_2\sin\alpha_2}.$$

(8.28)

Thus, one obtains

$$\tan \alpha_2 = \frac{\sin \beta_2}{\frac{U_2}{W_2} + \cos \beta_2} \tag{8.29}$$

or with $\frac{U_2}{C_0} = k_\mathrm{m} \frac{D_2}{D_\mathrm{m}}$:

$$\tan \alpha_2 = \frac{\sin \beta_2}{k_\mathrm{m} \frac{D_2}{D_\mathrm{m}} \frac{C_0}{W_2} + \cos \beta_2}. \tag{8.30}$$

In this equation, W_2/C_0 has already been given by Eq. (8.26), so that the relation $\alpha_2 = f(k_\mathrm{m})$ is principally also known.

The above calculations clearly form a system of closure equations which enables the upper limit of the peripheral speed coefficient to be determined. They can be easily performed in the tabulated numerical form, as presented in the following example. The example clearly shows that the exit condition, given by Eq. (8.20), is commonly well satisfied at all Pelton turbines.

Example
A Pelton turbine is considered as follows:

- Bucket width ratio $B/D_\mathrm{m} = 0.25$,
- Bucket root diameter ratio $D_2/D_\mathrm{m} = 0.65$,
- Exit flow angle in the bucket root zone $\beta_2 = 170°$,
- Distance to be covered by the exit flow $T = 1.5\,\mathrm{m}$,
- Thickness ratio $h_\mathrm{a}/T = 0.025$,
- Hydraulic head $H = 300\,\mathrm{m}$.

Let us consider nominal flow rate, which is given by the jet diameter $d_0 = B/3$. The terms of d_0/D_m in Eqs. (8.26) and (8.27) will then be replaced by $\frac{1}{3}B/D_\mathrm{m}$. Table 8.1 shows the related computational process and comparison with the required exit flow velocity. In the last line, the relevant applied equations are given.

When calculating the angle α_2 in Table 8.1, it must be observed that for $\tan \alpha_2 < 0$, the angle α_2 must be larger than 90°. Accordingly, it follows from Eq. (8.29) that

$$\alpha_2 = \pi + \arctan\left(\frac{\sin \beta_2}{U_2/W_2 + \cos \beta_2}\right). \tag{8.31}$$

Furthermore, the velocity ratio U_2/W_2 is calculated from

$$\frac{U_2}{W_2} = \frac{C_0}{W_2} \frac{U_\mathrm{m}}{C_0} \frac{D_2}{D_\mathrm{m}} = k_\mathrm{m} \frac{D_2}{D_\mathrm{m}} \frac{C_0}{W_2}. \tag{8.32}$$

Corresponding computational results are illustrated in Fig. 8.6. Obviously, the condition for free flight of water from the bucket root zone is satisfied by far for all values of k_m. Although this is only an example, the corresponding condition is expected to be fulfilled also at all other Pelton turbines. This can be easily and

Table 8.1   Actual exit flow velocity in the bucket root zone in comparison with the desired values

k_m	W_2/C_0	U_2/W_2	$\alpha_2(°)$	$(C_{2x}/C_0)_{real}$	$(C_{2x}/C_0)_{desired}$
0.44	0.52	0.55	158.4	0.231	0.058
0.45	0.51	0.57	157.1	0.210	0.056
0.46	0.50	0.60	155.6	0.190	0.054
0.47	0.48	0.63	153.6	0.169	0.052
Eqs.	(8.26)	(8.32)	(8.31)	(8.27)	(8.20)

Fig. 8.6 Real and minimum required exit flow velocity in the root zone of the bucket
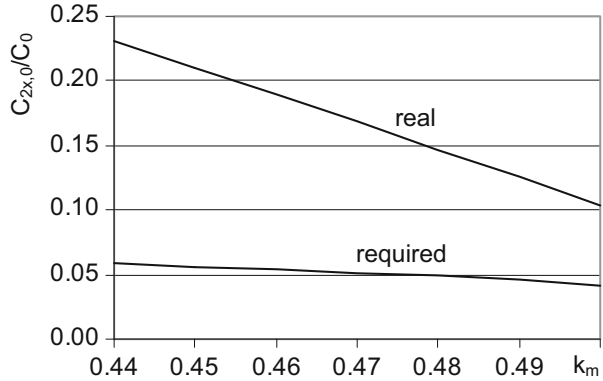
quickly confirmed by changing all relevant parameters in the executed tabular calculations. For this reason, it can be concluded that the exit flow in the bucket root zone is always sufficiently energetic to cover the distance T. The influence of the thickness ratio h_a/T in Eq. (8.20) is actually negligible.

The above consideration applies for the safe exit flow of water from the upper bucket halves. When the exit flow condition is very unfavorable, the upper and the lower bucket halves can be designed differently, as the lower bucket halves are free from any restrictions. Such a design of Pelton buckets, however, has not yet been implemented practically. The reason for this is evidently that spray water actually only slightly affects the hydraulic performance of a Pelton turbine, as will be shown in Sect. 8.3.3.

8.3.2   Exit Flow Condition at the Bucket Cutout

According to Fig. 8.5, it is, in particular, indispensable that the absolute exit flow velocity in the region of bucket cutout is also directed backwards. Quantitatively, this means that the energy invariance of the outermost jet layer ($y = d_0/2$, see also Fig. 8.1) must be positive. This means, in turn, that the energy invariance of the entire jet has to be greater than zero. For the outermost jet layer with $y = d_0/2$, one then obtains from Eq. (6.28) a new condition, namely,

Fig. 8.7 Maximum peripheral speed coefficient for the safe flight of exit flow in the area of the bucket cutout for turbines with vertical axes
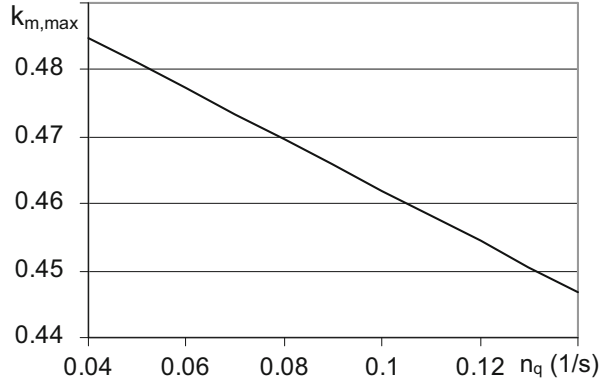
$$\frac{E_b}{C_0^2} = (1 - 2k_m) - \frac{n_q}{1.32} > 0. \tag{8.33}$$

From this, the maximum peripheral speed coefficient is obtained as

$$k_{m,max} = 0.5 - 0.38n_q. \tag{8.34}$$

This condition indicates that for Pelton turbines of high specific speeds, the peripheral speed coefficient k_m should be significantly reduced (Fig. 8.7). For a moderate specific speed of $n_q = 0.1$, for instance, the peripheral speed coefficient ought to be reduced approximately to $k_m = 0.46$. This value exactly corresponds to the real operation point of a Pelton turbine and thus has been successfully validated in practice.

Since the required peripheral speed coefficient, according to Eq. (8.34), is significantly smaller than 0.5, the former condition for safe flight of water from the bucket root over the Pelton wheel (Sect. 8.3.1) has been automatically satisfied. The peripheral speed coefficient, according to Eq. (8.34), thus ensures safe flight of all water, after leaving the bucket, over the Pelton wheel. Equation (8.34), therefore, can be considered as the design criterion for vertical Pelton turbines.

The requirement of the peripheral speed coefficient $k_m < 0.5$, as confirmed here by regarding the free flight of exit flow, is likely the second reason why the peripheral speed coefficient has always been confirmed to be smaller than 0.5. This is true, at least for vertical Pelton turbines. The first reason for choosing $k_m < 0.5$ arises from the coincidence and symmetry conditions (Sect. 5.4).

8.3.3 Impact of Spray Water When $k_m > k_{m,max}$

It has been shown that for free flight of exit flow, the condition $k_m \leq k_{m,max}$ has to be fulfilled. When $k_m > k_{m,max}$, part of the exit flows from the upper bucket halves will fall back on the Pelton wheel and get accelerated maximally to the circumferential

speed of the wheel U_{m}. The connected specific energy cost is $\frac{1}{2}U_{\mathrm{m}}^2$. When related to the specific energy $\frac{1}{2}C_0^2$ of the jet, the corresponding hydraulic loss is calculated to be $\Delta\eta_{\mathrm{i}} = k_{\mathrm{m}}^2$. Furthermore, it is assumed that about 5 % of all water from the upper bucket halves, i.e., 2.5 % of the total water flow in a turbine, leaves the Pelton wheel incorrectly and thus causes a loss of $\Delta\eta_{\mathrm{i}} = k_{\mathrm{m}}^2$. The total loss in the system efficiency will for $k_{\mathrm{m}} = 0.5$ be at most

$$\Delta\eta = 0.025 \cdot \Delta\eta_{\mathrm{i}} = 0.025 \cdot k_{\mathrm{m}}^2 \approx 0.6\,\%. \tag{8.35}$$

This loss is quite negligible. The method presented here can also be used to estimate the efficiency loss due to violent splashing water, which could at most again be accelerated to U_{m} by the Pelton wheel. It applies not only to vertical but also to horizontal turbines. In conclusion, the efficiency loss due to violent splashing water is usually no more than 1 %.

Since a small amount of water which drops back to the Pelton wheel has no severe consequences, the real peripheral speed coefficient may slightly exceed the maximum value given by Eq. (8.34). This will lead to a bit increase in the hydraulic efficiency because of reduction of exit swirling losses.

Reference

Raabe, J. (1989). *Hydraulische Maschinen und Anlagen*. VDI Verlag.

Chapter 9
Exit Flows and Hydraulic Losses

In order to calculate and enhance the system efficiency of a Pelton turbine, it is essential to know which hydraulic and mechanical losses exist and how they can be estimated and above all successfully reduced. The efficiency of a Pelton turbine has so far been almost exclusively determined through measurements which are either restricted to thermodynamic measurements directly taken in a power plant according to the standard IEC60041 or by model tests according to IEC60193. From such measurements, however, it is not readily possible to obtain detailed information on the effectiveness of each individual flow process in a Pelton turbine and to make statements about individual losses like swirling and exit losses, flow friction losses, mechanical windage, bearing friction losses, etc. Except for a few empirical equations pertinent to the mechanical losses, there has been hardly any available and reliable method to determine all relevant hydro-mechanical losses.

It is, therefore, significant to be able to separately quantify each individual loss in each flow process in a Pelton turbine. As the first step to assess all possible partial losses, both the swirling loss involved in exit flow out of the rotating buckets and the loss resulting from the disturbance of the exit flow will be calculated in this chapter. Other types of losses enumerated above will be treated in the subsequent chapters.

9.1 Swirling Losses

Swirling loss is related to the exit flow out of the rotating buckets and around the Pelton wheel. It arises because of the existence of rest kinetic energy which is still found in the exit flow. For a linearly translating bucket as a special case, such an exit loss has already been accounted for in efficiency calculations according to Eq. (2.16). To estimate the analogous loss in a Pelton turbine, Eq. (2.40) is applied which was simply taken over directly from the computational model of a linearly translating bucket. It implies the percentage of conversion of energy which exists in

a jet in the form of kinetic energy. For frictionless flows the hydraulic efficiency would be 100 % if the swirling loss were zero.

In Pelton turbines, the exit flow out of each rotating bucket is so arranged that it frees the way for the next bucket. The related criteria have already been worked out in Sects. 8.2 and 8.3. The swirling loss, thus, represents the unexploited kinetic energy which is present in the exit flow. The characteristic parameters for this sort of losses is the peripheral speed coefficient k_m.

Compared with the flow model of a linearly translating bucket at which all water particles have equal speed ratio ($k = U/C_0$), the flow model of a Pelton turbine is quite different. Because of the bucket rotation, each water particle in the jet has assigned its individual entry (time and position) at the bucket and therefore an individual ratio of velocities U/C_0 as well as its individual exit flow out of the bucket. Consequently, the overall power as well as the efficiency of the jet must be determined from summation of the individual contributions of all water particles. It is quite possible that the resulting hydraulic efficiency more or less differs from that calculated based on Eq. (2.40).

In order to determine the swirling losses, let the velocity triangle of the exit flow out of a bucket be considered as in Fig. 9.1. With the aid of cosine law, the absolute velocity is calculated as

$$C_2^2 = W_2^2 + U_2^2 + 2W_2U_2 \cos\beta_2. \tag{9.1}$$

The associated kinetic energy, as said above, is referred to as the swirling loss and expressed in terms of the efficiency loss as

$$\Delta\eta_{\text{swirl}} = \frac{C_2^2}{C_0^2}. \tag{9.2}$$

For the swirling loss and according to Eq. (9.1), the water particles in a jet, finally, differ from each other in the exit flow (U_2 and β_2). In this respect, the flow property of a water particle is first considered under the application of the invariance equation. For a water particle in the jet layer which is located by h_s, according to Fig. 6.4, the invariance equation is obtained from Eq. (6.23) as

$$E = W_2^2 - U_2^2 = C_0^2 - 2h_s\omega C_0. \tag{9.3}$$

From this equation, the term W_2^2 and, therefore, the velocity W_2 can be resolved and then inserted into Eq. (9.1). The absolute velocity at the bucket exit is, thus, given by

$$C_2^2 = C_0^2 + 2U_2^2 - 2h_s\omega C_0 + 2U_2 \cos\beta_2\sqrt{C_0^2 - 2h_s\omega C_0 + U_2^2}, \tag{9.4}$$

and the swirling loss of the considered particle is then calculable from Eq. (9.2) and yields

Fig. 9.1 Exit velocity triangle
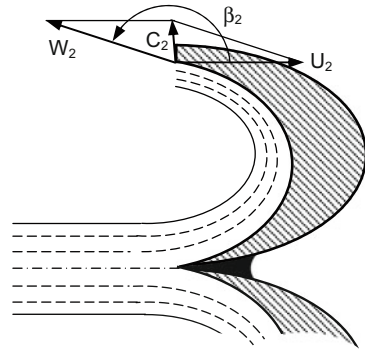
$$\Delta\eta_{\text{swirl}} = 1 - \frac{2}{C_0^2}\left(h_s\omega C_0 - U_2^2 - U_2\cos\beta_2\sqrt{C_0^2 - 2h_s\omega C_0 + U_2^2}\right). \quad (9.5)$$

If the peripheral speed U_2 in this equation is in the following replaced by $U_2 = (R_2/R_m)U_m$ and the peripheral speed coefficient $k_m = U_m/C_0$ is used, then

$$\Delta\eta_{\text{swirl}} = 1 - 2k_m\left(\frac{h_s}{R_m} - k_m\frac{R_2^2}{R_m^2} - \frac{R_2}{R_m}\cos\beta_2\sqrt{1 - 2k_m\frac{h_s}{R_m} + k_m^2\frac{R_2^2}{R_m^2}}\right) \quad (9.6)$$

is obtained. Thanks to the use of the invariance equation, the swirling loss is independent of the location and time when water particles enter the bucket. Only the site h_s of the jet layer is relevant. As soon as a jet layer and the peripheral speed coefficient k_m of a Pelton turbine are specified, then in accordance with Eq. (9.6), the swirling loss is only a function of the particle exit position and the corresponding exit flow angle, viz.,

$$\Delta\eta_{\text{swirl}} = f\left(\frac{R_2}{R_m}, \beta_2\right). \quad (9.7)$$

More on this dependence will be said below.

9.1.1 Influence of Exit Positions of Water Particles

The impact of exit positions (R_2) of water particles on the swirling loss according to Eq. (9.6) is shown in Fig. 9.2 for the case of an exit flow angle $\beta_2 = 170°$. Evidently, the influence of the particle exit positions on the swirling loss is rather insignificant compared with the influence of jet layer positions. For efficiency calculations, therefore, it is sufficient to only consider the mean value $R_2/R_m = 1$.

Fig. 9.2 Dependence of the hydraulic efficiency on the jet layer position and for different exit flows out of the bucket ($k_m = 0.47, \beta_2 = 170°$)
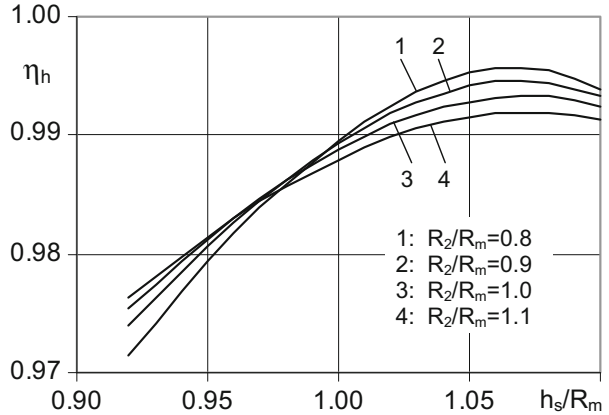
9.1.2 Influence of the Exit Flow Angle

Figure 9.3 shows the influence of the exit flow angle β_2 on the swirling loss. When changing the exit flow angle from $\beta_2 = 172°$ to $\beta_2 = 168°$, the swirling loss increases by approximately 0.6 %. In the practical design of Pelton buckets, the exit flow angle along the main trailing edge of buckets only changes insignificantly ($\Delta\beta_2 < 2°$). Thus, it is reasonable to use the exit flow angle at the periphery $R_2/R_m = 1$ to calculate the swirling losses. This is also justified because from required exit flow conditions, which have been depicted by Eq. (8.6) or (8.10) in Sect. 8.2, the calculated exit angle β_2 can be applied for the entire area along the main trailing edge of the bucket ($\beta_2 = $ const).

Calculations show that swirling losses in a Pelton turbine are only of the order of about 1 % of the total generated energy.

If only the jet layer in the vicinity $h_s/R_m \approx 1$ is considered and the exit position $R_2/R_m \approx 1$ is assumed, then Eq. (9.6) is simplified to

$$\Delta\eta_{swirl} = 1 - 2k_m(1 - k_m)(1 - \cos\beta_2). \tag{9.8}$$

The second term on the right-hand side of this equation is formally identical to Eq. (2.40), which as the hydraulic efficiency applies to the entire jet.

The influence of the exit flow angle on the swirling loss can also be represented as the influence of the discrepancy of the exit flow angle from $\beta_2 = 180°$. Because $\Delta\beta_2 = 180° - \beta_2$ and, thus, $\cos\beta_2 = -\cos\Delta\beta_2 \approx -\left(1 - \frac{1}{2}\Delta\beta_2^2\right)$ for small values of $\Delta\beta_2$, Eq. (9.8) is reformulated for $k_m = 0.5$ to

$$\Delta\eta_{swirl} \approx \frac{1}{4}\Delta\beta_2^2. \tag{9.9}$$

Fig. 9.3 Dependence of the hydraulic efficiency on the jet layer position for different flow angles at the bucket exit ($k_m = 0.47$, $R_2/R_m = 1$)
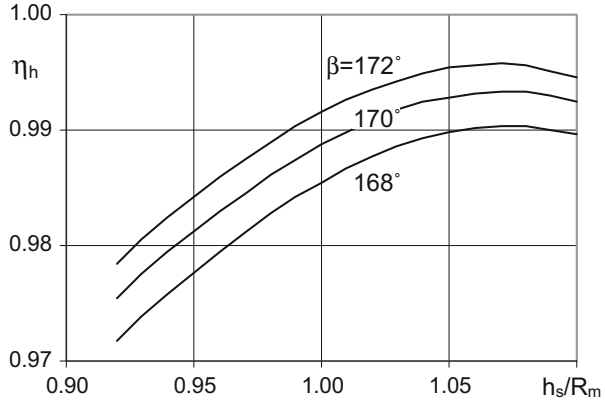
For $\Delta\beta_2 = 8°$, for instance, one obtains a swirling loss of approximately 0.5 %. If $\Delta\beta_2 = 10°$ is accepted, the swirling loss changes to 0.75 %. Obviously, a change in the exit flow angle by $2°$ thus will cause a change in the efficiency by about 0.25 %.

9.1.3   Influence of Jet Layer Positions

From the above considerations, it can be concluded that all water particles in the same jet layer are subjected to the same swirling loss. According to Eq. (9.6), the difference from one jet layer to another is solely due to the difference in $k_m h_s/R_m$. Among all jet layers, the one that minimally contributes to the swirling loss may be found by setting $\mathrm{d}(\Delta\eta_{\mathrm{swirl}})/\mathrm{d}h_s = 0$. It then follows from Eq. (9.6) that

$$k_m \frac{h_s}{R_m} = 0.5 + \frac{1}{2}k_m^2 \frac{R_2^2}{R_m^2}\sin^2\beta_2. \qquad (9.10)$$

Since the second term on the right-hand side of this equation is negligibly small, there follows immediately

$$k_m \frac{h_s}{R_m} = 0.5. \qquad (9.11)$$

This relation has indeed already been confirmed in Figs. 9.2 and 9.3, where for $k_m = 0.47$ the minimum swirling loss is found at the jet layer $h_s/R_m = 1.06$.

Fig. 9.4 Scheme for
integrating the hydraulic
efficiency of a jet
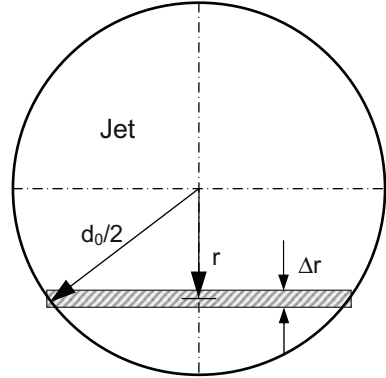
9.1.4   Swirling Loss of the Entire Jet

The swirling loss of an individual jet layer has been calculated by Eq. (9.6), where a
mean exit flow angle β_2 and $R_2/R_\mathrm{m} = 1$ can be assumed. The swirling loss of a
complete jet is determined by means of the following integration with an area-
weighting factor according to Fig. 9.4 of

$$\Delta\eta_\mathrm{swirl} = \frac{8}{\pi d_0^2} \int_{-d_0/2}^{d_0/2} \Delta\eta \sqrt{\left(\frac{d_0}{2}\right)^2 - r^2} \cdot \mathrm{d}r. \tag{9.12}$$

By dividing the jet into n layers, the above equation is simply converted to a
summation form as follows:

$$\Delta\eta_\mathrm{swirl} = \frac{8\Delta r}{\pi d_0^2} \sum_{i=1}^{n} \Delta\eta_i \sqrt{\left(\frac{d_0}{2}\right)^2 - r_i^2}. \tag{9.13}$$

In this calculation, considering the area fraction of each jet layer, the term
$\frac{8\Delta r \sqrt{(d_0/2)^2 - r_i^2}}{\pi d_0^2}$ behaves as a weighting factor.

Comparison between the swirling loss which is calculated by Eq. (9.13) and that
from Eq. (2.40) shows a difference of about 0.2 %, as illustrated in Fig. 9.5 for a
computational example.

9.2   Friction Effect on the Bucket Rear Side

In Chap. 8, exit flow conditions have been worked out for conditions of the free
flight of the exit flows. According to Eq. (8.6), the geometric exit flow angle β_2, for
instance, must be sufficiently smaller than 180°. On the other hand, the swirling

Fig. 9.5 Comparison
between efficiencies
resulting from the direct
calculation (simplified) and
the calculation based on the
jet layer method
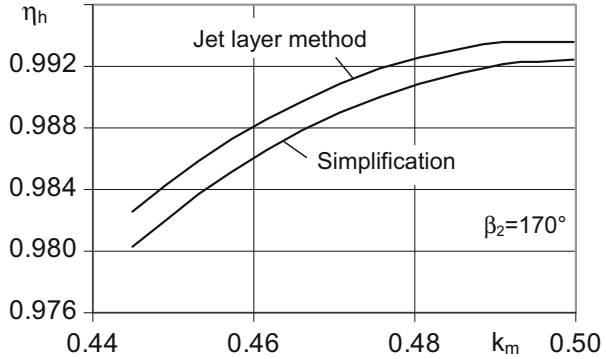
loss, according to Eq. (9.9), increases with an increase of the deviation angle
$180° - \beta_2$. In practical designs, the geometric deviation angle $180° - \beta_2$ has
often been chosen about $2°$ smaller than that obtained from Eq. (8.6). The possible
consequence is the deterioration of the free flight of the exit flows. Because traces of
wear have sometimes been observed on the bucket back side, it is necessary to
quantify the effect of the exit flow impingement on the rear side of the next bucket
(Fig. 9.6). On the one hand, water impingement slows down the bucket motion due
to viscous friction on the grinding area. On the other hand, the flight path of exit
flows will be deflected by the back side of the subsequent bucket. Both actions
cause additional losses and, thus, reduce the overall efficiency of the Pelton turbine.
The friction effect is analyzed in this section, and the deflection effect will be
treated in the next section.

The relative water velocities between the exit flows and the rotating buckets are
assumed to be $W_2 = C_0 - U_\mathrm{m}$. With the friction coefficient c_f, the shear stress on
the grinding area is obtained as

$$\tau = c_\mathrm{f}\frac{1}{2}\rho W_2^2 = c_\mathrm{f}\frac{1}{2}\rho(C_0 - U_\mathrm{m})^2, \qquad (9.14)$$

which, owing to $k_\mathrm{m} = U_\mathrm{m}/C_0$, can further be expressed as

$$\tau = c_\mathrm{f}\frac{1}{2}\rho C_0^2(1 - k_\mathrm{m})^2. \qquad (9.15)$$

The grinding area on the bucket rear side is supposed to be A_f, as shown in Fig. 9.6.
According to Eq. (7.7), the number of buckets which simultaneously undergo the
interaction with one jet is given by $2\lambda = 1/(1 - k_\mathrm{m})$ (with λ as multi-bucket factor).
With respect to two grinding areas at each bucket, the total friction force under a
full jet is, thus, obtained as

Fig. 9.6 Exit flow out of
the bucket and impingement
on the bucket behind

Grinding area A_f
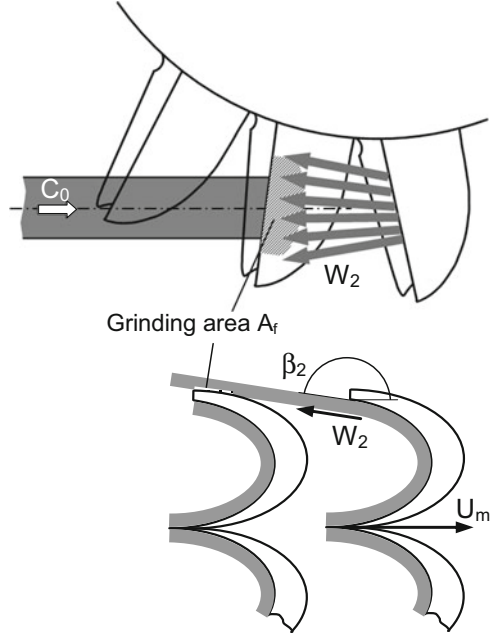
$$F_f = 2\tau A_f \cdot (2\lambda) = c_f(1 - k_m)\rho C_0^2 A_f. \tag{9.16}$$

Taking into account the angle between the friction force and the bucket speed, the
power required to overcome this friction force is given by

$$P_f = F_f U_m \cos(\pi - \beta_2) = c_f(1 - k_m)\rho C_0^2 A_f U_m \cos(\pi - \beta_2). \tag{9.17}$$

When related to the jet power $P_0 = \frac{1}{2}\rho C_0^2 \cdot A_0 C_0$, the resulting efficiency loss is
obtained. With $\cos(\pi - \beta_2) \approx 1$, it takes the form

$$\Delta\eta_f = \frac{P_f}{P_0} = 2c_f k_m(1 - k_m)\frac{A_f}{A_0}. \tag{9.18}$$

For making a quantitative evaluation of this type of friction effects, the friction
coefficient is assumed to be $c_f = 0.02$. With $k_m = 0.5$, as well as an area ratio
$A_f/A_0 = 0.5$, the associated efficiency drop is obtained as

$$\Delta\eta_f = 0.005. \tag{9.19}$$

It amounts to approximately 0.5 %.

9.3   Deflection Effect on the Bucket Rear Side

The impingement of the exit flow on the rear side of the following bucket exerts additionally a *deflection effect* as illustrated in Fig. 9.7. The deflection of the flow is always associated with a force directed against the flow. This means that the bucket receives an opposite force which tends to retard the bucket motion. To determine the associated efficiency loss, the law of momentum is applied in the coordinate system $\xi - \eta$ which rotates, according to Fig. 9.7, with the rotating buckets. The impingement of exit flow on the subsequent bucket rear side is considered in the rotating system. With the relative flow velocity W_2, the momentum flow rate of the exit flow before deflection is given by $I = \rho(\dot{Q}_w/2) \cdot W_2$, where the flow rate $\dot{Q}_w /2$ is referred to a half of the bucket. The force acting on the flow and, thus, causing the flow to be deflected is represented by the force components F_ξ and F_η. The deflection of the flow is denoted by the deflection angle δ. Then, both force components can be calculated by applying the law of momentum as

$$F_\xi = \frac{1}{2}\rho\dot{Q}_w W_2 \sin\delta, \tag{9.20}$$

$$F_\eta = \frac{1}{2}\rho\dot{Q}_w W_2(\cos\delta - 1). \tag{9.21}$$

The component of the force, which is oriented towards the bucket-motion direction, i.e., the direction of peripheral speed, is given by a coordinate transformation

$$F_u = -F_y = -\left(F_\eta \cos\theta - F_\xi \sin\theta\right), \tag{9.22}$$

with $\theta = \pi - \beta_2$. This is an opposite obstacle force which the bucket motion has to overcome. The required power is given by multiplying this resistance force by the peripheral speed of the Pelton wheel as

Fig. 9.7 Deflection of the exit flow on the bucket rear side
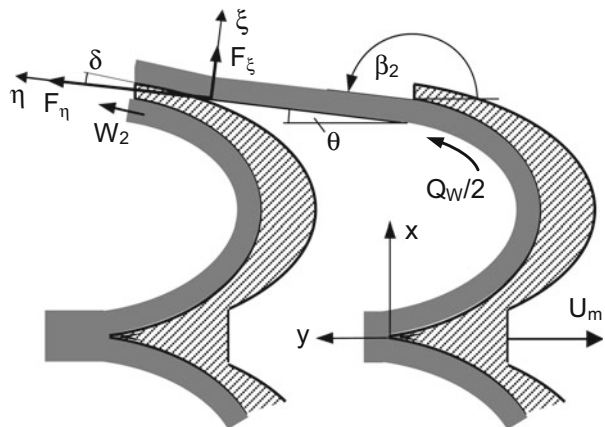
$$P_{\text{deflect}} = F_u U_m = \frac{1}{2}\rho \dot{Q}_w U_m W_2[\cos\theta - \cos(\theta+\delta)]. \tag{9.23}$$

The corresponding specific work is then given by

$$e_{\text{deflect}} = \frac{P_{\text{deflect}}}{\rho \dot{Q}_w/2} = W_2 U_m[\cos\theta - \cos(\theta+\delta)]. \tag{9.24}$$

Referring to the specific energy of the jet and with the assumption that $W_2 = C_0 - U_m$, the efficiency loss associated with the flow deflection takes the form

$$\Delta\eta_{\text{deflect}} = \frac{e_{\text{deflect}}}{C_0^2/2} = 2k_m(1-k_m)[\cos\theta - \cos(\theta+\delta)]. \tag{9.25}$$

Here, $k_m = U_m/C_0$ has again been used.

In order to make a quantitative estimation of the associated efficiency loss, two angles $\theta = 10°$ and $\delta = 4°$, as well as the peripheral speed coefficient $k_m = 0.5$, are assumed. It then follows from Eq. (9.25) that

$$\Delta\eta_{\text{deflect}} = 0.7\,\%. \tag{9.26}$$

At this point, it is worth mentioning the swirling loss, which has been considered in Sect. 9.1 and is given by Eq. (9.8) in its simplest form. If Eq. (9.25) is added to Eq. (9.8), there follows, with $\beta_2 = \pi - \theta$,

$$\Delta\eta_{\text{swirl}} + \Delta\eta_{\text{deflect}} = 1 - 2k_m(1-k_m)[1 + \cos(\theta+\delta)]. \tag{9.27}$$

This may be considered to be the total swirling loss existing in the exit flow. It is just equal to that value which is obtained by directly using the flow angle $(\theta+\delta)$ at the bucket exit.

In the above analysis, it has been tacitly assumed that the entire exit flow is deflected by an angle δ. If the amount of water being deflected on the rear side of the buckets is 50 % of the total amount of water, the associated partial efficiency loss will be reduced by 50 %.

The efficiency loss associated with the described flow deflection has been considered here as a partial loss. Another partial loss has already been discussed in Sect. 9.2. Since the sum of these two losses is not vanishingly small compared to the swirling loss, flow impingement on the bucket rear side should be avoided as much as possible. This means that the exit flow angle θ, i.e., $\beta_2 = \pi - \theta$ according to Fig. 9.7, should be designed without causing any flow impingement at the following bucket. For this reason it will be likely acceptable at the angle θ, i.e., β_2 to have a tolerance of about 1° to 2°, so that, for instance, $\beta_2 = 170°$ rather than $\beta_2 = 172°$ can be applied. The resulting increase in the swirling loss, according to Eq. (9.9), is only about 0.25 %.

Chapter 10
Friction Effects and FFT Theorem

Water in nature is a viscous fluid and adheres to solid surfaces when coming in contact with another material. In Pelton turbines, this viscous adhesion occurs in the form of frictional shear stresses between the moving water and the bucket surface. It has a direct consequence of slowing down the relative flow in the rotating bucket. The friction in the bucket flow additionally acts as both a positive driving and negative braking force on the rotation of Pelton wheel.

The friction effect on hydraulic efficiencies of Pelton turbines happens, according to Zhang and Müller (2006) and Zhang (2007), by the following mechanisms:

1. The friction force in the frontal part of the flow path of the bucket acts as a positive driving and afterward as a negative braking force. Correspondingly, the mechanical work done by the friction forces is first positive and then negative. In practical applications, however, there is no need to distinguish between them.
2. The friction on the surface of the bucket slows down the relative flow velocity along the bucket surface. This in turn reduces the intensity of the energy exchange between the flow and the Pelton buckets. Consequently, the hydraulic efficiency will be affected.
3. The overall effect of the friction forces on the reduction of the system efficiency consists of a direct friction effect (1) and an indirect effect via the reduction of the relative flow velocity (2).

These three aspects cover all hydraulic friction effects in a Pelton turbine and are described below in detail.
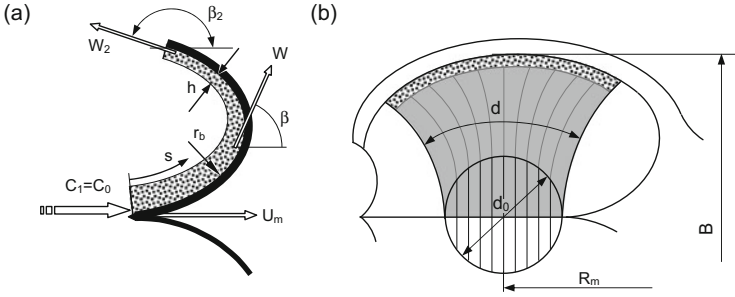
Fig. 10.1 Cross-flow through the bucket and parameter definitions

10.1   Friction Number

Since the friction is directly perceptible only in the Pelton buckets, it will be considered first in the relative flow in a rotating bucket. The spreading of the water sheet in the bucket is characterized, according to Fig. 10.1, by the fact that both the water-sheet width d and height h change along the flow path s. For establishing the equation of motion, an infinitesimal track $\mathrm{d}s$ is considered, at which in the direction of the flow, only the friction force and centrifugal force ($\vec{F}_{\mathrm{ct}}$) are available. According to the law of momentum, the change in the momentum flow rate is equal to the sum of all forces acting on the flow, so that one obtains in steady state

$$(\rho dh)W\mathrm{d}W = (\rho dh)\vec{F}_{\mathrm{ct}} \cdot \mathrm{d}\vec{s} - c_{\mathrm{f}}\frac{1}{2}\rho W^2 d\mathrm{d}s \qquad (10.1)$$

or in a simplified form

$$\mathrm{d}\left(\frac{1}{2}W^2\right) = \vec{F}_{\mathrm{ct}} \cdot \mathrm{d}\vec{s} - c_{\mathrm{f}}\frac{1}{2h}W^2\mathrm{d}s. \qquad (10.2)$$

This equation can also be interpreted as the energy equation. The change in the kinetic energy of the flow is, thus, equal to the works being done by all forces.

In the above equations, c_{f} is the friction coefficient which can be assumed to be constant for large Reynolds numbers as well as for Reynolds numbers with limited variations. This is automatically satisfied for Pelton turbines for which the Reynolds number as a function of the hydraulic head really only varies in a very limited range. It is, however, worth noting that one deals here with the flow of a water sheet with free surface. Since the Froude number in such a water-sheet flow is always greater than unity, i.e., $\mathrm{Fr} = W/\sqrt{gh} > 1$, the flow is of shooting type or supercritical. The corresponding friction coefficient is fundamentally different from those in boundary layers of pipe flows or in flumes and sheet flows with $\mathrm{Fr} < 1$.

For frictionless flows, Eq. (10.2) is reduced to Eq. (6.14), from which the invariance equation has been derived. Assuming that most part of the water flows transversely through the bucket (Fig. 10.1) and that, therefore, $U = U_m = \text{const}$, the component of the centrifugal force in the flow direction, i.e., along the streamlines is negligible. This simply means $\vec{F}_{ct} \cdot d\vec{s} = 0$, so that Eq. (10.2) reduces to

$$d\left(\frac{1}{2}W^2\right) = -c_f\frac{1}{2h}W^2 ds. \tag{10.3}$$

It should be noted here that two terms on the right-hand side of Eq. (10.2) are independent of one another and only slightly affect the relative velocity. This allows that the effects of the centrifugal force and the effects of the viscous friction can be separately considered and analyzed when both effects are present at the same time. To obtain the result for the total effect, two partial results need to be added.

For further calculations, the *friction number* is introduced, which is defined by

$$c_w = \int_0^s \frac{c_f}{h} ds. \tag{10.4}$$

In connection with spreading of the water sheet in the bucket, the friction number is a function of the height and position of the moving water sheet.

Integration of Eq. (10.3) is straightforward and implies

$$W = W_1 e^{-c_w/2} \approx W_1\left(1 - \frac{1}{2}c_w\right). \tag{10.5}$$

Here, W_1 is the relative flow velocity at the bucket inlet. The approximation considers the linear part of Taylor expansion of the exponential function with $c_w \ll 1$.

For further calculations, a second approximation based on Eq. (10.5) is used:

$$c_f W = c_f W_1 - \frac{1}{2}c_f c_w W_1 \approx c_f W_1. \tag{10.6}$$

The term $\frac{1}{2}c_f c_w W_1$, which is less than $c_f W_1$ by one order of magnitude, is neglected. It should, however, be noted that this approximation may not be simply interpreted as $W \approx W_1$. The approximation should only be used in the given form to estimate the friction effect as a given order of magnitude.

On the other hand, the friction shear stress in the form $\tau = c_f \frac{1}{2}\rho W^2$ leads to a drop of power, which is found in hydraulic dissipation during the water-sheet spreading,

$$\dot{E}_{diss} = \int_0^s c_f\frac{1}{2}\rho W^2 W d ds. \tag{10.7}$$

It is called the *dissipation rate*. The integration path s is defined for the time being as a variable, just like the case in defining the friction number, according to Eq. (10.4).

With $\dot{Q}_w/2 = Whd$ as the volume flow rate in a half of the bucket and regarding the approximation in Eq. (10.6), one obtains from Eq. (10.7)

$$\dot{E}_{\text{diss}} = \frac{1}{2}\rho W_1^2\frac{\dot{Q}_w}{2}\int_0^s c_f\frac{1}{h}\,ds \qquad (10.8)$$

or with the friction number as defined above

$$\dot{E}_{\text{diss}} = \frac{1}{2}c_w\rho W_1^2\frac{\dot{Q}_w}{2}. \qquad (10.9)$$

Since the dissipation rate is directly proportional to the friction number in the flow, this equation can also be regarded as the defining equation of the friction number.

From hydraulic dissipation in the relative flow, there follow the reduction of the relative flow velocity and, in turn, the change in kinetic energy $\Delta\dot{E} = \rho(\dot{Q}_w/2)\cdot\frac{1}{2}(W_1^2 - W^2)$ which holds for a half of the bucket. This change in kinetic energy is equalized to Eq. (10.9), so that

$$W^2 = W_1^2(1 - c_w). \qquad (10.10)$$

Because $c_w \ll 1$, the relative flow velocity is resolved to approximately

$$W = W_1\sqrt{1 - c_w} \approx W_1\left(1 - \frac{1}{2}c_w\right). \qquad (10.11)$$

This result, as obtained from the energy law, agrees with Eq. (10.5) which is the result from the law of momentum.

By considering the entire friction from bucket entry to exit, the overall *friction number* is obtained from Eq. (10.4) as

$$c_{w2} = \int_0^s c_f\frac{1}{h}\,ds. \qquad (10.12)$$

Consequently, the relative flow velocity at the bucket exit is given by

$$W_2^2 = W_1^2(1 - c_{w2}). \qquad (10.13)$$

In Chap. 7, the spreading of the water sheet in a Pelton bucket has been approximated by Eq. (7.8). The height of the water sheet is then determined from the conservation law of mass as follows:

$$\frac{1}{h} = \frac{Wd}{\dot{Q}_w/2} = \frac{W}{\dot{Q}_w/2}\left(d_0 + \frac{d_2 - d_0}{S}s\right). \tag{10.14}$$

The flow rate $\dot{Q}_w/2$ is referred to a half of the bucket and corresponds to the half of the jet flow as given by $\dot{Q}_w/2 = \frac{1}{8}\pi d_0^2 W_{0x,o}$ from Eq. (7.5). Since in the present consideration, according to Fig. 10.1, perpendicular entry of the jet into the bucket has been assumed, one has $W_{0x,o} = W_1$. Equation (10.14) is now inserted into Eq. (10.12). With the aid of Eq. (10.6), the overall friction number is then obtained by integration, thus yielding

$$c_{w2} = 4c_f \frac{d_0 + d_2}{\pi d_0^2} \cdot S. \tag{10.15}$$

The friction number in this form combines the friction coefficient, the bucket geometry which is specified by the bucket parameter S, and the flow rate, which is given by the jet thickness d_0. However, it is independent of the rotation of the buckets. On the numerical value, the magnitude of the friction number can be estimated. At nominal flow rate, $d_{2,N}/d_{0,N} = 2.5$, according to Eq. (7.9). For a length of the flow path in the bucket, $S/d_{0,N} = 3$, and a friction coefficient of $c_f = 0.015$, the friction number is calculated from Eq. (10.15) to $c_{w2,N} = 0.2$. For partial load operations with a partial flow rate ($d_0 < d_{0,N}$), the friction number is correspondingly larger.

It should be noted that the thin water-sheet flow in Pelton buckets is a kind of *shooting flows* with the Froude number greater than one ($\text{Fr} > 1$). The friction coefficients of such flows are generally unknown. The assumed friction coefficient of $c_f = 0.015$ is quite high if compared with common friction coefficients, e.g., in turbulent boundary layer flows. As is clear from Eq. (10.13), a friction number of $c_{w2,N} = 0.2$ results in a loss of the kinetic energy of 20 % or a reduction in the flow velocity of about 10 %. Such a value of velocity reduction in rotating buckets of a Pelton turbine has already been applied in practice [see, for instance, Dixon (2005)]. To complete the knowledge in the hydromechanics of Pelton turbines, the viscous effect in the boundary layer of shooting flows should be systematically investigated by experiments.

10.2   Direct Friction Effects

By the direct friction effect, one understands the viscous shear stress in the form of positive but also negative driving forces acting on the bucket. In the foremost part of the bucket ($\beta < \pi/2$ as shown in Fig. 10.1), the shear stress has a positive effect on the bucket motion. In the backmost part of the bucket ($\beta > \pi/2$), however, it counteracts and, thus, retards the bucket motion. In both cases, effective components of shear stresses are those in the direction of the bucket motion as given by

$c_f \frac{1}{2}\rho W^2 \cos\beta$. The power generated by friction shear stress on an infinitesimal area dds is calculated according to Fig. 10.1 by

$$dP_{w,d} = c_f \frac{1}{2}\rho W^2 \cos\beta U_m dds. \tag{10.16}$$

With this notation, it is agreed that the positive value of $dP_{w,d}$ depicts the positive friction power, i.e., the friction shear stress contributes to the power of the shaft. Because of the mass flow rate $\dot{m}_w/2 = \rho W dh$ in a half of the bucket, it follows from Eq. (10.16) that

$$dP_{w,d} = \frac{\dot{m}_w}{2}WU_m c_f \frac{1}{2h}\cos\beta ds. \tag{10.17}$$

From calculations in Chap. 7, or according to Eq. (7.7), it is known that the average number of buckets, which are involved in power exchange with each jet, is equal to $2\lambda = \dot{m}_c/\dot{m}_w$ (with λ as the multi-bucket factor). If both sides of Eq. (10.17) are multiplied with $\dot{m}_c/\dot{m}_w$, then the power related to 2λ bucket halves is given by

$$dP_d = \frac{\dot{m}_c}{2}WU_m c_f \frac{1}{2h}\cos\beta \, ds. \tag{10.18}$$

This power is directly detectable in the shaft power of a Pelton turbine. This also means that the power from direct friction forces in the rotating system is detected in the stationary system. Considering the approximation in Eq. (10.6), one obtains through integration of Eq. (10.18)

$$P_d = \frac{\dot{m}_c}{2}U_m W_1 \frac{1}{2}\int_0^S c_f \frac{1}{h}\cos\beta \, ds. \tag{10.19}$$

This power is referred to as the *direct friction power*. By relating it to the power $0.5(\dot{m}_c \frac{1}{2}C_0^2)$ of a half jet, its direct contribution to efficiency is given by

$$\eta_d = \frac{P_d}{0.5(\dot{m}_c \frac{1}{2}C_0^2)} = k_m(1-k_m)\int_0^S c_f \frac{1}{h}\cos\beta \, ds. \tag{10.20}$$

In this equation, $W_1 = C_0 - U_m$ and the peripheral speed coefficient $k_m = U_m/C_0$ have been used. For Pelton buckets with complex geometries and consequently a complex function for $\beta = f(s)$, the above integration can be transformed into a summation algorithm and then easily computed numerically.

A quantitative assessment of direct friction effect on turbine efficiencies should be made. The height of the water sheet in the Pelton bucket has already been specified by Eq. (7.10). For the case of a perpendicular entry of the jet into the bucket, one simply has $W_{0x,o} = W_1$. Thus, one obtains

$$h = \frac{1}{8}\pi d_0^2 \frac{1}{d}\frac{W_1}{W}.\tag{10.21}$$

Together with Eq. (7.8) for the water-sheet width, it follows from Eq. (10.20) that

$$\eta_d = \frac{8}{\pi d_0^2}k_m(1 - k_m)\int_0^S c_f\left(d_0 + \frac{d_2 - d_0}{S}s\right)\cos\beta ds.\tag{10.22}$$

In this equation, the approximation $c_f W \approx c_f W_1$, according to Eq. (10.6), has again been applied.

Here, a semicircular bucket is considered with a constant radius r_b and straight exit geometry ($\beta_2 = 180°$) as a special case. In this case, then, $s = \beta r_b$ and $S = \pi r_b$. For $c_f = $ const, Eq. (10.22) becomes

$$\eta_d = 8\frac{c_f}{\pi}k_m(1 - k_m)\cdot\frac{r_b}{d_0^2}\int_0^\pi\left(d_0 + \frac{d_2 - d_0}{\pi}\beta\right)\cos\beta d\beta.\tag{10.23}$$

The integration can be easily performed; the result is

$$\eta_d = -16k_m(1 - k_m)\frac{c_f}{\pi^2}\frac{r_b}{d_0}\left(\frac{d_2}{d_0} - 1\right).\tag{10.24}$$

The efficiency resulting from the direct friction force is negative. This exactly corresponds to the expectation. In the hindmost part of the bucket ($\beta > \pi/2$) where the friction force retards the bucket motion, the friction area and, thus, the friction force are greater than that in the foremost part of the bucket.

A numerical example on η_d will be given in Sect. 11.4.

10.3 Friction Effects via Changing the Pressure Distribution

Another direct consequence of viscous friction between the water sheet and the bucket surface is the deceleration of the relative flow while passing through the bucket. The reduction of the relative flow velocity, in turn, leads to the reduction of the pressure as the driving force on the bucket surface. This can be confirmed when Eq. (6.10) for the overpressure below the water sheet is concerned,

$$p_b = \frac{h}{r_b}\rho W^2,\tag{10.25}$$

where r_b is the local radius of curvature of the bucket inner surface.

The pressure force associated with this overpressure acts perpendicular to the bucket surface. Its effective component for driving the bucket is, however, the component in the direction of the bucket motion. The power provided by the pressure force in an infinitesimal bucket surface $d\,ds$ can thus be calculated according to Fig. 10.1 from

$$dP_{w,p} = p_b \sin \beta U_m d\,ds = \frac{h}{r_b} \rho W^2 U_m \sin \beta \, d\,ds. \qquad (10.26)$$

With the mass flow rate $\dot{m}_w/2 = \rho h dW$ in the rotating system and $ds = r_b d\beta$, Eq. (10.26) is rewritten as

$$dP_{w,p} = \frac{\dot{m}_w}{2} W U_m \sin \beta \, d\beta. \qquad (10.27)$$

As in Eq. (10.18), this expression for the flow in a half bucket is extended to the flow in 2λ bucket halves:

$$dP_p = \frac{\dot{m}_c}{2} W U_m \sin \beta \, d\beta. \qquad (10.28)$$

The integration over the entire flow path (from the entry to the exit) yields the overall power provided by the pressure force

$$P_p = \frac{\dot{m}_c}{2} U_m \int_0^{\beta_2} W \sin \beta \, d\beta. \qquad (10.29)$$

This is the power which is related to the flow of a half jet and is detectable directly in the shaft power of a Pelton turbine.

For further calculations, the flow velocity W has to be regarded as a variable. This means, according to Eq. (10.11), that the overall power is a function of the local friction number, so that

$$P_p = \frac{\dot{m}_c}{2} U_m W_1 \int_0^{\beta_2} \left(1 - \frac{1}{2}c_w\right) \sin \beta \, d\beta. \qquad (10.30)$$

For later comparison (Sect. 10.5), the integration in this equation is further performed. Using the integration by parts in the form $\int u dv = uv - \int v du$, and substituting $u = 1 - \frac{1}{2}c_w$ and $v = \cos \beta$, the above equation is rewritten as

$$\frac{P_p}{(\dot{m}_c/2)U_m W_1} = 1 - \left(1 - \frac{1}{2}c_{w2}\right)\cos \beta_2 - \frac{1}{2} \int_0^{c_{w2}} \cos \beta dc_w, \qquad (10.31)$$

in which at the lower bound of the integration $s = 0$, i.e., $\beta = 0$ with $c_w = 0$, has been implemented.

The integrand on the rhs of the above equation is nothing else than the integrand in Eq. (10.20), simply because $dc_w = (c_f/h)ds$ according to Eq. (10.4).

Accordingly, the efficiency contributed by the pressure force is obtained by relating the power P_p from Eq. (10.31) to the power of a half jet,

$$\eta_p = \frac{P_p}{0.5\left(\frac{1}{2}\dot{m}_c C_0^2\right)} = 2k_m(1 - k_m)\left[1 - \left(1 - \frac{1}{2}c_{w2}\right)\cos\beta_2 - \frac{1}{2}\int_0^{c_{w2}}\cos\beta dc_w\right].$$

(10.32)

The effects of the friction via the pressure reduction in the water sheet on the shaft power as well as on the turbine efficiency are presented in the last two equations. The special case of frictionless flow is obtained immediately by simplifying Eq. (10.32) to

$$\eta_{p,0} = 2k_m(1 - k_m)(1 - \cos\beta_2).$$

(10.33)

It is identical to Eq. (2.40). This identity clearly points out that the power exchange between the water flow and the rotating buckets in a Pelton turbine ultimately happens through the pressure force below the water sheet. It can also be seen that the efficiency, according to Eq. (10.32), is a type of hydraulic efficiency.

The efficiency loss caused by the viscous friction via the pressure reduction is then given by

$$\Delta\eta_p = \eta_{p,0} - \eta_p = 2k_m(1 - k_m)\left(-\frac{1}{2}c_{w2}\cos\beta_2 + \frac{1}{2}\int_0^{c_{w2}}\cos\beta dc_w\right).$$

(10.34)

A semicircular bucket with a constant radius r_b and the straight exit angle $\beta_2 = \pi$ is considered again. The integration in Eq. (10.32) is then calculated by applying $dc_w = (c_f/h)ds$ and $h = \frac{1}{8}\pi d_0^2 W_1/(Wd)$, from Eq. (10.21), as well as substitution of the water-sheet width from Eq. (7.8),

$$\frac{\eta_p}{2k_m(1 - k_m)} = 2 - \frac{1}{2}c_{w2} - \frac{4c_f}{\pi d_0^2}\int_0^S \cos\beta\left(d_0 + \frac{d_2 - d_0}{S}s\right)ds.$$

(10.35)

Moreover, the substitutions $s = r_b\beta$ and $ds = r_b d\beta$ are applied. The integration can then be easily performed. Thus, with the friction number c_{w2}, given by Eq. (10.15), and with $S = \pi \cdot r_b$, it finally follows from Eq. (10.35):

$$\eta_p = 4k_m(1 - k_m)\left\{1 - c_f\left[\frac{d_2}{d_0}\left(1 - \frac{4}{\pi^2}\right) + \left(1 + \frac{4}{\pi^2}\right)\right]\frac{r_b}{d_0}\right\}.$$

(10.36)

In this equation, the viscous friction between the water sheet and the Pelton buckets is considered directly by the friction coefficient c_f. As in Eq. (10.24), the effect of the viscous friction in the relative flow system on the turbine efficiency in the

absolute system has now been revealed. A quantitative computational example will be presented in Chap. 11.

10.4   Total Friction Effects

The hydraulic power of a Pelton turbine, including the influence of viscous friction, can be obtained, on the other hand, directly from the law of momentum. For this reason, the entry angle of the jet flow, while entering the rotating buckets, is assumed to be $\beta_1 = 0$. The entire hydraulic power of a Pelton turbine is calculated to be

$$P_h = \dot{m}_c (W_1 - W_2 \cos \beta_2) U_m. \tag{10.37}$$

The background of this equation goes back to Sect. 2.2, where the hydraulic power was calculated from the law of momentum. In fact, the impulsive force arising from the change of the relative velocity in one bucket is given by $\dot{m}_w (W_1 - W_2 \cos \beta_2)$ with $\dot{m}_w$ as the mass flow rate in the rotating system. With respect to the number of buckets ($2\lambda = \dot{Q}_c / \dot{Q}_w = \dot{m}_c / \dot{m}_w$), which interact with one jet, the total impulsive force related to one jet is then given by $\dot{m}_c (W_1 - W_2 \cos \beta_2)$. Its multiplication with the peripheral speed yields the hydraulic power.

For frictionless flow, the relative flow velocity remains constant ($W_2 = W_1 = W$). The above equation is then reduced to Eq. (2.38).

Since frictional flows are considered, the varying relative flow velocity has to be assumed according to Eq. (10.11). Then, it follows from Eq. (10.37) that

$$P_h = U_m \dot{m}_c W_1 \left[1 - \left(1 - \frac{1}{2} c_{w2} \right) \cos \beta_2 \right]. \tag{10.38}$$

Relating this power to the jet power results in the hydraulic efficiency given by

$$\eta_h = \frac{P_h}{\frac{1}{2} \dot{m}_c C_0^2} = 2 k_m (1 - k_m) \left[1 - \left(1 - \frac{1}{2} c_{w2} \right) \cos \beta_2 \right]. \tag{10.39}$$

As reference power, the frictionless power $P_{h,0}$ is used, which is obtained from Eq. (10.38) by setting $c_{w2} = 0$. The efficiency drop caused by the fluid friction is, thus, obtained as

$$\Delta \eta_\mu = \frac{P_{h,0} - P_h}{\frac{1}{2} \dot{m}_c C_0^2} = -c_{w2} k_m (1 - k_m) \cos \beta_2. \tag{10.40}$$

From this calculation, the following understandings can be concluded:

1. A virtual bucket is considered, which has an exit angle $\beta_2 < \pi/2$. Since the flow in the bucket is in the same direction as the bucket motion and is slowed down by the viscous friction, an intensified power exchange between the viscous flow and the moving bucket takes place. The friction acts as a positive driving force and generates an additional amount of power ($P_h > P_{h,0}$). According to the definition, the hydraulic loss in this case is negative, $\Delta\eta_\mu < 0$.

2. By assuming the bucket exit angle to be $\beta_2 = \pi/2$, Eq. (10.40) implies $\Delta\eta_\mu = 0$. This result implies that the exit flow leaving the bucket perpendicular to the bucket motion has no effect on the bucket motion. Therefore, it is immaterial whether and how the flow in the bucket is affected by viscous friction. In other words, the friction does not affect the power output, although it acts as a driving agent. The positive driving effect is completely compensated by the negative effect because of the pressure reduction according to Eq. (10.31). In fact, it follows from Eqs. (10.20) and (10.31) for $\beta_2 = \pi/2$, immediately $P_{p,0} - P_p = P_d$, with $P_{p,0}$ as the power for frictionless flows ($c_f = 0$).

3. In the hindmost part of the Pelton bucket, the exit flow angle is $\beta_2 > \pi/2$ which implies $\Delta\eta_\mu > 0$. This result points out that the viscous friction force on the bucket surface affects the hydraulic efficiency always negatively, although the friction in the foremost area of the bucket $\beta < \pi/2$ appears to have a positive influence.

4. For $k_m = 0.5$ and $\beta_2 \approx \pi$, as an approximation of real design and operation of Pelton turbines, Eq. (10.39) leads to

$$\eta_h = 1 - \frac{1}{4}c_{w2} \tag{10.41}$$

or, in the form of efficiency loss,

$$\Delta\eta_\mu = \frac{1}{4}c_{w2} = c_f \frac{d_0 + d_2}{\pi d_0^2} S. \tag{10.42}$$

This relation represents the mechanism of the friction effects in the rotating system on the real hydraulic efficiency of a Pelton turbine in a fixed system. The quality of the bucket surface is described by the friction coefficient. The length of the flow path is given by S. Finally, the impact of the flow rate has been represented by the jet diameter.

Under nominal operation conditions, i.e., nominal flow rates, a friction number of $c_{w2,N} = 0.2$ has been estimated in relation to Eq. (10.15). With this value, a drop in hydraulic efficiency of about $\Delta\eta_\mu = 5\%$ has to be expected. An efficiency drop of such a magnitude must be considered as very high, especially when compared to the efficiency losses from other sources which have already been described in detail in Chap. 9. At partial load, which is given by closing the injector nozzle, the drop in hydraulic efficiency, according to Eq. (10.42), will be

greater due to the reduction of the jet diameter. This is logical because the almost constant friction power is now related to a smaller jet power.

From Eq. (10.42), a significant measure to improve the system efficiency can be confirmed. It lies simply in the reduction of the friction coefficient between the flow and the Pelton buckets. This is likely to be very effective, because the viscous friction on the bucket surface seems to be confirmed as the most significant source causing the efficiency drop in a Pelton turbine. Such a statement has been pointed out by Zhang and Müller (2006) and Zhang (2007), as this will be shown in Chap. 11 in more details.

10.5 Flow Friction Theorem

In the foregoing sections, the direct friction effect, the friction effect via the pressure reduction, and the total friction effect from the law of momentum have been described in detail. One point to be demonstrated here is the lucid connection between the three terms of the friction effect. By comparing Eqs. (10.20), (10.32), and (10.39), the following relation has been found:

$$\eta_h = \eta_d + \eta_p. \tag{10.43}$$

Here, the integration parts in Eqs. (10.20) and (10.32) cancel out because $dc_w = (c_f/h)ds$.

The relation shown in Eq. (10.43) can also be represented by the respective efficiency drops. The power from the direct friction effect calculated in Sect. 10.2 is always negative in a Pelton turbine. This means that the friction force causes a direct efficiency drop that can be expressed by $\Delta\eta_d = -\eta_d$. From Eqs. (10.20), (10.34), and (10.40), the following relation is also obtained as

$$\Delta\eta_\mu = \Delta\eta_d + \Delta\eta_p. \tag{10.44}$$

The relations presented in Eqs. (10.43) and (10.44), respectively, are, according to Zhang (2007), called *flow friction theorem* (FFT) of Pelton turbine hydraulics.

Further considerations of the friction effects and computational examples will be shown in the next chapter.

References

Dixon, S. (2005). *Fluid Mechanics and Thermodynamics of Turbomachinery* (5th ed.). Amsterdam: Elsevier.

Zhang, Zh. (2007). Flow friction theorem of Pelton turbine hydraulics. *Proceedings of the IMechE Vol. 221, Part A: Journal of Power and Energy*, pp. 1173–1180.

Zhang, Zh., & Müller, J. (2006). The effect of flow friction in the rotating bucket of Pelton turbine on the hydraulic efficiency. Hydro 2006, Porto Carras, Greece.

Chapter 11
Viscous Cross-Flow Through the Bucket

In Pelton turbines, the water jets enter the buckets in large parts perpendicular to the bucket, more precisely perpendicular to the bucket main splitters. This form of entrance configuration ensures that the water in the bucket follows the path of constant peripheral speed and thus laterally across the bucket. Since approximately neither the centrifugal nor the Coriolis forces affect the relative flow, the friction effect could be separately treated in the last chapter. Under the same flow conditions, calculations in the last chapter will be further considered and quantified in greater detail in this chapter.

11.1 Combined Hydraulic Losses

The hydraulic efficiency of a Pelton turbine subjected to friction effects has been calculated by Eq. (10.39). The total loss of hydraulic efficiency is then obtained as

$$\Delta\eta_h = 1 - \eta_h = 1 - 2k_m(1 - k_m)(1 - \cos\beta_2) - c_{w2}k_m(1 - k_m)\cos\beta_2. \quad (11.1)$$

It is rewritten as the sum of two parts:

$$\Delta\eta_h = \Delta\eta_{Dr,0} + \Delta\eta_\mu, \quad (11.2)$$

in which the partial losses are expressed, respectively, by

$$\Delta\eta_{Dr,0} = 1 - 2k_m(1 - k_m)(1 - \cos\beta_2) \quad (11.3)$$

and

Fig. 11.1 Efficiency losses
in a Pelton turbine with
viscous cross-flow through
a rotating bucket,
$\beta_2 = 170°$, $c_{w2} = 0.2$
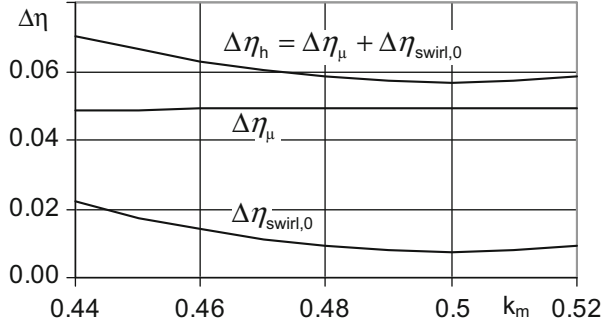
$$\Delta\eta_\mu = -c_{w2}k_m(1 - k_m)\cos\beta_2. \tag{11.4}$$

The first part corresponds to the frictionless swirling loss which has been given by
Eq. (9.8). The second part is friction dependent and has already been revealed by
Eq. (10.40). Because for friction-affected flows the exit velocity is also affected by
the viscous friction in the bucket, Eq. (11.3) does not represent the real swirling
loss. In actual reality, it is not absolutely necessary to calculate the real swirling loss
when the combined hydraulic loss in the system efficiency can be easily determined
from Eq. (11.2). Nevertheless, in order to gain insight into the real swirling loss,
explicit estimation will be presented in Sect. 11.2.

Based on Eq. (10.39), optimal hydraulic efficiency is found at $k_m = 0.5$.
According to Fig. 11.1, which graphically represents the loss contributions of
Eqs. (11.2), (11.3), and (11.4), only insignificant dependencies on the peripheral
speed coefficient k_m in the near vicinity of $k_m = 0.5$ are effective. In particular, the
loss $\Delta\eta_\mu$ is virtually independent of k_m. Practical operation designs of the peripheral
speed coefficient in the range $k_m = 0.45 - 0.48$, thus, do have their background
mainly in the coincidence and symmetry conditions given in Chap. 5 as well as in
the exit flow condition discussed in Chap. 8.

The partial and total hydraulic losses shown in Fig. 11.1 are valid for a friction
number $c_{w2} = 0.2$. This friction number is calculated in accordance with Sect. 10.1
for a friction coefficient $c_f = 0.015$. As mentioned already there, no information on
the friction effect in the shooting flow with $Fr > 1$ is known. With the assumed friction
number of $c_{w2} = 0.2$ one concludes from Fig. 11.1 that the partial loss $\Delta\eta_\mu \approx 0.05$
dominates in the combined efficiency loss in Eq. (11.2). Such a dominant friction
effect is surprising and will be frequently encountered in the following chapters.

11.2 Real Swirling Losses

Although the determination of the real *swirling loss*, according to the statement in
Sect. 11.1, seems to be unnecessary for efficiency considerations, a brief look into
the real swirling loss would help to better understand the friction effect. The real

swirling loss may be determined by accounting for the change in relative flow velocity in a rotating bucket. According to Eq. (10.3), the integration over the entire flow path is given by

$$\frac{1}{2}\left(W_1^2 - W_2^2\right) = \frac{1}{2}\int_0^S c_f \frac{1}{h} W^2 \mathrm{d}s. \tag{11.5}$$

Because of the insignificant change of the flow velocity along the flow path in the current case of the cross-flow, the mean value theorem of integration is used for further calculations; it yields

$$W_1^2 - W_2^2 = \frac{W_1^2 + W_2^2}{2}\int_0^S c_f \frac{1}{h} \mathrm{d}s = \frac{W_1^2 + W_2^2}{2} c_{w2}. \tag{11.6}$$

The *friction number* in this equation refers to the definition in Eq. (10.12).

For the exit velocity W_2, one obtains then

$$W_2^2 = \frac{1 - c_{w2}/2}{1 + c_{w2}/2} W_1^2 = \Phi W_1^2. \tag{11.7}$$

For small friction numbers, $c_{w2}/2 \ll 1$, there is $\Phi \approx 1 - c_{w2}$. This result has already been discussed in Sect. 10.1 and was used in Eq. (10.13).

The absolute flow velocity at the bucket exit is then calculated according to Fig. 9.1 by

$$C_2^2 = W_2^2 + U_2^2 + 2U_2 W_2 \cos\beta_2. \tag{11.8}$$

Together with Eq. (11.7), this is further transformed into

$$C_2^2 = \Phi W_1^2 + U_2^2 + 2U_2 W_1 \sqrt{\Phi} \cos\beta_2. \tag{11.9}$$

Because $U_2 = U_1 = U_m$ and $W_1 = C_0 - U_m$ as well as $k_m = U_m/C_0$, the real swirling loss in the exit flow is finally obtained as

$$\Delta\eta_{\mathrm{swirl}} = \frac{C_2^2}{C_0^2} = \Phi(1 - k_m)^2 + k_m^2 + 2k_m\sqrt{\Phi}(1 - k_m)\cos\beta_2. \tag{11.10}$$

For frictionless flows, we have $\Phi = 1$. Obviously, swirling losses in real frictional flows differ from those in frictionless flows. Figure 11.2 shows computational results, according to Eq. (11.10) for an example. For comparison, $c_{w2} = 0$ and $c_{w2} = 0.2$ (see Sect. 11.1) have been assumed. Obviously, the friction effect in the flow leads to a downshift of the peripheral speed coefficient for a minimum swirling loss. Such a shift indeed can also be confirmed by Eq. (11.10). For the same friction

Fig. 11.2 Swirling loss
comparison between the
frictionless and viscous
cross-flow through a
circular Pelton bucket,
$\beta_2 = 170°$, $c_{w2} = 0.2$
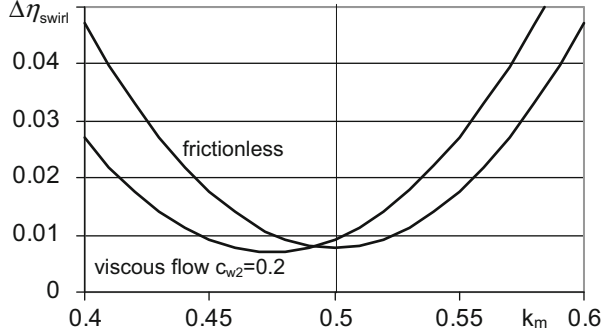
number $c_{w2} = 0.2$ from which a value $\Phi = 0.818$ is obtained, the peripheral speed coefficient for obtaining minimum swirling loss is found from Eq. (11.10) by setting $\mathrm{d}(\Delta\eta_{\mathrm{swirl}})/\mathrm{d}k_m = 0$

$$k_{m,\min} = \frac{\sqrt{\Phi}}{1 + \sqrt{\Phi}} = 0.475. \tag{11.11}$$

Although this result closely agrees with practical operation settings of Pelton turbines, it should not be concluded that practical operation settings for $k_m \approx 0.475$ simply aim to reduce swirling losses. As already indicated in Sect. 11.1, the combined hydraulic loss with its minimum is still found at $k_m = 0.5$. This condition, in turn, corresponds to the flow configuration of a linearly translating bucket. This is quite self-evident, since, according to Fig. 10.1 for approximated two-dimensional cross-flows, neither the centrifugal nor the Coriolis forces do affect the flows. In addition, $k_{m,\min} = 0.475$ in Fig. 11.2 is only related to a mathematical extreme value. As a matter of fact, the mathematically detected dependency of swirling losses on the peripheral speed coefficient in the range of $k_{m,\min} = 0.475$ is so weak that it cannot be perceived in practical operations of Pelton turbines.

Swirling loss calculations according to Eq. (11.10) can be simplified for $c_{w2}/2 \ll 1$. Due to the consequent approximations $\Phi \approx 1 - c_{w2}$ and $\sqrt{1 - c_{w2}} \approx 1 - c_{w2}/2$, one obtains from Eqs. (11.10) and (11.11), respectively,

$$\Delta\eta_{\mathrm{swirl}} = 1 - 2k_m(1 - k_m)(1 - \cos\beta_2) \\ - c_{w2}(1 - k_m)[1 - k_m(1 - \cos\beta_2)] \tag{11.12}$$

and

$$k_{m,\min} = \frac{1 - c_{w2}/2}{2 - c_{w2}/2}. \tag{11.13}$$

For $\beta_2 \approx \pi$ Eq. (11.12) implies

$$\Delta\eta_{\text{swirl}} = 1 - (1 - k_{\text{m}})[4k_{\text{m}} + c_{\text{w2}}(1 - 2k_{\text{m}})].\tag{11.14}$$

Since for Pelton turbines the peripheral speed coefficient k_{m} is always close to 0.47 and the friction number is of a small value (e.g., $c_{\text{w2}} = 0.2$), it applies $c_{\text{w2}}(1 - 2k_{\text{m}}) \ll 4k_{\text{m}}$. Thus, one obtains

$$\Delta\eta_{\text{swirl}} \approx 1 - 4k_{\text{m}}(1 - k_{\text{m}}).\tag{11.15}$$

This equation corresponds to Eq. (11.3) for $\beta_2 \approx \pi$. It clearly points out that the influence of flow friction on the swirling loss in the exit flow is negligible.

At this point, the significance of Eq. (11.13) in terms of minimum swirling losses should be discussed in detail. The minimum swirling losses are obviously expected according to Fig. 8.5, when the condition $\alpha_2 \approx \pi/2$ for exit flows is fulfilled. Accordingly, it follows from Eq. (8.30) with $\tan\alpha_2 = \infty$

$$k_{\text{m}}\left(\frac{D_2}{D_{\text{m}}}\right)\left(\frac{C_0}{W_2}\right) + \cos\beta_2 = 0.\tag{11.16}$$

The relative flow velocity W_2 at the bucket exit is replaced by $W_2 = W_1(1 - \frac{1}{2}c_{\text{w2}})$ according to Eq. (10.13). With $W_1 = C_0(1 - k_{\text{m}})$ and for $\beta_2 \approx \pi$ as well as $D_2 = D_{\text{m}}$ one obtains from Eq. (11.16)

$$k_{\text{m}} = \frac{1 - c_{\text{w2}}/2}{2 - c_{\text{w2}}/2}.\tag{11.17}$$

This equation agrees exactly with Eq. (11.13). It clearly signifies that minimum swirling losses in the exit flow are always related to the exit flow at right angle $\alpha_2 \approx \pi/2$. For $c_{\text{w2}} = 0.2$, one obtains $k_{\text{m,min}} = 0.474$.

11.3 Hydraulic Dissipation and Energy Balance

Friction-dependent hydraulic losses in Pelton turbines will now be explained in more details based on the energy conservation law. In the considered lateral cross-flows in each rotating bucket, the change of the relative flow velocity is caused by viscous frictions only. The change in the specific kinetic energy, thus, directly reflects the specific dissipation in the flow owing to the viscous friction, as expressed by

$$e_{\text{diss}} = \frac{1}{2}\left(W_1^2 - W_2^2\right).\tag{11.18}$$

With the aid of Eq. (10.13) one obtains

$$e_{\text{diss}} = c_{\text{w2}} \frac{1}{2} W_1^2. \tag{11.19}$$

This value is then scaled with the specific kinetic energy of the jet, yielding an efficiency loss given by

$$\Delta \eta_{\text{diss}} = \frac{e_{\text{diss}}}{C_0^2/2} = c_{\text{w2}} \frac{W_1^2}{C_0^2}. \tag{11.20}$$

Because $W_1 = C_0 - U_{\text{m}} = C_0(1 - k_{\text{m}})$, it is further represented as a function of the peripheral speed coefficient

$$\Delta \eta_{\text{diss}} = c_{\text{w2}}(1 - k_{\text{m}})^2. \tag{11.21}$$

As it is directly related to the dissipation in the flow, this type of efficiency loss is called *hydraulic dissipation*.

From Eq. (11.1) and (11.12), the following equilibrium equation can be established

$$\Delta \eta_{\text{swirl}} + \Delta \eta_{\text{diss}} = 1 - \eta_{\text{h}}. \tag{11.22}$$

In Sect. 11.2 and with Eq. (11.15), the approximation $\Delta \eta_{\text{swirl}} \approx \Delta \eta_{\text{swirl,0}}$ has already been shown. By comparing Eqs. (11.21) and (11.4) one obtains for $\beta_2 \approx \pi$ and $k_{\text{m}} \approx 0.5$ also the approximation

$$\Delta \eta_{\mu} \approx \Delta \eta_{\text{diss}} = \frac{c_{\text{w2}}}{4}. \tag{11.23}$$

This relation of friction-dependent losses has already been given in Chap. 10 by Eq. (10.42). Since for conditions $\beta_2 \approx \pi$ and $k_{\text{m}} \approx 0.5$ the swirling loss, according to Eq. (11.15), is practically zero, Eq. (11.23), thus, dominantly represents the total hydraulic loss. One needs only to determine the friction number c_{w2} according to Eq. (10.15). This has already been shortly explained in connection with Eq. (10.15) for the case of nominal operations and will be further illustrated in the next section on the basis of a calculation example.

11.4   Example of Friction Effects on the Hydraulic Efficiency

The extent of friction effects on the hydraulic efficiency of a Pelton turbine will now be demonstrated by an example. For simplicity a semicircular bucket with a constant radius r_{b} is considered. The relative flow angles at the bucket entry and exit are set equal to $\beta_1 = 0$ and $\beta_2 = \pi$, respectively. The spreading path length of the

water sheet through the bucket is given by $S = \pi r_b$. Following the conventions in the hydraulic design of Pelton turbines, the *bucket volumetric load* according to Eq. (2.21) is used. It is formulated for the present semicircular bucket as

$$\varphi_B = \left(\frac{d_0}{B}\right)^2 = \left(\frac{d_0}{4r_b}\right)^2. \tag{11.24}$$

Using this parameter allows the friction number, according to Eq. (10.15), to be rewritten as

$$c_{w2} = c_f\left(1 + \frac{d_2}{B\sqrt{\varphi_B}}\right) \cdot \frac{1}{\sqrt{\varphi_B}}. \tag{11.25}$$

For reference, the hydraulic efficiency for frictionless flows is considered. From Eq. (10.39) with $\beta_2 = \pi$ it immediately follows that

$$\eta_{h,0} = 4k_m(1 - k_m). \tag{11.26}$$

Under the application of the parameter φ_B according to Eq. (11.24), Eqs. (10.24), (10.36), and (10.39) are converted, respectively, to

$$\eta_d = -\eta_{h,0}\frac{c_f}{\pi^2}\left(\frac{d_2}{B\sqrt{\varphi_B}} - 1\right)\frac{1}{\sqrt{\varphi_B}}, \tag{11.27}$$

$$\eta_p = \eta_{h,0}\left\{1 - \frac{c_f}{4\sqrt{\varphi_B}}\left[\frac{d_2}{B\sqrt{\varphi_B}}\left(1 - \frac{4}{\pi^2}\right) + \left(1 + \frac{4}{\pi^2}\right)\right]\right\}, \tag{11.28}$$

$$\eta_h = \eta_{h,0}\left[1 - \frac{c_f}{4\sqrt{\varphi_B}}\left(1 + \frac{d_2}{B\sqrt{\varphi_B}}\right)\right]. \tag{11.29}$$

It can be verified that the conditions of the FFT theorem, according to Eq. (10.43), are fulfilled.

For the hydraulic losses in the system efficiency, one obtains accordingly

$$\Delta\eta_d = -\eta_d = \eta_{h,0}\frac{c_f}{\pi^2}\left(\frac{d_2}{B\sqrt{\varphi_B}} - 1\right)\frac{1}{\sqrt{\varphi_B}}, \tag{11.30}$$

$$\Delta\eta_p = \eta_{h,0} - \eta_p = \eta_{h,0}\frac{c_f}{4\sqrt{\varphi_B}}\left[\frac{d_2}{B\sqrt{\varphi_B}}\left(1 - \frac{4}{\pi^2}\right) + \left(1 + \frac{4}{\pi^2}\right)\right] \tag{11.31}$$

and
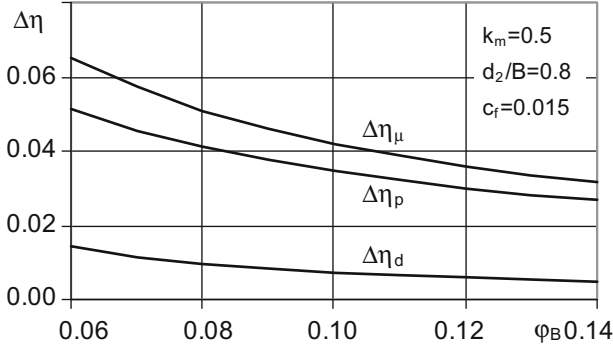
Fig. 11.3 Efficiency losses arising from the flow friction in a circular Pelton bucket

$$\Delta\eta_{\mathrm h} = \eta_{\mathrm{h},0} - \eta_{\mathrm h} = \eta_{\mathrm{h},0}\frac{c_{\mathrm f}}{4\sqrt{\varphi_{\mathrm B}}}\left(1 + \frac{d_2}{B\sqrt{\varphi_{\mathrm B}}}\right). \tag{11.32}$$

They are all shown as functions of the bucket volumetric load which is directly related to the flow rate in the jet.

A concrete example will be considered here in which the water-sheet width at the bucket exit is assumed to be $d_2 = 0.8B$ and the friction coefficient is $c_{\mathrm f} = 0.015$ (see Sect. 10.1). Figure 11.3 shows corresponding hydraulic losses as functions of the bucket volumetric load. Because of the additional assumption $k_{\mathrm m} = 0.5$, it applies for frictionless flows with $\eta_{\mathrm{h},0} = 1$.

It is evident that the direct friction effect on the system efficiency is very small against the friction effect via the pressure reduction beneath the water sheet. In addition, all losses noticeably increase with reduction of the bucket volumetric load. This can be explained by the fact that the almost constant friction power at partial load is related to a small value of the jet power, see also Sect. 10.4.

The combined total loss in the hydraulic efficiency, as caused by viscous frictions, has been confirmed to be considerable. In particular, it doubles if the friction coefficient rises to $c_{\mathrm f} = 0.03$. At Pelton buckets with eroded surfaces, because of sand abrasion, for instance, the friction coefficient and hence hydraulic losses will excessively increase. From these results, it can be concluded that the friction-dependent hydraulic loss in the system efficiency is the most significant loss in a Pelton turbine. For comparison, the swirling loss in the exit flow is only about 1 % (Fig. 9.5), see Chap. 9. As will be described and shown in Chap. 13, air friction and windage losses at Pelton wheels are simply in the order of less than 1 %.

Chapter 12
Viscous Longitudinal Flow Through the Bucket

The longitudinal flow in a rotating bucket is encountered when the jet according to Fig. 5.16 is intersected by the bucket cutout and the water then spreads toward the bucket root. In actual situations, the water does not purely radially move to the bucket root. This is basically because of the three-dimensional geometric bucket design. To simplify the calculations and especially to reveal the fluid mechanics in such cases with dominant radial flows, purely radial flows are supposed and considered in this chapter. Because the Coriolis force, which always acts perpendicular to the flow direction, does not lead to any change in the flow velocity, the motion of water in the rotating bucket is determined only by centrifugal and friction forces. This, however, does not mean that the Coriolis force would not provide any power. In fact, the Coriolis force always retains a force component perpendicular to the bucket inner surface and thus contributes to the bucket motion; see also Fig. 6.1 and the computational example in Fig. 6.9.

12.1 Kinematic Equation of Flow in a Rotating Bucket

Taking into account the influences of centrifugal and friction forces, the energy equation for the motion of a water sheet in a rotating bucket has already been given by Eq. (10.2) in general form as

$$d\left(\frac{1}{2}W^2\right) = \vec{F}_{ct} \cdot d\vec{s} - c_f \frac{1}{2h} W^2 ds. \qquad (10.2)$$

The first term on the right-hand side of the equation corresponds to Eq. (6.14), from which Eq. (6.17) has been obtained. Thus, the above equation is integrated to
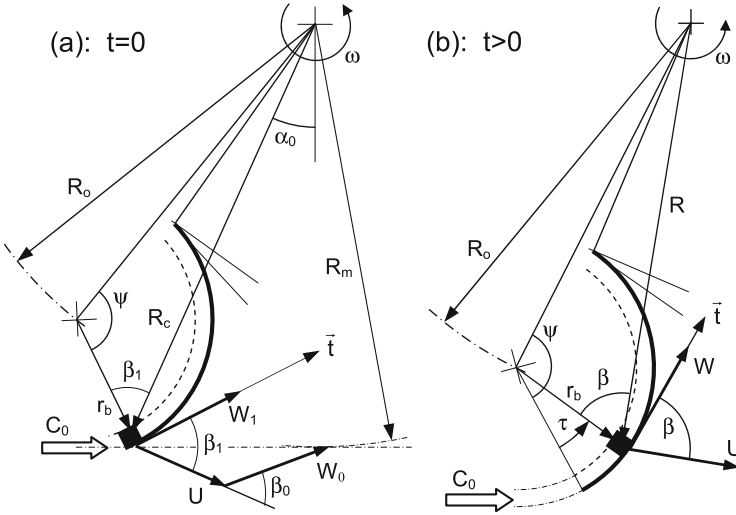
Fig. 12.1 (**a**, **b**) Parameter notation for longitudinal movement of a water particle through a Pelton bucket of circular form

$$\frac{1}{2}\left(W^2 - W_1^2\right) = \frac{1}{2}\omega^2\left(R^2 - R_1^2\right) - \int_0^s c_\text{f}\frac{1}{2h}W^2 \text{d}s. \tag{12.1}$$

This equation explicitly shows that the relative flow velocity in the rotating bucket depends on both the local peripheral speed of the bucket and the flow friction between the flow and the bucket surface. For frictionless flows ($c_\text{f} = 0$), it leads to Eq. (6.18). On the other hand, for a flow laterally across the bucket ($U = $ const), the computation in Eq. (12.1) reduces to the calculation that has already been fully treated in Chaps. 10 and 11.

Equation (12.1) represents a purely *kinematic equation* and can be used to calculate the radial flow in a rotating bucket. To this end some intermediate calculations for the radial position R of the flow in the bucket are required. For simplicity, a bucket of circular form is again assumed which has a radius of curvature r_b referring to Fig. 12.1. The assumption of a circular bucket is justified because the longitudinal, i.e., radial profile of a Pelton bucket, can be well approximated by a circular shape.

As starting point a water particle is considered whose height, according to Fig. 12.1a, is equal to the height of the water sheet. The position angle of the particle at the bucket entry is specified by $\tau = 0$. The related time is set to zero. The time-dependent position of the particle in the rotating bucket is then calculated from $r_\text{b}\text{d}\tau = W\text{d}t$ by

$$t = \int_0^\tau \frac{r_{\text{b}}}{W} \mathrm{d}\tau. \tag{12.2}$$

The integration shall be calculated over the position angle τ. The reason for such an integration form is that the upper limit of the integration, as a geometric quantity, is usually predefined. In particular, from the above integration, the rotation angle of the bucket is directly coupled with the position angle of the particle in the bucket:

$$\Delta\alpha = \omega t = r_{\text{b}}\omega \int_0^\tau \frac{1}{W} \mathrm{d}\tau. \tag{12.3}$$

According to Fig. 12.1b, the radial position of the water particle in the bucket is determinable by the law of cosines:

$$R^2 = r_{\text{b}}^2 + R_{\text{o}}^2 - 2r_{\text{b}}R_{\text{o}} \cos(\psi - \tau). \tag{12.4}$$

The angle ψ is a fixed value and can be calculated from the condition of $R = R_{\text{c}}$ at $\tau = 0$ as

$$\cos\psi = \frac{R_{\text{o}}^2 + r_{\text{b}}^2 - R_{\text{c}}^2}{2r_{\text{b}}R_{\text{o}}}. \tag{12.5}$$

The angle β for the relative flow velocity is calculated in a similar way by the use of the cosine law, viz.,

$$\cos\beta = \frac{R^2 + r_{\text{b}}^2 - R_{\text{o}}^2}{2r_{\text{b}}R}. \tag{12.6}$$

At the time $t = 0$, the particle is located at the bucket entry, as specified by

$$\cos\beta_1 = \frac{R_{\text{c}}^2 + r_{\text{b}}^2 - R_{\text{o}}^2}{2r_{\text{b}}R_{\text{c}}}. \tag{12.7}$$

The angle β_1 denotes the direction of relative velocity of a particle at the bucket entry and along the bucket surface. The relative flow angle of the particle before entering the bucket is denoted by β_0. Because there is usually $\beta_1 \neq \beta_0$, there occurs a *shock load* along the cutout edge of the bucket. The related flow mechanism and the power contribution of the shock load have already been calculated in Sect. 5.9. To calculate the overall hydraulic performance of a Pelton turbine, the outcome of this shock load must be included.

The above equations show only the geometric relations between the geometric parameters such as R, τ, $\Delta\alpha$, ψ, and β. The time- or position-dependent relative velocity of the particle in the bucket is determined by Eq. (12.1). Taking into account the relation $\sin\beta \mathrm{d}s = -\mathrm{d}R$ along the flow path s, it yields

$$\frac{1}{2}\left(W^2 - W_1^2\right) = \frac{1}{2}\omega^2\left(R^2 - R_1^2\right) + \int_{R_1}^{R} c_f \frac{W^2}{2h\sin\beta}dR. \tag{12.8}$$

The water-sheet height h can be determined just as in Chap. 7. The relative flow rate of the entire jet, according to Eq. (7.5), is given by

$$\dot{Q}_w = \frac{1}{4}\pi d_0^2 W_{0x,o}. \tag{12.9}$$

Here, the velocity component $W_{0x,o}$ is referred to the jet layer on the jet axis. It is, therefore, given by $W_{0x,o} = C_0 - U_m$ and remains constant for all particles in the same jet layer.

In Fig. 12.2, the width of the water sheet comprises two bucket halves which together are denoted by d. Since the flow rate is given by $\dot{Q}_w = hdW$, by equalizing it with Eq. (12.9), the water-sheet height is obtained as

$$h = \frac{\pi}{4}\frac{d_0^2}{d}\frac{W_{0x,o}}{W}. \tag{12.10}$$

At the bucket entry ($s = 0$), $d \approx d_0$ holds. Comparison with Eq. (7.6) shows a difference in the water-sheet height by a factor of two. This is because in the current case, the jet at the bucket cutout has a width d_0 for both bucket halves, while in Eq. (7.6), according to Fig. 7.3, the jet width d_0 applies for each half of the bucket. This difference must be taken into account particularly when the flow in the bucket is significantly different from a purely radial flow.

Fig. 12.2 Longitudinal flow of water through a Pelton bucket
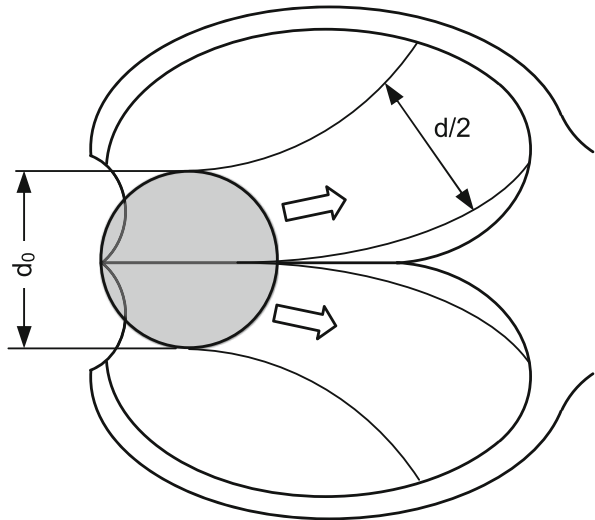
For simplicity, linear spreading of the water sheet is again assumed in two bucket halves as follows:

$$d = d_0 + \frac{d_2 - d_0}{S} s. \tag{12.11}$$

Here, d_2 denotes the total water-sheet width in both bucket halves at the bucket exit.

With the assumption of a constant friction coefficient, Eq. (12.8) is further simplified to

$$\frac{1}{2}\left(W^2 - W_1^2\right) = \frac{1}{2}\omega^2\left(R^2 - R_1^2\right) + \frac{2c_{\mathrm{f}}}{\pi d_0^2 W_{0\mathrm{x,o}}} \int_{R_1}^{R} \frac{W^3 d}{\sin\beta} \mathrm{d}R. \tag{12.12}$$

The integration can first be converted to a summation form and then numerically determined. This will be shown in Sect. 12.4 based on a computational example.

12.2 Dynamic Equations and Calculations of Hydraulic Powers

In order to represent the dynamic behavior of the flow in a rotating bucket, contributions of respective volume forces as well as the friction force should be quantified. As volume forces, both the centrifugal and Coriolis forces simultaneously act on the bucket with their components perpendicular to the bucket surface. The definitions of the centrifugal and Coriolis forces are found in Eqs. (6.1) and (6.2), respectively. Another volume force is the impulsive force in connection with the change of flow direction along the bucket surface. It has already been encountered in Eqs. (6.10) and (10.25), where it was the only effective force opposite to the pressure force below the water sheet.

In Fig. 12.3, all available force vectors as well as the bucket unit normal vector ($\vec{n}$) are shown. The sum of all force components perpendicular to the bucket surface represents the force acting on a fluid particle. Its magnitude is equal to the force exerted on the bucket. Thus, for a unit mass of fluid, the specific bucket driving force is given by

$$F_{\mathrm{n}} = \frac{W^2}{r_{\mathrm{b}}} - \vec{F}_{\mathrm{ct}} \cdot \vec{n} - \vec{F}_{\mathrm{Co}} \cdot \vec{n}. \tag{12.13}$$

Here, r_{b} is referred to as the local radius of curvature of the bucket inner surface.

The friction force that arises from the shear stress directly acts on the bucket surface tangentially in the direction of the flow. The direct friction force found in an infinitesimal area is obtained by

Fig. 12.3 Force
equilibrium on a water
particle with longitudinal
movement in a circular
Pelton bucket. F_{ct}, F_{Co}, and
F_n act on the water particle;
F_d acts on the bucket
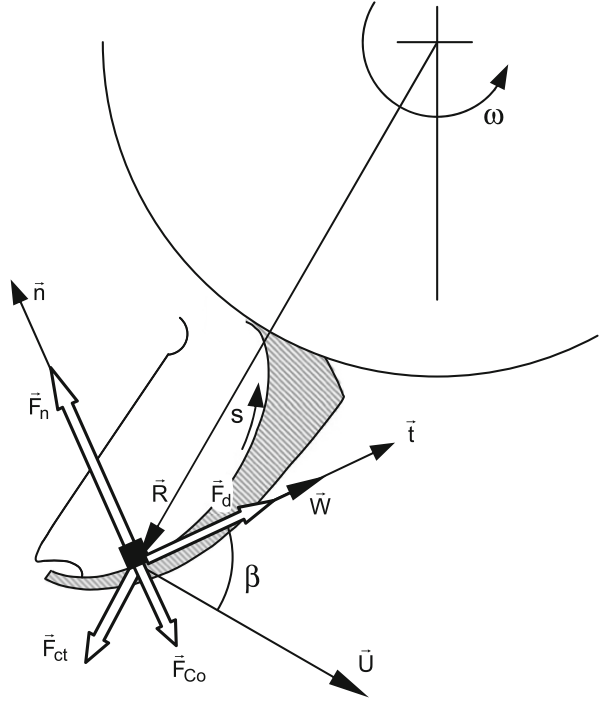
$$dF_d = c_f \frac{1}{2} \rho W^2 dds. \tag{12.14}$$

Since the bucket rotates, both the normal driving force and the friction force on the
bucket surface perform the mechanical work. It should be noted that the effective
force for performing mechanical work is always the force component in the
circumferential direction of the rotating bucket. The specific power provided by
all specific volume forces is, thus, calculated to

$$\dot{e} = \frac{de}{dt} = F_n(-\vec{n}) \cdot \vec{U} = -\frac{W^2}{r_b} \vec{n} \cdot \vec{U} + \left(\vec{F}_{ct} \cdot \vec{n}\right) \vec{n} \cdot \vec{U} + \left(\vec{F}_{Co} \cdot \vec{n}\right) \vec{n} \cdot \vec{U}. \tag{12.15}$$

It is actually the same as Eq. (6.50).

The power contribution of the direct friction force within an infinitesimal flow
path is given by

$$dP_d = dF_d \cos \beta U = c_f \frac{1}{2} \rho W^2 \cos \beta U dds. \tag{12.16}$$

This equation is comparable to Eq. (10.16).

To further process the above equations and calculations, the system of equations
must be supplemented by the *kinematic equation*, which is given by Eq. (12.12).

Respective mechanical powers can be obtained by integrating Eqs. (12.15) and (12.16) from the bucket entry to the exit. As mentioned in the previous section, the shock load force which is related to the sudden change of flow direction at the bucket cutout also contributes to the mechanical work. This contribution has to be additionally counted to the shaft power of a Pelton turbine.

12.3   Contributions of Flow Forces and Hydraulic Dissipation

In order to perform the vector analysis in Eq. (12.15), an orthogonal coordinate system (t, n, z), according to Fig. 12.3, is implemented. The z-coordinate agrees with the rotation axis of the Pelton wheel. Corresponding geometry and flow parameters have already been shown in Chap. 6 and are listed here again:

$$
\begin{aligned}
\vec{n} &= (0, \ 1, \ 0), \\
\vec{R} &= (-R\sin\beta, \ -R\cos\beta, \ 0), \\
\vec{\omega} &= (0, \ 0, \ \omega), \\
\vec{U} &= (\omega R\cos\beta, \ -\omega R\sin\beta, \ 0), \\
\vec{W} &= (W, \ 0, \ 0).
\end{aligned}
\tag{12.17}
$$

The contributions of diverse flow forces are considered below.

12.3.1   Shock Load at the Bucket Entry

While entering the bucket at the bucket cutout, the jet flow usually undergoes a sudden change in flow direction. Associated with it is the formation of the *shock load*, as already discussed in Chap. 5. The corresponding power contribution and partial efficiency have been calculated by Eqs. (5.68) and (5.71), respectively. For completeness of these computations in the current chapter, the related partial efficiency, according to Eq. (5.71) and Fig. 5.16, is written here again as

$$
\eta_{\text{shock}} = 2k_{\text{m}}^2 \frac{W_0}{U_{\text{m}}} \frac{R_{\text{c}}}{R_{\text{m}}} (\cos\beta_0 - \cos\beta_1).
\tag{12.18}
$$

This partial efficiency arising from the shock load is regarded as an incident quantity in contrast to other process quantities that can only be calculated through integrations.

12.3.2 Impulsive Force in the Bucket

The force associated with the continuous deflection of the flow in the bucket (congruent flow) has been described in Sect. 12.2 as an *impulsive force*. The specific work, which is done by this force over the time, can be calculated from the corresponding term in Eq. (12.15), based on Fig. 12.3, as follows:

$$e_{\mathrm{I}} = -\int_0^t \frac{W^2}{r_{\mathrm{b}}} \vec{n} \cdot \vec{U} \mathrm{d}t = \int_0^t \frac{W^2}{r_{\mathrm{b}}} \omega R \sin\beta \mathrm{d}t. \qquad (12.19)$$

Because $W \mathrm{d}t = \mathrm{d}s$ with s as the coordinate along the flow path and with relation $\sin\beta \mathrm{d}s = -\mathrm{d}R$, as shown in Fig. 12.3, Eq. (12.19) is converted to

$$e_{\mathrm{I}} = -\omega \int_{R_1}^R \frac{W}{r_{\mathrm{b}}} R \mathrm{d}R. \qquad (12.20)$$

This specific mechanical work should be related to the specific kinetic energy $\frac{1}{2} C_0^2$ of the jet. With the definition of k_{m} according to Eq. (2.18), one obtains the corresponding partial efficiency as

$$\eta_{\mathrm{I}} = \frac{e_{\mathrm{I}}}{C_0^2/2} = -2k_{\mathrm{m}}^2 \int_{R_1}^R \frac{1}{r_{\mathrm{b}}} \frac{W}{U_{\mathrm{m}}} \frac{R}{R_{\mathrm{m}}} \mathrm{d}R. \qquad (12.21)$$

As identifiable in Fig. 12.1, $R_1 = R_{\mathrm{c}}$ is the lower bound of integration. Since the corresponding upper bound is specified by the variable R, the above equation shows the time-dependent efficiency of the flow while passing through the bucket. This will be again illustrated below by means of a computational example.

The integral in Eq. (12.21) can be calculated when it is first converted to a summation form and then numerically solved in connection with the *kinematic equation*, i.e., Eq. (12.12). For frictionless flows in a circular bucket, the above equation reduces to Eq. (6.94).

12.3.3 Centrifugal Force

The specific centrifugal force is given by Eq. (6.1) and is equal to $R\omega^2$. Between the centrifugal force and the normal of the bucket surface, according to Fig. 12.3, an angle of $\pi - \beta$ is measured, so that the scalar product of $\vec{F}_{\mathrm{ct}}$ with $\vec{n}$ is given by $\vec{F}_{\mathrm{ct}} \cdot \vec{n} = -R\omega^2 \cos\beta$. The specific work which is done by the centrifugal force is calculated from the corresponding term in Eq. (12.15); the result is

$$e_{\text{ct}} = \int\limits_0^t \left(\vec{F}_{\text{ct}} \cdot \vec{n}\right) \vec{n} \cdot \vec{U} \mathrm{d}t = -\omega^3 \int\limits_{R_1}^R R^2 \cos\beta \frac{1}{W} \mathrm{d}R. \tag{12.22}$$

Here, relations $W\mathrm{d}t = \mathrm{d}s$ and $\sin\beta \mathrm{d}s = -\mathrm{d}R$ have been used.

The specific work given in Eq. (12.22) should be normalized by the specific kinetic energy of the jet. With respect to the definition of the peripheral speed coefficient k_{m}, one then obtains the related efficiency in the form

$$\eta_{\text{ct}} = -2k_{\text{m}}^2 \int\limits_{R_1}^R \frac{R^2}{R_{\text{m}}^3} \frac{U_{\text{m}}}{W} \cos\beta \mathrm{d}R. \tag{12.23}$$

As in Eq. (12.21), this partial efficiency is a process quantity.

12.3.4   Coriolis Force

The Coriolis force is given by Eq. (6.2) and its modulus equals to $2\omega W$. The corresponding vector product $\vec{F}_{\text{Co}} \cdot \vec{n}$ is calculated, according to Fig. 12.3, to $-2\omega W$. The negative sign is due to the fact that $\vec{F}_{\text{Co}}$ and $\vec{n}$ are antiparallel. By applying Eq. (12.17), the work which is done by the Coriolis force can be calculated from the corresponding term in Eq. (12.15), as given by

$$e_{\text{Co}} = \int\limits_0^t \left(\vec{F}_{\text{Co}} \cdot \vec{n}\right) \vec{n} \cdot \vec{U} \mathrm{d}t = 2\omega^2 \int\limits_0^t WR \sin\beta \mathrm{d}t. \tag{12.24}$$

Now, since $W\sin\beta = -W_{\text{r}} = -\mathrm{d}R/\mathrm{d}t$, the above calculation is simplified to

$$e_{\text{Co}} = -2\omega^2 \int\limits_{R_1}^R R\mathrm{d}R. \tag{12.25}$$

The integration then leads to

$$e_{\text{Co}} = \omega^2 \left(R_1^2 - R^2\right) = U_1^2 - U^2. \tag{12.26}$$

If related to the specific kinetic energy of the jet, as in Eq. (12.23), and with $R_1 = R_{\text{c}}$, the corresponding partial efficiency is then obtained as

$$\eta_{\mathrm{Co}} = 2k_{\mathrm{m}}^2 \left(\frac{R_{\mathrm{c}}^2}{R_{\mathrm{m}}^2} - \frac{R^2}{R_{\mathrm{m}}^2} \right). \tag{12.27}$$

It is independent of the path followed by the fluid particles. Because it is also independent of fluid viscosity, Eq. (12.27) is the same as Eq. (6.81) for frictionless flows.

12.3.5   Direct Friction Force

Viscous friction has also a direct effect on the mechanical power. This can be determined from Eq. (12.16) as

$$P_{\mathrm{d}} = c_{\mathrm{f}} \frac{1}{2} \rho \int_0^s W^2 U d \cos \beta \mathrm{d}s. \tag{12.28}$$

Substituting relation $\sin \beta \mathrm{d}s = -\mathrm{d}R$ leads to

$$P_{\mathrm{d}} = -c_{\mathrm{f}} \frac{1}{2} \rho \int_{R_1}^R W^2 U \frac{d}{\tan \beta} \mathrm{d}R. \tag{12.29}$$

Since according to Fig. 12.2 the water-sheet width d is referred to both bucket halves, the above calculation applies to a complete Pelton bucket. Furthermore, the number of buckets undergoing impingement of one jet has been given by 2λ; see Chap. 7 and Eq. (7.7). Under these circumstances, the partial efficiency from direct viscous friction is obtained by relating the corresponding power to the jet power P_0 as follows:

$$\eta_{\mathrm{d}} = \frac{2\lambda P_{\mathrm{d}}}{\frac{1}{4}\pi d_0^2 C_0 \frac{1}{2} \rho C_0^2} = -\frac{4c_{\mathrm{f}}}{\pi d_0^2} \frac{k_{\mathrm{m}}^3}{1 - k_{\mathrm{m}}} \frac{1}{U_{\mathrm{m}}^3} \int_{R_1}^R \frac{dW^2 U}{\tan \beta} \mathrm{d}R. \tag{12.30}$$

As will be shown, this partial efficiency is expected to be negative and is also negligible when computing the integral for $R = R_2$ (until the bucket exit). A similar result has already been obtained in Chap. 11 for cross-flows with $U = \mathrm{const}$.

12.3.6   Hydraulic Dissipation

The viscous friction force in an infinitesimal area on the bucket surface is given by Eq. (12.14). The related infinitesimal dissipation rate is then calculated by

$$d\dot{E}_{\text{diss}} = W dF_{\text{d}} = c_{\text{f}} \frac{1}{2} \rho W^3 dds. \tag{12.31}$$

The cumulative dissipation rate can be calculated as a function of the path length of the flow in the rotating bucket, as given by the following integration:

$$\dot{E}_{\text{diss}} = c_{\text{f}} \frac{1}{2} \rho \int_0^s W^3 dds. \tag{12.32}$$

Since according to Fig. 12.2 the water-sheet width d is referred to both bucket halves, the above calculation is in effect for a complete Pelton bucket. In addition, there are always 2λ buckets simultaneously undergoing impingement of each jet, as this has been revealed in Sect. 7.1; see Eq. (7.7). The total dissipation rate in 2λ buckets is then related to the jet power. This results in the *dissipative efficiency loss*

$$\Delta\eta_{\text{diss}}(s) = \frac{2\lambda\dot{E}_{\text{diss}}}{P_0} = \frac{4c_{\text{f}}}{\pi d_0^2} \frac{1}{1 - k_{\text{m}}} \frac{1}{C_0^3} \int_0^s W^3 dds. \tag{12.33}$$

Because $\sin\beta ds = -dR$ from Fig. 12.3, the above equation is also written as

$$\Delta\eta_{\text{diss}}(R) = -\frac{4c_{\text{f}}}{\pi d_0^2} \frac{1}{1 - k_{\text{m}}} \frac{1}{C_0^3} \int_{R_1}^R \frac{W^3 d}{\sin\beta} dR. \tag{12.34}$$

It represents here again a process quantity with starting point at the bucket entry, i.e., the bucket cutout edge. For water flow throughout the bucket, the upper bound of integration in the above equations is replaced by $s = S$ and $R = R_2$, respectively.

Combining Eq. (12.34) with the kinematic equation, i.e., Eq. (12.12), yields for $R = R_2$ and thus $U = U_2$ (for through flow)

$$\Delta\eta_{\text{diss}} = \frac{1}{1 - k_{\text{m}}} \frac{W_{0\text{x,o}}}{C_0^3} \left[(W_1^2 - U_1^2) - (W_2^2 - U_2^2) \right]. \tag{12.35}$$

With $W_{0\text{x,o}} = C_0 - U_{\text{m}}$ and $k_{\text{m}} = U_{\text{m}}/C_0$ as well as the energy invariance $E_1 = W_1^2 - U_1^2$ and $E_2 = W_2^2 - U_2^2$, it finally follows

$$\Delta\eta_{\text{diss}} = \frac{E_1 - E_2}{C_0^2}. \tag{12.36}$$

The viscous friction effect in this case can be evidenced in the difference $E_1 - E_2$. When the energy invariance $E_2 = W_2^2 - U_2^2$ is replaced by $E_2 = \left(W_2^2 - W_{20}^2\right) + \left(W_{20}^2 - U_2^2\right) = \left(W_2^2 - W_{20}^2\right) + E_{20}$ with E_{20} for the case of frictionless flow, then, because of $E_{20} = E_1$, i.e., energy invariance, Eq. (12.36) becomes

$$\Delta\eta_{\text{diss}} = \frac{W_{20}^2 - W_2^2}{C_0^2}. \tag{12.37}$$

This equation combines the dissipation rate in the bucket flow with the exit flow velocity W_2 out of the bucket. It exactly agrees with one's expectation.

Consider next again Eq. (12.33). The water-sheet width d in the equation will be replaced by Eq. (12.10). With $W_{0x,o} = C_0 - U_m$ and $k_m = U_m/C_0$, it follows then

$$\Delta\eta_{\text{diss}}(s) = \frac{1}{C_0^2} \int_0^s c_f \frac{1}{h} W^2 \mathrm{d}s. \tag{12.38}$$

For $s = S$ and equalizing this with Eq. (12.37), one obtains

$$W_2^2 = W_{20}^2 - \int_0^S c_f \frac{1}{h} W^2 \mathrm{d}s. \tag{12.39}$$

Sometimes it may be convenient to introduce a *dissipation coefficient* c_{w2} as defined by

$$\frac{W_2^2}{W_{20}^2} = 1 - \frac{1}{W_{20}^2} \int_0^S c_f \frac{1}{h} W^2 \mathrm{d}s = 1 - c_{w2}. \tag{12.40}$$

This dissipation coefficient is comparable to the friction number which has been defined in Eq. (10.12) for lateral cross-flows. For this reason the dissipation coefficient can also be denoted as *friction number*.

12.3.7 Overall Efficiency

The sum of all partial efficiencies provides the overall hydraulic efficiency of the supposed model with purely radial flow according to Fig. 12.1, as given by

$$\eta_h = \eta_{\text{shock}} + \eta_I + \eta_{ct} + \eta_{Co} + \eta_d. \tag{12.41}$$

The difference of this hydraulic efficiency to the value of 100 % has to be equal to the sum of friction-dependent hydraulic dissipation and the swirling loss which is connected to the exit flow:

$$\Delta\eta_{\text{diss}} + \Delta\eta_{\text{swirl}} = 1 - \eta_h. \tag{12.42}$$

As will be shown in the concrete computational example below, the friction-dependent hydraulic dissipation $\Delta\eta_{\text{diss}}$ again represents the dominant part in the total efficiency loss in the considered flow model.

12.4   Computations for a Concrete Realistic Example

In order to show the computational process of determining all force effects and respective contributions to partial efficiencies, a flow model of a longitudinally circular bucket form is considered. This flow model approaches the flow in a real Pelton turbine when the jet is cut off by the bucket cutout. Parameter specifications of a used reference Pelton turbine are summarized in Table 12.1.

Computations can be performed by the numerical method of using the tabular algorithms, at which, for instance, 20 computational steps are defined from bucket entry to exit. Table 12.2 shows the corresponding computational scheme. The jet circle radius (R_m) and the corresponding peripheral speed (U_m) are used as references.

The absolute flow velocity C/C_0 in each computational step is obtained by considering velocity triangles. Calculations of W/U_m go back to Eq. (12.8) which is differentiated to yield

Table 12.1 Parameter specification of a reference Pelton turbine

Specific speed n_q	1/s	0.10
Peripheral speed coefficient k_m	–	0.47
Bucket volumetric load $\varphi_B = (d_0/B)^2$	–	0.11
Bucket width B/D_m	–	0.24
Jet diameter d_0/D_m	–	0.08
Cutout circle diameter D_c/D_m	–	1.21
Radius of curvature of bucket inner surface r_b/B	–	0.50
Position of the center of curvature of bucket inner surface R_o/R_m	–	1.10
Entry flow angle β_1	°	56.0
Exit flow angle β_2	°	173.0
Angle ψ according to Eq. (12.5)	°	113.0
Friction coefficient c_f	–	0.015

Table 12.2 Scheme of flow computations in a circular bucket according to Fig. 12.1

τ	$\frac{R}{R_m}$	β	$\frac{d}{d_0}$	$\frac{h}{R_m}$	$\left(\frac{W}{U_m}\right)^2$	$\Delta\alpha$	η_{ct}	η_{Co}	η_l	η_d	η_h	$\left(\frac{C}{C_0}\right)^2$	$\Delta\eta_{diss}$
0.0	1.20	0.95	1.00	0.120	1.375	0	0	0	0	0	0.02	0.982	0
4.5	1.19	1.02	1.06	0.115	1.342	0.01	0.004	0.013	0.040	0.000	0.08	0.924	0.0006
9.0	1.17	1.10	1.12	0.111	1.309	0.03	0.007	0.027	0.081	0.000	0.13	0.864	0.0012
..	..	..	..	..	..	..	..	..	..	..	..	..	..
Eqs.	(12.4)	(12.6)	(12.11)	(12.10)	(12.8)	(12.3)	(12.23)	(12.27)	(12.21)	(12.30)	(12.41)	–	(12.34)

$$\mathrm{d}\left(\frac{W^2}{U_{\mathrm{m}}^2}\right) = 2\left(\frac{R}{R_{\mathrm{m}}} + \frac{c_{\mathrm{f}}}{\sin\beta}\frac{R_{\mathrm{m}}}{2h}\frac{W^2}{U_{\mathrm{m}}^2}\right)\mathrm{d}\left(\frac{R}{R_{\mathrm{m}}}\right). \tag{12.43}$$

For numerical solution this equation is then digitized as

$$\left(\frac{W^2}{U_{\mathrm{m}}^2}\right)_i = \left(\frac{W^2}{U_{\mathrm{m}}^2}\right)_{i-1} + 2\left(\frac{R}{R_{\mathrm{m}}} + \frac{c_{\mathrm{f}}}{\sin\beta}\frac{R_{\mathrm{m}}}{2h}\frac{W^2}{U_{\mathrm{m}}^2}\right)\left(\frac{R_i}{R_{\mathrm{m}}} - \frac{R_{i-1}}{R_{\mathrm{m}}}\right). \tag{12.44}$$

Computational results for the radial flow in a rotating bucket of the considered Pelton turbine are shown in Fig. 12.4. In the diagram, the partial efficiency due to the shock load at the bucket entry is confirmed at $\tau = 0$ to $\eta_{\mathrm{shock}} = \eta_{\mathrm{h}} = 2.0\,\%$. Obviously, the centrifugal force in the flow by reaching the bucket exit only contributes to a very small but negative value of the mechanical power. The direct friction effect on the hydraulic efficiency is less than 0.5 %. Both the Coriolis and impulsive forces dominate contributions to the overall hydraulic efficiency. While the flow reaches the bucket exit ($\tau = 107°$), the overall hydraulic efficiency reaches a value of 98.1 %. Accordingly, the total hydraulic loss is approximately 1.9 %. It includes the viscous dissipation during the flow through the bucket and the swirling loss at the bucket exit.

In the performed tabular calculations, both the viscous dissipation and the swirling loss have also been determined. Figure 12.5 shows the corresponding numerical results as functions of the rotation angle $\Delta\alpha$ of the bucket. The flow reaches the bucket exit, after the bucket has rotated by an angle of approximately 28°. The hydraulic efficiency is the same as that shown in Fig. 12.4. The square of the velocity ratio $(C/C_0)^2$ at the bucket exit represents the swirling loss in the considered hydraulic system. As can be confirmed from the calculations, the swirling loss is only of about 0.37 %, while the efficiency loss arising from the viscous dissipation measures 1.5 %. The total efficiency loss is thus 1.9 %. This result straightforwardly confirms the given relation in Eq. (12.42).

Fig. 12.4 Calculation example of the partial and overall efficiencies in a flow system according to Fig. 12.3. Parameter specification according to Table 12.1
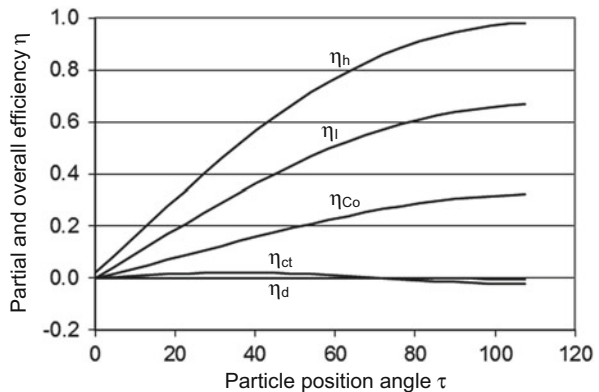
Fig. 12.5 Time-dependent overall efficiency, absolute speed, and dissipation in a flow system according to Fig. 12.3
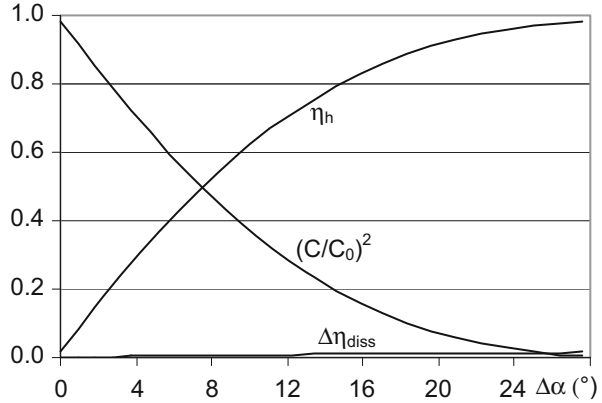
In accordance with $\Delta\eta_{\mathrm{diss}} = 1.5\,\%$ from the viscous dissipation, the dissipation coefficient has been obtained as $c_{\mathrm{w2}} = 0.1$ (not shown in Table 12.2) The real flow velocity at the bucket exit, if related to that for frictionless flow, is obtained from Eq. (12.40) to $W_2/W_{20} = 0.95$.

The current computational example again indicates that the viscous friction on the bucket surface is a source causing the main loss in hydraulic efficiencies of a Pelton turbine, although it only takes 1.5 % in the current example.

In performing presented tabular calculations, influences of all other parameters such as k_{m}, c_{f}, and β_2 on the flow as well as on the hydraulic efficiency can be visualized and evaluated in a very simple way. In the conducted calculations, it has been confirmed, for instance, that swirling losses at the bucket exit are hardly affected by viscous friction. Such a flow property has already been indicated in Chap. 11 by Eq. (11.15).

Chapter 13
Friction and Windage Losses in Pelton Wheels

Friction and windage losses in Pelton wheels arise because the air around the Pelton wheel is continuously entrained to circulate and the rotation of Pelton wheels is persistently resisted by air friction on the wheel surface. These effects are therefore referred to as *internal mechanical losses*, and in practical applications, these two types of losses depend on designs of the turbine casing, wheel size, and rotational speed of the wheel. They are strongly coupled so that they cannot be separated from each other, neither in calculations nor from measurements. In particular, air mixture as enriched by water sprays plays a special role because of its specific density.

The simplest model with friction and windage losses is a disk which rotates in the open air. According to Dubs (1954) based on past experiences and also according to the IEC60041 standard (1991), friction and windage losses are calculated by the formula

$$P_{\mathrm{wi}} = 75.6 n^3 D^5 \left(1 + 1.8\frac{B}{D}\right) \times 10^{-3} (\mathrm{W}). \tag{13.1}$$

The parameters B and D represent the disk thickness and diameter, respectively. For the rotational speed n, the unit 1/s must be used. The expression in parentheses takes into account the total exposed surface of the disk. It is noticeable that friction and windage losses depend on the 3rd power of the rotational speed and the 5th power of the wheel diameter. The above law reveals, from dimensional analysis, that the numerical factor in Eq. (13.1) simply possesses the dimension of the specific mass density (kg/m^3). It, thus, clearly implies that, strictly speaking, it is only valid for a mean specific density of the ambient air.

The law given in Eq. (13.1) as a function of the speed and the wheel diameter has been generally validated in practice. It has also been applied, for instance, to determine the friction loss in the side room of impellers in other types of turbomachinery (Pfleiderer and Petermann 1986).

For a Pelton turbine, the object to be considered is the Pelton wheel with buckets in a closed casing. Because of bucket effects, the friction and windage losses are

significantly higher than at a simple disk in open air. In addition, the friction and
windage losses depend on the casing design of Pelton turbines, so that one has to
distinguish between the horizontal and the vertical installations of Pelton wheels
(Gerber 1956). Furthermore, for Pelton turbines always wet air is involved, which is
actually a mixture of air and spray water and, thus, may be of quite different specific
densities from case to case.

13.1   Pelton Turbines with Horizontal Axes

For Pelton turbines with horizontal rotation axes, all relevant geometric design
parameters are shown in Fig. 13.1. The power that is required to compensate for the
friction and windage losses is calculated using IEC60041 standard (1991) as
follows:

$$P_{\mathrm{wi}} = 15 n^3 D^5 \left(\frac{B_a}{D}\right)^{1/4} \left(\frac{B_{io}}{D}\right)^{3/4} \left(\frac{B_{iu}}{D}\right)^{5/4} \left(\frac{R_{io}}{D}\right)^{7/4} (\mathrm{W}). \qquad (13.2)$$

Dimensionally, this is the same law as in Eq. (13.1), but influences of all casing
parameters on the windage power are taken into account. The unit of rotational
speed n is again 1/s. For a given Pelton turbine, Eq. (13.2) is rewritten in the
following abbreviated form:
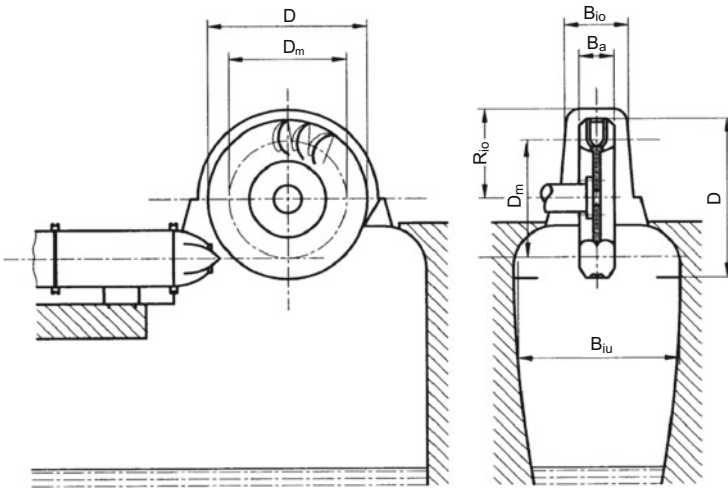
Fig. 13.1 Parameter definition for calculations of friction and windage losses in a horizontal
Pelton turbine according to IEC60041 (1991)

$$P_{\text{wi}} = a \cdot n^3 D^5 (\text{W}). \tag{13.3}$$

Here, a is a constant which combines the air property and design parameters of the turbine casing. Its dimension is kg/m^3, i.e., the same as the dimension of the specific density.

For comparison with Eq. (13.1), a particular Pelton turbine is considered here as an example. The turbine casing is given by $B_{\text{a}}/D = 0.2$, $B_{\text{io}}/D = 0.3$, $B_{\text{iu}}/D = 1$, and $R_{\text{io}}/D = 0.6$, for which one obtains from Eq. (13.2)

$$P_{\text{wi}} = 1.7 n^3 D^5 (\text{W}). \tag{13.4}$$

The friction and windage losses at the Pelton turbine in this example are about 16 times greater than at a comparable disk in open air. This is not only because of the presence of the turbine casing, but mainly because of the presence of Pelton buckets and also of comparably high specific density of the air-water mixture. It should be noted that Eq. (13.2) is valid only for a mean specific density of wet air in the turbine casing and is therefore expected to have a limited accuracy of $\pm 50\,\%$ in practical applications. This statement is again based on the fact that the constant a in Eq. (13.3) has the same dimension as the specific density. Exact friction and windage losses depend on the design of turbine casings and can be directly determined, for instance, by so-called retardation tests. They will be considered in Sect. 13.3 in more details.

The magnitude of the friction and windage losses should somewhat further be treated. To this end, the nominal power of the Pelton turbine, as given by $P_{0,\text{N}} = Z_{\text{jet}} \rho g H \dot{Q}_{\text{jet}}$ with Z_{jet} as the number of installed injectors (jets), is then used as a scaling, so that

$$\Delta \eta_{\text{wi}} = \frac{P_{\text{wi}}}{P_{0,\text{N}}} = \frac{a}{\rho Z_{\text{jet}}} \cdot \frac{n^3 D^5}{g H \dot{Q}_{\text{jet}}}. \tag{13.5}$$

The second fraction term on the right-hand side of this equation should be further represented as a function of the specific speed n_{q}. For this purpose, $D \approx D_{\text{c}}$ is assumed (for D_{c} see Figs. 2.4 and 2.5). Then for the nominal rotational speed n_{N}, the second fraction term in the above equation is extended as

$$\frac{n_{\text{N}}^3 D^5}{g H \dot{Q}_{\text{jet}}} = \frac{2^{2.5} g^{1.5}}{\pi^5} \left(\frac{\pi n_{\text{N}} D_{\text{m}}}{\sqrt{2gH}} \right)^5 \left(\frac{H^{3/4}}{n_{\text{N}} \sqrt{\dot{Q}_{\text{jet}}}} \right)^2 \frac{D_{\text{c}}^5}{D_{\text{m}}^5}. \tag{13.6}$$

With the aid of Eq. (2.31) for $D_{\text{c}}/D_{\text{m}}$ and the definitions for k_{m} and n_{q}, according to Eq. (2.18) and Eq. (2.22), respectively, the above equation is rewritten as

$$\frac{n_{\mathrm{N}}^3 D^5}{gH\dot{Q}_{\mathrm{jet}}} = 0.57 k_{\mathrm{m,N}}^5 \left(1 + 2n_{\mathrm{q}}\right)^5 \frac{1}{n_{\mathrm{q}}^2}. \tag{13.7}$$

Accordingly, for the specific density of water $\rho = 1000\,\mathrm{kg/m^3}$ and the rotational speed n as a variable, the friction and windage losses as given in Eq. (13.5) are represented as

$$\Delta\eta_{\mathrm{wi}} = 0.57 \times 10^{-3} \frac{a}{Z_{\mathrm{jet}}} k_{\mathrm{m,N}}^5 \left(1 + 2n_{\mathrm{q}}\right)^5 \frac{1}{n_{\mathrm{q}}^2} \frac{n^3}{n_{\mathrm{N}}^3}, \tag{13.8}$$

or, commonly, for $k_{\mathrm{m,N}} = 0.47$, as

$$\Delta\eta_{\mathrm{wi}} = 1.3 \times 10^{-5} \frac{a}{Z_{\mathrm{jet}}} \left(1 + 2n_{\mathrm{q}}\right)^5 \frac{1}{n_{\mathrm{q}}^2} \frac{n^3}{n_{\mathrm{N}}^3}. \tag{13.9}$$

A new dimensionless number called *windage number* is introduced and defined as

$$\mathrm{Wi} = g^{1.5} \frac{\left(1 + 2n_{\mathrm{q}}\right)^5}{n_{\mathrm{q}}^2}. \tag{13.10}$$

Like the specific speed n_{q}, according to Eq. (2.26), the *windage number* is also a geometrical parameter.

With the windage number, the friction and windage losses are then expressed as

$$\Delta\eta_{\mathrm{wi}} = 4.2 \times 10^{-7} \mathrm{Wi} \frac{a}{Z_{\mathrm{jet}}} \frac{n^3}{n_{\mathrm{N}}^3}. \tag{13.11}$$

For the nominal rotational speed and single-jet turbines, there is

$$\Delta\eta_{\mathrm{wi,N}} = 4.2 \times 10^{-7} a\mathrm{Wi}. \tag{13.12}$$

In accordance with its definition, the windage number is in effect a function of the specific speed, as shown in Fig. 13.2. It should be noted, however, that in Eq. (13.11) the full dependence of the friction and windage losses on the specific speed is not only due to the windage number but equally also because of the design parameter a. In reality, the design parameter a depends on the design of the turbine casing and, therefore, on the specific speed of the turbine wheel.

For a single-jet Pelton turbine, for instance, with a specific speed of $n_{\mathrm{q}} = 0.1$ and a design constant of $a = 1.7$, according to Eq. (13.4), the total friction and windage loss are calculated as

Fig. 13.2 Windage number as a function of the specific speed
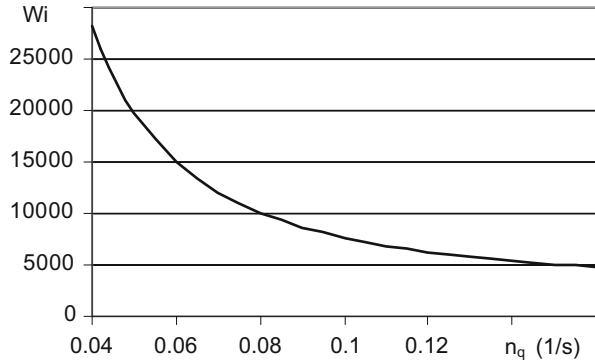
$$\Delta\eta_{\mathrm{wi}} = 0.0055\left(\frac{n}{n_{\mathrm{N}}}\right)^{3}. \tag{13.13}$$

Under the nominal rotational speed, it is about 0.55 %. In multi-jet Pelton turbines, the friction and windage losses will be even smaller because of Eq. (13.11).

In the above considerations, the dependence on the specific speed has been derived. Since the specific speed is only defined for the nominal flow rate, calculations of Eqs. (13.8)–(13.13), therefore, only apply for operations of Pelton turbines under nominal flow rate. The corresponding power loss is thus calculated as

$$P_{\mathrm{wi}} = \Delta\eta_{\mathrm{wi}}P_{0,\mathrm{N}}. \tag{13.14}$$

It only depends on the rotational speed of the Pelton wheel, but not on the flow rate.

13.2   Pelton Turbines with Vertical Axes

For Pelton turbines with vertical rotation axes, all relevant geometric design parameters are shown in Fig. 13.3. The power required to compensate for the friction and windage losses is structurally the same as Eq. (13.2) and will be estimated by the following equation according to the IEC60041 standard (1991):

$$P_{\mathrm{wi}} = 22 \cdot n^{3}D^{5}\left(\frac{B_{\mathrm{a}}}{D}\right)^{2/3}\left(\frac{B_{\mathrm{i}}}{D}\right)^{4/3}\left(\frac{R_{\mathrm{i}}}{D}\right) = a \cdot n^{3}D^{5}. \tag{13.15}$$

For the same reason as in Sect. 13.1, this estimation basically applies only for a mean specific density of wet air in the turbine casing. For the case of a geometric configuration with $B_{\mathrm{a}}/D = 0.2$, $B_{\mathrm{i}}/D = 0.3$, and $R_{\mathrm{i}}/D = 1$, one obtains from the above equation

Fig. 13.3 Parameter
definition for calculations of
friction and windage losses
in a vertical Pelton turbine
according to IEC60041
(1991)
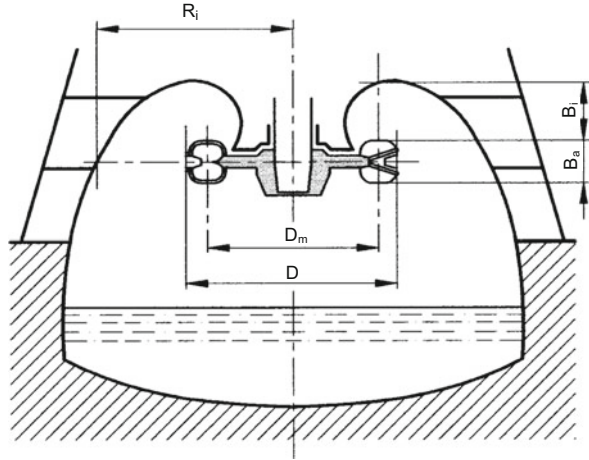
$$P_{\mathrm{wi}} = 1.5 \cdot n^3 D^5. \tag{13.16}$$

This equation is similar to Eq. (13.4) which applies to Pelton turbines with
horizontal rotation axes. To calculate efficiency losses, Eqs. (13.9) and (13.11)
can directly be used. One needs only to use the respective constant a.

The method of retardation test for accurately determining the friction and
windage losses is described in the next section.

13.3   Retardation Test Method

As is apparent from the above considerations, friction and windage losses depend
on both the design of the turbine casings and the geometries of the Pelton wheels.
Since the specific density of wet air is not taken into account as a variable in
calculations, the friction and windage losses can in no case be exactly calculated.
To accurately estimate the friction and windage losses, the so-called *retardation
test* or *running down test* has been found to be particularly convenient. The method
also enables the determination of the mechanical loss due to friction in the bearing.
In fact, the friction and windage losses together with friction from the bearing
constitute the total mechanical loss of a Pelton turbine. Since the friction loss due to
the bearing against the rotational speed behaves differently (Chap. 14) from the
friction and windage losses, it can be separately resolved from a retardation test. In
this chapter, the principle of a retardation test for the experimental determination of
the total mechanical losses will be shown, while the bearing friction loss will be
discussed in more details in Chap. 14.

The retardation of a Pelton wheel rotation begins when all jets of a Pelton turbine
are deflected and the load on the side of the generator is rejected. The rotation of the

Pelton wheel is slowing down purely due to the total mechanical braking effects both at the Pelton wheel and in the shaft bearings. During the retardation test, the time-dependent rotational speed of the Pelton wheel in the form $n = f(t)$ should be measured. By knowing the moment of inertia J of the entirety of the rotating parts (Pelton wheel, shaft, rotor of the generator), the attenuation of the Pelton turbine rotation is described by the angular momentum equation:

$$J \frac{d\omega}{dt} = M_{wi} + M_{be}. \tag{13.17}$$

Here, M_{wi} and M_{be} denote the *windage torque* at the Pelton wheel and the *friction torque* at the shaft bearings, respectively. According to Eqs. (13.4) and (13.16), the windage torque M_{wi} at the Pelton wheel can be considered to be proportional to the square of the rotational speed, so that

$$M_{wi} = \frac{K_{wi}}{2\pi} n^2. \tag{13.18}$$

For the determination of the bearing friction torque M_{be}, hydrodynamic plain bearings are assumed which are often used for Pelton turbines. According to Chap. 14, for instance, the following approach for heavy-loaded plain bearings can be applied:

$$M_{be} = \frac{K_{be}}{2\pi} n^{0.5}. \tag{13.19}$$

From Eq. (13.17) one obtains with $\omega = 2\pi n$

$$\frac{dn}{dt} = \frac{1}{4\pi^2 J} \left(K_{wi} n^2 + K_{be} n^{0.5} \right) = k_{wi} n^2 + k_{be} n^{0.5}. \tag{13.20}$$

Once the rotational speed of the rotating system during the retardation test is measured, the function $dn/dt = f(n)$ can be calculated and displayed. The curve is then approximated by the function shown in Eq. (13.20) to find out the constants k_{wi} and k_{be}. It actually deals with a curve-fitting calculation (nonlinear least-squares method). From the constants k_{wi} and k_{be}, other constants K_{wi} and K_{be} can then be further determined by knowing J. Such a test has already been carried out by Taygun (1946). A solution of the differential equation, i.e., Eq. (13.20), was also indicated there.

In case that due to the type of used plain bearings or due to other operational behaviors of fluid dynamic bearings, the exponent in Eq. (13.19) cannot simply be assumed to be 0.5, it is then advisable to determine the most appropriate exponent by precisely evaluating the retardation test curve. If necessary, the retardation curve $n = f(t)$ for bearing friction losses can be approached by partial curves with different exponential functions.

References

Dubs, R. (1954). Der Luftwiderstand von Schwungrädern, Riemenscheiben, Kupplungen und Scheiben. Bulletin des Schweizerischen Elektrotechnischen Vereins, Nr. 20.

Gerber, H. (1956). Ventilationsverluste von Freistrahlturbinen-Laufrädern, Bulletin des Schweizerischen Elektrotechnischen Vereins, Nr. 9.

IEC 60041. (1991). Field acceptance tests to determine the hydraulic performance of hydraulic turbines, storage pumps and pump-turbines (3rd ed.).

Pfleiderer, C., & Petermann, H. (1986). *Strömungsmaschinen*. Heidelberg: Springer. 5. Auflage.

Taygun, F. (1946). Untersuchungen über den Einfluss der Schaufelzahl auf die Wirkungsweise eines Freistrahlrades. Diss., Eidgenössische Technische Hochschule in Zürich.

Chapter 14
Power Loss Due to Bearing Frictions

For Pelton turbines hydrodynamic plain bearings of various constructions are almost exclusively applied. Depending on the type of Pelton turbines, either radial bearings for turbines with horizontal axes or axial bearings for vertical turbines are used. These bearings are all hydrodynamically lubricated. Hydrodynamic plain bearings operate on the principle of lubricating wedges which are formed by themselves between the sliding surfaces. The load-bearing capacity of the lubricating wedges is reached by the pressure buildup in them. Both the friction and the wear rate can, thus, be reduced to the minimum. In contrast to the rolling bearings, hydrodynamically lubricated plain bearings are used even for heavy loads. They have a long service life and run silently. The load capacity of hydrodynamic bearings depends on the pressure buildup in the lubricating film and, thus, strongly on the rotational speed of the bearing. For the detailed descriptions of the hydrodynamic lubrication theory, the reader is referred to the literatures for the design of machine elements, e.g., by Decker (2007) and Haberhauer and Bodenstein (2007).

In connection with the present intention, only the friction losses in hydrodynamically lubricated plain bearings are considered in more details. The friction force in a plain bearing is, after Coulomb's law, proportional to the loading force:

$$F_{be} = \mu F_N. \tag{14.1}$$

Accordingly, the friction power is given by multiplying the friction force with the sliding speed to

$$P_{be} = \mu F_N u. \tag{14.2}$$

Here, μ is referred to as friction coefficient. The total power required to resist the bearing frictions, thus, depends not only on the bearing types, the bearing surface texture, the properties of the lubricant, and the bearing temperature but also on the radial and axial loads and the bearing rotational speed. The dependence of the friction coefficient on the rotational speed is described by the *Stribeck curve* as
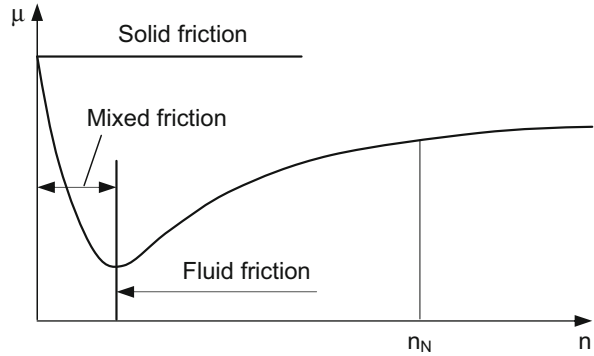
shown in Fig. 14.1. If no relative movement is available, then static, i.e., solid, friction prevails. During a starting-up or running-down phase of the machine, the hydrodynamic bearings inevitably fall into the operation range of mixed friction. Because of the direct touch between two solid surfaces, large friction and excessive wear could happen. Only beyond a certain sliding speed, i.e., an operating shaft speed, a lubricating film between the sliding surfaces can be formed. The hydrodynamic lubrication in plain bearings is, thus, achieved. It represents a lubrication condition to which the operation of the machine has to be matched with respect to the rotational speed.

Friction existing in the lubricant film is called sliding or fluid friction. Basically, the wear in the range of liquid friction is lowest. The re-increase of the friction coefficient with the speed is due to internal friction of the liquid, as with the increasing speed, the shear rate of the lubricant increases. Because of this hydrodynamic lubrication behavior, the bearing friction power in the range of fluid friction is expressed, according to Eq. (14.2), to

$$P_{be} = K_{be}n^q. \tag{14.3}$$

Accordingly, the *bearing friction torque* is calculated with $\omega = 2\pi n$ to

$$M_{be} = \frac{K_{be}}{2\pi}n^{q-1}. \tag{14.4}$$

Here, K_{be} is the bearing friction coefficient. It is a function of the type of bearing, bearing load, dynamic viscosity of the lubricant, and bearing temperature. In order to achieve the fluid friction at high bearing loads, the lubricant with the higher dynamic viscosity should be used. The transition from mixed friction into fluid friction takes place at a speed which is higher, the greater the bearing load is. The relevant relation is given by the *Sommerfeld number* (So), see Decker (2007) and Haberhauer and Bodenstein (2007). The exponent q in Eq. (14.3) also depends on the geometrical and the operational characteristics of the plain bearings and lies between 1.5 and 2. According to Vogelpohl (1967), see also Haberhauer and Bodenstein (2007), the

exponent $q = 1.5$ is used for the high load cases (So > 1) and $q = 2$ for the low load cases (So < 1).

The bearing friction constant in Eq. (14.3) can be determined by experiments. A well-proven method in practice is the retardation test method which has been described in the last chapter (Sect. 13.3). One needs only to specify the exponent q. In the experiment of Taygun (1946), for instance, $q = 1.5$ has been applied.

The dependence of the friction power on the shaft rotational speed, as represented in Eq. (14.3), will be used in Chap. 17 to determine the real runaway speed of the Pelton turbines.

Other comparable mechanical losses are the friction losses existing at all shaft seals. Since shaft seals are not loaded and also have very small slide surface area, the friction loss at each shaft seal is negligible compared to the losses at the loaded bearings. For this reason no further discussion will be given in the context of this book. Through the retardation test which has already been described in Chap. 13, the shaft seal losses will be recorded together with the bearing friction losses because of the similar friction laws.

References

Decker, K. (2007). *Maschinenelemente* (16. Auflage). Hanser Verlag.

Haberhauer, H., & Bodenstein, F. (2007). *Maschinenelemente*. Heidelberg: Springer. 14. Auflage.

Taygun, F. (1946). Untersuchungen über den Einfluss der Schaufelzahl auf die Wirkungsweise eines Freistrahlrades. Diss., Eidgenössische Technische Hochschule in Zürich.

Vogelpohl, G. (1967). *Betriebssichere Gleitlager* (2. Auflage). Berlin: Springer.

Chapter 15
Hydraulic and Mechanical Efficiency

15.1 Hydraulic Efficiency

The basic formula for determining the *hydraulic efficiency* of a Pelton turbine is Eq. (2.40). This equation has been taken over directly from the equation of frictionless flow in a linearly translating bucket. It only takes into consideration the exit swirling loss. Since the efficiency is calculated there for a constant peripheral speed coefficient (k_m) and in effect each water particle has its individual form in the interaction with the bucket, the calculation for a constant peripheral speed coefficient is only an approximation. Its comparison with the computational results from the so-called jet layer method (Sect. 6.2.2) showed a small difference of only about 0.2 % (Fig. 9.5).

The most significant aspect in Pelton turbines is that the best system efficiency is found for a peripheral speed coefficient $k_\mathrm{m} = 0.45$ to 0.48 instead of $k_\mathrm{m} = 0.5$. Obviously, the equation for the system efficiency computation, i.e., Eq. (2.40), requires a modification. If the best efficiency of a Pelton turbine is found at the nominal operation condition with the peripheral speed coefficient $k_\mathrm{m,N}$, then Eq. (2.40) should be modified for the variation of the peripheral speed coefficient, for instance, as a result of head variations. According to Zhang (2007), this modification is given by

$$\eta_\mathrm{h} = \frac{P_\mathrm{h}}{P_0} = \frac{k_\mathrm{m}}{k_\mathrm{m,N}} \left(1 - 0.5\frac{k_\mathrm{m}}{k_\mathrm{m,N}} \right)(1 - \cos\beta_2). \tag{15.1}$$

The dependence of the efficiency on the peripheral speed coefficient as in Eq. (2.40) is preserved. The hydraulic efficiency in this form only applies to the frictionless flow and considers only the swirling loss (Chap. 9). The influence of viscous friction on the hydraulic efficiency has been investigated in detail in Chaps. 10–12. Analogous to Eq. (15.1), now Eq. (10.39) is correspondingly modified to

$$\eta_{\mathrm{h}} = \frac{k_{\mathrm{m}}}{k_{\mathrm{m,N}}} \left(1 - 0.5\frac{k_{\mathrm{m}}}{k_{\mathrm{m,N}}} \right) \left(1 - \cos\beta_2 + \frac{1}{2}c_{\mathrm{w2}}\cos\beta_2 \right). \qquad (15.2)$$

The hydraulic efficiency in this form is basically complete. Besides the exit swirling loss, the friction loss has also been taken into account. In addition and as expected, the maximum efficiency is found at the peripheral speed coefficient $k_{\mathrm{m,N}}$, corresponding to the real operation of a Pelton turbine. It should be noted that the relation in Eq. (15.2), i.e., the dependence on the peripheral speed coefficient (k_{m}), is valid only for a limited range of k_{m}. Effectively, this means $k_{\mathrm{m}} < 0.55$. The real efficiency curve as a function of the peripheral speed coefficient in the whole range of the speed variation up to the runaway speed will be calculated in Chap. 16.

The hydraulic efficiency in Eq. (15.2) refers to the conversion rate of the jet power. If the efficiency is intended to refer to the net head in front of the injector, then Eq. (15.2) must be multiplied by the injector efficiency.

15.2   Mechanical Efficiency

The *mechanical efficiency* describes the power transfer from the turbine to the shaft, at the end of which the rotor of the electric generator is positioned. The possible mechanical resistances and the resulting efficiency losses in the power transmission are friction and windage losses in the turbine casing and the frictions in the shaft bearings and seals. The corresponding losses have been dealt with in Chaps. 13 and 14. The shaft bearings considered are hydrodynamic plain bearings which are commonly applied in Pelton turbines. A general property of the mechanical losses is the dependence on the rotational speed of the shaft. According to Chap. 13, it applies for the friction and windage losses in the Pelton wheel, viz.,

$$\Delta\eta_{\mathrm{wi}} = \frac{K_{\mathrm{wi}}n^3}{P_0}. \qquad (15.3)$$

For the bearing friction loss, there is, from Chap. 14, the formula

$$\Delta\eta_{\mathrm{be}} = \frac{K_{\mathrm{be}}n^q}{P_0}. \qquad (15.4)$$

Here, P_0 is the hydraulic power of the total number of water jets. The exponent q in Eq. (15.4) lies, according to Chap. 14, between 1.5 and 2, depending on the geometrical and operational characteristics of the hydrodynamic plain bearings. With the rotational speed as a variable, the two equations represent the characteristics of the respective mechanical losses. Obviously, the related efficiency losses increase when the turbine operates at partial load ($P_0 < P_{0,\mathrm{N}}$). For this reason, it is often advantageous to speak of the mechanical power loss which is determined by

the rotational speed but not by the operation settings like the hydraulic loads of the turbine.

From Eqs. (15.3) and (15.4), the mechanical efficiency of a Pelton turbine is given by

$$\eta_{\mathrm{mech}} = 1 - \Delta\eta_{\mathrm{wi}} - \Delta\eta_{\mathrm{be}}. \tag{15.5}$$

Reference

Zhang, Zh. (2007). Flow interactions in Pelton turbines and the hydraulic efficiency of the turbine system. *Proceedings of the IMechE Vol. 221, Part A: Journal of Power and Energy*, pp. 343–357.

Chapter 16
Real Hydraulic Efficiency Characteristics

The hydraulic efficiency which is calculated according to Eq. (15.1) or (15.2) is a function of the peripheral speed coefficient k_m. It is mathematically of symmetrical form about the nominal value $k_{m,N}$ at which the maximum efficiency is found. In reality, such a symmetrical function only applies for a limited variation of the independent peripheral speed coefficient around the nominal value. Under certain circumstances, the calculation can also be used and regarded as reliable for peripheral speed coefficients down to zero value when some inaccuracy is acceptable and a qualitative statement on the influence of the peripheral speed coefficient should be made. The validity of the calculations is, however, limited for values of k_m not higher than $k_m = 0.55$ by the fact that beyond this value a part of the jet will bypass the Pelton wheel without making any energy exchange with the rotating buckets. Such occurrences will considerably distort the efficiency curve away from its symmetrical form according to Eq. (15.2). The peripheral speed coefficient at which any water particle in the jet bypasses the rotating buckets for the first time is referred to as the lower critical peripheral speed coefficient. Beyond this speed Eq. (15.2) is no longer applicable. The upper critical peripheral speed coefficient is reached when the bypass of water particles occurs for the first time in all jet layers simultaneously. Taking into account the partial bypass of the jet flow, the real hydraulic characteristics of a Pelton turbine in the upper range of the peripheral speed coefficient will be calculated in this chapter.

16.1 Critical Peripheral Speed Coefficient

Because of the periodic interaction between the jet and the rotating Pelton buckets, only one bucket is considered here. The bucket cutout edge is located on the radius R_c. As illustrated in Fig. 5.3, the bucket at position α_a begins to cut off the jet. The amount of water that gets into the bucket has been identified by the jet piece *abcd*. According to Eq. (5.14), the length of this jet piece is given by

Fig. 16.1 Positional
relation of the water jet to a
Pelton bucket
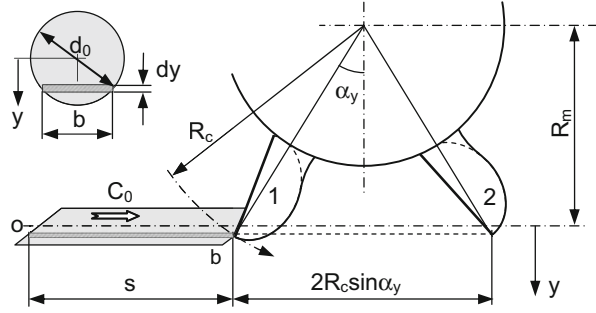
$$s = \frac{1}{k_{\mathrm{m}}} \cdot \frac{2\pi}{N} R_{\mathrm{m}}, \tag{16.1}$$

in which N refers to the number of buckets of the Pelton wheel.

After Fig. 16.1 a jet layer of thickness $\mathrm{d}y$ at the distance y from the jet axis is considered. This jet layer reaches the bucket at the bucket position α_{y} (position 1) and begins to enter the bucket. Under normal operating conditions, this jet layer can fully get into the bucket before the bucket changes to position 2. When the Pelton wheel rotates at a speed which is sufficiently higher than the nominal value, then it could happen that part of the water in the considered jet layer evades entering the rotating bucket. The critical rotational speed of the Pelton wheel is designated as such, when the last droplet of water in a jet layer will just reach the bucket at bucket position 2. For the jet layer at y, the corresponding condition is formulated with

$$s + 2R_{\mathrm{c}} \sin \alpha_{\mathrm{y}} = C_0 t_{\mathrm{y}}. \tag{16.2}$$

The interaction time is given by $t_{\mathrm{y}} = 2\alpha_{\mathrm{y}}/\omega_{\mathrm{cr}}$, with ω_{cr} as the critical angular speed of the Pelton wheel. Together with Eqs. (2.18) and (16.1), the critical peripheral speed coefficient for the considered jet layer is evaluated from Eq. (16.2) to yield

$$k_{\mathrm{m,cr}} = \frac{\alpha_{\mathrm{y}} - \pi/N}{\sin \alpha_{\mathrm{y}}} \frac{R_{\mathrm{m}}}{R_{\mathrm{c}}}. \tag{16.3}$$

This critical peripheral speed coefficient varies from layer to layer across the jet. Because of the relation $R_{\mathrm{m}} + y = R_{\mathrm{c}} \cos \alpha_{\mathrm{y}}$, which means $\alpha_{\mathrm{y}} = f(y)$, the critical peripheral speed coefficient in the above equation is a function of y which specifies a certain jet layer. The corresponding dependence for a concrete Pelton wheel has been shown in Fig. 16.2. Obviously, the lower critical peripheral speed coefficient is found at the jet layer $y/d_0 = 0.5$. With the corresponding bucket position α_{b}, this lower critical value is evaluated as

Fig. 16.2 Critical peripheral speed coefficient arranged to the jet layer. The range between the upper and lower values is denoted as the critical or the transition range
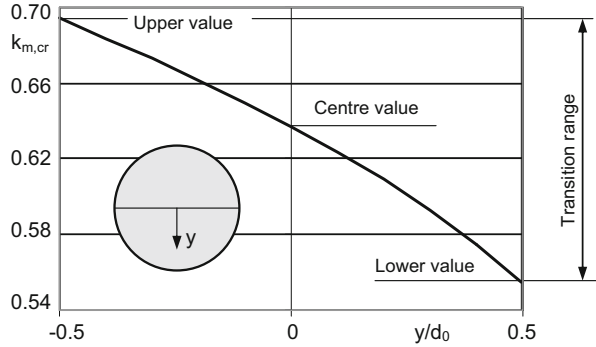
$$k_{m,cr} = \frac{\alpha_b - \pi/N}{\sin \alpha_b} \frac{R_m}{R_c}. \tag{16.4}$$

In this regard, the critical peripheral speed coefficient is also a function of the number of buckets. The equation can therefore be used to determine the minimum number of buckets of a Pelton wheel, if for the Pelton wheel the peripheral speed coefficient is given. From Eq. (16.4) it follows accordingly that

$$N_{min} = \frac{\pi}{\alpha_b - k_m \frac{R_c}{R_m} \sin \alpha_b} = \frac{\pi}{\alpha_b - \frac{U_c}{C_0} \sin \alpha_b}. \tag{16.5}$$

This equation for determining the minimum number of buckets has already been shown in Sect. 5.2 by Eq. (5.7). Since in practical designs of Pelton turbines the bucket number is significantly higher than necessarily minimal (see Sect. 5.5), the jet will never bypass the Pelton wheel which rotates under nominal speed.

The upper critical peripheral speed coefficient is obtained when the jet layer at $y/d_0 = -0.5$ is viewed from Fig. 16.2. The range between the lower and the upper speed is referred to as the critical or the *transition speed range* and has to be especially considered if the real efficiency curve will be calculated for the upper range of the speed.

While the bypass of water begins at the outermost jet layer $y/d_0 = 0.5$, the extent of the happening is still low because this jet layer has only a small segment in the jet cross section. For this reason and for the practical applications, the critical value that refers to the jet layer on the jet axis is called the *critical peripheral speed coefficient* of the entire jet. Thus, from Eq. (16.3) with $y = 0$ and under consideration of $\cos \alpha_o = R_m/R_c$, one obtains

$$k_{m,cr} = \frac{\alpha_o - \pi/N}{\tan \alpha_o}. \tag{16.6}$$

Here, α_o denotes the bucket position at which the bucket cutout edge on the radius R_c just cuts off the jet layer on the jet axis ($y = 0$). It corresponds to the bucket position α_{o1} in Fig. 5.7.

Since the bucket-position angle α_o, according to Eq. (2.30), is a function of the specific speed, Eq. (16.6) can be accordingly shown as a function of such a parameter:

$$k_{\mathrm{m,cr}} = \frac{1}{2}\left(\arccos\frac{1}{1+2n_{\mathrm{q}}} - \frac{\pi}{N}\right)\frac{1}{\sqrt{n_{\mathrm{q}}(1+n_{\mathrm{q}})}}. \qquad (16.7)$$

Because $k_{\mathrm{m,cr}} = \pi D_{\mathrm{m}} n_{\mathrm{cr}}/C_0$ and since the nominal peripheral speed coefficient equals $k_{\mathrm{m,N}} = \pi D_{\mathrm{m}} n_{\mathrm{N}}/C_0$, the corresponding critical speed of the Pelton wheel is obtained as

$$n_{\mathrm{cr}} = \frac{k_{\mathrm{m,cr}}}{k_{\mathrm{m,N}}} n_{\mathrm{N}}. \qquad (16.8)$$

16.2   Reaction Degree of the Jet

If the rotational speed of the Pelton wheel increases so that the critical speed is reached, then a part of the jet will evade, i.e., bypass the rotating buckets without doing mechanical work. In order to quantitatively describe this situation, the jet layer of thickness $\mathrm{d}y$ at position y, as shown in Fig. 16.1, is considered. The amount of water that enters the bucket is determined by

$$\mathrm{d}Q_+ = \left(C_0 t_y - 2R_{\mathrm{c}}\sin\alpha_y\right)b\mathrm{d}y. \qquad (16.9)$$

The jet layer width is given by $b = 2\sqrt{(d_0/2)^2 - y^2}$. With $t_y = 2\alpha_y/\omega$ as the duration of the bucket movement from position 1 to position 2, the above equation is transformed into

$$\mathrm{d}Q_+ = 4\left(C_0\frac{\alpha_y}{\omega} - R_{\mathrm{c}}\sin\alpha_y\right)\sqrt{\left(\frac{d_0}{2}\right)^2 - y^2}\cdot\mathrm{d}y. \qquad (16.10)$$

Furthermore, the jet speed C_0 is replaced by the peripheral speed coefficient according to Eq. (2.18). The result of this transformation is

$$\mathrm{d}Q_+ = 2R_{\mathrm{m}}\left(\frac{\alpha_y}{k_{\mathrm{m}}} - \frac{R_{\mathrm{c}}}{R_{\mathrm{m}}}\sin\alpha_y\right)d_0^2\sqrt{1 - 4\left(\frac{y}{d_0}\right)^2}\cdot\mathrm{d}\left(\frac{y}{d_0}\right). \qquad (16.11)$$

In this calculation, $\sin \alpha_y$ itself is a function of the jet layer position y. In order to represent the amount of water dQ_+ directly as a function of y, the following relation, according to Fig. 16.1, is used:

$$R_m + y = R_c \cos \alpha_y, \tag{16.12}$$

which is further rewritten as

$$\alpha_y = \arccos\left(\frac{R_m}{R_c} + \frac{y}{R_c}\right). \tag{16.13}$$

Because $y/R_c \ll R_m/R_c$, this equation is linearized to

$$\alpha_y \approx \arccos\left(\frac{R_m}{R_c}\right) - \frac{1}{\sqrt{1 - \cos^2\alpha_o}}\frac{y}{R_c} = \alpha_o - \frac{1}{\sin\alpha_o}\frac{y}{R_c}, \tag{16.14}$$

as well as to

$$\sin \alpha_y = \sin\left(\alpha_o - \frac{1}{\sin\alpha_o R_c}y\right) \approx \sin\alpha_o - \frac{1}{\tan\alpha_o}\frac{y}{R_c}. \tag{16.15}$$

Equations (16.14) and (16.15) are inserted into Eq. (16.11). It then follows with $\cos\alpha_o = R_m/R_c$

$$dQ_+ = 2R_m\left[\left(\frac{\alpha_o}{k_m} - \tan\alpha_o\right) - \frac{1}{\sin\alpha_o R_c}\frac{d_0}{\left(\frac{1}{k_m} - 1\right)}\frac{y}{d_0}\right] \cdot d_0^2$$

$$\times \sqrt{1 - 4\left(\frac{y}{d_0}\right)^2} \cdot d\left(\frac{y}{d_0}\right). \tag{16.16}$$

To determine the total amount of water that is intercepted by the bucket, the above equation must be integrated over the jet thickness. Here, both the transition speed range and the following upper speed range must be treated separately.

16.2.1 Reaction Degree in the Transition Speed Range

The critical, i.e., the transition, speed range has been specified in Fig. 16.2. Within this range each speed is arranged to a jet layer which is given by y_{cr}. For a given speed to which the jet layer y_{cr} belongs, all jet layers with $y > y_{cr}$ suffer from a partial bypass of the Pelton wheel. Of all these jet layers, the amount of water which effectively exchanges power with a rotating bucket can be determined through integration of Eq. (16.16) from y_{cr} to $y = 0.5d_0$. The result of this integration is

Fig. 16.3 Area of a
segment in the jet cross
section
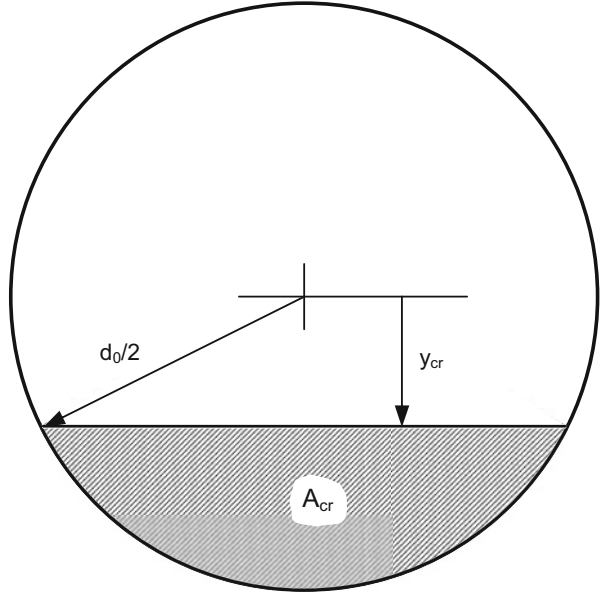
$$Q_+(y_{cr}) = R_m \cdot d_0^2 \left(\frac{\alpha_o}{k_m} - \tan \alpha_o\right) \left[\frac{\pi}{4} - \frac{y_{cr}}{d_0}\sqrt{1 - \left(2\frac{y_{cr}}{d_0}\right)^2} - \frac{1}{2}\arcsin\left(2\frac{y_{cr}}{d_0}\right)\right]$$

$$-\frac{1}{6}\frac{d_0^3}{\tan \alpha_o}\left(\frac{1}{k_m} - 1\right)\left[1 - \left(2\frac{y_{cr}}{d_0}\right)^2\right]^{3/2}. \quad (16.17)$$

In this equation, y_{cr} and k_m are related together by Eq. (16.3) because $\alpha_y = f(y)$.

The total amount of water in all jet layers $y > y_{cr}$, as summarized in a segment section according to Fig. 16.3, is obtained as

$$Q(y_{cr}) = sA_{cr} = \frac{1}{k_m}\frac{2\pi}{N}R_m\left(\arccos\frac{y_{cr}}{d_0/2} - \frac{y_{cr}}{d_0/2}\sqrt{1 - \left(\frac{y_{cr}}{d_0/2}\right)^2}\right)\frac{d_0^2}{4}. \quad (16.18)$$

The volume of water which bypasses a rotating bucket is accordingly

$$\Delta Q(y_{cr}) = Q(y_{cr}) - Q_+(y_{cr}). \quad (16.19)$$

On the other hand, the total amount of water in the jet of length s is given by

$$Q = \frac{\pi}{4} d_0^2 s = \frac{\pi}{4} d_0^2 \frac{1}{k_{\mathrm{m}}} \frac{2\pi}{N} R_{\mathrm{m}}. \tag{16.20}$$

In order to specify the amount of water, which effectively reacts with the rotating bucket in the percentage term, the *reaction degree of the jet* is introduced. After Zhang and Müller (2007), this is defined by

$$R_{\mathrm{Q}} = \frac{Q_+}{Q} = 1 - \frac{\Delta Q(y_{\mathrm{cr}})}{Q}. \tag{16.21}$$

The reaction degree of this definition will be used to calculate the real efficiency curve in the transition speed range.

16.2.2   Reaction Degree in the Upper Range

If the rotational speed of the Pelton wheel further increases until the upper critical speed is reached as shown in Fig. 16.2, then from this speed all the jet layers undergo a partial bypass at the Pelton wheel. The effective amount of water which exchanges the power with a rotating bucket can be obtained through integration of Eq. (16.16) from $y_{\mathrm{cr}}/d_0 = -0.5$ to $y_{\mathrm{cr}}/d_0 = 0.5$ or directly from Eq. (16.17) with $y_{\mathrm{cr}}/d_0 = -0.5$:

$$Q_+ = \frac{1}{2} \pi R_{\mathrm{m}} \cdot d_0^2 \left(\frac{\alpha_{\mathrm{o}}}{k_{\mathrm{m}}} - \tan \alpha_{\mathrm{o}} \right). \tag{16.22}$$

Correspondingly, the reaction degree of the entire jet is then obtained as

$$R_{\mathrm{Q}} = \frac{Q_+}{Q} = \frac{N \alpha_{\mathrm{o}}}{\pi} \left(1 - k_{\mathrm{m}} \frac{\tan \alpha_{\mathrm{o}}}{\alpha_{\mathrm{o}}} \right). \tag{16.23}$$

As will be shown, because of its simple form, this reaction degree can also be applied as an approximation for the transition speed range which has just been treated in the last section.

16.2.3   Example for Reaction Degree of the Jet

Based on the above considerations and the introduction of the reaction degree, it has been indicated that the real efficiency curve of a Pelton turbine has to be divided into the lower, transition, and upper speed ranges. A concrete Pelton turbine has been considered in Sect. 16.1 in connection with Fig. 16.2. For this turbine the

Fig. 16.4 Reaction degree
of the jet in three speed
ranges. The transition range
may be optionally replaced
by extending the lower and
the upper speed ranges
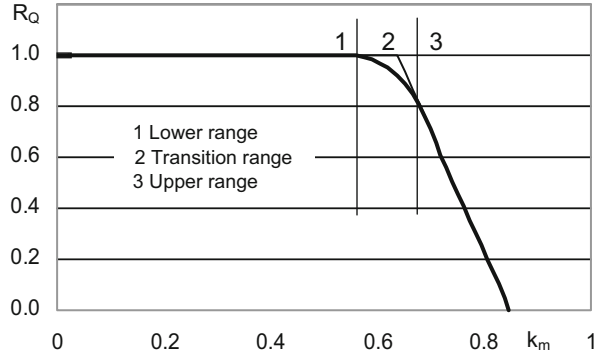
reaction degrees of the jet in the mentioned three speed ranges will now be calculated and shown. While in the lower speed range the reaction degree is equal to 1, in the transition and the upper speed ranges, they need to be calculated by Eqs. (16.21) and (16.23), respectively. Figure 16.4 shows the calculated results of the jet reaction degrees in all three speed ranges. In the first approximation, the transition speed range can be replaced by extending the lower and the upper speed ranges.

16.3   Real Hydraulic Efficiency Characteristics

The hydraulic efficiency given in Eq. (15.2) applies in principle only to the lower range of the peripheral speed coefficient. Both in the transition and the upper speed ranges, the reaction degrees of the jet must be considered in the calculation of the turbine efficiency. The partial amount of water which interacts with the rotating buckets provides only a partial power. For this amount of water, it can be assumed that the corresponding efficiency is still given by Eq. (15.2). The overall efficiency of the total water in the jet is then calculated by taking into account the jet reaction degree, yielding

$$\eta_h = \frac{k_m}{k_{m,N}} \left(1 - 0.5\frac{k_m}{k_{m,N}} \right) \left(1 - \cos\beta_2 + \frac{1}{2}c_{w2}\cos\beta_2 \right) R_Q. \tag{16.24}$$

From the structure of this equation, it can be seen that in the calculation of the hydraulic efficiency, all three losses participate:

- Swirling loss
- Friction loss
- Water loss

A large water loss also leads to the change in the flow within the bucket, for instance, in the form of reduction in the water-sheet thickness. Then, according to

Fig. 16.5 Real efficiency curve of a Pelton turbine (KWA) with $k_{m,N} = 0.470$. The transition range is given at $k_{m,cr} = 0.547$ to 0.687. The runaway speed constant is $k_{R0} = 0.848$
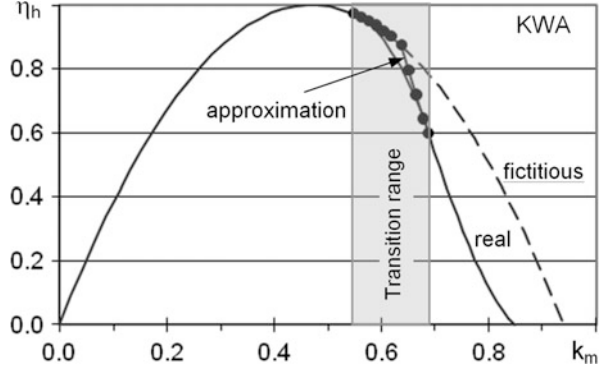
Eq. (10.12), the friction number c_{w2} and, in turn, the friction loss will also change. This change, however, is negligible if compared to the water loss which can be up to 100 % in the upper speed range. This signifies that the influence of the water loss dominates in Eq. (16.24), as soon as it occurs.

Equation (16.24) can also be directly displayed as a function of the rotational speed. According to Eq. (2.18), the peripheral speed coefficient depends on the rotational speed and the jet speed (thus on the hydraulic head). It is now assumed that the turbine operates under the nominal hydraulic head. Then one has

$$\frac{k_m}{k_{m,N}} = \frac{n}{n_N}. \tag{16.25}$$

With $\beta_2 \approx \pi$, Eq. (16.24) is rewritten to

$$\eta_h = 2\left(1 - \frac{1}{4}c_{w2}\right)\frac{n}{n_N}\left(1 - 0.5\frac{n}{n_N}\right) \cdot R_Q. \tag{16.26}$$

Figure 16.5 shows a calculation example of the real efficiency curve of a Pelton turbine. For simplicity $c_{w2} = 0$ and $\beta_2 = \pi$ have been assumed. It is about the same Pelton turbine which has already been considered in Figs. 16.2 and 16.4. The peripheral speed coefficient for the nominal operation point is $k_{m,N} = 0.47$. From the diagram it is evident that the efficiency characteristic of the Pelton turbine is considerably deformed for $k_m > 0.687$ compared to the symmetrical fictitious characteristic, which only applies for the linearly translating bucket. The figure also shows how closely the efficiency curve in the transition speed range can be approximated by extrapolating the reaction degree of Eq. (16.23). It must be mentioned that in practical applications of Pelton turbines, the requirement of the precise characteristic in this transition speed range is rarely available. For this reason, the reaction degree, given by Eq. (16.23), may also be applied for the transition speed range.

Reference

Zhang, Zh., & Müller, J. (2007). Efficiency and runaway characteristics of a Pelton turbine. Hydro 2007, Granada, Spain.

Chapter 17
Runaway Speed and Acceleration Profile

Under normal operating conditions, the Pelton turbine is loaded by the electric generator which provides a mechanical counter-torque on the turbine shaft and in so doing ensures the dynamic balance of the rotating system. If this counter-torque falls out by load shedding of the generator, the rotation of the Pelton wheel under the full load of water jet begins to accelerate. The maximum speed that can be reached at the Pelton wheel is called the *runaway speed*, at which the jet almost completely bypasses the Pelton wheel, without transferring its energy to the rotating buckets. The runaway speed is about twice the nominal speed of the Pelton wheel. Regarding the mechanical safety and the construction costs primarily of the generator and occasionally of the gearbox, the runaway speed is an important factor that must be taken into account already in the design phase of a Pelton turbine.

From the nominal speed towards the runaway speed with full escape of the jet at the Pelton wheel, the efficiency and power curves tend to rapidly decrease. If such a characteristic, as shown in Fig. 16.5, is known, the maximum runaway speed can be directly read out. The related calculation method will be explained in this chapter.

17.1 Theoretical Runaway Speed

The runaway speed of a Pelton wheel is a rotational speed at which almost no power exchange between the jet and the rotating buckets takes place. This condition can also be so expressed that, at the instance when the runaway speed is reached, the reaction degree of the jet (see Chap. 16) vanishes. Such a relation between the runaway speed and the reaction degree of the jet enables the theoretical runaway speed to be immediately determined. From Eq. (16.23) with $R_Q = 0$, the peripheral speed coefficient at the runaway speed is obtained as

$$k_{R0} = \frac{\alpha_o}{\tan \alpha_o}.$$

(17.1)

According to Zhang and Müller (2007), this value is called the *runaway speed coefficient*. As can be confirmed from a comparison with Eq. (16.11), the runaway speed coefficient of the entire jet is equal to the runaway speed coefficient of the middle jet layer on the jet axis. This means that from Eq. (16.11) for $dQ_+ = 0$ and $y = 0$, the same result as Eq. (17.1) are obtained.

The runaway speed coefficient, according to Eq. (17.1), represents a geometric parameter of the Pelton wheel. It is independent of the flow rate ($\dot{Q}$) and the bucket number (N) of the Pelton wheel. Since the characteristic bucket-position angle α_o, according to Eq. (2.30), is a function of the specific speed, so must also be the runaway speed coefficient. By using Eq. (2.30), the runaway speed coefficient given in Eq. (17.1) may then be written as

$$k_{R0} = \frac{1}{2} \frac{\arccos \frac{1}{1+2n_q}}{\sqrt{n_q(1+n_q)}}.$$

(17.2)

Figure 17.1 shows the computed results of the runaway speed coefficient as a function of the specific speed n_q. At Pelton turbines with low specific speeds, the runaway speed coefficient is close to 1. In practice, most Pelton turbines are designed with a specific speed between 0.6 and 1.3. For this reason, Eq. (17.2) can be well approximated by

$$k_{R0} \approx 1 - 1.15 n_q.$$

(17.3)

With the aid of the definition of the peripheral speed coefficient, according to Eq. (2.18), the theoretical runaway speed is determined from the runaway speed coefficient as

Fig. 17.1 Runaway speed coefficient in dependence on the specific speed of Pelton turbines, valid for $k_m = 0.475$ and $\varphi_B = 0.11$
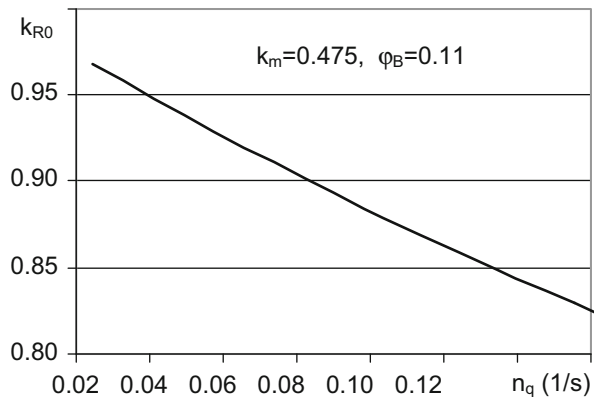
$$n_{R0} = k_{R0}\frac{C_0}{\pi D_{\mathrm{m}}}. \tag{17.4}$$

It is proportional to the jet speed which in turn depends only on the hydraulic head. Under the nominal operation condition, given by $k_{\mathrm{m,N}} = \pi D_{\mathrm{m}} n_{\mathrm{N}}/C_0$, the runaway speed can also be expressed as

$$n_{R0} = k_{R0}\frac{n_{\mathrm{N}}}{k_{\mathrm{m,N}}}. \tag{17.5}$$

The computational runaway speed given here must be interpreted as the theoretical or frictionless runaway speed. It, thus, represents the maximum reachable speed of a Pelton wheel. The real runaway speed is slightly below this maximum value, because the Pelton wheel needs to receive a small amount of energy from the jet to compensate for all possible mechanical losses, including the friction and windage losses at the Pelton wheel. The computational method for the determination of the real runaway speed will be described in the next section.

On the Pelton wheel, the associated peripheral speed of the pitch circle, i.e., the jet circle of diameter D_{m}, is determinable as

$$U_{\mathrm{m,R0}} = k_{R0}C_0. \tag{17.6}$$

This equation shows that by reaching the runaway speed, the peripheral speed of the Pelton wheel is not equal to the jet speed. This also explains why the runaway speed according to Eq. (17.5) is not simply equal to the ratio $n_{\mathrm{N}}/k_{\mathrm{m,N}}$, but this quantity multiplied with a factor $k_{R0} < 1$.

An example of computing the complete efficiency curve has already been shown in Fig. 16.5. The friction-free runaway speed coefficient of $k_{R0} = 0.848$ was directly confirmed there. The ratio to the nominal operation at $k_{\mathrm{m,N}} = 0.47$ is 1.80, i.e., $n_{R0}/n_{\mathrm{N}} = 1.80$.

By applying the runaway speed coefficient according to Eq. (17.1), the reaction degree of the jet, according to Eq. (16.23) for the upper range of the speed, is also expressible as

$$R_Q = \frac{N\alpha_{\mathrm{o}}}{\pi}\left(1 - \frac{k_{\mathrm{m}}}{k_{R0}}\right) = \frac{N\alpha_{\mathrm{o}}}{\pi}\left(1 - \frac{n}{n_{R0}}\right). \tag{17.7}$$

The reaction degree is, thus, a linear function of the rotational speed of the Pelton wheel.

17.2   Real Runaway Speed

The runaway speed, which has been calculated in the foregoing section, applies for
the turbine operations without mechanical losses and is therefore referred to as the
theoretical runaway speed. In reality, the friction forces at the Pelton wheel and at
the shaft bearings behave as braking forces and always cause mechanical losses.
The real runaway speed of a Pelton wheel, thus, represents a speed, at which the
dynamical balance between the active torque from the hydraulic force and the
counter-torque from all the mechanical braking forces is reached. In other words,
the hydraulic power, which is transferred from the jet to the Pelton buckets, must be
equal to the total mechanical losses. From such a dynamical balance, the real
runaway speed can be determined which is slightly below the theoretical runaway
speed.

17.2.1   Mechanical Power Loss

The mechanical losses in a Pelton turbine include the friction and windage losses at
the Pelton wheel and the friction losses at the bearings and the shaft seals. These
have already been treated in Chaps. 13 and 14 and summarized in Chap. 15. Mostly,
such losses are given together with the efficiency specifications at the nominal
operation point, i.e., at the nominal rotational speed. Since the mechanical losses
only depend on the rotational speed of the shaft, they can be well determined for
any other speeds based on the data at the nominal speed.

According to Eq. (15.3), the friction and windage losses depend on the third
power of the speed. This applies to both vertical and horizontal turbines. Under
nominal operation conditions with the speed n_N and the flow rate $\dot{Q}_N$, the resulting
loss of efficiency is given by

$$\Delta\eta_{wi,N} = \frac{K_{wi}n_N^3}{\rho g H_N \dot{Q}_N}. \tag{17.8}$$

In this equation, the constant K_{wi} represents the ratio of the dissipated mechanical
power to the third power of the speed.

In the same way, the bearing friction loss is calculated from Eq. (15.4). For
hydrodynamic plain bearings with $q = 2$, this yields

$$\Delta\eta_{be,N} = \frac{K_{be}n_N^2}{\rho g H_N \dot{Q}_N}. \tag{17.9}$$

The ratio of the mechanical friction loss to the second power of the speed is referred
to as the coefficient K_{be}.

Provided that the corresponding mechanical losses at the nominal operation point are known, the coefficients K_{wi} and K_{be} can be obtained from the above equations. They are then applied to represent the total mechanical loss, i.e., the mechanical characteristics, as follows:

$$\Delta P_{mech} = K_{wi}n^3 + K_{be}n^2. \tag{17.10}$$

Together with the hydraulic power curve, it will be used to determine the real runaway speed of the Pelton turbine.

17.2.2   Effective Hydraulic Power

The operation of a Pelton turbine is defined by the hydraulic head H and the total flow rate $\dot{Q}$. Thus, the input hydraulic power is given by $P_0 = \rho g H \dot{Q}$. From Eqs. (16.26) and (17.7), the converted hydraulic power, also called shaft power, is determined by

$$P_h = 2\left(1 - \frac{1}{4}c_{w2}\right)\frac{N}{\pi}\alpha_o P_0\left(1 - 0.5\frac{n}{n_N}\right)\left(1 - \frac{n}{n_{R0}}\right)\frac{n}{n_N}, \tag{17.11}$$

or in abbreviated form as

$$P_h = \widetilde{P}\left(1 - 0.5\frac{n}{n_N}\right)\left(1 - \frac{n}{n_{R0}}\right)\frac{n}{n_N}, \tag{17.12}$$

with

$$\widetilde{P} = 2\left(1 - \frac{1}{4}c_{w2}\right)\frac{N}{\pi}\alpha_o P_0. \tag{17.13}$$

The term $\widetilde{P}$ is a constant parameter. It combines the wheel parameters and the jet power. For the purpose of determining the realistic runaway speed, the friction number c_{w2} can be assumed to be practically zero without reasonably affecting the calculations (Zhang and Müller 2007).

17.2.3   Realistic Runaway Speed

The realistic runaway speed results from the dynamic balance between the total mechanical power losses and the effective hydraulic power from the jet. From Eqs. (17.10) and (17.12), one obtains with $n = n_R$ straight away

1: theoretical runaway speed
2: real runaway speed
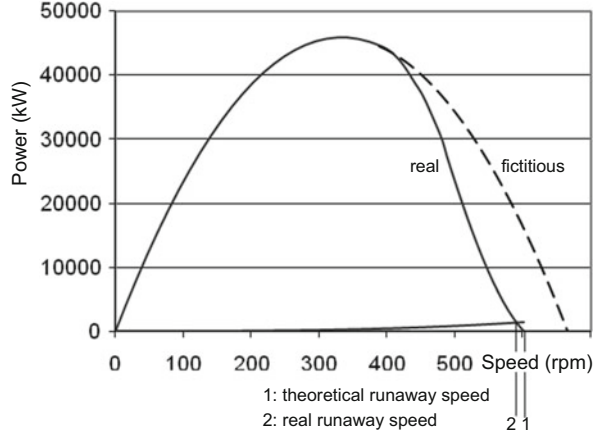
$$\left(K_{\mathrm{wi}} n_{\mathrm{N}} - \frac{0.5\widetilde{P}}{n_{\mathrm{N}} n_{\mathrm{R0}}} \right) n_{\mathrm{R}}^2 + \left(K_{\mathrm{be}} n_{\mathrm{N}} + \frac{\widetilde{P}}{n_{\mathrm{R0}}} + \frac{0.5\widetilde{P}}{n_{\mathrm{N}}} \right) n_{\mathrm{R}} - \widetilde{P} = 0. \qquad (17.14)$$

From this quadratic equation, the real runaway speed n_{R} can be determined imme-
diately. The graphical determination method is shown in Fig. 17.2 and applied to
the known example that has already been considered in Chap. 16. The crossing
point of the hydraulic power curve and the mechanical loss curve represents the
realistic runaway speed. As can be seen from the diagram, the real runaway speed is
only slightly smaller than the frictionless runaway speed. From the viewpoint that
the runaway speed should never be underestimated, the frictionless runaway speed,
according to Eq. (17.4) or (17.5), should always be used. This is furthermore
particularly advantageous since the calculation is extremely simple.

As has been demonstrated by Zhang and Müller (2007), the inaccuracy of the
presented method to determine the runaway speed of a Pelton turbine is generally
less than 1 %. This corresponds to the lower limit of the general measurement
inaccuracy and can, thus, be well accepted.

For the application of Eq. (17.14), the following points should be considered:

- In the calculation of the parameter $\widetilde{P}$, according to Eq. (17.13), $\dot{Q}$ is considered to
  be the total flow rate corresponding to the actual operation (full- or part-load and
  multi-jet operation).
- If the ordinate in Fig. 17.2 is normalized by P_0 to unity, then it deals with the
  efficiency characteristic; see Zhang and Müller (2007).
- The quadratic equation (17.14) has been obtained from Eqs. (17.10) and (17.12).
  In Eq. (17.10), the speed appears in the second and the third power, respectively.
  If the bearing friction takes place in the form of $n^{1.5}$, for instance, then $n_{\mathrm{R}}^{0.5}$ will
  appear in Eq. (17.14). In this case and because of $(n_{\mathrm{R0}} - n_{\mathrm{R}}) \ll n_{\mathrm{R0}}$, the
  expression $n_{\mathrm{R}}^{0.5}$ can be linearized at n_{R0} as

$$n_R^{0.5} = [n_{R0} - (n_{R0} - n_R)]^{0.5} = 0.5 n_{R0}^{0.5} \left(1 + \frac{n_R}{n_{R0}} \right). \tag{17.15}$$

In this way, Eq. (17.14) with $n_R^{0.5}$ is again reconverted to a quadratic equation.

17.3 Acceleration Process to the Runaway Speed

In the case of load shedding of the generator, the rotation of the Pelton wheel under the impingement of the jets begins to accelerate until the stable runaway speed is reached. The acceleration process depends not only on the active torque transmitted by the jet but also on the total moment of inertia of the Pelton wheel, the shaft, and the generator rotor. As a system parameter, the total moment of inertia is usually known. Else it can be easily calculated. To calculate the acceleration process of the Pelton wheel, the jet impact force must be known which changes with the acceleration process, i.e., as a function of the speed of the Pelton wheel. To this end, the reaction degree of the jet flow needs to be considered, just like that in the calculation of the hydraulic power curve. Obviously the lower and the upper speed ranges have to be handled differently. For simplicity, the transition speed range can be neglected by extending the lower and the upper ranges according to Fig. 16.4.

The dynamical acceleration of the entire rotating unit (Pelton wheel, shaft, and rotor of the generator) is subject to the conservation law of angular momentum. Neglecting the mechanical losses, the rotation of the rotor system is described by

$$J \frac{d\omega}{dt} = F_{wheel} \frac{D_m}{2}. \tag{17.16}$$

Here, the total moment of inertia of the rotating system is denoted by J. The total hydraulic force received by the Pelton wheel is given by F_{wheel}. In effect, it is the force component acting tangentially to the jet circle of the diameter D_m. The hydraulic force referred to one jet has been given by Eq. (2.37). Taking into account the total flow rate and the reaction degree of the jet, the effective hydraulic force exerted on the Pelton wheel is calculated to

$$F_{wheel} = \rho \dot{Q} C_0 (1 - k_m)(1 - \cos \beta_2) R_Q, \tag{17.17}$$

in which the total mass flow at a Pelton turbine is denoted by $\rho \dot{Q}$.

If Eq. (17.17) is inserted into Eq. (17.16), one obtains with $\beta_2 \approx \pi$

$$\frac{dn}{dt} = \frac{\rho \dot{Q} C_0 D_m}{2\pi J} \left(1 - \frac{\pi D_m n}{C_0} \right) R_Q. \tag{17.18}$$

For further calculations the lower and the upper speed ranges must be treated separately.

17.3.1 Lower Speed Range: $n < n_{cr}$

The lower speed range is specified by the rotational speed which varies from n_N up to n_{cr} as well as by the jet reaction degree $R_Q = 1$. Accordingly, it follows from Eq. (17.18) that

$$\int_{n_N}^{n} \frac{dn}{1 - \pi D_m/C_0 n} = \frac{\rho \dot{Q} \, C_0 D_m}{2\pi J} t. \tag{17.19}$$

The integration yields

$$\ln \frac{1 - \pi D_m/C_0 \cdot n_N}{1 - \pi D_m/C_0 \cdot n} = \frac{\rho \dot{Q} \, D_m^2}{2J} t. \tag{17.20}$$

To simplify the calculation and the presentation, the reciprocal of the coefficient is defined as the *first time constant*

$$\tau_1 = \frac{2J}{\rho \dot{Q} \, D_m^2}. \tag{17.21}$$

Using $k_{m,N} = \pi D_m n_N/C_0$ as the initial parameter at the nominal speed and $k_m = \pi D_m n/C_0$ as the process parameter, Eq. (17.20) is finally rewritten as

$$k_m = 1 - (1 - k_{m,N})e^{-t/\tau_1}, \tag{17.22}$$

or in the form of the rotational speed

$$n = \frac{n_N}{k_{m,N}} \left[1 - (1 - k_{m,N})e^{-t/\tau_1} \right]. \tag{17.23}$$

It represents the acceleration of the Pelton wheel rotation. The time for reaching the critical speed ($n = n_{cr}$) is calculated from Eq. (17.22) as

$$t_{cr} = \tau_1 \ln \frac{1 - k_{m,N}}{1 - k_{m,cr}}. \tag{17.24}$$

17.3.2 *Upper Speed Range:* $n > n_{\text{cr}}$

In the upper speed range, a partial escape of the jet at the Pelton wheel occurs. Taking into account the reaction degree of the jet, given by Eq. (17.7), there follows from Eq. (17.18) the time-dependent change in the rotational speed:

$$\frac{dn}{dt} = \frac{\rho \dot{Q} \, C_0 D_{\text{m}} N \alpha_{\text{o}}}{2\pi^2 J} \left(1 - \frac{\pi D_{\text{m}} n}{C_0}\right)\left(1 - \frac{n}{n_{\text{R0}}}\right), \tag{17.25}$$

or in integration form

$$\int_{n_{\text{cr}}}^{n} \frac{dn}{\left(1 - \pi \frac{D_{\text{m}}}{C_0} n\right)\left(1 - \frac{n}{n_{\text{R0}}}\right)} = \frac{\rho \dot{Q} \, C_0 D_{\text{m}} N \alpha_{\text{o}}}{2\pi^2 J} (t - t_{\text{cr}}). \tag{17.26}$$

The integration can be performed analytically. Indeed one easily obtains

$$\ln\left(\frac{1 - \pi \frac{D_{\text{m}}}{C_0} n}{1 - \pi \frac{D_{\text{m}}}{C_0} n_{\text{cr}}} \cdot \frac{1 - \frac{n_{\text{cr}}}{n_{\text{R0}}}}{1 - \frac{n}{n_{\text{R0}}}}\right) = \frac{t - t_{\text{cr}}}{\tau_2}, \tag{17.27}$$

in which τ_2 is a *second time constant* which applies to the upper speed range and is defined as

$$\frac{1}{\tau_2} = \left(\frac{1}{n_{\text{R0}}} - \frac{\pi D_{\text{m}}}{C_0}\right)\frac{\rho \dot{Q} \, C_0 D_{\text{m}} N \alpha_{\text{o}}}{2\pi^2 J}. \tag{17.28}$$

In order to calculate the time-dependent rotational speed from Eq. (17.27), a further constant is introduced and defined as

$$K = \frac{1 - \pi D_{\text{m}} n_{\text{cr}}/C_0}{1 - n_{\text{cr}}/n_{\text{R0}}} = \frac{1 - k_{\text{m,cr}}}{1 - n_{\text{cr}}/n_{\text{R0}}} = \frac{1 - k_{\text{m,cr}}}{1 - k_{\text{m,cr}}/k_{\text{R0}}}. \tag{17.29}$$

The time-dependent rotational speed of the Pelton wheel in the upper speed range is then obtained from Eq. (17.27). With $k_{\text{R0}} = \pi D_{\text{m}} n_{\text{R0}}/C_0$ as the runaway speed coefficient, one finds

$$\frac{n}{n_{\text{R0}}} = \frac{1 - K\exp\left(\frac{t - t_{\text{cr}}}{\tau_2}\right)}{k_{\text{R0}} - K\exp\left(\frac{t - t_{\text{cr}}}{\tau_2}\right)}. \tag{17.30}$$

Theoretically, this implies $n = n_{\text{R0}}$ when $t \to \infty$.

Fig. 17.3 Acceleration of a
Pelton wheel after the load
shedding
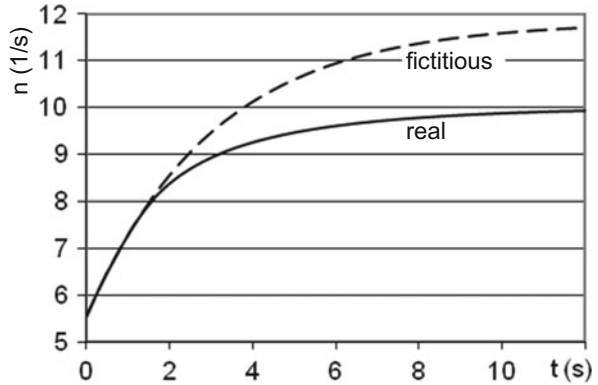
17.3.3   Entire Acceleration Curve

The above calculations show that the entire process of rotation acceleration of the
Pelton wheel after load shedding comprises the lower and upper ranges. Figure 17.3
shows the calculated acceleration curve for the exemplary Pelton turbine that has
already been considered in Figs. 16.5 and 17.2. The moment of inertia of the entire
rotating system has been assumed to be $J = 10^5 \, \text{kg} \, \text{m}^2$. For comparison, the
fictitious acceleration curve has also been shown, which is calculated under the
assumption that the reaction degree is equal to unity in the whole acceleration curve
until reaching the runaway speed. The fictitious acceleration profile is indeed the
extension of the acceleration profile of the lower speed range up to the entire upper
speed range. The resulting stable end speed corresponds to the end speed which
results from the symmetrical efficiency curve according to Fig. 17.2.

It is evident that the real acceleration curve is significantly different from the
fictitious acceleration curve.

Reference

Zhang, Zh., & Müller, J. (2007). Efficiency and runaway characteristics of a Pelton turbine. Hydro
2007, Granada, Spain.

Chapter 18
Hydraulic Design of Pelton Turbines

18.1 Dimensioning of the Pelton Wheel

For the hydraulic design of a Pelton turbine, the net head on the pressure side and the desired flow rate are two fundamental parameters. They determine the available hydraulic power supply and therefore the size of the turbine. The design of a Pelton turbine starts with the dimensioning of the Pelton wheel, the choice of the rotational speed, and the determination of the number of injectors. To this end the following indications arising from the practical operations of Pelton turbines aid in establishing the design procedure:

- The peripheral speed coefficient k_m is in the range of 0.45 to 0.48.
- The bucket width is approximately three times of the jet diameter at full load, characterized by $B \approx 3d_0$ or $\varphi_B \approx 0.11$, respectively.
- The specific speed, which is referred to the nominal flow rate at an injector, is usually confined to $n_q < 0.13$. This criterion is based on the fact that no significant flow separation at the bucket cutout edge should take place, as described in Sects. 5.7 and 5.8. According to Eq. (2.27), the wheel form is given by $D_m/B > 3$. If a small specific speed is preferred, a relatively larger Pelton wheel must be expected according to Eq. (2.27).

All these points have to be combined, in order to define the wheel size, the number of injectors, and the rotational speed of the Pelton wheel at the beginning of the first design stage of each Pelton turbine. For this purpose, the specific speed should be applied, which in effect represents the shape of the Pelton wheel (Chap. 2). Considering the total flow rate and the number of injectors, Eq. (2.22) is rewritten as

$$n_q = n \frac{\sqrt{\dot{Q}}}{\sqrt{Z_{jet}} \cdot H^{3/4}}. \tag{18.1}$$

For a given specific speed $n_q < 0.13$, the combined injector number and rotational speed of the Pelton turbine in the form $n/\sqrt{Z_{jet}}$ are obtainable. To determine the rotational speed, the power line frequency (f) and the pole pair number (p) of the generator must be additionally taken into account. The speed then has to be rounded to the nearest synchronous speed of the generator:

$$n = \frac{f}{p} (1/s). \tag{18.2}$$

The line frequency is usually standardized at 50 Hz. In the USA and Canada, the line frequency is partly found at 60 Hz.

For the generator the minimum number of pole pairs is limited to 2. The synchronous speed is thus 25 in 1/s, i.e., 1500 in 1/min. Under certain circumstances, for instance, for large generators, this speed may be too high. Then, the pole pair number of the generator should be raised, until an appropriate synchronous speed from the view of the hydraulic and mechanical design is reached.

With consideration of Eq. (18.2), diverse combinations of the injector number and the speed of the Pelton turbine can be estimated for choice by the use of Eq. (18.1). To each combination, the wheel size is fixed and can be calculated from the definition of the peripheral speed coefficient according to Eq. (2.18), viz.,

$$D_m = \frac{k_m \sqrt{2gH}}{\pi \cdot n}. \tag{18.3}$$

The bucket size, which is represented by the bucket width B, is determined from Eq. (2.27) as

$$\frac{B}{D_m} = \frac{n_q}{2.63 k_m \sqrt{\varphi_B}}. \tag{18.4}$$

For nominal operation, with $\varphi_B = 0.11$ and $k_m = 0.47$, it finally follows that

$$B = 2.5 n_q D_m. \tag{18.5}$$

The above calculations mainly apply to determine the number of injectors and the speed of the turbine with respect to the wheel size. To illustrate the calculation process of this first design step of a Pelton turbine, an example is shown here.

Task

A Pelton turbine is to be designed for a hydraulic head $H = 750\,$m and a flow rate $\dot{Q} = 8\,$m^3/s. The specific speed of the turbine should be below 0.12.

Solution

- With an assumed number of injectors, the rotational speed is calculated from Eq. (18.1):

$$n = \frac{n_q \cdot H^{3/4}}{\sqrt{\dot{Q}/Z_{jet}}}. \tag{a}$$

- Upward rounded number of pole pairs:

$$p > 50/n. \tag{b}$$

- The rotational speed is synchronized to

$$n = 50/p. \tag{c}$$

- Specific speed according to Eq. (18.1) is recalculated as

$$n_q = n\frac{\sqrt{\dot{Q}/Z_{jet}}}{H^{3/4}}. \tag{d}$$

- The peripheral speed coefficient is assumed to be $k_m = 0.475$. The pitch circle diameter is then calculated as

$$D_m = 0.475\sqrt{2gH}/(\pi n). \tag{e}$$

- The bucket width is determined by Eq. (18.5) to

$$B = 2.5 n_q D_m. \tag{f}$$

- The bucket number is obtained from Eq. (5.30) to

$$N = 15 + 0.62/n_q. \tag{g}$$

The following table shows the corresponding calculations for the use of one, two, and three injectors, respectively. The parameter design begins with a specific speed of $n_q = 0.12$. After synchronizing the rotational speed, the specific speed is recalculated according to step (d) (Table 18.1).

In the last two rows of the table, both the theoretical jet diameter and the runaway speed have also been given. They are calculated from the conservation law of mass with the jet velocity $C_0 = \sqrt{2gH}$ and from Eq. (17.4), respectively.

The calculations in the two columns for the case of using three injectors serve to illustrate what would happen if the pole pair number of the generator is selected by one larger than necessary. The speed of the generator is reduced from 600 to

Table 18.1 Computational example of designing a Pelton turbine with $H = 750$ m and $\dot{Q} = 8\,\mathrm{m}^3/\mathrm{s}$

$n_q = 0.12$					
Z_{jet}	1	2	3	3	Equations
n (1/s)	6.1	8.6	10.5	10.5	(a)
Pole pairs	9	6	5	6	(b)
n (1/s)	5.56	8.3	10.0	8.3	(c)
n (1/min)	333	500	600	500	
n_q (1/s)	0.110	0.116	0.114	0.095	(d)
D_m (m)	3.30	2.20	1.83	2.20	(e)
B	0.90	0.64	0.52	0.52	(f)
N	21	20	20	22	(g)
d_0 (m)	0.290	0.205	0.167	0.167	
n_{R0} (1/min)	613	912	1100	935	(17.4)

500 rpm. Correspondingly the jet circle diameter D_m has to increase from 1.83 m to 2.2 m, which will result in higher construction costs. However, the smaller specific speed ($n_q = 0.095$) proves to be advantageous regarding the interaction between the jet and the Pelton buckets as well as the entry condition, as already discussed in Chap. 5 (see Sects. 5.7 and 5.8).

According to the calculations in the above table concerning the dimension and the type of the turbine, the Pelton turbine can be well built with two injectors. The specific speed of the Pelton wheel is then 0.116 with which the sound entry flow at the buckets can be ensured. The advantage of the design with two instead of three injectors is that the Pelton turbine can also be built with horizontal axis. The Pelton wheel has a diameter of $D_m = 2.2$ m. The bucket width is $B = 0.64$ m. The runaway speed is calculated to be $n_{R0} = 912\,1/\mathrm{min}$.

The example shows the method of determining the number of injectors and the speed of the Pelton turbine. By changing the specific speed which is given as a predefined parameter, one can easily compare the different design options. To a new design selection, both the jet circle diameter D_m and the bucket width B must be again optimized. This can be done by means of the detailed analyses in terms of both the hydraulic and the mechanical aspects. If, for instance, the Pelton turbine mainly operates in the partial load range, the bucket width B can be reduced accordingly.

18.2   Elliptical Bucket Form

The inside profile of the Pelton buckets must be configured so that water in it spreads as smoothly and steadily as possible. The profile should have no discontinuity. This is so required not only because of hydraulic aspects but equally also by concerns of mechanical manufacture of the buckets, for instance, by milling machines. Perfect smoothness of the bucket profile is achieved if the profile in each cross section can be outlined by a smooth mathematical curve without kinks.

Fig. 18.1 Geometric boundary conditions at the entry and exit of a Pelton bucket. Bucket width $B = 2x_2$
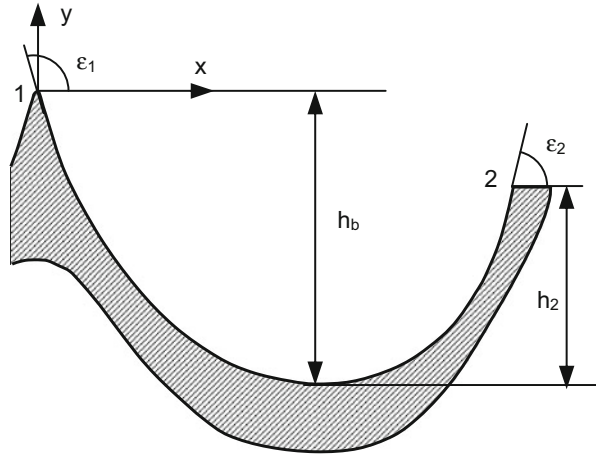
Among various mathematical functions, an ellipse model is obviously of very suitable form. When using such a model, one must determine how the ellipse parameters can be determined and with which section of the ellipse the bucket profile should be approximated. The ellipse or the elliptic section must meet those necessary conditions that have been defined by parameter studies in the bucket design. According to Fig. 18.1 with the given coordinate system, the geometric boundary conditions can be formulated as follows:

- At the bucket entry: $x_1 = 0$, $y_1 = 0$, and entry angle ε_1
- At the bucket exit: $x = x_2$, $y = y_2$, and exit angle ε_2
- Bucket depth: h_b

To meet these geometric boundary conditions by a section of an ellipse in the same coordinate system as in Fig. 18.1, the ellipse in its basic form needs a suitable coordinate transformation which is composed of a translation and a rotation of the coordinates. According to Fig. 18.2a, the basic form of the ellipse is described by

$$\frac{x'^2}{a^2} + \frac{y'^2}{b^2} = 1. \tag{18.6}$$

The ellipse is first transformed into the coordinate system (x'', y'') by a coordinate translation (u, v). With the origin of the new coordinate system on the ellipse, the ellipse equation is now given by

$$\frac{\left(x'' - u\right)^2}{a^2} + \frac{\left(y'' - v\right)^2}{b^2} = 1. \tag{18.7}$$
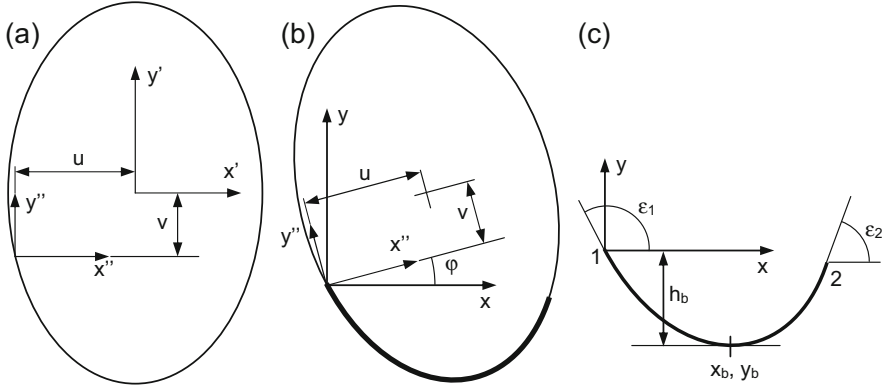
Fig. 18.2 Coordinate transformation of an ellipse to create a bucket profile

Furthermore, the ellipse model together with the coordinate axes x'' and y'' is rotated for an angle φ against the fixed coordinate system (x, y) (Fig. 18.2b). In the fixed coordinate system, the ellipse is then described by

$$\frac{(x\cos\varphi + y\sin\varphi - u)^2}{a^2} + \frac{(-x\sin\varphi + y\cos\varphi - v)^2}{b^2} = 1. \qquad (18.8)$$

The bucket profile as a portion of the transformed ellipse is schematically shown in Fig. 18.2c in which the significant geometric boundary conditions are also illustrated.

The above equation contains five variables (a, b, u, v, and φ) which must be able to ensure the prescribed conditions. To specify all five variables, five equations need to be created from the given boundary conditions. To this end, it is agreed that the coordinate origin is located on the bucket inlet as shown in Fig. 18.1 and also in Fig. 18.2c:

Boundary Condition 1
The origin of the two coordinates is located on the ellipse, so that with $x_1 = y_1 = 0$
at the bucket entry, one has

$$\frac{u^2}{a^2} + \frac{v^2}{b^2} = 1. \qquad (18.9)$$

Boundary Condition 2
At the bucket entry with $x_1 = y_1 = 0$, the entry angle, as shown in Fig. 18.1 and Fig. 18.2c, is given by $dy/dx = \tan\varepsilon_1$. From Eq. (18.8) it then follows

$$\frac{u}{v} \cdot \frac{\cos\varphi + \tan\varepsilon_1 \sin\varphi}{-\sin\varphi + \tan\varepsilon_1 \cos\varphi} = -\frac{a^2}{b^2}. \tag{18.10}$$

Boundary Condition 3

At the bucket exit, $x = x_2$ and $y = y_2$. Accordingly, one obtains from Eq. (18.8)

$$\frac{(x_2 \cos\varphi + y_2 \sin\varphi - u)^2}{a^2} + \frac{(-x_2 \sin\varphi + y_2 \cos\varphi - v)^2}{b^2} = 1. \tag{18.11}$$

Boundary Condition 4

At the bucket exit with $x = x_2$ and $y = y_2$, the exit angle is given by $dy/dx = \tan\varepsilon_2$.
One then obtains

$$\frac{(x_2 \cos\varphi + y_2 \sin\varphi - u)(\cos\varphi + \tan\varepsilon_2 \sin\varphi)}{(-x_2 \sin\varphi + y_2 \cos\varphi - v)(-\sin\varphi + \tan\varepsilon_2 \cos\alpha)} = -\frac{a^2}{b^2}. \tag{18.12}$$

Boundary Condition 5

The bucket depth as shown in Fig. 18.2c is given by $h_b = -y_b$. The exact position of
the lower vertex point can be determined by computing x_b. In a first step, the
appropriate geometric boundary condition can be derived from $dy/dx = 0$. From
Eq. (18.8) it then follows that

$$\frac{(x_b \cos\varphi + y_b \sin\varphi - u)\cos\varphi}{(-x_b \sin\varphi + y_b \cos\varphi - v)\sin\varphi} = \frac{a^2}{b^2}. \tag{18.13}$$

Because the vertex point (x_b, y_b) is on the ellipse, Eq. (18.8) implies in addition the
condition

$$\frac{(x_b \cos\varphi + y_b \sin\varphi - u)^2}{a^2} + \frac{(-x_b \sin\varphi + y_b \cos\varphi - v)^2}{b^2} = 1. \tag{18.14}$$

By introducing the fifth boundary condition for the bucket depth, an additional
unknown, namely, the coordinate x_b, appears. From the boundary conditions 1–5,
totally six equations have been established. They represent a closed system of
equations for the solution of six unknown parameters (a, b, u, v, φ, and x_b). Because
a direct solution of all unknown parameters is difficult, the fifth boundary condition
is first disregarded. In the equation system implied by the boundary conditions 1–4,
the rotation angle φ of the ellipse is considered as predetermined. The reduced
equation system, consisting of four equations, is then for four unknown parameters
(a, b, u, v). The presetting of the rotation angle φ simply means that this angle

behaves as a control parameter. As will be shown, this angle finally determines the
bucket depth.

To solve the equations with the boundary conditions 1–4, the following substitution parameters are introduced:

$$A = a^2, \quad B = b^2$$
$$M = x_2 \cos \varphi + y_2 \sin \varphi, \quad N = -x_2 \sin \varphi + y_2 \cos \varphi,$$
$$D_1 = \cos \varphi + \tan \varepsilon_1 \sin \varphi, \quad E_1 = -\sin \varphi + \tan \varepsilon_1 \cos \varphi,$$
$$D_2 = \cos \varphi + \tan \varepsilon_2 \sin \varphi, \quad E_2 = -\sin \varphi + \tan \varepsilon_2 \cos \varphi.$$

Equations (18.9)–(18.12) then become

$$\frac{u^2}{A} + \frac{v^2}{B} = 1, \tag{18.15}$$

$$\frac{(M-u)^2}{A} + \frac{(N-v)^2}{B} = 1, \tag{18.16}$$

$$\frac{uD_1}{vE_1} = -\frac{A}{B}, \tag{18.17}$$

$$\frac{(M-u)D_2}{(N-v)E_2} = -\frac{A}{B}. \tag{18.18}$$

The unknowns are the variables A, B, u, and v. From Eqs. (18.15) and (18.16), one
obtains

$$\frac{AN}{BM} = -\frac{M-2u}{N-2v}. \tag{18.19}$$

Because of Eq. (18.17), one then deduces from Eq. (18.19)

$$\frac{D_1 N \cdot u}{E_1 M \cdot v} = \frac{M-2u}{N-2v}. \tag{18.20}$$

Combining Eqs. (18.17) and (18.18) leads to

$$\frac{D_1 u}{D_2 v} = \frac{(M-u)E_1}{(N-v)E_2}. \tag{18.21}$$

These last two equations represent a new equation system for the determination of
the unknown parameters u and v. The unknown parameter v is solved from
Eq. (18.21) with the result

$$v = \frac{D_1 E_2 N \cdot u}{D_2 E_1 M - D_2 E_1 \cdot u + D_1 E_2 \cdot u}. \tag{18.22}$$

This expression is again inserted into Eq. (18.20) from which one finally obtains

$$u = \frac{E_1 M (E_2 M - D_2 N)}{2E_1 E_2 M - (D_2 E_1 + D_1 E_2) N}. \tag{18.23}$$

Substituting this result into Eq. (18.22) leads to the determination of the unknown parameter v as

$$v = \frac{D_1 N (E_2 M - D_2 N)}{(D_2 E_1 + D_1 E_2) M - 2D_1 D_2 N}. \tag{18.24}$$

Finally, Eqs. (18.15) and (18.17) are combined to solve for the unknowns A and B, leading to

$$A = a^2 = u^2 - uv \frac{D_1}{E_1} \tag{18.25}$$

and

$$B = b^2 = v^2 - uv \frac{E_1}{D_1}. \tag{18.26}$$

The elliptical bucket profile so found meets the specified entry and exit conditions. In this case, the rotation angle φ of the ellipse still behaves as a free variable, i.e., as a control parameter. The role played by it is demonstrated in Fig. 18.3. As can be confirmed, the control parameter actually only determines the bucket depth, while all entry and exit conditions remain unchanged. If the bucket depth is specified, then the rotation angle φ is also fixed. At the same time, the vertex point (x_b, y_b) can be determined. To this end, the equations of the fifth boundary condition are further considered. For simplicity the following substitutions are introduced for the calculation:

$$T_1 = x_b \cos \varphi + y_b \sin \varphi - u, \tag{18.27}$$
$$T_2 = -x_b \sin \varphi + y_b \cos \varphi - v. \tag{18.28}$$

Then, it follows from Eqs. (18.13) and (18.14) that

$$\frac{T_1}{T_2} = \frac{a^2}{b^2} \tan \varphi \tag{18.29}$$

and

Fig. 18.3 Functionality of the inclination angle as a control parameter to adjust the appropriate bucket depth
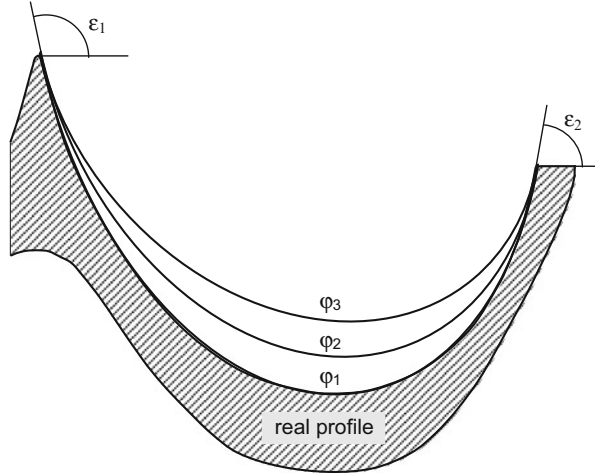
$$\frac{T_1^2}{a^2} + \frac{T_2^2}{b^2} = 1, \tag{18.30}$$

respectively. The parameter T_2 obtained from the first equation is inserted into the second equation from which T_1 is then solved as

$$T_1 = \pm \frac{a^2 \tan \varphi}{\sqrt{a^2 \tan^2 \varphi + b^2}}. \tag{18.31}$$

Two solutions are expected here, since the condition $dy/dx = 0$ is met at two locations on an ellipse. To uniquely determine the solution T_1, Eq. (18.27) is considered. Because in most bucket designs, the effective bucket entry angle $\varepsilon_1 - 90°$, see Fig. 18.2, is greater than the effective exit angle $90° - \varepsilon_2$, one has $\varphi > 0$. Due to $y_b < 0$ and $u > 0$, it is then often the case that $T_1 < 0$.

For the same reason, one obtains from Eq. (18.29)

$$T_2 = -\frac{b^2}{\sqrt{a^2 \tan^2 \varphi + b^2}}. \tag{18.32}$$

From Eqs. (18.27) and (18.28), the coordinates of the vertex point are then calculated as

$$x_b = (T_1 + u) \cos \varphi - (T_2 + v) \sin \varphi, \tag{18.33}$$
$$y_b = (T_1 + u) \sin \varphi + (T_2 + v) \cos \varphi. \tag{18.34}$$

As mentioned earlier, the rotation angle φ of the ellipse behaves as a control parameter, with which the bucket depth is controlled. In other words, the rotation

Fig. 18.4 Longitudinal section of an elliptical bucket profile
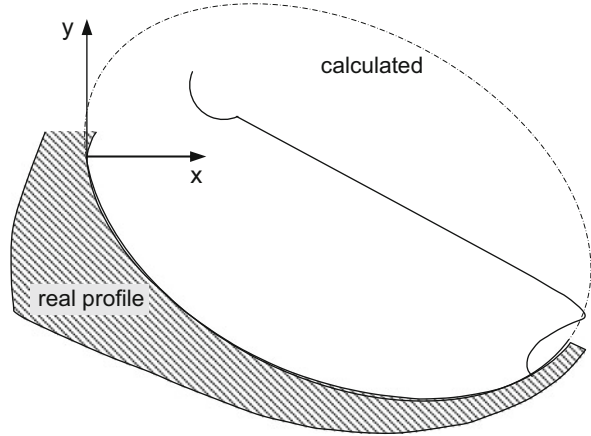
angle must be accordingly adjusted to meet the given bucket depth. In general, the bucket depth in the bucket section on the pitch circle (of diameter D_m) represents a reference depth of the bucket. This depth is referred to as h_2, measured from the bucket trailing edge as shown in Fig. 18.1. The ratio of the bucket depth to the bucket width at the cross section on the bucket pitch circle lies usually in the range

$$\frac{h_2}{B} = 0.275 - 0.285. \tag{18.35}$$

Once the rotation angle of the ellipse is determined by considering the bucket depth, the elliptical bucket profile is fixed that meets all the prescribed conditions according to Figs. 18.1 and 18.2c. The radius of curvature of the bucket inner profile at the bucket bottom is obtained as

$$R = \frac{a^2}{b}. \tag{18.36}$$

One example has already been shown in Fig. 18.3 where it is very close to a real bucket profile of a Pelton turbine which is installed at the Oberhasli Hydroelectric Power Company (KWO). The calculated elliptical bucket profile for the rotation angle φ_1 exactly matches the existing bucket profile. This comparison indicates that the application of the elliptical bucket profile has already been accepted in practice. Figure 18.4 shows another example, at which the longitudinal section of the considered bucket can also be well approximated by an elliptical profile.

Chapter 19
Multi-jet Pelton Turbines

19.1 Minimum Offset Angle Between Injectors

In mountain areas where plenty of water is available, Pelton turbines are often designed with two to maximum six injectors (Fig. 19.1). Of concern in the design is the minimum displacement, i.e., the offset angle between two adjacent injectors. The jet is allowed to enter the bucket only when the bucket is relieved from the loading by the upstream jet.

The minimum necessary offset angle between two adjacent injectors can be determined based on the analyses in Chap. 5. According to Fig. 5.3, the jet piece *abcd* entering a bucket uniquely specifies two special bucket positions α_a and α_d at which the first and the last water particle on the jet surface will get into the bucket. During the interaction with the jet piece *abcd*, the bucket turns an angle $\Delta\alpha$ equal to

$$\Delta\alpha = \alpha_a - \alpha_d. \tag{19.1}$$

For undisturbed operation the offset angle between two injectors must be at least $\Delta\alpha$. The time that the last water particle requires for leaving the bucket does not need to be considered for the time being, since the last particle at point *d* will leave the bucket elsewhere than at the bucket cutout.

According to Fig. 5.3 and by assuming $\alpha_b - \alpha_d = \alpha_{o1} - \alpha_{o2}$, Eq. (19.1) is also written as

$$\Delta\alpha = (\alpha_{o1} - \alpha_{o2}) + (\alpha_a - \alpha_b). \tag{19.2}$$

In Sect. 5.4, it has been pointed out that owing to the symmetry condition, one has $\alpha_{o2} \approx 0$. Thus, the above equation becomes

$$\Delta\alpha = \alpha_{o1} + \alpha_a - \alpha_b. \tag{19.3}$$
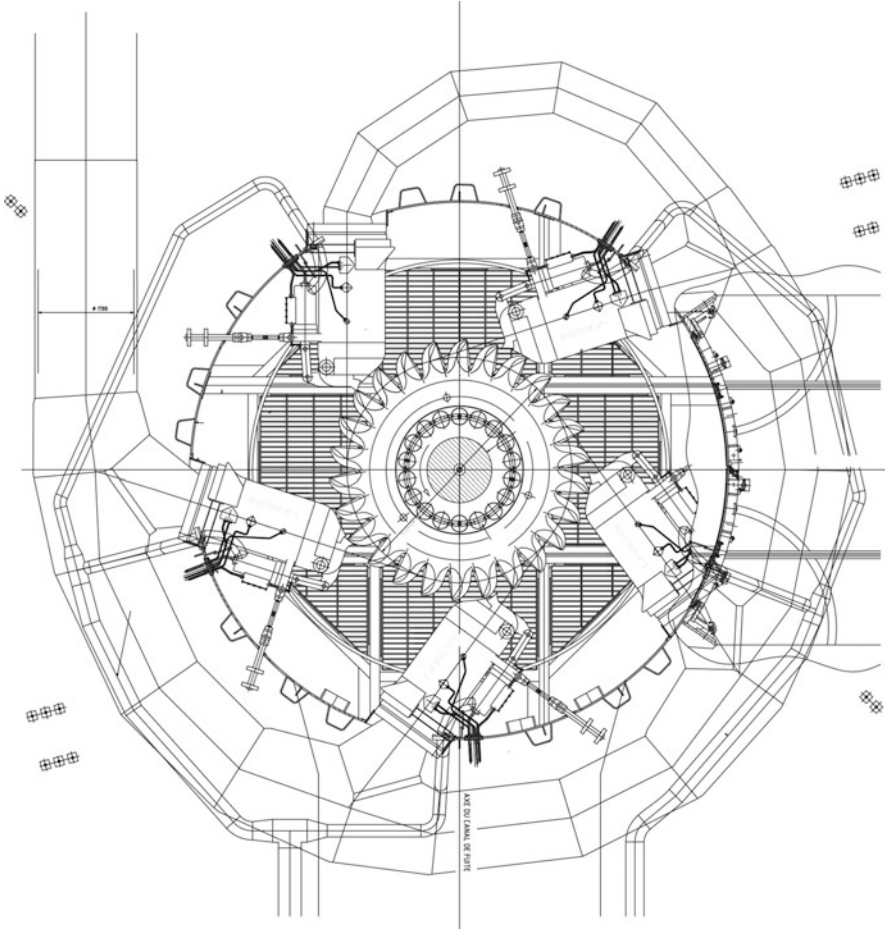
Fig. 19.1 Pelton turbine with five injectors in hydropower plant Bieudron. Hydraulic head $H = 1883\,\text{m}$, nominal flow rate $\dot{Q} = 25\,\text{m}^3/\text{s}$, rotational speed $n = 428\,\text{rpm}$, $n_\text{q} = 0.056\,1/\text{s}$, and power output $P = 423\,\text{MW}$

The aim of further calculations is that the angle difference $\Delta\alpha$ should be represented as a function of the peripheral speed coefficient and the specific speed. The present consideration is focused on the nominal operation so that the bucket volumetric load is set equal to $\varphi_\text{B} = 0.11$. From Eq. (2.29), to which the approach $D_\text{c} - D_\text{m} = 0.85B$ applies, one obtains with $\alpha_\text{o} = \alpha_\text{o1}$

$$\cos\alpha_\text{o1} = \frac{k_\text{m}}{k_\text{m} + n_\text{q}}. \tag{19.4}$$

With the same approximation and from Eqs. (5.9) and (2.27), there follows

Fig. 19.2 Minimum offset angle between two injectors in multi-jet Pelton turbines
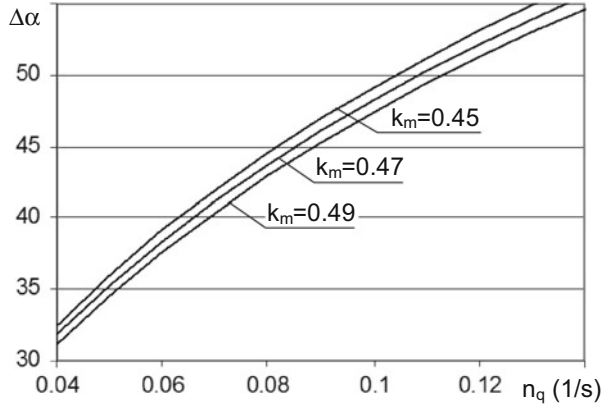
$$\cos \alpha_a = \frac{k_m - 0.38 n_q}{k_m + n_q}. \tag{19.5}$$

Similarly, from Eqs. (5.11) and (2.27), one may deduce

$$\cos \alpha_b = \frac{k_m + 0.38 n_q}{k_m + n_q}. \tag{19.6}$$

Because of Eqs. (19.4), (19.5), and (19.6), the angle difference $\Delta \alpha$ in Eq. (19.3) is a function of the peripheral speed coefficient and the specific speed. The computational results for three different peripheral speed coefficients are shown in Fig. 19.2. At the Pelton wheels with large specific speeds, the angle difference is large too. This circumstance must be taken into account when a two- or multi-jet Pelton turbine is being designed. The offset angle between two adjacent injectors must be greater than the angle given in Fig. 19.2 to prevent the interference between the two jets in the same bucket. Since $\alpha_{o2} = 0$ has been assumed in the above calculations, the calculated angle difference $\Delta \alpha$ is about 1° to 3° smaller than actually required. In the specification of the offset angle between two injectors, such a small angle discrepancy should be considered accordingly. It can also be seen from the calculations that the peripheral speed coefficient only slightly influences the angle difference $\Delta \alpha$. If the peripheral speed coefficient $k_m = 0.47$ is generally used, the above equations accordingly reduce to Eqs. (2.30), (5.10), and (5.12).

19.2 Injector Protection Shelter

In the case of a multi-jet Pelton turbine, it often occurs that the water droplets found on the jet surface at an injector may severely damage the next injector downstream. The formation of the *water-droplet string* is illustrated already in Fig. 4.4. Its direct

fluid dynamic cause is secondary swirling flow in the jet. The initial source, however, is found to be in the swirling flow ahead of the injector, as caused by the bend of the pressure pipeline. Thus, it is almost impossible to avoid the formation of the water-droplet string on the jet surface. The insertion of a flow straightener downstream of the pipe bend, to attenuate the swirl in the flow, is rather difficult to realize. This is because otherwise it would result not only in an undesirable pressure drop in the flow but also in a blockage of the injector.

To protect the downstream injector from the droplet impingement, a well-designed protection shelter is often used. At high hydraulic heads, the droplet impingement is so powerful that the material of the protection shelter only resists for a short period of time. In practice under certain condition, the installation of a water basin on the top of the injector has been proved to be effective. The persistently filled water basin serves to absorb the kinetic energy of the high-speed water droplets. Such an application has already been shown in Fig. 4.5. Because of the inaccurate positioning of the water basin, the material damage has clearly arisen on the basin edge. In some other applications of such water basins, high-level noises in the operation have been reported.

Chapter 20
Geometric and Hydraulic Similarities

In the previous chapters, most relevant hydraulic aspects of Pelton turbines have been analyzed in detail. The analyses and the results contribute to the hydraulic design of Pelton turbines. They serve, on the one hand, to detect the possible potential of further increasing the hydraulic efficiency and, on the other hand, as guidelines for the hydraulic design. From the analyses it emerged, for instance, that viscous friction in the bucket flow causes the biggest loss in hydraulic efficiency of a Pelton turbine. To its minimization, the bucket surface should be kept as smoothly as possible. By contrast, the swirling loss in the exit flow only plays a subordinate role and can effectively not be further reduced.

In the long history of Pelton turbines, developments concerning the hydraulic aspects and efficiencies have been mainly conducted by experimental investigations. Particularly, the flow optimization has been primarily achieved through model tests. In compliance with the general laws of similitude in fluid mechanics, the results of the model tests can be directly applied to the prototypes. For this purpose, therefore, basically both geometric and hydraulic similarities between the model and the prototype are required. However, it is also known that in contrast to the geometric similarity, the hydraulic similarity cannot be fully achieved. For Pelton turbines this fact primarily lies in the Reynolds number because of the viscous effects. On the other hand, however, the high-degree hydraulic similarity in Pelton turbines is rather achieved by other flow parameters like the peripheral speed coefficient and the bucket volumetric load. The discrepancy of the Reynolds numbers between the model and prototype has a weakly perceptible effect on the hydraulic efficiency only. This is mainly due to the fact that friction in Pelton turbines represents the most significant source of hydromechanical losses, and its ratio to other forces depends on the Reynolds number. For this reason, the appropriate conditions for the hydraulic similarity in Pelton turbines should be agreed to without involving the Reynolds number. The resulting deviation in hydraulic efficiency between the model and prototype turbines must be separately estimated. In the terminology of Pelton turbines, for instance, the related method is known as the *scale-up method*, with which the efficiency of the model turbine is scaled up to

the prototype. In the following two sections, both the geometric and hydraulic similarities between two turbines are defined, while the scale-up method and the computational procedure will be explained in the next chapter.

20.1   Geometric Similarity

It has already been concluded in Chap. 2 that the geometric form of a Pelton wheel is basically determined by the specific speed n_q. This is mainly based on Eq. (2.27) in which the ratio of the bucket width to the wheel diameter is determined by the specific speed. The determining equations of other geometric parameters as functions of the specific speed are summarized in Appendix C. On the other hand, however, the specific speed, for instance, does not exactly define the bucket number despite Eqs. (5.27) and (5.30). Therefore, two Pelton wheels of equal specific speed cannot be simply said to be exactly of geometric similarity.

The geometric similarity of two Pelton wheels is only available if the two wheels have equal bucket number and, with respect to all the geometric length scales, also equal aspect ratio. Such a geometric similarity is always required when the hydraulic behavior of a Pelton turbine should be determined by experimental tests with a geometrically similar model. The complete geometric similarity between two Pelton turbines also includes the geometric similarities of the distributors, the injectors, and the turbine casings. Sometimes, this appears to demand too much. From Chaps. 10–12, one knows that for system efficiency the viscous friction in the bucket flow, i.e., on the bucket surface, is most crucial and, thus, decisive. Both the injector and the turbine casing do not exercise a significant impact on the system's efficiency. The hydraulic efficiencies of the injectors, for instance, all remain at about 99 %. For this reason, the geometric similarity between two Pelton turbines could be presumed, if simply the specific speed and the bucket number of two Pelton wheels are equal.

20.2   Hydraulic Similarity

In Chap. 3, the restricted similarity of injector flows has been demonstrated. Except for the head effect on the flow rate, which has been identified in Sect. 3.4 to be a Reynolds number effect, the flows in the injector nozzles of similar geometries are similar. This can be observed by the fact that the dimensionless discharge coefficients as well as their computational formulas according to Eq. (3.12), for instance, all apply to both the model and the prototype Pelton turbines. In particular, there exists also an extended similarity: an injector nozzle with built-in needles of different vertex angles follows the same approach of computing the flow rate when the effective opening area of the nozzle is used as reference area (see Eq. (3.19) and Fig. 3.4). Another point to the hydraulic similarity of the jet is

found in the jet itself. Within a relevant traveling path, the jet expansion can generally be neglected (see Sect. 4.3).

From the viewpoint of fluid mechanics, the flows in geometrically similar buckets also behave similar when all the volume forces in the flow are of the same proportion. Generally, this implies the same differential equations of motion and the same boundary conditions for prototype and model. To meet such similarity conditions, as will be demonstrated, two dimensionless parameters will be applied. For simplicity, the following discussion is limited to frictionless fluids.

First, the flow in a rotating bucket and at the point which is located by the radial position R is considered, as shown in Fig. 20.1. A local cylindrical coordinate system (with r as the radial coordinate) is implemented. Its origin is situated at the center of curvature of the bucket inner surface. Since the stream surface is congruent to the bucket surface, the r-component of the relative flow velocity vanishes. The Euler equation of motion is applicable here; the radial component is given by

$$F_R - \frac{1}{\rho}\frac{\partial p}{\partial r} = -\frac{W^2}{r},\tag{20.1}$$

in which F_R represents the sum of radial components of all existing volume forces. In the rotating system, apart from the neglected gravity force, only the centrifugal and Coriolis forces are effective, which are given by $R\omega^2$ and $2\omega W$, respectively. Thus, the force component F_R in Eq. (20.1) can be replaced by the corresponding components of the centrifugal and Coriolis forces as follows:

$$G_1 R\omega^2 + G_2 2\omega W - \frac{1}{\rho}\frac{\partial p}{\partial r} = -\frac{W^2}{r}.\tag{20.2}$$

In this equation, G_1 and G_2 are the geometric factors for the correction of both force effects. For pure longitudinal flows in the bucket, for instance, according to
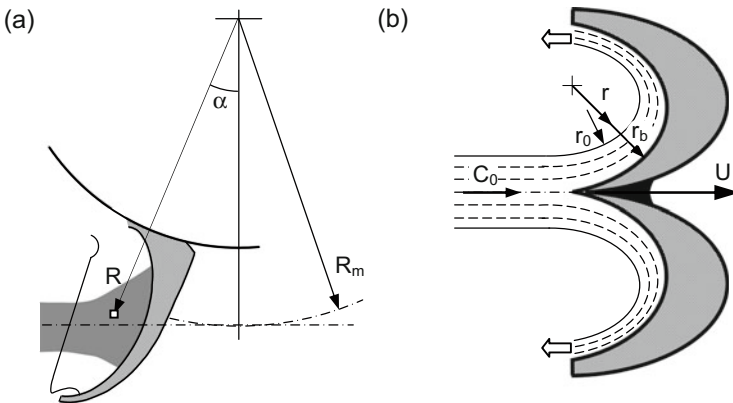

Fig. 20.1 Spreading of the flow in the rotating bucket

Fig. 12.3, the two factors are correspondingly determined as $G_1 = \cos\beta$ and $G_2 = 1$. Equation (20.2) is then equivalent to Eq. (12.13). For approximately two-dimensional cross-flows according to Fig. 5.6, both the centrifugal and Coriolis forces are in the direction parallel to the bucket surface, so that in this situation $G_1 = 0$ and $G_2 = 0$.

For the considered flow at the given position in the bucket according to Fig. 20.1b, Eq. (20.2) is integrated over the height $h = r_b - r_0$ of the water sheet. The overpressure beneath the water sheet is then obtained as

$$\frac{p_b}{\rho} = \int_{r_o}^{r_b} \left(G_1 R\omega^2 + 2G_2\omega W + \frac{W^2}{r} \right) dr. \tag{20.3}$$

The first term in the integration is independent of the integration variable r, while the integration of the second term gives the average relative flow velocity. Thus, from Eq. (20.3) one obtains

$$\frac{p_b}{\rho} = G_1 R\omega^2 h + 2G_2\omega\overline{W}h + \int_{r_o}^{r_b} \frac{W^2}{r} dr. \tag{20.4}$$

For the remaining integration, the mean value theorem of integration is used, so that

$$\int_{r_o}^{r_b} \frac{W^2}{r} dr = \overline{W^2} \int_{r_o}^{r_b} \frac{1}{r} dr = \overline{W^2}\ln\frac{r_b}{r_o} = \overline{W^2}\ln\frac{r_b}{r_b - h} \approx \overline{W^2}\frac{h}{r_b}. \tag{20.5}$$

The approximation made in this equation is based on the assumption $h \ll r_b$.

With the additional assumption, $\overline{W^2} \approx \overline{W}^2$, also because of $h \ll r_b$, Eq. (20.4) is then scaled with the specific kinetic energy, i.e., dynamic pressure, of the jet. One obtains

$$\frac{p_b}{\rho C_0^2/2} = \frac{2h}{R}\frac{\overline{W}^2}{C_0^2}\left(G_1\frac{R^2\omega^2}{\overline{W}^2} + 2G_2\frac{R\omega}{\overline{W}} + \frac{R}{r_b} \right). \tag{20.6}$$

Obviously, there is a hydraulic similarity between the flows in two geometrically similar systems if respective flow-related proportions h/R, $\overline{W}/C_0$, and $R\omega/\overline{W}$ are equal in both systems. Based on this circumstance, the known peripheral speed coefficient and the bucket volumetric load can be derived and demonstrated as the most relevant parameters for the hydraulic similarity.

At first, the reciprocal of $R\omega/\overline{W}$, i.e., $\overline{W}/U$, is considered, with U as the local circumferential speed of the bucket. From the invariance equation, according to Eq. (6.18), one obtains

$$\frac{\overline{W}^2}{U^2} = \frac{\overline{W}_1^2 - U_1^2 + U^2}{U^2} = \frac{\overline{W}_1^2}{U_1^2}\frac{R_1^2}{R^2} - \frac{R_1^2}{R^2} + 1. \tag{20.7}$$

The speed ratio $\overline{W}_1/U_1$ at the bucket entry can be generally represented by the speed ratio U_m/C_0 in applying the velocity triangle. Thus, the speed ratio $\overline{W}/U$ in Eq. (20.7) is ultimately a function of the speed ratio U_m/C_0, which was referred to in previous considerations as the peripheral speed coefficient k_m. Therefore, one has $\overline{W}/U = f(k_m)$. Analogously, the speed ratio $\overline{W}/C_0$ in Eq. (20.6) can also be shown to be a function of the peripheral speed coefficient.

For the parameter h/R in Eq. (20.6), the volume flow rate in the bucket is considered. As indicated in Chap. 12 in association with Eq. (12.10), the water-sheet thickness changes with the spreading of the water in the bucket. In general, this can be formulated as

$$\frac{h}{R} = G\frac{\pi}{8}\frac{1}{R}\frac{d_0^2}{d}\frac{W_{0x,o}}{W}, \tag{20.8}$$

with G as another geometric parameter. For the longitudinal flow through the bucket, the value of G is $G = 2$. Equation (20.8) is then reduced to Eq. (12.10). For the flow transversely across the bucket, $G = 1$ is available; then one obtains Eq. (7.6).

Equation (20.8) connects the flow to the bucket size. Since the relative velocity $W_{0x,o}$ can be expressed as $W_{0x,o} = C_0 - U_m$ (Chap. 7) and, thus, the speed ratio $W_{0x,o}/W$ is a function of the peripheral speed coefficient, Eq. (20.8) is transformed to

$$\frac{h}{R} = G\frac{\pi}{8}\frac{B}{R}\frac{B}{d}\frac{d_0^2}{B^2} \cdot f(k_m). \tag{20.9}$$

The water-sheet width d can be obtained from Eq. (12.11); it is a function of the jet diameter. Thus, the right-hand side of the above equation, except for the function $f(k_m)$, simply represents the geometrical property of a Pelton wheel and the jet diameter. The ratio d_0^2/B^2 is referred to as the bucket volumetric load φ_B, so that Eq. (20.6) is expressible in the general form

$$c_p = \frac{p_b}{\rho C_0^2/2} = f(\text{Geometry, } \varphi_B, k_m). \tag{20.10}$$

From this relation, it can be concluded that between two Pelton turbines with geometric similarity, the hydraulic similarity only exists when the respective peripheral speed coefficients and the bucket volumetric loads are equal. The derived relation also represents the power ratio in a Pelton turbine, as the power exchange between the jet and the rotating buckets ultimately results from the pressure distribution below the water sheet, i.e., on the bucket surface. In Sect. 7.3, the corresponding ratio was designated as the overpressure coefficient; see also Eq. (7.14).

Chapter 21
Model Turbine Tests and Efficiency Scale-Up

Due to the complex flow relations in Pelton turbines, the efforts to improve the flow conditions and to increase the hydraulic efficiency have been limited for a long time mostly to model tests. The transfer of the observation and the measurement results from the model tests to the prototype presumes geometric and hydraulic similarities. From the last chapter, it is known that under the given geometric similarity, the entire similarity between two hydraulic turbines is only achieved when the peripheral speed coefficients and the bucket volumetric loads, both, are equal in both turbines. The condition for the hydraulic similarity, however, is only valid by ignoring the effects of both the gravity and the viscous friction in the flow. The effect of gravity, strictly speaking, is expressed by the fact that the jet, on the one hand and after the injector, is no longer straight-aligned. On the other hand, the gravity of the water in the bucket performs the extra mechanical work owing to the geodetic height difference of the water at the bucket entry and exit, respectively. This influence must be taken into consideration or eliminated when the system efficiency is in focus, which should often be known within an inaccuracy of no more than 0.2 %. The effect of gravity is negligible if the pressure head at the injector is sufficiently high. The jet, after leaving the injector and within the path before reaching the bucket, can be considered to be straight-aligned. For this reason the minimum pressure head for the model tests is prescribed. According to the code IEC60193 (1999) for Pelton turbines, it is about 50 m.

A direct effect of the viscous friction between the flow and the bucket inner surface is the slowdown of the relative flow in the bucket. According to Chaps. 11 and 12, this has negligible impact on the exit swirling loss, so that the flow pattern in the bucket remains nearly unaffected. By contrast and according to Chaps. 10–12, the efficiency of a Pelton turbine is considerably affected by friction because of the related energy dissipation. According to Eq. (15.2), the friction effect is represented by the friction number c_{w2}, i.e., the friction coefficient c_f, and, thus, the Reynolds number. If a model test is conducted, aiming at measuring the turbine efficiency, then different hydraulic efficiencies in the model turbine and its prototype must be expected.

Obviously, in addition to the conditions of both the equal peripheral speed coefficient (k_m) and the equal bucket volumetric load (φ_B), according to Chap. 20, two additional conditions are needed to specify the influences of gravity and the viscous friction on the turbine efficiencies (model and prototype). While the influence of gravity can be eliminated by keeping the minimum pressure head in the model tests sufficiently high, the influence of the viscous friction on the efficiency obviously must be represented as a function of the Reynolds number. The efficiency conversion from the model turbine to the prototype under consideration of the Reynolds number and other influence factors is called the efficiency scale-up.

21.1   Efficiency Scale-Up

To convert the hydraulic efficiencies of a model turbine to the prototype scale, the computational method reported by Grein et al. (1986) has been used for a long time. This is an empirical computational method, which has been developed based on practical operations of Pelton turbines from parameter analyses using the Buckingham Π theorem in dimensional analysis. The computational method has also been stipulated by the IEC standard (1999). In this method, the scale-up calculation of the hydraulic efficiency from the model turbine to the prototype was given by using diverse dimensionless numbers and operation parameters. Besides the bucket volumetric load φ_B, especially the Reynolds, Froude, and Weber numbers have been considered as the decisive influence parameters. It has obviously been supposed that these three dimensionless Π-products independently affect the turbine efficiencies. This assumption was refuted by Zhang (2006) on the fact that, for instance, the Weber number can be precisely interpreted by the Reynolds and the Froude numbers. For this reason, Grein et al.'s computational method was reevaluated by Zhang (2006). The deduced revaluation method as a simplification of the old scale-up method will be presented below. The Weber number is of negligible influence and no longer used.

In the simplified calculations, only the Reynolds and the Froude numbers have been used, as defined by

$$\text{Fr} = \sqrt{\frac{2gH}{gB}}, \tag{21.1}$$

$$\text{Re} = \frac{\sqrt{2gH} \cdot B}{\nu}. \tag{21.2}$$

Here, H and B are the net pressure head and the bucket width, respectively.

The corresponding proportion parameters between the model turbine and its prototype are denoted as

$$C_{Fr} = \frac{Fr_P}{Fr_M}, \tag{21.3}$$

$$C_{Re} = \frac{Re_P}{Re_M}. \tag{21.4}$$

The scale-up calculation of the turbine efficiencies is conducted by considering the difference in the efficiencies between the model and the prototype turbines:

$$\eta_P = \eta_M + \Delta\eta, \tag{21.5}$$

with

$$\Delta\eta = \frac{8.5 \times 10^{-7}}{\varphi_B^2} \left(C_{Fr}^{0.3} C_{Re} - 1 \right) + 5.7 \cdot \varphi_B^2 \left(1 - C_{Fr}^{0.3} \right). \tag{21.6}$$

The corresponding diagrams are shown in Fig. 21.1. It should be noted that from the present calculations with only Reynolds and Froude numbers, highly equal scale-up results are obtained as with the method of Grein et al. (1986) or according to the code IEC60193 (1999).

21.2   Reynolds Number and Jet Impact Force

In this section, the physical meaning of the Reynolds number, defined in Eq. (21.2), will be revealed. According to Eq. (2.34), with $\beta_2 = 180°$, the jet impact force exerted on the bucket is given by

$$F_{\text{bucket}} = 2\dot{m}_c C_0 (1 - k_m)^2. \tag{21.7}$$

The flow rate of the jet is given by $\dot{m}_c = \rho \frac{1}{4}\pi d_0^2 \cdot \sqrt{2gH}$. Its substitution into the above equation, with $C_0 = \sqrt{2gH}$, yields
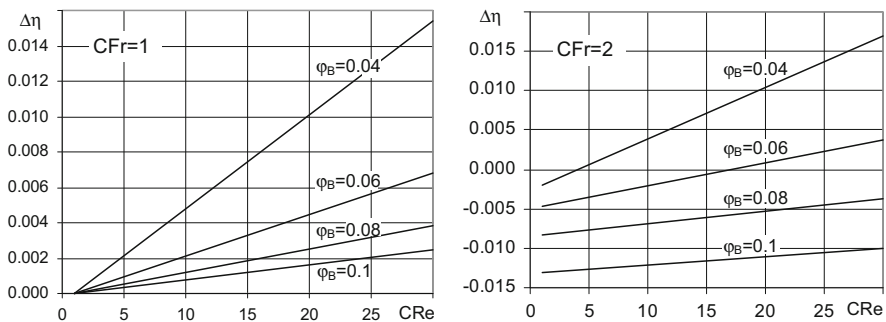

Fig. 21.1   Diagrams for scaling up the efficiencies from the model turbine to the prototype

$$F_{\text{bucket}} = \pi g \rho \cdot d_0^2 (1 - k_{\text{m}})^2 H. \tag{21.8}$$

With respect to the bucket volumetric load $\varphi_{\text{B}} = d_0^2/B^2$, this equation can also be written as

$$F_{\text{bucket}} = \pi g \rho \cdot \varphi_{\text{B}} (1 - k_{\text{m}})^2 H B^2, \tag{21.9}$$

and, when compared with Eq. (21.2),

$$F_{\text{bucket}} = \frac{\pi \rho \nu^2}{2} \varphi_{\text{B}} (1 - k_{\text{m}})^2 \text{Re}^2. \tag{21.10}$$

The Reynolds number in effect represents nothing more than the jet impact force acting on the bucket. Especially for water at 20 °C and for the operation at $\varphi = 0.11$ and $k_{\text{m}} = 0.47$, it becomes

$$F_{\text{bucket}} = 50 \left(\frac{\text{Re}}{10^6} \right)^2 (\text{N}). \tag{21.11}$$

From Eq. (21.10), a dimensionless parameter, equivalent to the Reynolds number, can be defined, referred herein as the *force coefficient*:

$$k_{\text{force}} = \frac{F_{\text{bucket}}}{\rho \nu^2} = \frac{\pi}{2} \varphi_{\text{B}} (1 - k_{\text{m}})^2 \text{Re}^2. \tag{21.12}$$

For $\varphi = 0.11$ and $k_{\text{m}} = 0.47$, one obtains

$$k_{\text{force}} \approx 0.05 \text{Re}^2. \tag{21.13}$$

Although the jet impact force acting on the bucket can be determined from the force coefficient, i.e., from the Reynolds number, it should still be calculated directly from Eq. (21.7) or (21.8).

References

Grein, H., Meier, J., & Klicov, D. (1986). Efficiency scale effects in Pelton turbines. *Proceedings of the XIII IAHR Symposium on Hydraulic Machinery and Cavitation*, Montreal, Canada.

IEC 60193. (1999). Hydraulic turbines, storage pumps and pump-turbines – Model acceptance tests.

Zhang, Zh. (2006). Improvement of scale-up method for efficiency conversion of Pelton turbines. *14th International Seminar on Hydropower Plants* (pp. 63–68), Vienna, Austria.

Chapter 22
Sand Abrasion and Particle Motion in the Bucket Flow

One important issue in the operation of Pelton turbines is the *sand abrasion* in the rotating buckets, which is often called *hydroabrasive wear* or *hydroabrasive erosion*. The problem becomes serious, when the water is richly loaded with suspended sediment particles. This is always encountered where the water from glaciers or river water during/after floods, for instance, is guided to Pelton turbines without previously passing a lake. The sand abrasion often leads to serious mechanical damages on components of Pelton turbines, including the injector nozzles and the buckets. Figure 22.1 shows the sand abrasion on the surface of an injector needle. The sand erosions at the bucket main splitters and on the inner surface of the buckets have been shown in Fig. 5.17. In Chap. 5 (see Sect. 5.10), the effect of eroded main splitters of Pelton buckets on the efficiency drop has been evaluated. Significant such efficiency drops could occur, especially at large relative widths of the eroded bucket splitters (see Figs. 5.22 and 5.23).

The hydroabrasive erosion on the injector needle surface results from both the rapid flow acceleration around the needle vertex and the pressure increase toward the needle surface, which is caused by the streamline curvature (Fig. 3.2). The increased roughness of the needle surface leads to a rise of the frictional shear stress and further to a reduction of the water speed in the jet core. This, in turn, leads to the deterioration of the jet core structure and hence to the increase of turbulence intensities.

For the same reason, the outcomes of the hydroabrasive erosion in the inner surface of Pelton buckets are increases of the surface roughness and the associated fluid friction. This may have serious consequence, because, according to Chaps. 10 and 11, the flow friction between the water and the bucket surface is most effective in downrating the system efficiency. Simply for this reason, a Pelton wheel must be repeatedly dismantled and repaired after a short operation time.

In general, the hydroabrasive erosion on the bucket surface at Pelton turbines must be ascribed to the high speed of flows if compared with the flow, for instance, in a "high-head" Francis turbine. The related hydraulics can be confirmed by making a quantitative comparison between the two types of turbines. The jet

Fig. 22.1 Sand abrasion on the surface of an injector needle after 165 operating hours (Photo KWO)

speed of a Pelton turbine at a head $H = 800\,\text{m}$, for instance, is about $C_0 = 125\,\text{m/s}$. The relative velocity in the Pelton bucket, when the peripheral speed coefficient is assumed to be $k_m = 0.48$, is obtained to be 65 m/s. For comparison reason, a Francis turbine[1] is considered which operates at a head $H = 400\,\text{m}$. The nominal discharge flow is $\dot{Q} = 20\,\text{m}^3/\text{s}$. For the sake of simplicity, the pressure head coefficient of the turbine is assumed to be $\psi = 2$; this concerns the perpendicular inlet flow into the impeller (Fig. 22.2 with $\beta_1 = 90°$). According to the Euler equation, we have $U_1 C_{1u} = C_{1u}^2 = gH$, which alternatively means $W_1^2/gH = \tan^2 \alpha_1$ because $W_1 = C_{1r}$, with C_{1r} as the radial velocity component. With the guide vane angle $\alpha_1 = 15°$ for the nominal flow rate, the relative velocity at the impeller inlet is obtained as $W_1 = \sqrt{gH} \tan \alpha_1 = 17\,\text{m/s}$.

---

[1] The Francis turbine in the hydropower station Gr. 2 of the company KWO at a head of $H = 400$ m and the nominal discharge flow rate $Q = 20$ m^3/s is considered here in the example with a small modification.
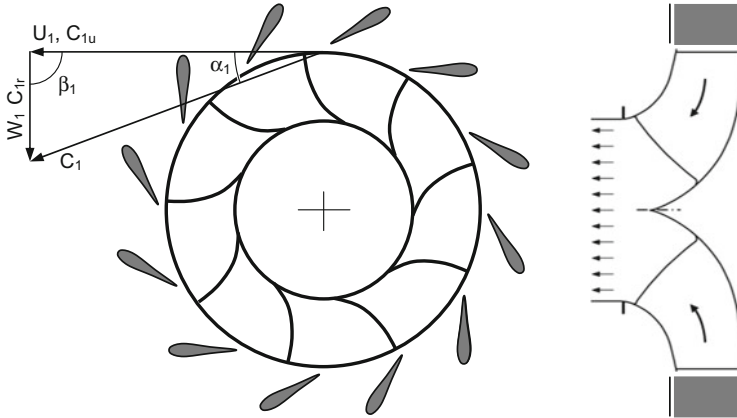
Fig. 22.2 Velocity triangle at the impeller inlet of a Francis turbine with a pressure head coefficient $\psi = 2.0$

Obviously, the relative velocity in the considered Pelton turbine at $W_1 = 65\,\text{m/s}$ is about four times greater than that in the Francis turbine. In other words, a particle in the flow within the buckets of the considered Pelton turbine possesses a kinetic energy which is about 16 times larger than a particle of equal size encountered in the considered Francis turbine. Such a hydraulic performance of particles in Pelton turbines clearly explains why the hydroabrasive erosion in Pelton turbines is a big and serious problem, if compared with other types of turbines. At this point, it is worth additionally mentioning that the power loss due to viscous friction in the considered Pelton turbine is 16 times as high as that in the considered Francis turbine, if equal frictional surfaces are assumed. This is simply because the friction force is proportional to the square of the relative flow velocities.

The primitive and available measure to avoid sand abrasion in Pelton turbines is to shut off the turbines during the flooding flow period. This essentially requires online measurements of sediment particle load in the flooding flow, including the particle concentration and sizes. Corresponding investigations with online measurements of sediment particles can be found, for instance, in Boes (2009), Felix et al. (2012, 2013, 2015), and Gruber et al. (2011).

Sand abrasion in Pelton turbines depends on flow velocity, particle size and concentration, particle hardness, and bucket material. A great number of investigations have been completed about this topic, e.g., Grein and Krause (1994) and Winkler (2014), mainly aiming to describe the phenomena and the related dependences. To protect the bucket surface, a well-improved method against sand abrasion is the coating of the inner surface of the Pelton buckets. The coating technique is based on the thermal spray of hard materials like Stellite and tungsten carbide.

Concerning the hydroabrasive wear in Pelton buckets, one is basically interested how a sand particle in the flow will move across the water sheet toward the bucket surface. Such a cross-motion of particles is mainly determined by the impulsive

force because of the curved streamlines. Besides some qualitative indications as given in Thapa and Brekke (2004), a rough quantitative estimation of the cross-motion of particles was given by Blaser and Bühler (2001) by assuming circular bucket form and constant particle velocity, i.e., a velocity component toward the bucket surface. Because such assumptions are quite far from reality, the conclusion found in Blaser and Bühler (2001) is not quite convincing and often causing disputations. For this reason, a much more accurate estimation of the motion of particles in the water sheet will be presented in this chapter.[2] The analyses and numerical computations presume known bucket profile and flow distribution in the bucket.

22.1 Jet Spreading and Water-Sheet Flow in the Bucket

For simplicity, the jet is assumed to perpendicularly enter the bucket, i.e., perpendicular to the bucket main splitter, as shown in Fig. 22.3. The lateral spreading of the water sheet toward the bucket exit can be approximated by the linear increase of the water sheet width along the bucket surface. Such a flow simplification has already been applied in Chap. 7 [see Eq. (7.8)]. Because of the almost constant relative velocity, the water-sheet thickness is then given by Eq. (7.11). At the bucket exit, the water-sheet width and thickness are $d_{2,\mathrm{N}} = 2.5d_0$ and $h_{2,\mathrm{N}} = 0.05B$, respectively [see Eqs. (7.9) and (7.13)].

Although the water spreading in the bucket is generally three dimensional, for the determination of the relative motions of sand particles in the water sheet,
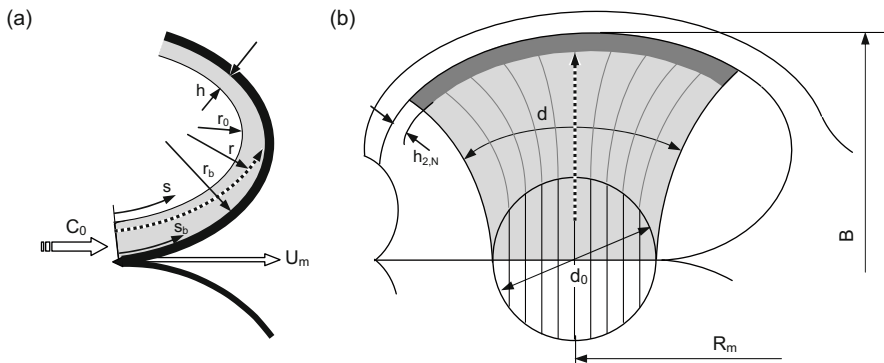

Fig. 22.3 Lateral cross-flow and spreading of the jet in the bucket; modeling of the lateral motion ($R_\mathrm{m} = $ const) of a sand particle in the water sheet

however, the lateral motion of the particle along the path of constant radius (R_m = const) should be considered, as illustrated in Fig. 22.3. With this restriction, both the velocity and pressure distributions within the height of the water sheet are most relevant flow parameters which determine the particle motion in the flow. Because of the presence of the free surface of the water sheet, the interested distributions of velocity and pressure (above the ambient pressure) within the height of the water sheet can be approximated by Eqs. (6.7) and (6.5), respectively, as rewritten here for further considerations:

$$W = W_0 \frac{r_0}{r}, \tag{22.1}$$

$$\frac{p}{\rho} + \frac{1}{2} W^2 = \text{const.} \tag{22.2}$$

The velocity distribution according to Eq. (22.1) supposes, when considered locally within the height of the water sheet, that all curved streamlines are concentric and thus have the same center of curvature. The local radius of curvature of the free surface of the water sheet is denoted by r_0. The radial coordinate r also behaves as the radius of curvature of respective curved streamlines. Such a flow is a potential flow because its initial form, i.e., the jet flow itself, is irrotational.

On the free surface of the water sheet, from bucket inlet to exit, the velocity W_0 remains constant. On the solid surface of the bucket, the flow velocity and the pressure are therefore obtained as

$$W_\mathrm{b} = \frac{r_0}{r_\mathrm{b}} W_0 = \left(1 - \frac{h}{r_\mathrm{b}}\right) W_0, \tag{22.3}$$

$$p_\mathrm{b} = p_0 + \frac{1}{2} \rho \left(W_0^2 - W_\mathrm{b}^2\right). \tag{22.4}$$

For thin water-sheet flows, say $h/r_\mathrm{b} \ll 1$ with r_b as the radius of curvature of the bucket surface, Eq. (22.4) can be approximated to be a function of the height of the water sheet $h = r_\mathrm{b} - r_0$, as found in Eq. (6.10). Because of the concentric streamlines across the height of the water sheet, the radial component of the flow velocity, i.e., perpendicular to the bucket surface, disappears ($W_\mathrm{r} = 0$).

22.2 Motion Equation of Sand Particles

The motion of a sand particle within the water sheet is subjected to Newton's second law of motion. By assuming lateral flow through the bucket (Fig. 22.3), the effects of both the centrifugal and Coriolis forces on the particle motion can be neglected. The deviation of the particle track from the streamlines, as sketched in Fig. 22.3a, is then purely due to the streamline curvatures and the difference in the

specific densities of the water and the particles. While the geometrical pattern and the flow properties of the water sheet are fully representable according to Sect. 22.1, Eqs. (22.1) and (22.2), the particle motion is governed by diverse forces which impose the particle to move across the streamlines and toward the bucket surface. The active external forces, which balance the inertial force of the particle, are mainly the impulsive force owing to the curved flow path of the particle, the pressure force (also known as *buoyancy force*) because of the pressure gradient in the flow, and the viscous force because of the difference in velocities between the flow and the particle. In addition, as a result of nonconstant relative motion of the particle in the water flow, there exists also a force due to the added mass. All these forces must be taken into account, in order to trace the particle in the flow within the bucket.

In general, the relative motion of the particles in the water sheet is unsteady and two-dimensional. As for the first, the particles travel across the streamlines and, thus, do have a nontrivial radial velocity component ($W_{p,r} \neq 0$). As for the second, the carrier flow velocity itself along each streamline, except for that on the free surface of the water sheet under the constant ambient pressure, changes from position to position. This implies that along the streamline the particle will also be accelerated or decelerated. The difference in the stream-wise components of velocities between the water flow and the particle motion, however, can be neglected for small particles, as demonstrated in Appendix F. This approximation will significantly contribute to the computational simplicity.

Therefore, only the radial motion of particles across the streamlines needs to be considered. This implies that only the radial components of all external forces exerted on the particle need to be accounted for.

(a) **Impulsive force**: The impulsive force is caused by the curved track of the particles. Because the particle motion does not coincide with the streamline of the flow, both the curvature of the track of the particle and the particle velocity actually differ from those of the streamlines. For a given particle of diameter d_p and specific density ρ_p, the impulsive force exerted on the particle is calculated as

$$F_{I,r} = \rho_p \frac{1}{6} \pi d_p^3 \frac{W_p^2}{r_p}, \tag{22.5}$$

with r_p as the radius of curvature of the curved track of the particle. For the sake of clearness, the subscript r in the impulsive force is used to denote the radial component, although the impulsive force is actually always radial, i.e., perpendicular to the curved track lines of the particle.

For small particles, however, the tangential, i.e., stream-wise component of the particle velocity, is nearby equal to the velocity of the streamline of the flow ($W_{p,t} \approx W_f$, see Appendix F). Moreover, the radial velocity component (perpendicular to the streamline) of the particle is much smaller than the stream-wise component. For this reason, the curvature of the particle track

can be assumed to be equal to the local curvature of the streamlines ($r_p \approx r$). This further implies that the particle velocity in Eq. (22.5) can be approximated by its stream-wise component and thus by the flow velocity along the streamlines of the flow ($W_p \approx W_f$).

(b) **Pressure force**: According to Eq. (6.4), for the pressure gradient in the flow, the radial component of the pressure force exerted on the particle is given by

$$F_{P,r} = -\frac{1}{6}\pi d_p^3 \frac{\partial p}{\partial r} = -\frac{1}{6}\pi d_p^3 \rho_f \frac{W_f^2}{r}. \tag{22.6}$$

Because of $\partial p/\partial r > 0$, the pressure force is oriented in the negative direction of the r-coordinate.

(c) **Viscous drag force**: The drag force exerted on the particle is proportional to the projection area of the particle and the square of the relative velocity between the particle and the flow. For the radial component, i.e., the component perpendicular to the streamlines ($W_{f,r} = 0$), this is formulated as follows:

$$F_{D,r} = -\frac{1}{4}\pi d_p^2 c_D \frac{1}{2}\rho_f W_{p,r}^2. \tag{22.7}$$

For a velocity component $W_{p,r} > 0$, the drag force is in the negative r-direction. The viscous drag coefficient is actually a function of the particle Reynolds number and can, for $Re_p < 1000$, be approximated by

$$c_D = \frac{24}{Re_p}\left(1 + 0.15 Re_p^{0.687}\right). \tag{22.8}$$

For small spherical particles and small velocities relative to the flow, implying $Re_p < 1$, the Stokes drag law, $c_D = 24/Re_p$, applies. In the real case of Pelton turbines with sand abrasion in the Pelton buckets, the condition $Re_p < 1$ is usually not fulfilled. For a sand particle of the size $d_p = 0.04$ mm and a relative velocity with $W_{p,r} = 2$ m/s, for instance, the Reynolds number is calculated to be about $Re_p = 80$. In the numerical computations, the expression in parentheses in Eq. (22.8), however, can be assumed to be quasi-constant, so that it follows from Eq. (22.7) that

$$F_{D,r} = -3\pi\mu d_p W_{p,r}\left(1 + 0.15 Re_p^{0.687}\right). \tag{22.9}$$

(d) **Force arising from the added mass**: This force is related to the relative acceleration between the particle and the fluid flow. Owing to $W_{f,r} = 0$ and, thus, $W_{p,r} - W_{f,r} = W_{p,r}$ for the radial velocity component, it can be calculated as

$$F_{\text{add,r}} = -\frac{1}{2} \cdot \frac{1}{6} \pi d_{\text{p}}^3 \rho_{\text{f}} \frac{\partial W_{\text{p,r}}}{\partial t}. \tag{22.10}$$

The particle motion in the fluid flow is governed by Newton's second law of motion. For the flow of the particles across the streamlines, i.e., in the radial direction, we, thus, obtain

$$\rho_{\text{p}} \frac{1}{6} \pi d_{\text{p}}^3 \frac{\mathrm{d}W_{\text{p,r}}}{\mathrm{d}t} = F_{\text{I,r}} + F_{\text{P,r}} + F_{\text{D,r}} + F_{\text{add,r}}. \tag{22.11}$$

By inserting all the effective external forces with respect to $r_{\text{p}} \approx r$ and $W_{\text{p}} \approx W_{\text{f}}$, one obtains

$$\left(1 + \frac{\rho_{\text{f}}}{2\rho_{\text{p}}}\right) \frac{\mathrm{d}W_{\text{p,r}}}{\mathrm{d}t} = \left(1 - \frac{\rho_{\text{f}}}{\rho_{\text{p}}}\right) \frac{W_{\text{f}}^2}{r} - \frac{1 + 0.15\text{Re}_{\text{p}}^{0.687}}{\tau} W_{\text{p,r}}, \tag{22.12}$$

in which the time constant τ is defined by

$$\tau = \frac{\rho_{\text{p}} d_{\text{p}}^2}{18\mu}. \tag{22.13}$$

Because the velocity distribution in the water sheet is given by Eq. (22.1), Eq. (22.12) is altered to

$$\left(1 + \frac{1\rho_{\text{f}}}{2\rho_{\text{p}}}\right) \frac{\mathrm{d}W_{\text{p,r}}}{\mathrm{d}t} = W_0^2 \frac{r_0^2}{r^3} \left(1 - \frac{\rho_{\text{f}}}{\rho_{\text{p}}}\right) - \frac{1 + 0.15\text{Re}_{\text{p}}^{0.687}}{\tau} W_{\text{p,r}}. \tag{22.14}$$

This differential equation can be digitized into finite difference form and then numerically solved. The Reynolds number can be assumed to be quasi-constant. With $A = 1 + \frac{1}{2}\rho_{\text{f}}/\rho_{\text{p}}$ and $1/\tau_{\text{Re}} = \left(1 + 0.15\text{Re}_{\text{p}}^{0.687}\right)/\tau$ as well as $\Delta W_{\text{p,r}} = W_{\text{p,r},i} - W_{\text{p,r},i-1}$ and $\overline{W}_{\text{p,r}} = \left(W_{\text{p,r},i-1} + W_{\text{p,r},i}\right)/2$, it then follows from the above equation:

$$
\begin{aligned}
W_{\text{p,r},i} = W_{\text{p,r},i-1} \\
+ \left[\frac{W_0^2}{2A}\left(1 - \frac{\rho_{\text{f}}}{\rho_{\text{p}}}\right)\left(\frac{r_{0,i}^2}{r_i^3} + \frac{r_{0,i-1}^2}{r_{i-1}^3}\right) - \frac{1}{2\tau_{\text{Re},i-1}A}\left(W_{\text{p,r},i} + W_{\text{p,r},i-1}\right)\right]\Delta t.
\end{aligned}
\tag{22.15}
$$

The particle velocity, i.e., its radial component $W_{\text{p,r},i}$ at the ith step of time (t_i), is then resolved as

$$W_{\mathrm{p,r},i} = \frac{1}{1 + \dfrac{\Delta t}{\tau_{\mathrm{Re},i-1}}\dfrac{1}{2A}} \left[\left(1 - \frac{\Delta t}{\tau_{\mathrm{Re},i-1}}\frac{1}{2A} \right) W_{\mathrm{p,r},i-1} + \frac{W_0^2}{2A}\left(1 - \frac{\rho_{\mathrm{f}}}{\rho_{\mathrm{p}}} \right)\left(\frac{r_{0,i}^2}{r_i^3} + \frac{r_{0,i-1}^2}{r_{i-1}^3} \right)\Delta t \right].$$

$$(22.16)$$

It represents a function of $W_{\mathrm{p,r},i} = f(r_i)$ or $W_{\mathrm{p,r},i} = f(t_i)$ because of $r_i = f(t_i)$. The numerical solution of this digitized equation will be shown in the next section.

It should be mentioned that in the estimation of Blaser and Bühler (2001), the force balance only involved the impulsive, pressure, and Stokes drag (for $\mathrm{Re} < 1$) forces. The radial velocity component $W_{\mathrm{p,r}}$ was also assumed to be constant, when applied to the flow along a surface of circular form. For this reason, the results and statements caused vital discussions.

22.3   Application Example

In order to calculate the particle motion in the water sheets of Pelton buckets, as from Eq. (22.16), a concrete flow must be considered. This means that the flow distribution in a given bucket must first be calculated. This includes not only the spreading form of the water sheet in the bucket but also the velocity and pressure distributions within the height of the water sheet as well as along the streamlines. The related numerical computational algorithms will be presented in this section.

22.3.1   Pelton Turbine and Bucket Form

For the computational purpose, a Pelton turbine is considered which is operated by a hydraulic head $H = 650$ m and a flow rate $\dot{Q} = 4\,\mathrm{m^3/s}$ through an injector. The design parameters of the Pelton turbine are given by

$D_{\mathrm{m}} = 2300\,\mathrm{mm}$, $B = 656\,\mathrm{mm}$, $n = 428.6\,\mathrm{rpm}$, $k_{\mathrm{m}} = 0.46$.

With the jet speed $C_0 = \sqrt{2gH} = 113\,\mathrm{m/s}$, the jet diameter is obtained from $\dot{Q} = \frac{1}{4}\pi d_0^2 C_0$, leading to $d_0 = 212\,\mathrm{mm}$. As can be confirmed, it is about one third of the bucket width ($d_0/B \approx 1/3$). With the given circumferential speed coefficient $k_{\mathrm{m}} = 0.46$, the relative velocity in the bucket flow is calculated to $W_0 = C_0 - k_{\mathrm{m}}C_0 = 61\,\mathrm{m/s}$. For the assumed lateral flow across the bucket (see Fig. 22.3) with $R_{\mathrm{m}} = \mathrm{const}$, this relative velocity remains unchanged on the free surface of the water sheet from the bucket inlet to the exit.

As to the form of the Pelton bucket, the elliptical profile is prescribed according to Fig. 18.3, by Eq. (18.8). The profile on the pitch circle of radius $R_{\mathrm{m}} = D_{\mathrm{m}}/2$ (see Fig. 2.5) is specified by the following parameters (lengths in mm):
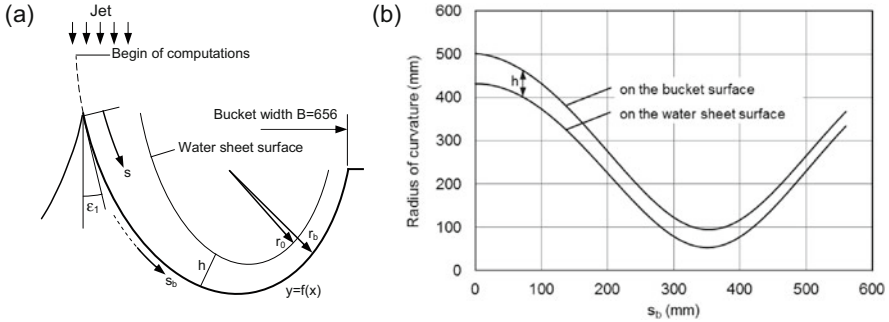
Fig. 22.4 Radii of curvature of the solid surface of the bucket and the free surface of the water sheet

$$a = 165, b = 288, u = 165.2, v = 9.6, \varphi = 12°.$$

Such a bucket profile is shown in Fig. 22.4a.

Since the pressure distribution within the height of the water sheet depends on the curvature of streamlines [see Eqs. (22.1) and (22.2)], the curvature of the surface profile of the Pelton bucket will be applied in further computations. First, one obtains from Eq. (18.8) for the derivatives,

$$y' = \frac{\frac{a^2}{b^2}(x\sin\varphi - y\cos\varphi + v)\sin\varphi + (x\cos\varphi + y\sin\varphi - u)\cos\varphi}{\frac{a^2}{b^2}(x\sin\varphi - y\cos\varphi + v)\cos\varphi - (x\cos\varphi + y\sin\varphi - u)\sin\varphi}, \quad (22.17)$$

$$y'' = \frac{\frac{a^2}{b^2}\left(\sin\varphi - y'\cos\varphi\right)^2 + \left(\cos\varphi + y'\sin\varphi\right)^2}{\frac{a^2}{b^2}(x\sin\varphi - y\cos\varphi + v)\cos\varphi - (x\cos\varphi + y\sin\varphi - u)\sin\varphi}. \quad (22.18)$$

The curvature of the basic profile of the bucket surface is then given by

$$\frac{1}{r_b} = \frac{y''}{\left(1 + y'^2\right)^{3/2}} = f(x, y). \quad (22.19)$$

The curvature of the curved free surface of the water sheet is diminished by the height of the water sheet. This concern is based on the prerequisite that all the streamlines are assumed to be locally concentric, as stated in connection with Eq. (22.1) and illustrated in Fig. 22.4a. Thus, one has

$$r_0 = r_b - h. \quad (22.20)$$

Figure 22.4b shows the computed radii of curvature of both the basic profile of the bucket surface and the free surface of the water sheet, respectively. The difference

between them, from the inlet to the exit of the bucket, is equal to the height of the water sheet for the given flow with $\dot{Q} = 4\,\mathrm{m}^3/\mathrm{s}$.

At this point, the relation between the curvature of the streamlines and the pressure gradient is in focus. As in Fig. 22.4a, when assuming the straight streamlines in the jet before entering the bucket, the abrupt deflection of the jet at the bucket inlet to an angle ε_1 leads computationally to an abrupt change in the curvature of all streamlines. This, in turn, leads to a discontinuity in the pressure distribution at the bucket entrance. To avoid such a computational unsteady discontinuity, the beginning of the flow calculations should, thus, lie some steps ahead of the bucket entrance. This means that the bucket inlet profile should be prolonged to a fictitious entry where $\mathrm{d}y/\mathrm{d}x = \tan(\pi/2) = \infty$ is valid and the curvatures of all streamlines can be simply set equal to zero. From this fictitious point to the bucket inlet, a linear increase of the curvature of the fictitious profile can be assumed.

22.3.2   Flow Distribution in the Bucket

For the purpose of computing the particle motion in the flow, the flow distribution in the bucket must be more precisely described than up to now by simply giving the height and width of the water sheet. On the free surface of the water sheet, the relative velocity remains constant and is equal to $W_0 = 61\,\mathrm{m/s}$ for the considered Pelton turbine in the last section. The flow velocity and the pressure distribution on the bucket surface can be calculated by Eqs. (22.3) and (22.4). The calculation procedure is shown in Table 22.1, in which the coordinate along the bucket surface is computed by $s_\mathrm{b} = \Sigma\Delta s_\mathrm{b}$ with $\Delta s_\mathrm{b} = \sqrt{(\Delta x)^2 + (\Delta y)^2}$. The velocity along the streamline at half height of the water sheet is denoted by $W_{1/2}$. It is simply calculated by Eq. (22.1) with $r_{1/2} = (r_0 + r_\mathrm{b})/2$. The computational results are displayed in Fig. 22.5 as a function of the path s_b along the bucket surface. The pressure is shown in terms of the pressure head (meter of water column). The time which is used by the flow along the bucket surface from entry to exit is about 0.012 s.

From the results, shown in Fig. 22.4 as well as in Fig. 22.5, the velocity gradients $\mathrm{d}W/\mathrm{d}r$ on both the solid surface of the bucket and the free surface of the water sheet can be calculated, as obtained from Eq. (22.1) and given by $\mathrm{d}W/\mathrm{d}r = -W/r$. Based on the numerical data in Table 22.1, the velocity gradients on the bucket surface, at the half height and on the free surface of the water sheet, respectively, are shown in Fig. 22.6 as functions of the path length along the bucket surface. Obviously, the water-sheet flow in the Pelton bucket is a kind of strong shear flow and surely causes the large dissipation and further great losses in the hydraulic efficiency. About the hydraulic aspects of the viscous friction effects, the readers are referred to Chaps. 10–12.

On the other hand, the velocity gradient along an arbitrary streamline appears to be highly significant, when evaluating the capability of particles of tracking the
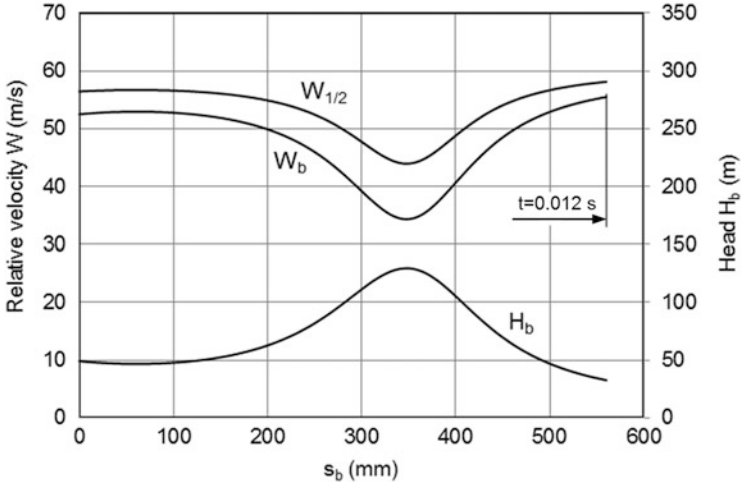
Table 22.1 Numerical solution and computational steps of the flow in the water sheet

x	y	y'	y''	r_b	Δs_b	s_b	d	h	r_0	w_b	$w_{1/2}$	H_b	dw_b/dr	dw_b/ds
mm	mm	–	–	mm	mm	mm	mm	mm	mm	m/s	m/s	m	m/s/m	m/s/m
−11.7	79.4	−15.6	8.11	9999	0.0	−80.3	212	83	9917					
−10.6	65.0	−10.6	2.49	2007	14.5	−65.9	219	81	1927					
−9.0	50.5	−8.0	1.07	1116	14.6	−51.3	226	78	1038					
−6.9	36.0	-6.5	0.56	773	14.6	−36.7	234	76	697					
−4.5	21.6	−5.4	0.33	591	14.7	−22.0	241	73	518					
−1.6	7.2	−4.6	0.21	502	14.7	−7.3	248	71	431					
0.0	0.0	−4.3	0.18	502	7.3	0.0	252	70	432	52.5	56	49	−105	16
1.7	−7.1	−4.1	0.15	501	7.3	7.3	256	69	432	52.6	56	49	−105	14
3.5	−14.2	−3.8	0.12	499	7.3	14.7	259	68	431	52.7	57	48	−106	12
5.4	−21.3	−3.6	0.11	496	7.3	22.0	263	67	429	52.7	57	48	−106	10
..	..	..	..	..	..	..	..	..	..	..	..	..	..	..

Fig. 22.5 Flow velocities and pressure head along the streamlines on the bucket surface (W_b, H_b), and at the half height of the water sheet ($W_{1/2}$)
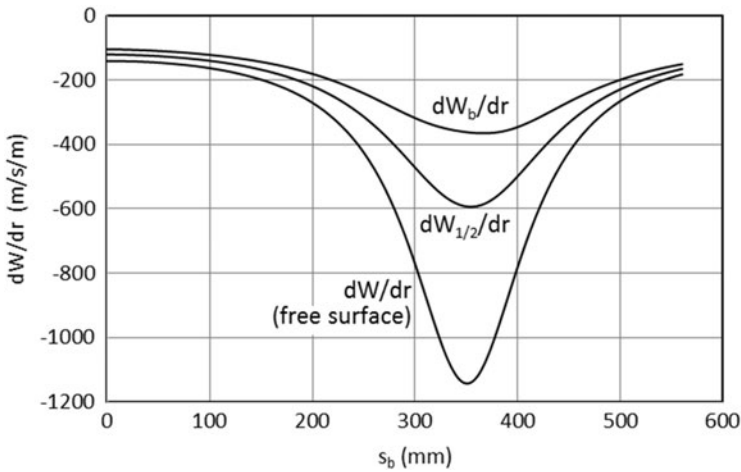

Fig. 22.6 Velocity gradient in the carrier flow transverse to the streamlines on the bucket surface, at the half height and on the free surface of the water sheet, respectively

flow with curved streamlines. On the bucket surface, $(dW/ds)_b$ can be directly obtained from the velocity distribution $W_b(s_b)$, which is involved in Table 22.1 and was also shown in Fig. 22.5. For the velocity gradient along other streamlines, which have their own flow path coordinate unlike that on the bucket surface, the following calculations must be performed:

A streamline at a distance xh from the bucket surface is considered, with h as the local height of the water sheet and x, varying from 0 to 1, as the percentage of h. The flow velocity on the considered streamline is based on Eq. (22.1) and given by

$$W_x = W_0 \frac{r_0}{r_x}. \tag{22.21}$$

The velocity gradient along the given streamline is calculated as

$$\frac{\partial W_x}{\partial s_x} = W_0 \frac{\partial}{\partial s_b} \left(\frac{r_0}{r_x} \right) \frac{ds_b}{ds_x}. \tag{22.22}$$

The chain rule of differentiation is here needed, because in the tabular calculation, the stream-wise coordinate is uniquely given by s_b along the solid surface of the bucket. Thus, the finite change of Δs_b in Table 22.1 can be directly applied. To evaluate the derivative ds_b/ds_x, the relation of $ds_b/ds_x = r_b/r_x$, according to Fig. 22.7a, is applied. It then follows from the above equation with $r_x = r_b - xh = r_b - x(r_b - r_0)$ that

$$\frac{\partial W_x}{\partial s_x} = W_0 \frac{r_b}{r_b - xh} \frac{\partial}{\partial s_b} \left(\frac{r_0/r_b}{1 - x(1 - r_0/r_b)} \right). \tag{22.23}$$

Finally, one obtains

$$\frac{\partial W_x}{\partial s_x} = W_0 \frac{(1-x)r_b^3}{(r_b - xh)^3} \frac{\partial}{\partial s_b} \left(\frac{r_0}{r_b} \right). \tag{22.24}$$

This is the equation from which the stream-wise velocity gradient at the given height xh from the bucket surface can be calculated. The derivative on the right-hand side of the equation can be computed in Table 22.1 by means of $\Delta(r_0/r_b)$ and Δs_b.

At the half height of the water sheet, the velocity gradient along the streamline is obtained with $x = 0.5$. It follows then from Eq. (22.24), with $h = r_b - r_0$, that

$$\frac{\partial W_{1/2}}{\partial s_{1/2}} = \frac{4W_0}{(1 + r_0/r_b)^3} \frac{\partial}{\partial s_b} \left(\frac{r_0}{r_b} \right). \tag{22.25}$$

On the bucket surface, it follows, from Eq. (22.24) with $x = 0$,

$$\frac{\partial W_b}{\partial s_b} = W_0 \frac{\partial}{\partial s_b} \left(\frac{r_0}{r_b} \right), \tag{22.26}$$

which represents an alternative way to the evaluation of $(dW/ds)_b = (\Delta W/\Delta s)_b$ in Table 22.1.
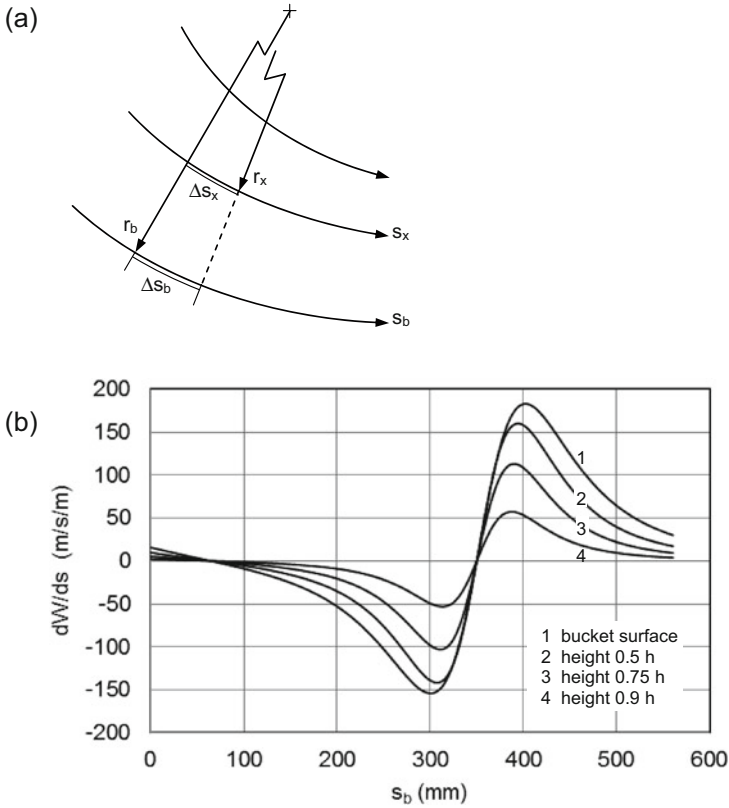
Fig. 22.7 Stream-wise velocity gradient at different heights of the water sheet

Figure 22.7b shows four curves representing the velocity gradients along the streamlines, respectively, on the bucket surface, at 0.5, 0.75, and 0.9 times the height of the water sheet. The maximum magnitude of the stream-wise velocity gradient is about $\partial W_b/\partial s_b = 150\,\text{m/s/m}$ on the bucket surface. This value will be used to confirm the capability of particles in tracking the flow (see the next section).

The calculations in this section are based on the condition that the considered flow in the Pelton bucket is only a function of spatial coordinates but independent of the time. The method applied is actually the Eulerian method. In contrast, the Lagrangian method will be applied in the next section to track the particle motion in the flow.

22.3.3   Particle Motion in the Bucket

The basic equation for the determination of the relative motion of particles in the water sheet is Eq. (22.16). As it states, the calculation presumes knowledge of the actual position r_i of the particle in the flow. This can be obtained, when assuming that the particle, for instance, is initially found on the free surface of the water sheet, by

$$r_i = r_{0,i} + \sum_{j=1}^{i} \Delta r_j = r_{0,i} + \sum_{j=1}^{i} W_{\mathrm{p,r},j}\Delta t_j. \qquad (22.27)$$

In this equation, the radius of curvature $r_{0,i}$ of the free surface of the water sheet changes with time, i.e., the coordinate s_b along the bucket surface. The time and the time interval Δt are referred to the particle motion. It should be mentioned that in further tabular calculations, the time interval Δt is generally not a constant and must be calculated in each numerical step. This is because the numerical step in Table 22.1 is initially determined by x and y values in the first and second column, respectively. Note even the length step Δs_b along the bucket surface is not constant.

For computing the time step Δt, the relation $ds/ds_\mathrm{b} = r/r_\mathrm{b}$, which was applied in deriving Eq. (22.23) from Eq. (22.22) and is also illustrated in Fig. 22.7a, can be again implemented, in the finite form of $\Delta s/\Delta s_\mathrm{b} \approx r/r_\mathrm{b}$, in the following calculation estimation:

$$\Delta t_i = \frac{\Delta s_i}{W_{\mathrm{f},i}} \approx \frac{\Delta s_{\mathrm{b},i}}{W_{\mathrm{f},i}} \frac{r_i}{r_{\mathrm{b},i}}. \qquad (22.28)$$

With the aid of Eqs. (22.27) and (22.28), the radial velocity component $W_{\mathrm{p,r},i}$ of the particle can be calculated from Eq. (22.16). The corresponding radial traveling length of the particle within the time interval Δt is then given by $\Delta r = W_{\mathrm{p,r}}\Delta t$. The cumulative radial length $\Sigma \Delta r_i$ has to be considered to be measured from its initial position on the free surface of the water sheet. After a time $\Sigma \Delta t$ and a stream-wise traveling length $\Sigma \Delta s_\mathrm{b}$, the particle is found at a new position which is given by $\Sigma \Delta r$ beneath the free surface or at a distance $h_\mathrm{p} = h - \Sigma \Delta r$ from the bucket surface (with h as the water-sheet height).

The procedure of the numerical computations is shown in Table 22.2, which, in reality, is a continuation of the calculations in Table 22.1. The local flow velocity W_f is computed by Eq. (22.1) with given r_0 of the free surface and the particle position r_p.

Figure 22.8 shows the stream-wise and the radial velocity components of two particles of different diameters (specific density $\rho_\mathrm{p} = 2650\,\mathrm{kg/m^3}$) as functions of the coordinate s_b along the bucket surface. The lower stream-wise velocity of the large particle against that of the small particle is ascribed to the fact that the large

Table 22.2 Numerical solution and computational steps of the particle motion in the water sheet, continuous calculation of Table 22.1

| r_p	w_f	Δt_p	t_p	$w_{p,r}$	Δr	$\Sigma \Delta r$	τ_{Re}	h_p	F_I	$-F_P$	$-F_D$	$-F_{add}$
		10^{-3}	10^{-3}				10^{-3}		10^{-6}	10^{-6}	10^{-6}	10^{-6}
mm	m/s	s	s	m/s	mm	mm	s	mm	N	N	N	N
9916	61.0	0.00	0.00	0.00	0.00	0.00	0.13					
1927	61.0	0.23	0.23	0.08	0.01	0.01	0.10					
1038	61.0	0.22	0.45	0.17	0.03	0.04	0.09					
697	61.0	0.22	0.67	0.25	0.05	0.08	0.08					
518	61.0	0.21	0.88	0.32	0.06	0.14	0.08					
431	61.0	0.21	1.09	0.38	0.07	0.21	0.07					
432	61.0	0.10	1.19	0.39	0.04	0.25	0.07	69.8	0.32	0.12	0.20	0.00
432	61.0	0.10	1.30	0.39	0.04	0.30	0.07	68.8	0.32	0.12	0.20	0.00
431	61.0	0.10	1.40	0.39	0.04	0.34	0.07	67.8	0.32	0.12	0.20	0.00
429	61.0	0.10	1.51	0.39	0.04	0.38	0.07	66.8	0.32	0.12	0.20	0.00
:	:	:	:	:	:	:	:	:	:	:	:	:
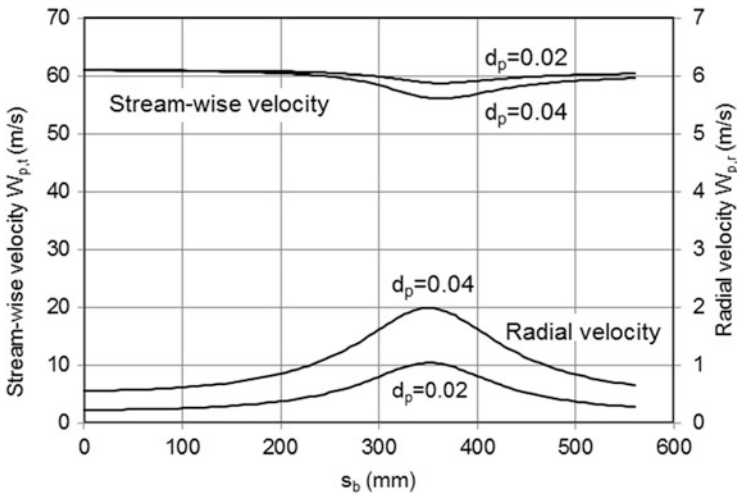
Fig. 22.8 Velocity components of the particles while passing through the bucket (particle initially on the free surface of the water sheet)

particle penetrates toward the bucket surface rather more than the small particle and toward the bucket surface the flow velocity decreases. The radial velocity component of the large particle is remarkably larger than that of the small particle, mainly because of the difference in the impulsive forces. With certain limitations, the radial velocity component is linearly proportional to the particle size.
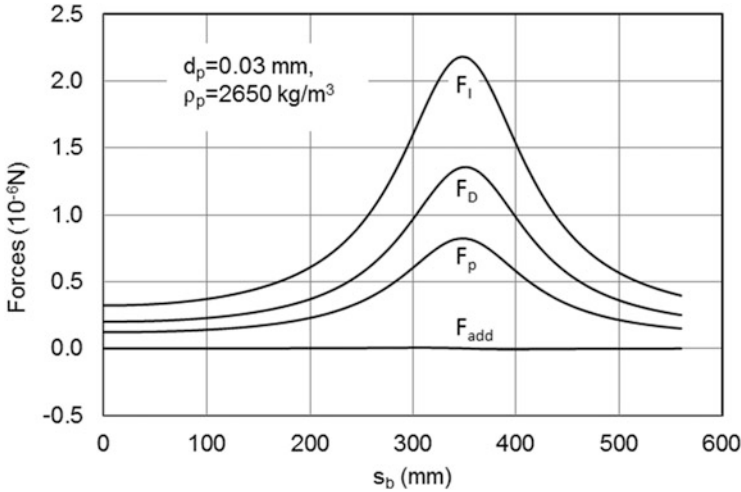
Fig. 22.9 Active forces exerted on the particle, including the impulsive (F_I), viscous drag (F_D) and pressure forces (F_P), as well as the negligible force due to the added mass (F_{add})

While the tangential velocity components of the particles are determined by the flow velocity which changes with the streamlines, the radial velocity components are governed by all external forces exerted on the particles. As the external forces, according to Sect. 22.2, the impulsive force, the pressure force (buoyancy force), the viscous drag force, and the force due to the added mass are considered. While performing the tabular computations in Table 22.2, all these forces are also calculated for a given particle size, as shown in Fig. 22.9 for comparison.

As can be confirmed, the effect of the added mass, which is related to the acceleration or deceleration of the particle relative to the carrier flow, is negligibly small. Because the inertial force of the particle, according to Eq. (22.11), is $2\rho_p/\rho_f$ times of the force due to the added mass after Eq. (22.10), the inertial force of the particle basically is also negligibly small. This implies that the impulsive force is mainly balanced by the pressure and viscous drag forces, as this can also be confirmed in Fig. 22.9.

The position of the particle in the flow is calculated in Table 22.2 by the parameter h_p as the distance from the solid surface of the bucket. For the current example of the Pelton turbine, three particles of different sizes and initially on the free surface of the water sheet are considered. Figure 22.10 shows the computational results. All three particles have not reached the bucket surface.

Figure 22.11 shows the paths of three particles which are again of different sizes but are initially found at the half height of the water sheet. Even in this case, no particle will reach the bucket surface.
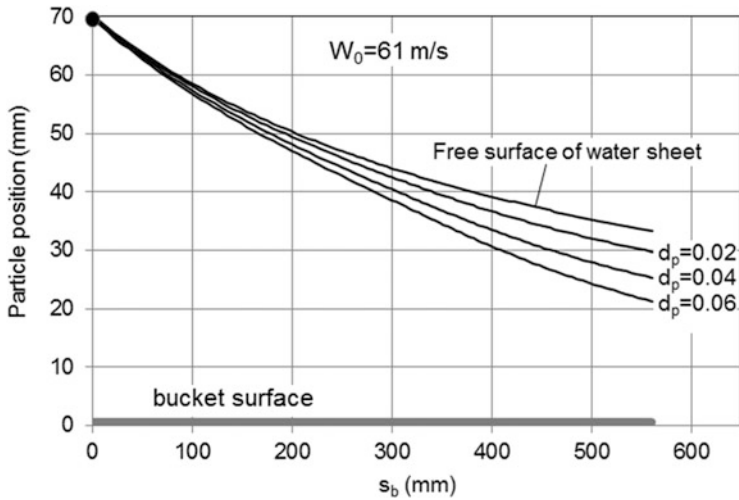
Fig. 22.10 Radial position of the sand particle being initially found on the free surface of the water sheet (relative velocity $W_0 = 61$ m/s)
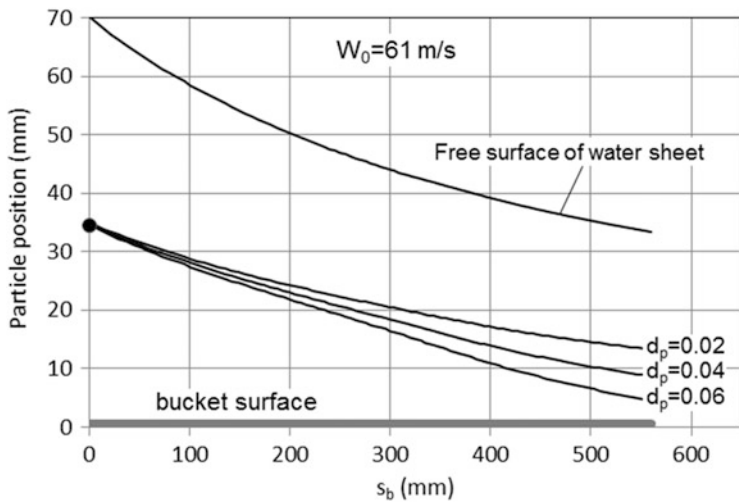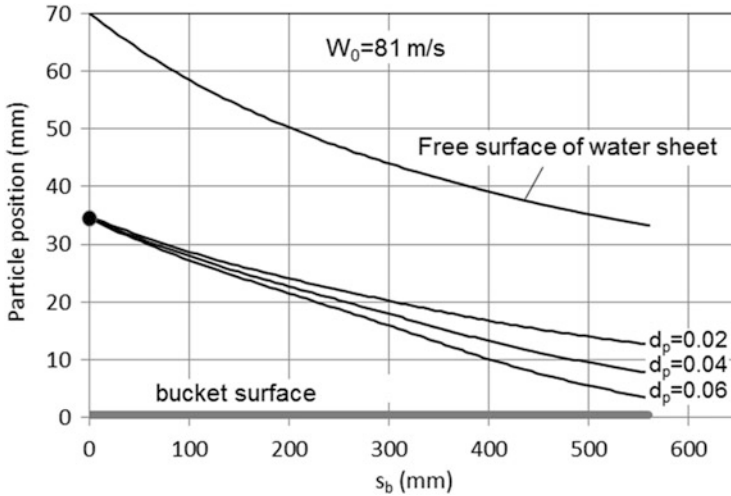

Fig. 22.11 Radial position of the sand particle being initially found at the half height of the water sheet (relative velocity $W_0 = 61$ m/s)

22.3.4 Extended Example

The computational results that have been shown in Fig. 22.11 are related to the operation of a Pelton turbine with a head $H = 650$ m, $\dot{Q} = 4\,\mathrm{m^3/s}$, and a rotational speed $n = 428.6$ rpm (see Sect. 22.3.1). The same Pelton turbine can also be applied

Fig. 22.12 Radial position of the sand particle being initially found at the half height of the water sheet (relative velocity $W_0 = 81$ m/s)

to another hydraulic head, for instance, $H = 1200$ m. The jet speed in this case takes $C_0 = \sqrt{2gH} = 153$ m/s. For keeping the same circumferential speed coefficient $k_m = 0.46$, the Pelton turbine has to run at a rotational speed of $n = 600$ rpm. The relative velocity in the bucket flow is then calculated to be $W_0 = C_0 - k_m C_0 = 81$ m/s. For getting the same jet thickness of $d_0 = 212$ mm, the flow rate is then set to $\dot{Q} = 5.4$ m^3/s.

For such an operation of the Pelton turbine and flow in the Pelton bucket, similar computations (flow distributions and particle track in the flow) as in the forgoing sections can be easily performed. Three particles of different sizes are again assumed to be initially found at the half height of the water sheet. Figure 22.12 shows the computed particle tracks in the flow from the bucket inlet to exit. Against the computational results presented in Fig. 22.11 for the flow velocity $W_0 = 61$ m/s, the particles considered in this extended example move only slightly more toward the bucket surface. This indicates that all volume forces exerted on the particles remain at about the same ratio and are therefore almost independent of the relative flow velocity in the Pelton buckets.

22.4   Simplification of Calculations

In relation with the computational results which are shown in Fig. 22.9, it has been confirmed that the effect of both the volume force due to added mass and the inertial force are all negligibly small. This implies that by neglecting these two forces, the calculations can be significantly simplified. In place of Eq. (22.14), then one has

$$W_{p,r} = \frac{\tau}{1 + 0.15\mathrm{Re}_p^{0.687}} W_0^2 \left(1 - \frac{\rho_f}{\rho_p}\right) \frac{r_0^2}{r^3}. \tag{22.29}$$

For numerical solution, this equation is then written as

$$W_{p,r,i} = \frac{\tau}{1 + 0.15\mathrm{Re}_p^{0.687}} W_0^2 \left(1 - \frac{\rho_f}{\rho_p}\right) \frac{r_{0,i}^2}{r_i^3}. \tag{22.30}$$

In this equation, $r_{0,i}$ is still determined by the water-sheet flow. The calculations in Table 22.1 remain the same. To calculate the radial position r_i of the particle in the flow, Eqs. (22.27) and (22.28) must be again considered and likewise implemented in the numerical calculation in Table 22.2. This represents an easy way to numerically track the particle motion in the water-sheet flow within the Pelton bucket.

A special case is encountered when the carrier flow is a quasi-stationary flow within a bucket of circular form and additionally the water sheet is sufficiently thin against the radius of curvature of the bucket surface ($h/r_b \ll 1$). Because of $r/r_0 \approx 1$, or equivalently $r/r_b \approx 1$, Eq. (22.29) is simplified to

$$W_{p,r} = \frac{\tau}{1 + 0.15\mathrm{Re}^{0.687}} W_0^2 \left(1 - \frac{\rho_f}{\rho_p}\right) \frac{1}{r_b}. \tag{22.31}$$

When the Stokes drag force for $\mathrm{Re}_p < 1$ is again applied [see Eq. (22.8)], then one obtains

$$W_{p,r} \approx \tau W_0^2 \left(1 - \frac{\rho_f}{\rho_p}\right) \frac{1}{r_b}. \tag{22.32}$$

It simply represents a constant particle velocity in the carrier flow. Such a simplification was already applied by Blaser and Bühler (2001). The radial velocity component $W_{p,r}$ is a function of the time constant τ which in turn is a function of the particle size [see Eq. (22.13)]. When two particles of a size ratio $d_{p2}/d_{p1} = 2$ and, thus, of a ratio of the time constants $\tau_{p2}/\tau_{p1} = 4$ are considered, then the ratio between two velocities should be of the same factor and equal to 4. This feature of the particle flow in the Pelton buckets, however, could not be validated, when the radial velocities in Fig. 22.8 for two particle sizes are considered. In Fig. 22.8, the radial velocity of the particle $d_p = 0.04$ mm is approximately only twice the radial velocity of the particle $d_p = 0.02$.

Obviously, the simplification of Eq. (22.32) is not applicable for flows in Pelton buckets. First, the Stokes drag force coefficient is valid only for $\mathrm{Re} < 1$. In the flow within the Pelton buckets with sediment particles of common size, the Reynolds number of the particles is much higher than 1. Second, the assumption $h/r_b \ll 1$

leading to Eq. (22.31) is neither fulfilled, especially, at the bucket bottom where the maximum curvature of the bucket surface is measured. For the considered example, as from Fig. 22.4b, a ratio of $h/r_b \approx 1/3$ at $s_b = 350$ mm can be read off.

References

Blaser, S., & Bühler, J. (2001). Werden durchlaufende Sedimentpartikel in hydraulischen Maschinen fragmentiert? *Wasser Energie Luft, 93*(11/12), 305–311.

Boes, R. (2009). Real-time monitoring of SSC and PSD in the headwater way of a high-head hydropower plant. *Proceedings of the 33rd IAHR Congress* (pp. 4037–4044), Vancouver, Canada.

Felix, D., Albayrak, I., Abgottspon, A., Boes, R., & Gruber, P. (2012), Suspended sediment and Pelton turbine wear monitoring: Experimental investigation of various optical and acoustic devices and beginning of the case study at HPP Fieschertal. *17th International Seminar on Hydropower Plants* (pp. 483–494), Vienna, Austria.

Felix, D., Albayrak, I., Boes, R., Abgottspon, A., Deschwanden, F., & Gruber, P. (2013). Measuring suspended sediment: Results of the first year of the case study at HPP Fieschertal in the Swiss Alps. Hydro 2013, Innsbruck, Austria.

Felix, D., Albayrak, I., & Boes, R. (2015). Field measurements of suspended sediment using several methods. *Proceedings of the 36th IAHR World Congress*, the Hague, the Netherlands.

Grein, H., & Krause, M. (1994). Research and prevention of hydroabrasive wear. *Proceedings of the XVII IAHR Symposium on Hydraulic Machinery and Cavitation*, Beijing, China.

Gruber, P., Staubli, T., Roos, D., & Lüscher, B. (2011). Monitoring water conditions by analyzing ultrasonic signal parameters. Hydro 2011, Practical solution for a sustainable future, Prague, Czech Republic.

Thapa, B., & Brekke, H. (2004). Effect of sand particle size and surface curvature in erosion of hydraulic turbine. *Proceedings of the 22nd IAHR Symposium on Hydraulic Machinery and Systems*, Stockholm, Sweden.

Winkler, K. (2014). Hydro-abrasive erosion: Problems and solutions. *Proceedings of the 27th IAHR Symposium on Hydraulic Machinery and Systems, IOP Conference Series: Earth and Environmental Science* 22.

Chapter 23
Bucket Mechanical Strength and Similarity Laws

23.1 Dynamic Tension in the Bucket Root Area

The buckets of a Pelton turbine are subject to strong dynamic and periodic loads of the jet and therefore highly stressed possibly affecting their material strength. The greatest material stress occurs in the bucket root area. When designing the bucket geometry, great care must always be devoted to ensure that the maximum stress in the bucket root area does not exceed a predetermined threshold value. The forces acting on a bucket are the periodic jet impact force and the constant centrifugal force due to the bucket's own mass. In the prediction of the bucket strength, the maximum jet impact force under full load must always be applied. As derived in Sect. 2.2.3, given by Eq. (2.34), the largest jet impact force occurs for an exit angle $\beta_2 = 180°$. It follows then that

$$F_{\text{bucket}} = 2\dot{m}_{\text{c}} C_{\text{jet}} \cdot (1 - k_{\text{m}})^2. \tag{23.1}$$

A direct estimation of the jet impact force on the rotating bucket is available from Eq. (21.9) for $\varphi = 0.11$ and $k_{\text{m}} = 0.47$; it is given by

$$\frac{F_{\text{bucket}}}{B^2} = \pi g \rho \cdot \varphi_{\text{B}} (1 - k_{\text{m}})^2 H \approx 900H \tag{23.2}$$

and is directly proportional to the pressure head.

In a Pelton bucket, such a jet impact force causes a bending moment, which leads to the greatest mechanical stresses within the bucket section at the bucket root. Because of the complex bucket geometry, the stresses and the stress distribution in the interested bucket section basically can be only accurately computed by means of the finite element methods (FEMs). However, there is often the need to estimate the maximum mechanical stress in the root area of the bucket in a simple way, before a complex FEM computation is undertaken. To this end, the dynamic bucket
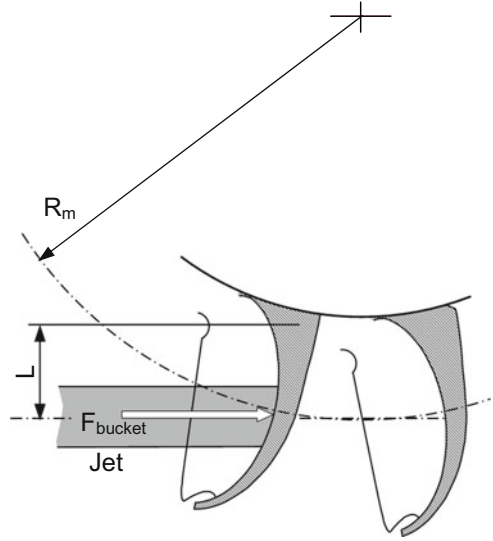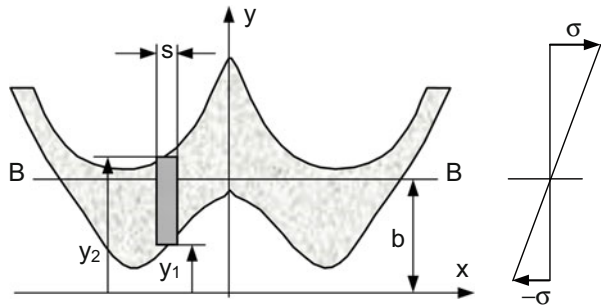
load of Eq. (23.1) should first be considered. The force is assumed to be exerted
tangentially on the pitch circle with diameter $D_m = 2R_m$. According to Fig. 23.1,
the considered cross section is assumed to have a distance L to the pitch circle of the
wheel, so that the bending moment at the interested section can be calculated as

$$M = F_{bucket}L = 2\dot{m}_c C_{jet} \cdot (1 - k_m)^2 L. \tag{23.3}$$

This bending moment causes tensile and compressive stresses in the considered
bucket section. To estimate such mechanical stresses, their linear distribution is
assumed within the cross section. This means, according to Fig. 23.2 with the given
coordinate system, that the normal stresses are linearly distributed perpendicular to
the neutral bending line B-B, viz.,

$$\sigma = a(y - b). \tag{23.4}$$

The distance of the neutral bending line from the reference x-axis is denoted by b which remains for the time being unknown. Also unknown is the constant a in the above equation. It is comprehensible that above the bending axis ($y > b$), tensile stresses are acting, and below it ($y < b$) compressive stresses are present. This stress distribution applies only if the stresses are not yet superimposed by the static stress from the centrifugal force due to the bucket's own mass.

For determining the stress distribution in the bucket cross section, i.e., to determine the unknown constants a and b in Eq. (23.4), the cross section under study is divided into N vertical strips of constant width s. The positions of the lower and upper edges of each strip are denoted by y_1 and y_2, respectively. Since only the bending moment at the observed cross section is present, the sum of all tensile and compressive stresses must be equal to zero. The corresponding condition is thus formulated by

$$\sum_{i=1}^{N} \left[\int_{y_1}^{y_2} \sigma \cdot s \cdot dy \right]_i = a \cdot s \sum_{i=1}^{N} \left[\int_{y_1}^{y_2} (y - b)_i dy \right] = 0. \tag{23.5}$$

After performing the integration in this equation, one obtains

$$\sum_{i=1}^{N} \left[(y_2 - b)_i^2 - (y_1 - b)_i^2 \right] = 0. \tag{23.6}$$

The unknown constant b is then solved to be

$$b = \frac{1}{2} \frac{\displaystyle\sum_{i=1}^{N} (y_2^2 - y_1^2)_i}{\displaystyle\sum_{i=1}^{N} (y_2 - y_1)_i}. \tag{23.7}$$

The neutral bending line B-B has been thus fixed.

The determination of the unknown constant a in Eq. (23.4) arises from the condition that the bending moment obtained from the integration over the bucket section must be equal to the bending moment from Eq. (23.3). The corresponding equilibrium is given by

$$\sum_{i=1}^{N} \left[\int_{y_1}^{y_2} \sigma \cdot s(y - b) \cdot dy \right]_i = M. \tag{23.8}$$

The stress distribution of Eq. (23.4) is used. After performing the integration in the above equation, one obtains the determining equation for the unknown constant a:

$$a\frac{1}{3}s\sum_{i=1}^{N}\left[(y_2-b)_i^3-(y_1-b)_i^3\right]=M. \tag{23.9}$$

The expression on the left side, without the constant a, represents the area moment of inertia J of the considered section area to the reference axis B-B in Fig. 23.2. Thus, Eq. (23.9) takes the form

$$aJ=M. \tag{23.10}$$

The constant a is, thus, also obtainable.

The greatest tensile and compressive stresses in the observed bucket section occur where the maximum and minimum y values among all elemental strips are found. Accordingly, from Eq. (23.4), one follows

$$\sigma_{\text{max, tensile}}=a(y_{\text{max}}-b), \tag{23.11}$$

$$\sigma_{\text{max, compr}}=a(y_{\text{min}}-b). \tag{23.12}$$

Since these stresses are always found on the free surface of the bucket, where no shear stress exists, they may be regarded as the main stresses. They represent, thus, the maximum amplitude of the dynamic alternation of the stresses caused by the jet impingement.

For estimating the bucket strength, the constant centrifugal force due to the rotation of the bucket's own mass must be additionally taken into account. To this end the bucket mass m_{bucket} is assumed to be approximately lying on the pitch circle $(R=D_{\text{m}}/2)$ or just below it at $R=(D_{\text{m}}-0.2B)/2$. Thus, the static centrifugal force is calculated to be

$$F_{\text{B, mass}}=m_{\text{bucket}}R\omega^2. \tag{23.13}$$

The mass of a Pelton bucket can be calculated when the bucket design is put forward in detail. However, for estimating the bucket mass, it can be assumed that the volume of the material of a bucket is about a tenth of the volume which is given by B^3 with B as the bucket inner width. The mass of a Pelton bucket is then estimated as

$$m_{\text{bucket}}=0.1\cdot\rho B^3, \tag{23.14}$$

where ρ is the specific density of the bucket material, e.g., for steel, $\rho\approx 7850\,\text{kg/m}^3$.

Over the considered bucket section (A), the tensile stress, resulting from the centrifugal force, is constant, i.e., of uniform distribution:
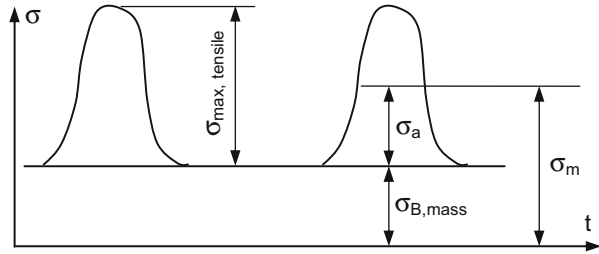
$$\sigma_{\mathrm{B,mass}} = \frac{F_{\mathrm{B,mass}}}{A}. \qquad (23.15)$$

This mechanical stress should be added to Eq. (23.11) in order to obtain the maximum tensile stress in the bucket section at the bucket root. The composition of both stresses ($\sigma_{\mathrm{max,tensile}}$ and $\sigma_{\mathrm{B,mass}}$) has a qualitative form as shown in Fig. 23.3. Turbine manufacturers usually require values of both the average stress σ_{m} and the dynamic stress amplitude σ_{a}. These are calculated by

$$\sigma_{\mathrm{a}} = \frac{\sigma_{\mathrm{max,tensile}}}{2} \qquad (23.16)$$

and

$$\sigma_{\mathrm{m}} = \sigma_{\mathrm{a}} + \sigma_{\mathrm{B,mass}}. \qquad (23.17)$$

23.2   Similarity Laws in the Bucket Mechanical Loading

The static and dynamic loadings of Pelton buckets are basic data for the determination of the mechanical stress states in the considered buckets. To calculate such mechanical stresses, as revealed by the above considerations, only the bucket geometry and the jet impact force are relevant. Although each Pelton turbine is specifically designed with respect to the wheel geometry and the specific speed, the bucket geometries are always more or less similar. In other words, the ratios of the bucket width, length, and depth do not significantly vary from case to case. This property in the bucket geometry can be exploited to considerably simplify the mechanical stress calculations. When, for instance, the mechanical stress state under a given condition is known, then the stress state of Pelton buckets of other dimensions and under any other hydraulic loads can be estimated straightforwardly. This calculation method is based on the similarity laws in the mechanical loadings, as presented below.

Two Pelton wheels with buckets of similar geometries but different bucket sizes (B_1 and B_2) are considered. From Eqs. (23.9) and (23.10), it is known that the area

moment of inertia J has a dimension (m^4). This mechanical property directly leads to

$$\frac{J_2}{J_1} = \frac{B_2^4}{B_1^4}. \tag{23.18}$$

On the other hand, one obtains from Eq. (23.3) with $L_2/L_1 = B_2/B_1$ the ratio of the bending moments as

$$\frac{M_2}{M_1} = \frac{\dot{m}_{c,2} C_{\text{jet},2} (1 - k_{m,2})^2 B_2}{\dot{m}_{c,1} C_{\text{jet},1} (1 - k_{m,1})^2 B_1}. \tag{23.19}$$

From Eq. (23.10) the ratio a_2/a_1 is formed. Taking account of Eqs. (23.18) and (23.19) yields

$$\frac{a_2}{a_1} = \frac{M_2}{M_1} \frac{J_1}{J_2} = \frac{B_1^3}{B_2^3} \frac{\dot{m}_{c,2} C_{\text{jet},2} (1 - k_{m,2})^2}{\dot{m}_{c,1} C_{\text{jet},1} (1 - k_{m,1})^2}. \tag{23.20}$$

Accordingly, it follows from Eq. (23.11) with $\frac{(y_{\max} - b)_2}{(y_{\max} - b)_1} = \frac{B_2}{B_1}$ that

$$\frac{\sigma_{\max,2}}{\sigma_{\max,1}} = \frac{B_1^2}{B_2^2} \frac{\dot{m}_{c,2} C_{\text{jet},2} (1 - k_{m,2})^2}{\dot{m}_{c,1} C_{\text{jet},1} (1 - k_{m,1})^2}. \tag{23.21}$$

Starting with the mechanical stress state for a reference bucket (index 1), the stress state for another geometrically similar bucket (index 2) can directly be calculated. The operation conditions, including the pressure head and the peripheral speed coefficient, do not need to be the same. Compared with Eq. (23.1), it is evident that Eq. (23.21) is actually about the ratio of the jet impact forces, given by

$$\frac{\sigma_{\max,2}}{\sigma_{\max,1}} = \frac{B_1^2}{B_2^2} \frac{F_{\text{bucket},2}}{F_{\text{bucket},1}}. \tag{23.22}$$

This relation is called the *first law of mechanical similarities*. Its applicability can be easily verified by carrying out the FEM calculations on two similar Pelton buckets of different sizes. When the jet impact forces relative to the square of the bucket width are kept to be the same, then equal maximum stresses must arise at both buckets. As an example, corresponding calculations have been performed as shown in Fig. 23.4 for comparison. A scale factor $B_2/B_1 = 2.6$ between two CAD design models of the Pelton wheel was applied. The almost exactly equal stress distributions in the notch area of the two buckets confirm with convincing satisfaction the reliability of the similarity law, i.e., Eq. (23.22).

Equation (23.21) is further simplified for special operation conditions, as considered below for two cases.
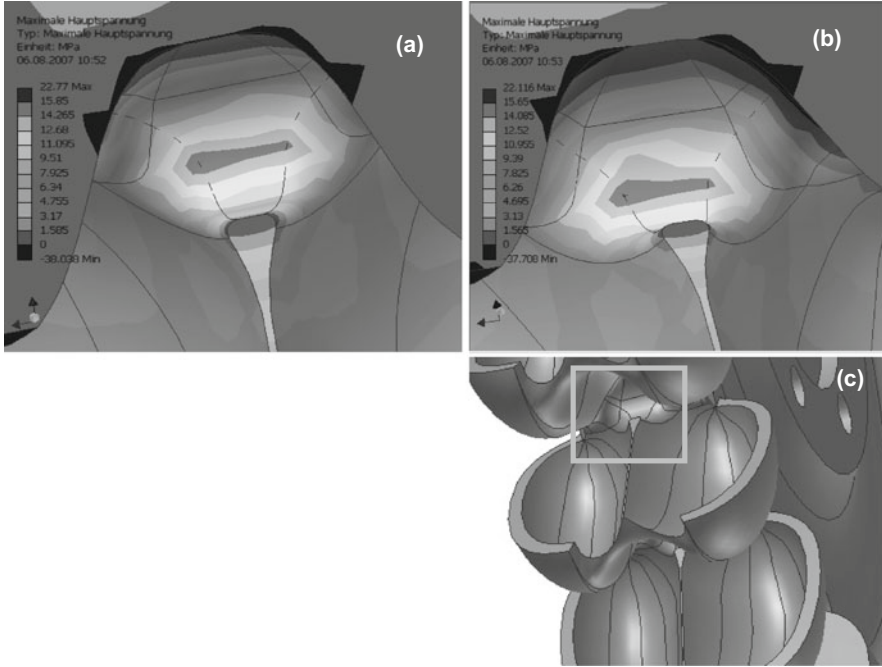
Fig. 23.4 (**a–c**) Stress state and distributions on the bucket surface in the root area obtained with FEM calculations. Comparison between two models of similar geometries and different sizes under similar mechanical loads ($F_{bucket}/B^2 = $ const). (**a**) Original model. (**b**) Model of reduced size by a scale factor 2.6. (**c**) View of the calculation area

Case 1

$k_{m,2} = k_{m,1}$ and $\varphi_{B,2} = \varphi_{B,1}$.

Both turbines operate with the same peripheral speed coefficient and the same bucket volumetric load. The operation condition $\varphi_{B,2} = \varphi_{B,1}$ means, according to Eq. (2.21) with d_0 as the jet diameter, the equality of $d_{0,2}/d_{0,1} = B_2/B_1$. As a result the ratio of the mass flow is calculated to be

$$\frac{\dot{m}_{c,2}}{\dot{m}_{c,1}} = \frac{\pi/4 \cdot d_{0,2}^2 C_{jet,2}}{\pi/4 \cdot d_{0,1}^2 C_{jet,1}} = \frac{B_2^2 C_{jet,2}}{B_1^2 C_{jet,1}}. \tag{23.23}$$

Then, Eq. (23.21) with $C_{jet} = \sqrt{2gH}$ is simplified to

$$\frac{\sigma_{max,2}}{\sigma_{max,1}} = \frac{H_2}{H_1}. \tag{23.24}$$

This relation is called the *second law of mechanical similarity*. It shows that the maximum stress in a bucket cross section is primarily linearly dependent on the

pressure head. At Pelton turbines with high heads (up to 1800 m), special attention must be paid to the material strength of the buckets.

Case 2

$k_m = $ const, $H = $ const, and $B = $ const.

When a Pelton turbine operates under the constant-pressure head, then for variable flow rate, Eq. (23.21) implies

$$\frac{\sigma_{max,2}}{\sigma_{max,1}} = \frac{\dot{m}_{c,2}}{\dot{m}_{c,1}}. \tag{23.25}$$

Under consideration of $\dot{m}_c = \rho_W \frac{1}{4}\pi d_0^2 \sqrt{2gH}$, as well as $H_1 = H_2$ and $B = $ const, it follows further that

$$\frac{\sigma_{max,2}}{\sigma_{max,1}} = \frac{d_{0,2}^2}{d_{0,1}^2} = \frac{\varphi_{B,2}}{\varphi_{B,1}}. \tag{23.26}$$

This relation is called the *third law of mechanical similarity*. It links the stress in the bucket section directly to the hydraulic load of the buckets.

The derived similarity laws have been demonstrated for estimating the maximum stresses occurring at the outside edge (y_{max}) of the cross section of a bucket. In fact, they also apply to calculate the mechanical stresses at any proportional points in the bucket cross section.

Appendix A: Nomenclature

Symbols

Symbol	Unit	Meaning
A	m^2	Area
A_0	m^2	Cross-sectional area of the jet
A_{D0}	m^2	Aperture area of the injector nozzle
A_D	m^2	Opening area of the injector nozzle
b	m	Width of eroded main splitter of the bucket
B	m	Bucket inner width
C_0	m/s	Jet speed
C_{Re}		Reynolds number ratio
C_{Fr}		Froude number ratio
c_f		Friction coefficient
c_w, c_{w2}		Friction numbers
c_p		Overpressure coefficient
d	m	Water-sheet width in the bucket
d_0	m	Jet diameter
d_2	m	Water-sheet width at the bucket exit
D_0	m	Aperture diameter of the injector nozzle
D_a	m	Outside diameter of the Pelton wheel
D_b	m	Inner diameter of the Pelton wheel
D_c	m	Diameter of the bucket cutout edge circle
D_m	m	Pitch circle diameter of the Pelton wheel
D_N	m	Injector needle diameter
D_P	m	Relief piston diameter
D_s	m	Tip circle diameter (main splitter)
e	J/kg	Specific energy, specific work
$\dot{e}$	W/kg	Specific power
E	m^2/s^2	Energy invariance

(continued)

Symbol	Unit	Meaning
$\dot{E}$	J/s	Energy flow rate
F	N	Force
F_{bucket}	N	Jet impact force at a Pelton bucket
F_{jet}	N	Jet impact force at 2λ Pelton buckets (one jet)
F_{wheel}	N	Jet impact force at a Pelton wheel (jet number Z_{jet})
F_{shock}	N	Shock load force at bucket entry
F_{ct}	N/kg	Specific centrifugal force
$F_{B, mass}$	N	Centrifugal force caused by the mass of the bucket
F_{Co}	N/kg	Specific Coriolis force
g	m/s^2	Gravitational acceleration
h	m	Water-sheet height in the bucket
h_2	m	Bucket depth, measured at the bucket exit
h_b	m	Bucket depth, measured at the bucket bottom
h_s	m	Jet layer distance to the wheel axis
h_v	m	Head loss in the injector flow
H	m	Head
I	N	Momentum flow rate
J	kgm^2	Moment of inertia
J	m^4	Area moment of inertia
k_m		Peripheral speed coefficient
$k_{m,cr}$		Critical peripheral speed coefficient
$k_{m,N}$		Nominal peripheral speed coefficient
k_{R0}		Runaway speed coefficient
$\dot{m}_c$	kg/s	Mass flow in the stationary coordinate system
$\dot{m}_w$	kg/s	Mass flow in the rotating system
M	Nm	Torque
n	1/s	Rotational speed
n_{cr}	1/s	Critical speed
n_q	1/s	Specific speed
n_{R0}	1/s	Frictionless runaway speed
n_R	1/s	Runaway speed
N		Number of bucket
p	Pa	Static pressure
P	W	Power
$\dot{Q}$	m^3/s	Flow rate in a Pelton turbine
$\dot{Q}_{jet}$	m^3/s	Flow rate of a jet from an injector
r_a	m	Base circle radius of the bucket trailing edge
r_b	m	Curvature radius of the bucket inner surface
r_s	m	Base circle radius of the bucket main splitter
r, R	m	Radial coordinate
R	m	Radius
R_Q		Reaction degree of the jet
s	m	Needle stroke

Symbol	Unit	Meaning
s	m	Coordinate along the flow path
s_1	m	Jet cutting line length
s_2	m	Jet length
S	m	Length of the flow path from bucket entry to exit
t	s	Time
U	m/s	Peripheral speed
U_m	m/s	Circumferential speed of the pitch circle
W	m/s	Relative flow velocity
x, y, z	m	Coordinate
Y	m^2/s^2	Specific work
Z_{jet}		Number of injectors (jets)

Symbol	Unit	Meaning
α	°	Bucket position angle
α_D	°	Contraction angle of the injector nozzle
α_N	°	Needle vertex angle
α_s	°	Bucket distribution angle
β	°	Relative flow angle
γ	°	Angle in the velocity plan
ε	°	Wedge angle of the main splitter
ε_b	°	Geometric angle at the bucket cutout
η		Ordinate in $\xi-\eta$ coordinate system
η_h		Hydraulic efficiency
η_m		Mechanical efficiency
η_M		Efficiency of the model turbine
η_P		Efficiency of the prototype turbine
η_{Co}		Partial efficiency from the Coriolis force
η_{ct}		Partial efficiency from the centrifugal force
η_d		Partial efficiency from direct friction in the bucket
η_{shock}		Partial efficiency from the shock load force
κ		Time factor
λ		Multi-bucket factor
μ		Friction coefficient in the hydraulic plain bearing
μ	kg/ms	Dynamic viscosity
ν	m^2/s	Kinematic viscosity
ξ		Abscissa in $\xi-\eta$ coordinate system
ρ	kg/m^3	Specific density
σ	Pa	Normal stress
τ	Pa	Shear stress
τ		Position angle of the water particle in the bucket
τ_1, τ_2	s	Time constant
φ		Angle
φ_B		Bucket volumetric load

(continued)

Symbol	Unit	Meaning
φ_{Do}		Discharge coefficient with the reference area A_{D0}
φ_{D}		Discharge coefficient with the reference area A_{D}
ψ		Pressure coefficient
ω	1/s	Angular speed
$\Delta\eta_{\text{diss}}$		Efficiency loss due to the hydraulic dissipation
$\Delta\eta_{\text{swirl}}$		Swirling loss
$\Delta\eta_{\text{wi}}$		Friction and windage losses
$\Delta\eta_{\text{be}}$		Bearing loss
$\Delta\eta_{\mu}$		Frictional hydraulic loss

Indices

0	Ambient pressure
1	Entry
2	Exit
b	Bucket
be	Bearing friction
Co	Coriolis force
ct	Centrifugal force
d	Direct friction
diss	Dissipation
D	Viscous Drag force
F	Fluid
h	Hydraulic
I	Impulsive force
m	Mechanic/mean value
max	Maximum
n	Normal direction of the surface
N	Nominal operation (speed, flow rate, head)
N	Needle
p	Particle
P	Pressure and Pressure force
r	Radial
R	Runaway speed
t	Tangential
tot	Total
wi	Friction and windage
x, y, z	Coordinates

Appendix B: Definition of Derived Parameters

Parameter terms	Definition	References
Jet speed	$C_0 = \sqrt{2gH}$	Eq. (2.1)
Peripheral speed coefficient	$k_m = \frac{U_m}{C_0} = \frac{n\pi D_m}{C_0}$	Eq. (2.18)
Discharge coefficient	$\varphi_{D0} = \frac{\dot{Q}_D}{\pi/4 \cdot D_0^2 C_0}$	Eq. (3.7)
Bucket volumetric load	$\varphi_B = \frac{\dot{Q}_D}{\pi/4 \cdot B^2 C_0} = \left(\frac{d_0}{B}\right)^2$	Eq. (2.21)
Specific speed	$n_q = n\frac{\sqrt{\dot{Q}_D}}{H^{3/4}} = 333 n_y$	Eq. (2.22)
Overpressure coefficient	$c_p = \frac{p_b}{\frac{1}{2}\rho C_0^2} = 2(1-k_m)^2 \frac{h}{r_b}$	Eq. (7.14)
Force coefficient	$k_{force} = \frac{F_{bucket}}{\rho \nu^2}$	Eq. (21.12)
Reaction degree of the jet	$R_Q = \frac{N}{\pi}\left(1-\frac{n}{n_{R0}}\right)\alpha_o$	Eq. (17.7)
Runaway speed coefficient	$k_{R0} = \frac{\alpha_o}{\tan \alpha_o}$	Eq. (17.1)
Max. runaway speed	$n_{R0} = k_{R0}\frac{n_N}{k_{m,Be}}$	Eq. (17.5)
Froude number	$Fr = \sqrt{\frac{2gH}{gB}}$	Eq. (21.1)
Reynolds number	$Re = \frac{\sqrt{2gH}\cdot B}{\nu}$	Eq. (21.2)
Windage number	$Wi = g^{1.5}\frac{(1+2n_q)^5}{n_q^2}$	Eq. (13.10)

Appendix C: Specific Speed and Application in Pelton Turbines

1. Basic Definitions and Equivalent Representations (1/s)

Basic definition	Equivalent 1	Equivalent 2
$n_q = n \dfrac{\sqrt{\dot{Q}_D}}{H^{3/4}}$ Eq. (2.22)	$n_q = 2.63 k_m \dfrac{d_0}{D_m}$ Eq. (2.26)	$n_q = 2.63 k_m \sqrt{\varphi_B} \dfrac{B}{D_m}$ Eq. (2.27)

Because the specific speed clearly reflects the geometric shape of Pelton wheels, they should always be calculated in the basic definition with the nominal flow rate. Correspondingly, both the jet diameter d_0 and the bucket volumetric load φ_B in the equivalent expressions always refer to the nominal operation point.

2. Application for $k_m = 0.47$, $\varphi_B = 0.11$ and $D_c - D_m = 0.85B$

Application	Calculations	References
Jet diameter d_0	$\dfrac{d_0}{D_m} = 0.81 n_q$	Eq. (2.26)
Bucket width B	$\dfrac{B}{D_m} = 2.44 n_q$	Eq. (2.27)
Bucket position a	$\cos \alpha_a = \dfrac{1 - 0.81 n_q}{1 + 2 n_q}$	Eq. (5.10)
Bucket position o	$\cos \alpha_o = \dfrac{1}{1 + 2 n_q}$	Eq. (2.30)
Bucket position b	$\cos \alpha_b = \dfrac{1 + 0.81 n_q}{1 + 2 n_q}$	Eq. (5.12)
Cutout edge D_c	$\dfrac{D_c}{D_m} = 1 + 2 n_q$	Eq. (2.31)
Speed U_c	$\dfrac{U_c}{C_0} = k_m (1 + 2 n_q)$	Eq. (2.33)
Max. peripheral speed coefficient	$k_{m,max} = 0.5 - 0.38 n_q$	Eq. (8.34)
Critical peripheral speed coefficient	$k_{m,cr} = \dfrac{1}{2} \left(\arccos \dfrac{1}{1 + 2 n_q} - \dfrac{\pi}{N} \right) \dfrac{1}{\sqrt{n_q (1 + n_q)}}$	Eq. (16.7)
Energy invariance	$\dfrac{E_o}{C_0^2} = 1 - 2 k_m$	Eq. (6.26)
Energy invariance	$\dfrac{E_b}{C_0^2} = (1 - 2 k_m) - 0.76 n_q$	Eq. (6.28)

(continued)

Application	Calculations	References
Runaway speed coefficient	$k_{R0} = \frac{1}{2} \frac{\arccos\frac{1}{1+2n_q}}{\sqrt{n_q(1+n_q)}}$ $k_{R0} \approx 1 - 1.15n_q$	Eq. (17.2) Eq. (17.3)
Jet piece length s_1	$\frac{s_1}{D_m} = 0.46\sqrt{\frac{n_q}{1+n_q}}$	Eq. (D.10)
Jet piece length ratio	$\frac{s_1}{s_2} \approx \frac{0.5}{1+n_q}$	Eq. (D.14)
Bucket number (theoretical)	$N = \frac{\pi}{k_m} \frac{2\lambda - 1}{\sqrt{n_q(1+n_q)}}$	Eq. (5.27)
Bucket number (practical)	$N = 15 + 1.3\frac{k_m}{n_q} \approx 15 + \frac{0.62}{n_q}$	Eq. (5.29)
Reference angle for the bucket rear side	$\varphi_a = 1500 n_q^2 - 610 n_q + 63$	Eq. (5.45)
Windage number	$\mathrm{Wi} = g^{1.5} \frac{(1+2n_q)^5}{n_q^2}$	Eq. (13.10)

Appendix D: Specification of the Jet Piece for a Bucket

To calculate the interaction between the jet and the rotating buckets, it is necessary to quantify the jet piece that enters a single bucket. Such a jet piece is outlined in Fig. D1 by *abcd*. For simplicity, the bucket is assumed to have a plane cutout edge on the circle of radius R_c. This plane edge begins ($t_a = 0$) to cut off the jet on the jet upper side at the point *a*. The corresponding bucket position is given by angle α_a which is calculated from

$$\cos \alpha_a = \frac{R_m - d_0/2}{R_c}. \tag{D.1}$$

To calculate the intersection line *ab*, a temporal local (x, y) coordinate system is set at the point *a*. At time $t > 0$, the bucket cutout edge is found within the jet and receives the water particle which lays on the intersection line *ab* at the time $t_a = 0$. By considering this, the following relations are established:

$$x + R_c(\sin \alpha_a - \sin \alpha_t) = C_0 \cdot t, \tag{D.2}$$

$$y = R_c(\cos \alpha_t - \cos \alpha_a), \tag{D.3}$$

with $\alpha_t = \alpha_a - \omega t$. The jet speed is denoted by C_0.

Eliminating the time t from these two equations yields

$$\left(\frac{y}{R_c} + \cos \alpha_a\right)^2 + \left[\frac{x}{R_c} + \sin \alpha_a - \frac{C_0}{\omega R_c}\alpha_a + \frac{C_0}{\omega R_c}\arccos\left(\frac{y}{R_c} + \cos \alpha_a\right)\right]^2$$
$$= 1. \tag{D.4}$$

This equation basically describes the intersection line *ab* in the form of the function $y = f(x)$. To simplify this equation, the relation $\cos \alpha_a = (R_m - d_0/2)/R_c$ is applied. Because of $\frac{d_0/2}{R_c} \ll \frac{R_m}{R_c}$ and $\frac{|y - d_0/2|}{R_c} \ll \frac{R_m}{R_c}$, Eq. (D.4) is finally linearized to

Fig. D1 Determination of the jet piece *abcd*

$$\frac{x}{R_c} = \left(\frac{C_0}{\omega R_c} - \frac{R_m}{R_c}\right)\frac{1}{\sqrt{1 - (R_m/R_c)^2}}\frac{y}{R_c}, \tag{D.5}$$

or with $k_m = \omega R_m/C_0$

$$\frac{x}{R_m} = \frac{1}{\sqrt{(R_c/R_m)^2 - 1}}\left(\frac{1}{k_m} - 1\right)\frac{y}{R_m}. \tag{D.6}$$

For $y = d_0$, one has $x = s_1$ according to Fig. D1. It then follows from Eq. (D.6)

$$\frac{s_1}{R_m} = \frac{d_0}{R_m}\frac{1}{\sqrt{(R_c/R_m)^2 - 1}}\left(\frac{1}{k_m} - 1\right). \tag{D.7}$$

The jet piece length s_2 is calculated from the condition

$$\Delta t = \frac{s_2}{C_0} = \frac{2\pi}{\omega \cdot N}, \tag{D.8}$$

so that

$$\frac{s_2}{R_m} = \frac{1}{k_m} \cdot \frac{2\pi}{N}, \tag{D.9}$$

where N is the number of buckets of the Pelton wheel.

Taking account of Eqs. (2.26) and (2.31) and for the common operation setting, $k_m = 0.47$, the partial length of the jet, given in Eq. (D.7), is also shown as a function of the specific speed

$$\frac{s_1}{D_m} = 0.46 \sqrt{\frac{n_q}{1 + n_q}}. \tag{D.10}$$

The aspect ratio s_1/s_2 is calculated from Eqs. (D.9) and (D.10) to

$$\frac{s_1}{s_2} = 0.068 N \sqrt{\frac{n_q}{1 + n_q}}. \tag{D.11}$$

In Sects. 5.4 and 5.5, the number of buckets has been derived in accordance with Eq. (5.27) as functions of the specific speed as follows:

$$N = \frac{\pi}{k_m} \frac{2\lambda - 1}{\sqrt{n_q(1 + n_q)}}. \tag{D.12}$$

Here, λ is called the multi-bucket factor; see Sect. 5.4 and 5.5.

This last equation is inserted into Eq. (D.11). For $k_m \approx 0.47$, the result is

$$\frac{s_1}{s_2} = \frac{0.45(2\lambda - 1)}{1 + n_q} \tag{D.13}$$

and for $\lambda \approx 1.05$

$$\frac{s_1}{s_2} \approx \frac{0.5}{1 + n_q}. \tag{D.14}$$

In general, the value of the length ratio s_1/s_2 lies between 0.43 and 0.46.

Appendix E: Specification of the Bucket Positions

In Appendix D, the jet piece *abcd* that enters a single bucket has been calculated. To assess the interaction between the jet and the rotating buckets, it is further significant to calculate the corresponding position angles of the bucket for each water particle in the depicted jet piece when entering the bucket. According to Fig. E1, the bucket begins ($t = 0$) at the position angle α_a to cut off the jet on the upper surface at point a. Subsequently, the particle at point b on the lower side of the jet reaches the bucket at the bucket position angle α_b (not shown in the figure). These two special bucket positions are directly obtained from Fig. E1 as

$$\cos \alpha_a = \frac{R_m - d_0/2}{R_c}, \qquad (E.1)$$

$$\cos \alpha_b = \frac{R_m + d_0/2}{R_c}. \qquad (E.2)$$

The water particle at the middle point o_1 on the intersection line ab reaches the bucket at the bucket position angle α_{o1}, which is given by

$$\cos \alpha_{o1} = \frac{R_m}{R_c}. \qquad (E.3)$$

The time at which any other water particle in the jet reaches the bucket can be calculated accordingly. To mark the bucket entry, the connection line between the tip of the main splitter and the axis of the Pelton wheel according to Fig. E1 is considered. While this is somewhat arbitrary, it can be regarded as close to reality. In addition, this agreement considerably simplifies the further calculations.

A water particle at an arbitrary point $p(x, y)$ in the jet reaches the bucket at the time t. The corresponding bucket position is given by $\alpha_t = \alpha_a - \omega t$. On the basis of the distance relations shown in Fig. E1, the following relation in the implicit form of $\alpha_t = f(x, y)$ is obtained:

Fig. E1 Jet piece *abcd* with respective bucket positions

$$C_0 t = x + \left(R_m - \frac{d_0}{2}\right) \cdot \tan \alpha_a - \left(R_m - \frac{d_0}{2} + y\right) \cdot \tan \alpha_t. \qquad \text{(E.4)}$$

Considering $k_m = \omega R_m / C_0$ and $\alpha_a - \alpha_t = \omega t$, the above equation is again represented as

$$\frac{x}{R_m} = \frac{\alpha_a - \alpha_t}{k_m} - \left(1 - \frac{d_0}{2R_m}\right) \cdot \tan \alpha_a + \left(1 - \frac{d_0}{2R_m} + \frac{y}{R_m}\right) \cdot \tan \alpha_t. \qquad \text{(E.5)}$$

Obviously, for a water particle which is initially given at $p(x, y)$ in the jet, the corresponding bucket position α_t for receiving this particle has to be iteratively calculated. For two water particles on the jet axis ($y = d_0/2$), respectively, at the points o_1 and o_2, the corresponding bucket position angles are calculated from

$$\frac{s_1/2}{R_m} = \frac{\alpha_a - \alpha_{o1}}{k_m} - \left(1 - \frac{d_0}{2R_m}\right) \cdot \tan \alpha_a + \tan \alpha_{o1} \qquad \text{(E.6)}$$

and

$$\frac{s_1/2 + s_2}{R_m} = \frac{\alpha_a - \alpha_{o2}}{k_m} - \left(1 - \frac{d_0}{2R_m}\right) \cdot \tan \alpha_a + \tan \alpha_{o2}. \qquad \text{(E.7)}$$

From these two equations, one obtains

$$\frac{s_2}{R_m} = \frac{\alpha_{o1} - \alpha_{o2}}{k_m} + \tan \alpha_{o2} - \tan \alpha_{o1}. \qquad \text{(E.8)}$$

With the jet length s_2/R_m, which was calculated in Appendix D by Eq. (D.9), Eq. (E.8) implies

$$\alpha_{o1} - \alpha_{o2} = \frac{2\pi}{N} + k_m(\tan\alpha_{o1} - \tan\alpha_{o2}). \qquad (E.9)$$

With this angle difference, the so-called coincidence condition for describing the interaction between the jet and the rotating bucket was derived (see Sect. 5.4).

Since the bucket position angle α_{o2} normally tends to zero, the approximation $\tan\alpha_{o2} \approx \alpha_{o2}$ can be applied. Thus, from Eq. (E.9) one obtains

$$\alpha_{o2} = \frac{\alpha_{o1} - k_m\tan\alpha_{o1} - 2\pi/N}{1 - k_m}. \qquad (E.10)$$

The angle difference $\alpha_{o1} - \alpha_{o2}$ is then given by

$$\alpha_{o1} - \alpha_{o2} = \frac{k_m(\tan\alpha_{o1} - \alpha_{o1}) + 2\pi/N}{1 - k_m}. \qquad (E.11)$$

The bucket position angles α_c and α_d, at which the initial water particles at c and d on the jet will reach the bucket, are obtained as

$$\alpha_c = \alpha_a - (\alpha_a - \alpha_c) = \alpha_a - (\alpha_{o1} - \alpha_{o2}) \qquad (E.12)$$

and

$$\alpha_d = \alpha_b - (\alpha_b - \alpha_d) = \alpha_b - (\alpha_{o1} - \alpha_{o2}). \qquad (E.13)$$

Here, the approximation $(\alpha_a - \alpha_c) \approx (\alpha_b - \alpha_d) \approx (\alpha_{o1} - \alpha_{o2})$ was applied. The angle difference $(\alpha_{o1} - \alpha_{o2})$ can be obtained from Eq. (E.11).

Appendix F: Particle Motion Along the Streamlines in the Pelton Bucket

The purpose of this appendix is to demonstrate that the difference in the stream-wise, i.e., tangential velocity components between the water flow and the particles is generally negligibly small and, thus, insignificant for small particles. According to Fig. F1, the flow in the first part of the bucket is decelerated because of the increase of the curvature of all streamlines and the resulted pressure gradient towards the bucket surface. For such a deceleration flow, it is generally required to known, how far a spherical sand particle could track the flow. For this purpose, the stream-wise components of all external forces exerted on the particles must be taken into account. These are Stokes drag force, the pressure force, and the force due to added mass.

1. **Viscous Drag force:**
   With the difference in the tangential velocity component $W_{p,t} - W_f$ between the particle and the flow, the viscous drag force exerted on the particle of diameter d_p is computed as

$$F_{D,t} = -\frac{1}{4}\pi d_p^2 c_D \frac{1}{2}\rho_f\left(W_{p,t} - W_f\right)\left|W_{p,t} - W_f\right|. \tag{F.1}$$

   For a great variation range of Reynolds number ($1 < \mathrm{Re} < 1000$), the viscous drag coefficient can be approximated by

$$c_D = \frac{24}{\mathrm{Re}_p}\left(1 + 0.15\mathrm{Re}_p^{0.687}\right). \tag{F.2}$$

   The Reynolds number is calculated with the velocity difference $\left|W_{p,t} - W_f\right|$. With respect to $\left(W_{p,t} - W_f\right) > 0$ in the decelerated flow, Eq. (F.1) is written as

Fig. F1 Water-sheet flow
in the Pelton bucket
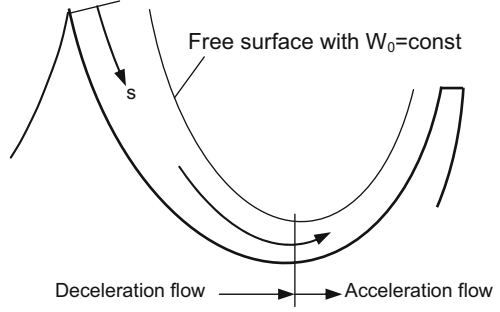
$$F_{\text{D,t}} = -\frac{3\pi\rho_f}{\text{Re}_p} d_p^2 \left(1 + 0.15\text{Re}_p^{0.687}\right)\left(W_{\text{p,t}} - W_f\right)^2. \tag{F.3}$$

2. **Pressure force (buoyancy force):**
   The pressure force exerted on the particle in the direction along the streamlines
   is related with the velocity gradient and given by

$$F_{\text{P,t}} = -\frac{1}{6}\pi d_p^3 \frac{dp}{ds} = \frac{1}{6}\pi d_p^3 \rho_f W_f \frac{dW_f}{ds}. \tag{F.4}$$

3. **Force due to the added mass**
   The force due to the added mass is given by

$$F_{\text{add, t}} = -\frac{1}{2}\frac{1}{6}\pi d_p^3 \rho_f \frac{d\left(W_{\text{p,t}} - W_f\right)}{dt}. \tag{F.5}$$

The motion of the particle in the flow is described by Newton's second law. One
obtains

$$\rho_p \frac{1}{6}\pi d_p^3 \frac{dW_{\text{p,t}}}{dt} = F_{\text{P,t}} + F_{\text{D,t}} + F_{\text{add,t}}. \tag{F.6}$$

Inserting the respective force expressions and with $ds/dt = W_p \approx W_f$ we obtain

$$\frac{dW_{\text{p,t}}}{ds} = \frac{\rho_f}{\rho_p}\frac{dW_f}{ds} - \frac{1 + 0.15\text{Re}_p^{0.687}}{\tau}\left(\frac{W_{\text{p,t}}}{W_f} - 1\right) - \frac{1}{2}\frac{\rho_f}{\rho_p}\frac{d\left(W_{\text{p,t}} - W_f\right)}{ds}. \tag{F.7}$$

In this equation, the time constant is defined by

$$\tau = \frac{\rho_p d_p^2}{18\mu}. \tag{F.8}$$

Due to the flow deceleration in the first half of the bucket, the particle in the flow gets less decelerated than the carrier flow. The flow deceleration in the current case is comparable with the flow in a diffuser. Equation (F.7) is thus equal to the general differential equation for the particle motion in the diffuser or nozzle flow, as given in Zhang (2010). The Reynolds number in Eq. (F.7) may be considered to be quasi-constant. The corresponding solution of Eq. (F.7) has been given in Zhang (2010). The maximum possible ratio of velocities between the particle and the carrier fluid is accordingly found as

$$\left(\frac{W_{p,t}}{W_f}\right)_{max} = 1 - \left(1 - \frac{\rho_f}{\rho_p}\right)\frac{\tau}{1 + 0.15\mathrm{Re}_p^{0.687}}\frac{dW_f}{ds}. \tag{F.9}$$

In Sect. 22.3.2, the flow distribution in a concrete Pelton turbine has been analyzed. As can be read out from Fig. 22.7b, the maximum velocity deceleration along the bucket surface is about $-150(\mathrm{m/s/m})$. The velocity ratio given in the above equation is additionally a function of the density ratio ρ_p/ρ_f and the particle size which is involved in both the time constant τ and the Reynolds number. For a quantitative estimation of the particle behaviors in the decelerated flow, a particle of a diameter $d_p = 0.04\,\mathrm{mm}$ and the density $\rho_p = 2650\,\mathrm{kg/m^3}$ for instance is considered. When the flow velocity is assumed to be $W_f = 60\,\mathrm{m/s}$ and the particle velocity is 1 % more, then the Reynolds number takes $\mathrm{Re}_p = 24$. For the velocity gradient $dW_f/ds = -150\,\mathrm{m/s/m}$, one obtains from Eq. (F.9) $\left(W_{p,t}/W_f\right)_{max} = 1.01$. The particle velocity is only slightly higher than the fluid velocity. The particle can thus be considered to be able to well follow the flows along the streamlines.

Figure F2, based on Eq. (F.9), shows more about the tracing capability of the particle along the streamlines, as the functions of both the deceleration rate of the
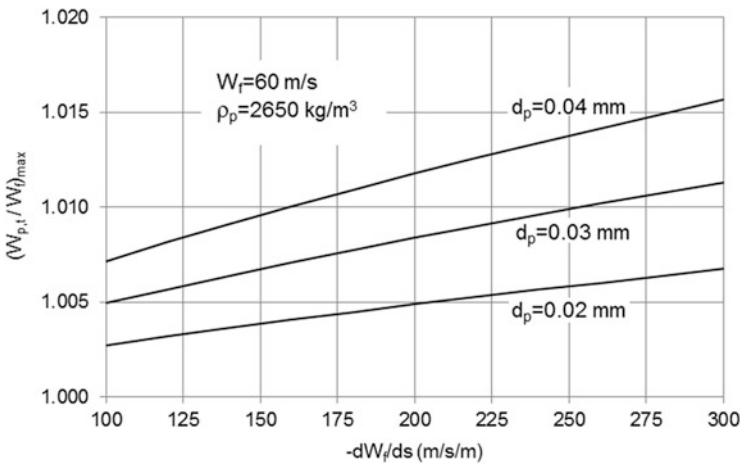
Fig. F2 Maximum velocity ratio of particles to the flow velocity in the water sheet in a Pelton bucket as a function of the velocity deceleration along the streamlines

flow $-(\mathrm{d}W_\mathrm{f}/\mathrm{d}s)$ and the particle size. The Reynolds number in Eq. (F.9) is calculated each time from the calculated velocity W_f by means of the iterative algorithms. In general, it can be confirmed that the particles in the water sheet in the Pelton bucket do well follow the stream-wise flow. The difference in the stream-wise velocity components between the flow and the particles can thus be neglected.

With respect to the small ratio of the radial to the stream-wise components of the particle velocity (see Fig. 22.8), the curvature of the particle path can be approximated to be equal to the curvature of the streamlines of the carrier flow.

Reference

Zhang, Zh. (2010). *LDA Application Methods*. Berlin, Heidelberg: Springer.

References

Haberhauer, H., & Bodenstein, F. (2007). *Maschinenelemente* (14. Auflage). Heidelberg: Springer.

Keck, H., Vullioud, G., & Joye, P. (2000). *Commissioning and operation experience with the world's largest Pelton turbines Bieudron*. Charlotte: Hydro Vision.

Zhang, Zh., & Parkinson, E. (2001). Strömungsuntersuchungen am Freistrahl der Pelton-Turbine und Anpassen des LDA-Verfahrens. 9. GALA-Tagung, Lasermethoden in der Strömungsmesstechnik, Winterthur, Schweiz, Seite 43.1–43.7.

Zhang, Zh., & Parkinson, E. (2002). LDA application and the dual-measurement-method in experimental investigations of the free surface jet at a model nozzle of a Pelton turbine. *11th International Symposium on Applications of Laser Anemometry to Fluid Mechanics*, Lisbon, Portugal.

Index